2008

Magnetic properties of RT2Zn20 R = rare earth, T = Fe, Co , Ru, Rh , Os and Ir

Shuang Jia
Iowa State University

Magnetic properties of RT_2Zn_{20}

R = rare earth, T = Fe, Co , Ru, Rh , Os and Ir

by

Shuang Jia

A dissertation submitted to the graduate faculty

in partial fulfillment of the requirements for the degree of

DOCTOR OF PHILOSOPHY

Major: Condensed Matter Physics

Program of Study Committee:
Paul C. Canfield, Major Professor
Sergey L. Bud'ko
Bruce N. Harmon
Ruslan Prozorov
R. William McCallum
James Cochran

Iowa State University

Ames, Iowa

2008

DEDICATION

I would like to dedicate this thesis to my grandmother Huanyun Ping. You will live in my heart forever. I would like to thank my lovely wife Lei, who has been one of the most important parts of my life and supported me through the time when nobody else could have. Finally I would also like to thank my parents and parents in law for their loving help during the writing of this work.

TABLE OF CONTENTS

LIST OF TABLES vi

LIST OF FIGURES vii

CHAPTER 1. Introduction 1

CHAPTER 2. Overview of the magnetic properties of rare earth and transition metal intermetallic compounds 7

2.1 $4f$ electron and local moment magnetism 8

2.1.1 Hund's rules 10

2.1.2 Magnetic moment and Curie law 10

2.1.3 Weiss Molecular field theory 13

2.1.4 Arrott plot 14

2.1.5 RKKY interaction and de Gennes scaling 16

2.2 d electron and Itinerant magnetism 17

2.2.1 Pauli paramagnetism 18

2.2.2 Stoner theory 20

2.3 Crystalline Electric field 23

2.3.1 Steven's equivalent operators 24

2.3.2 Cubic symmetry 24

2.4 Heavy fermion compounds 27

2.4.1 Anderson Model 28

2.4.2 Single ion Kondo effect 31

2.4.3 Physical properties of heavy Fermions 33

CHAPTER 3. Crystal structure of RT_2Zn_{20} compounds 39

CHAPTER 4. Experiment methods 44

4.1 Crystal Growth 44

4.2 Measurement methods 48

4.2.1 X-ray diffraction measurements 48

4.2.2 Magnetization measurement 49

4.2.3 Resistivity measurement 50

4.2.4 Specific heat measurement 51

CHAPTER 5. Nearly ferromagnetic Fermi-liquid behavior in YFe_2Zn_{20} and high-temperature ferromagnetism of $GdFe_2Zn_{20}$ 52

5.1 Introduction 52

5.2 Results and analysis 53

5.3 Discussion 58

5.4 Conclusion and Summary 60

CHAPTER 6. Variation of the magnetic ordering in GdT_2Zn_{20} (T= Fe, Ru, Os, Co, Rh and Ir) and its correlation with the electronic structure of isostructural YT_2Zn_{20} 62

6.1 Introduction 62

6.2 Results and analysis 63

6.2.1 GdT_2Zn_{20}(T = Fe, Co, Ru, Rh, Os and Ir) 63

6.2.2 YT_2Zn_{20}(T = Fe, Co, Ru, Rh, Os and Ir) 77

6.2.3 Electronic Structure 82

6.3 Discussion 87

6.4 Summary 91

CHAPTER 7. Magnetic properties of $Gd_xY_{1-x}Fe_2Zn_{20}$: dilute, large, S-moments in a nearly ferromagnetic Fermi liquid 93

7.1 Introduction 93

7.2 Experimental Methods 94

7.3 Experiments Results 96
7.4 Analysis and Discussion 111
7.5 Summary 117

CHAPTER 8. Magnetic properties of RFe_2Zn_{20} and RCo_2Zn_{20}(R = Y, Nd, Sm, Gd - Lu) 118

8.1 Introduction 118
8.2 Experiments and Results 120
8.2.1 Y(Lu)Fe_2Zn_{20} and Y(Lu)Co_2Zn_{20} 120
8.2.2 RCo_2Zn_{20} (R = Nd, Sm, Gd - Tm) 127
8.2.3 RFe_2Zn_{20} (R = Gd - Tm) 140
8.2.4 $YbFe_2Zn_{20}$ and $YbCo_2Zn_{20}$ 157
8.3 Data Analysis and Discussion 160
8.4 Summery 171

CHAPTER 9. Thermodynamic and transport properties of YbT_2Zn_{20} (T= Fe, Ru, Os, Co, Rh and Ir) 172

9.1 Introduction 172
9.2 Result 173
9.3 Data Analysis 175
9.4 Discussion 181

CHAPTER 10. Summary and Conclusion 182

APPENDIX A. Sample dependent, magnetic transitions for $TbFe_2Zn_{20}$ . . . 184

APPENDIX B. Determination of CEF parameters of RT_2Zn_{20} system by point charge model 186

BIBLIOGRAPHY 187

LIST OF TABLES

Table 2.1 Properties of the ground state for the magnetic rare earth ions 11

Table 3.1 Summary of attempted growth of RT_2Zn_{20} compounds 41

Table 3.2 Atomic coordinates and refined site occupancies for $GdFe_2Zn_{20}$ and $GdRu_2Zn_{20}$ 43

Table 6.1 Thermodynamic and transport properties for GdT_2Zn_{20} (T = Fe, Ru, Os, Co, Rh, Ir) 73

Table 6.2 Low temperature thermodynamic properties of YT_2Zn_{20} (T = Fe, Ru, Os, Co, Rh, Ir) 82

Table 6.3 Calculated electronic properties for YT_2Zn_{20} and GdT_2Zn_{20} (T = Fe, Ru and Co) 87

Table 8.1 Thermodynamic and transport properties for RCo_2Zn_{20} compounds (R = Nd, Gd - Yb) 131

Table 8.2 CEF parameters of RCo_2Zn_{20} compounds (R = Nd, Tb - Yb) 140

Table 8.3 Thermodynamic and transport properties for RFe_2Zn_{20} compounds (R = Gd - Yb) 142

Table 9.1 Summary of structural, thermodynamic and transport properties on YbT_2Zn_{20} compounds (T = Fe, Co, Ru, Rh, OS and Ir) 180

LIST OF FIGURES

Figure 2.1 Radial extent of different shells in the free gadolinium ion 9

Figure 2.2 Diagram of Arrott's plot 15

Figure 2.3 Diagram of Pauli paramagnetism 19

Figure 2.4 Diagram of Stoner theory 21

Figure 2.5 CEF induced magnetic properties of Yb^{3+} in cubic symmetry 26

Figure 2.6 Diagram of Anderson model 30

Figure 2.7 Diagram of the AFM interaction formation in Anderson model 31

Figure 2.8 Schematic diagram of the resistivity Kondo minimum 32

Figure 2.9 Low-temperature magnetic behavior of a diluted Kondo system 34

Figure 2.10 Doniach's phase diagram 35

Figure 2.11 Susceptibility and specific heat of the Coqblin-Schrieffer model 37

Figure 3.1 Crystal structure of RT_2Zn_{20} compounds 40

Figure 3.2 Lattice constants of GdT_2Zn_{20} and YT_2Zn_{20} 42

Figure 3.3 Lattice constants for RFe_2Zn_{20} and RCo_2Zn_{20} 42

Figure 4.1 Binary phase diagram of Gd - Zn and Fe - Zn 45

Figure 4.2 Growth profile of RFe_2Zn_{20} single crystals 46

Figure 4.3 Single crystal of YFe_2Zn_{20} 48

Figure 5.1 T-dependent thermodynamic and transport properties for $GdFe_2Zn_{20}$ and $GdCo_2Zn_{20}$ 53

Figure 5.2 Magnetic properties of $GdFe_2Zn_{20}$ and $GdCo_2Zn_{20}$ 54

Figure 5.3 Density of states for $LuFe_2Zn_{20}$ and $LuCo_2Zn_{20}$ 55

Figure 5.4 Lattice constants of $Gd(Fe_xCo_{1-x})_2Zn_{20}$ and $Y(Fe_xCo_{1-x})_2Zn_{20}$ 56
Figure 5.5 T-dependent thermodynamic properties for $Y(Fe_xCo_{1-x})_2Zn_{20}$ 56
Figure 5.6 Magnetic properties of $Gd(Fe_xCo_{1-x})_2Zn_{20}$ 57
Figure 5.7 Thermodynamic properties for $Y(Fe_xCo_{1-x})_2Zn_{20}$ versus x 58
Figure 5.8 Magnetic properties for $Gd(Fe_xCo_{1-x})_2Zn_{20}$ 59

Figure 6.1 Temperature dependent magnetization of GdT_2Zn_{20} 64
Figure 6.2 Low-temperature magnetization isothermal for GdT_2Zn_{20} 65
Figure 6.3 Temperature dependent H/M for GdT_2Zn_{20} 66
Figure 6.4 Thermodynamic and transport properties of $GdFe_2Zn_{20}$ 68
Figure 6.5 Arrott plot for $GdFe_2Zn_{20}$ 69
Figure 6.6 Thermodynamic and transport properties of $GdRu_2Zn_{20}$ 70
Figure 6.7 Arrott plot for $GdRu_2Zn_{20}$ 71
Figure 6.8 Thermodynamic and transport properties of $GdOs_2Zn_{20}$ 72
Figure 6.9 Arrott plot for $GdOs_2Zn_{20}$ 73
Figure 6.10 Thermodynamic and transport properties of $GdCo_2Zn_{20}$ 74
Figure 6.11 Thermodynamic and transport properties of $GdRh_2Zn_{20}$ 75
Figure 6.12 Thermodynamic and transport properties of $GdIr_2Zn_{20}$ 76
Figure 6.13 Magnetization of $GdFe_2Zn_{20}$ and $GdRu_2Zn_{20}$ under pressure 78
Figure 6.14 Pressure dependent T_C for $GdFe_2Zn_{20}$ and $GdRu_2Zn_{20}$ 79
Figure 6.15 Temperature dependent magnetization of YT_2Zn_{20} 79
Figure 6.16 Low temperature magnetic isothermal of YT_2Zn_{20} 80
Figure 6.17 Low temperature specific heat of YT_2Zn_{20}. 80
Figure 6.18 Calculated density of states of YFe_2Zn_{20} 83
Figure 6.19 Calculated density of states of YT_2Zn_{20} (T = Fe, Ru and Co) 84
Figure 6.20 Calculated density of states of GdT_2Zn_{20}(T = Fe, Ru and Co) 86
Figure 6.21 Magnetic properties of $GdFe_2Zn_{20}$ in the paramagnetic state 89
Figure 6.22 Magnetic properties of $Gd(Fe_xCo_{1-x})_2Zn_{20}$ in their paramagnetic states 90

Figure 7.1 Powder X-ray diffraction pattern of $Gd_xY_{1-x}Fe_2Zn_{20}$ 95
Figure 7.2 Magnetization versus applied field for $Gd_{0.5}Y_{0.5}Fe_2Zn_{20}$ at varied temperature 97
Figure 7.3 Gd concentration measurements results for $Gd_xY_{1-x}Fe_2Zn_{20}$ 98
Figure 7.4 Magnetic properties of $Gd_xY_{1-x}Fe_2Zn_{20}$ in their paramagnetic states . 100
Figure 7.5 Temperature dependent magnetization of $Gd_xY_{1-x}Fe_2Zn_{20}$ 101
Figure 7.6 Low temperature isothermal of $Gd_xY_{1-x}Fe_2Zn_{20}$ 102
Figure 7.7 Arrott plots for $Gd_xY_{1-x}Fe_2Zn_{20}$ 104
Figure 7.8 Temperature dependent resistivity for $Gd_xY_{1-x}Fe_2Zn_{20}$ 105
Figure 7.9 Temperature dependent $\Delta\rho$ for $Gd_xY_{1-x}Fe_2Zn_{20}$ 107
Figure 7.10 Temperature variation of specific heat of $Gd_xY_{1-x}Fe_2Zn_{20}$ 108
Figure 7.11 Temperature dependent ΔC for $Gd_xY_{1-x}Fe_2Zn_{20}$ 109
Figure 7.12 $\Delta C/x$ versus T/T_C 110
Figure 7.13 Overview of magnetic properties of $Gd_xY_{1-x}Fe_2Zn_{20}$ 112
Figure 7.14 Fitting of the T_C values by *s-d* model 115
Figure 7.15 Fitting of the magnetization by *s-d* model 116

Figure 8.1 Magnetization of Y(Lu)Fe_2Zn_{20} and Y(Lu)Co_2Zn_{20} 121
Figure 8.2 Temperature dependent M/H for $LuFe_2Zn_{20}$ 123
Figure 8.3 $\Delta M/\Delta H$ for $LuFe_2Zn_{20}$ at varied temperature. 123
Figure 8.4 Low temperature specific heat for Y(Lu)Fe_2Zn_{20} and Y(Lu)Co_2Zn_{20} . 124
Figure 8.5 Temperature dependent resistivity of Y(Lu)Fe_2Zn_{20} and Y(Lu)Co_2Zn_{20} 126
Figure 8.6 ρ versus T^2 for Y(Lu)Fe_2Zn_{20} and Y(Lu)Co_2Zn_{20} 127
Figure 8.7 Temperature dependent magnetization of RCo_2Zn_{20} (R = Nd and Sm) 128
Figure 8.8 C_p data for RCo_2Zn_{20} (R = Nd, Sm and Y) 129
Figure 8.9 Temperature dependent magnetization of RCo_2Zn_{20} (R = Gd - Yb) . . 130
Figure 8.10 Temperature dependent H/M RCo_2Zn_{20} (R = Gd - Yb) 131
Figure 8.11 C_p data for RCo_2Zn_{20} (R = Gd - Tm, Y and Lu) 132
Figure 8.12 Normalized magnetic part of entropy for RCo_2Zn_{20} (R = Dy - Tm) . . 134

Figure 8.13 Field dependent magnetization for $Tb_{0.5}Y_{0.5}Co_2Zn_{20}$ 135
Figure 8.14 Field dependent magnetization for $DyCo_2Zn_{20}$ 136
Figure 8.15 Field dependent magnetization for $HoCo_2Zn_{20}$ 137
Figure 8.16 Field dependent magnetization for $ErCo_2Zn_{20}$ 138
Figure 8.17 Field dependent magnetization for $TmCo_2Zn_{20}$ 139
Figure 8.18 Temperature dependent magnetization of RFe_2Zn_{20} (R = Gd - Tm) . . 141
Figure 8.19 Temperature dependent H/M for RFe_2Zn_{20} (R = Gd - Tm) 142
Figure 8.20 Thermodynamic and transport properties of $TbFe_2Zn_{20}$ 143
Figure 8.21 Arrott plot for $TbFe_2Zn_{20}$ 144
Figure 8.22 Magnetic anisotropy of $TbFe_2Zn_{20}$ at 2 K 145
Figure 8.23 Thermodynamic and transport properties of $DyFe_2Zn_{20}$ 146
Figure 8.24 Arrott plot for $DyFe_2Zn_{20}$ 147
Figure 8.25 Magnetic anisotropy of $DyFe_2Zn_{20}$ at 2 K 148
Figure 8.26 Thermodynamic and transport properties of $HoFe_2Zn_{20}$ 150
Figure 8.27 Arrott plot for $HoFe_2Zn_{20}$ 151
Figure 8.28 Magnetic anisotropy of $HoFe_2Zn_{20}$ at 2 K 152
Figure 8.29 Thermodynamic and transport properties of $ErFe_2Zn_{20}$ 153
Figure 8.30 Arrott plot for $ErFe_2Zn_{20}$ 154
Figure 8.31 Magnetic anisotropy of $ErFe_2Zn_{20}$ at 2 K 155
Figure 8.32 Thermodynamic and transport properties of $TmFe_2Zn_{20}$ 156
Figure 8.33 Arrott plot for $TmFe_2Zn_{20}$ 157
Figure 8.34 Magnetic anisotropy of $TmFe_2Zn_{20}$ at 2 K 158
Figure 8.35 Temperature dependent M/H and ρ for $YbFe_2Zn_{20}$ and $YbCo_2Zn_{20}$. 159
Figure 8.36 de Gennes scaling of T_C, θ_C and the maximum value on $\Delta\rho$ for RFe_2Zn_{20} (R = Gd - Tm) 161
Figure 8.37 Magnetic anisotropy for $Er(Tm)_{0.1}Y_{0.1}Fe_2Zn_{20}$ 163
Figure 8.38 Magnetic part of specific heat for RFe_2Zn_{20} (R = Gd - Tm) 165
Figure 8.39 Single-ion CEF splitting energy levels for RCo_2Zn_{20} (R = Tb - Tm . . 166

Figure 8.40 Temperature dependent Resistivity for RFe_2Zn_{20} (R = Gd - Tm) . . . 168

Figure 9.1 Low temperature thermodynamic properties of YbT_2Zn_{20} 174

Figure 9.2 Temperature dependent resistivity of YbT_2Zn_{20} 174

Figure 9.3 Low temperature resistivity and specific heat of $YbCo_2Zn_{20}$ 175

Figure 9.4 Kadowaki-woods plot of YbT_2Zn_{20} 177

Figure 9.5 Coqblin-Schrieffer analysis of $YbFe_2Zn_{20}$ thermodynamic properties . . 178

Figure 9.6 Coqblin-Schrieffer analysis of $YbRh_2Zn_{20}$ thermodynamic properties . 179

A.1 Magnetic properties of $TbFe_2Zn_{20}$ from different growth conditions . . 185

CHAPTER 1. Introduction

It is well known that rare earth intermetallic compounds have versatile, magnetic properties associated with the $4f$ electrons: a local moment associated with the Hund's rule ground state is formed in general, but a strongly correlated, hybridized state may also appear for specific $4f$ electronic configuration (eg. for rare earth elements such as Ce or Yb) [Szytula and Leciejewicz, 1994, Hewson, 1993]. On the other hand, the conduction electrons in rare earth intermetallic compounds, certainly ones associated with non hybridizing rare earths, usually manifest non-magnetic behavior and can be treated as a normal, non-interacted Fermi liquid, except for some $3d$-transition metal rich binary or ternary systems which often manifest strong, itinerant, d electron dominant magnetic behavior. Of particular interest are examples in which the band filling of the conduction electrons puts the system in the vicinity of a Stoner transition: such systems, characterized as nearly or weakly ferromagnet, manifest strongly correlated electronic properties [Moriya, 1985]. For rare earth intermetallic compounds, such systems provide an additional versatility and allow for the study of the behaviors of local moments and hybridized moments which are associated with $4f$ electron in a correlated conduction electron background.

The dilute, rare-earth-bearing, intermetallic series RT_2Zn_{20} (R = rare earth and T = transition metal in and near the Fe, Co, and Ni columns) crystallize in a cubic, $CeCr_2Al_{20}$ structure (space group: $Fd\bar{3}m$) in which the R and T ions occupy their own, single, unique crystallographic site with cubic and trigonal point symmetry respectively, whereas the Zn ions have three unique crystallographic sites (see Fig. 3.1) [Nasch et al., 1997]. Both R and T ions are fully surrounded by shells consisting of the nearest neighbors (NNs) and the next nearest neighbors (NNNs) of Zn, meaning that there are no R-R, T-T or R-T NNs and the shortest

R-R spacing is ~ 6 Å. These series of compounds provide multiple degrees of freedom to study strongly correlated electronic states, for either f or d electrons, by allowing for controlled substitutions on a number of unique crystallographic sites. Furthermore, with less than 5 atomic percent of rare earth, RT_2Zn_{20} compounds provide an opportunity to study the rare earth local moment as well as hybridizing rare earth ions close to the single ion limit, while still preserving their periodicity.

The most conspicuous local moment magnetic behavior appears in $GdFe_2Zn_{20}$, which has a remarkably high ferromagnetic (FM) ordering temperature of 86 K. In contrast, the isostructural $GdCo_2Zn_{20}$ orders antiferromagnetically at a more representative Néel temperature, $T_N = 5.7$ K, due to its very dilute nature and the large Gd ion spacing. Magnetization and specific heat measurements on the non-local-moment-bearing Y analogues show that YFe_2Zn_{20} has an enhanced, temperature-dependent susceptibility and large electronic specific heat coefficient, and can be treated as an archetypical example of a nearly ferromagnetic Fermi liquid (NFFL), whereas YCo_2Zn_{20} manifests non-correlated normal metal behavior. These results are consistent with the band structure calculations which show a larger density of states at the Fermi level $[N(E_F)]$ for YFe_2Zn_{20} and $LuFe_2Zn_{20}$ than for the Co analogues. The study of the pseudo-ternary compounds, $Y(Fe_xCo_{1-x})_2Zn_{20}$, reveals that by changing the band filling, this conduction electron background can be tuned from the edge of the Stoner limit to being well removed from it. Correspondingly, the magnetic ordering temperature of $Gd(Fe_xCo_{1-x})_2Zn_{20}$ drops monotonically as x varies from 0 to 1. In light of these results, the anomalously high FM ordering temperature of $GdFe_2Zn_{20}$ can be understood as the result of large Heisenberg moments associated with the Hund's rule ground state of Gd^{3+} embedded in a NFFL.

In order to expand our understanding of the magnetism of the RT_2Zn_{20} series of compounds beyond T = Fe and Co, the thermodynamic and transport properties of RT_2Zn_{20} compounds were examined for the T = Ru, Rh, Os, and Ir analogues. The R = Gd members were thoroughly studied because they give the clearest indication of the strength and sign of the magnetic interaction without any complications associated with crystalline electric field (CEF) splitting of the Hund's rule ground state multiplet. Ferromagnetic ordering of the local moment

Gd^{3+} sublattice was found with T being a member of the iron column (with enhanced FM ordering temperature T_C values for T = Fe and Ru) and lower temperature, antiferromagnetic (AFM) ordering was found for the cobalt column members. Consistent with these results, enhanced paramagnetism and a relatively large electronic specific heat coefficient was also found in the T = Ru analogue of YT_2Zn_{20}.

The concept of Heisenberg moments embedded in a NFFL for $GdFe_2Zn_{20}$ motivated us to study the pseudo-ternary series of compounds, $Gd_xY_{1-x}Fe_2Zn_{20}$, which can be used as a model for studying the effects of titrating very dilute local moments into a NFFL. Given the unique crystal structure of the RFe_2Zn_{20} system, the dilution of Gd onto the Y site changes neither the band filling nor all Zn local environment of either the Gd or Fe ions. Thermodynamic and transport measurements revealed FM ordering of the Gd^{3+} local moment above 1.8 K for a Gd concentration above $x = 0.02$. This persistence of the local moment ordering in the NFFL was discussed within the framework of the so-called *s-d* model [Shimizu, 1981a], based on the mean field approximation.

Further study of the RT_2Zn_{20} series was focused on other rare earth ions associated with well defined $4f$ local moments. With non-zero orbital angular momentum in its Hund's rule ground state, the $4f$ local moment will be affected by the CEF effect. A comparative study of the thermodynamic and transport properties of the RFe_2Zn_{20} and RCo_2Zn_{20} showed the nature of the magnetic ordering, as well as CEF induced magnetic anisotropy and specific heat anomalies for R = Tb - Tm compounds. For the RCo_2Zn_{20} series, only Gd and Tb members manifest AFM ordering above 2 K, and the magnetic properties for R = Dy - Tm clearly manifest features associated with single ion CEF effects on the R ions in the cubic symmetry coordination. For the R = Tb - Tm members in the Co series, the CEF parameters can be inferred by the fitting anisotropic magnetization and the specific heat data. In contrast, for the RFe_2Zn_{20} series, the well-defined local moment members (R = Gd - Tm) all manifest enhanced FM ordering with T_C values that roughly scale with the de Gennes factor. The R = Tb - Tm members in the Fe series show moderate magnetic anisotropy in their ordered states, mainly due to the CEF effect on the R ions, which is consistent with the magnetic anisotropy for the

Co members.

Finally, in addition to these well-defined local-moment-bearing rare-earth compounds, a more exotic low temperature ground state emerges in the six Yb-based compounds (YbT_2Zn_{20} for T = Fe, Co, Ru, Rh, Os, and Ir) in which the Yb ions hybridize with conduction electrons and manifest so-called heavy fermion behavior. These six strongly correlated Yb-based intermetallic compounds not only effectively double the number of known Yb-based heavy fermions, but also provide a route to studying how the degeneracy of the Yb ion at Kondo temperature, T_K, effects the low temperature-correlated state. Thermodynamic and transport measurements show that all these six Yb compounds manifest a low temperature, Fermi liquid state with the electronic specific heat coefficient $\gamma > 500$ mJ/mol K^2. $YbCo_2Zn_{20}$, showing extremely large γ value ($\simeq 8000$ mJ/mol K^2), has a substantially lower T_K. For the other five compounds, further analysis of the Kadowaki-Woods ratio, as well as the magnetic susceptibility and specific heat data by using the Coqblin-Schrieffer model, reveal that the Fermi liquid states of these five compounds are indeed associated with different degeneracy of the Yb ion for T = Fe, Ru and T = Rh, Os and Ir. The primary effect of changing T_K/T_{CEF} is to cause a change in the coefficient of the low temperature, T^2 electrical resistivity.

This work will be presented as follows. A review of the physics of rare earth intermetallic compounds, including magnetism and magnetic ordering for both local moment and itinerant electronic system, the CEF effect on the $4f$ local moments, and heavy fermion physics, will be presented in the next chapter. The crystal structure of RT_2Zn_{20} will be introduced in chapter 3. The following chapter is dedicated to details of crystal growth of RT_2Zn_{20} compounds from Zn solution, as well as a review of the measurement techniques used in characterizing these compounds. As an introduction to the magnetic properties of RT_2Zn_{20} system, chapter 5 presents the magnetic properties of $GdFe_2Zn_{20}$ and $GdCo_2Zn_{20}$ as well as their Y analogous. Chapter 6 expands the phase space including T = Ru, Rh, Os and Ir compounds. The study of the thermodynamic and transport properties of $Gd_xY_{1-x}Fe_2Zn_{20}$ pseudo-ternary compounds will be presented in the following chapter. Chapter 8 will be dedicated to a comparative study of the magnetic properties of the RFe_2Zn_{20} and RCo_2Zn_{20} as R = Tb - Tm series. And finally, a

study of the six Yb-based heavy fermion compounds (YbT_2Zn_{20}) will be introduced in chapter 9. Chapter 10 summarizes the results of this work and outlines some further paths of on going or proposed investigation.

Before starting into the details of the research, it is important to note that this work represents collaborations between many people within the Ames Laboratory, Iowa State University, and beyond. The work presented in chapters 5, 6, 7 and 9 was published, and the work in chapter 8 will be submitted for publication. The co-authors of the papers associated with chapters 5–8 include Ni Ni, S. L. Bud'ko and P. C. Canfield (Ames Laboratory and Department of Physics, Iowa State University), participating in sample preparation, thermodynamic and transport measurements and data analysis; G. D. Samolyuk (Ames Laboratory), contributing in band structure calculations; A. Safa-Sefat (Ames Laboratory), Hyunjin Ko and G. J. Miller (Ames Laboratory and Department of Chemistry, Iowa State University), contributing in single crystal x-ray diffraction measurements; and K. Dennis (Ames Laboratory), participating in energy dispersive spectra (EDS) measurements. The co-authors of the papers associated with chapters 9 include M. S. Torikachvili (Ames Laboratory and Department of Physics, San Diego State University), S. L. Bud'ko and P. C. Canfield (Ames Laboratory and Department of Physics, Iowa State University), participating in thermodynamic and transport measurements and data analysis; E. D. Mun (Ames Laboratory and Department of Physics, Iowa State University), participating in data analysis; S. T. Hannahs (National High Magnetic Field Laboratory), participating in low temperature transport measurements; and R. C. Black, W. K. Neils and Dinesh Martien (Quantum Design Inc.), participating in low temperature specific heat measurements. As the first author of the papers associated with chapters 5–8 and the second author of the paper associated with chapter 9, I dedicated in the sample synthesis and characterization (powder x-ray diffraction and EDS measurements), thermodynamic and transport measurements, and data analysis. I'd like to also thank J. Frederich and M. Lampe (Ames Laboratory) for samples synthesis, and L. Tan (Ames Laboratory) Laue x-ray measurements. All of my work was guided by S. L. Bud'ko and P. C. Canfield, and supported by the Director for Energy Research, Office of Basic Energy Sciences. Ames Laboratory is

operated for the U.S. Department of Energy by Iowa State University under Contract No. DE-AC02-07CH11358.

CHAPTER 2. Overview of the magnetic properties of rare earth and transition metal intermetallic compounds

It is well-known that the magnetic properties of rare earths and transition metals as well as their intermetallic compounds are mainly determined by the unfilled d or $4f$ electronic shell. However, the magnetism of $4f$ and d electrons in metals are described by two intrinsically different models, the localized model and the itinerant electron models respectively, with diametrically different starting points. In the localized electron model, each f electron remains localized on an given atom. The intra-atomic electron-electron interactions are large and determine the atomic magnetic moments on each atom; the exchange interactions between the local moments determine the magnetic order. In the itinerant electron model, each electron is itinerant and moves in the average field of the other electrons and ions. The weak electron-electron interaction stabilizes ordered magnetic states characterized by different number of up- and down-spin electrons. Although a unified picture of magnetism has been established by the so-called spin fluctuation theory [Moriya, 1985], these two simple models are still generally used in the analysis of the experimental results due to their relatively easy implementation. In this chapter, these two models of magnetism are introduced in the first two sections.

Given their highly localized nature, the magnetic properties of rare earth intermetallic compounds are also strongly affected by their local environment. The rare earth ions are located in a crystalline lattice and the surrounding atoms and conduction electrons lead to an electrostatic field, which is known as crystalline electric field (CEF). The CEF effect affects the magnetic properties of the rare earth ions together with the magnetic interactions. The related concepts and theories are introduced in the third section of this chapter. For some rare earth elements (Ce, Yb or Eu), the $4f$ electrons may lose their local moment magnetism due

to the hybridization with the conduction electrons. In some cases this anomaly leads to so-called 'heavy Fermion' behaviors. The theories about the 'heavy Fermion' systems are briefly reviewed in the final section of this chapter.

2.1 $4f$ electron and local moment magnetism

In the local moment magnetism picture, the magnetic atoms manifest fixed local moments due to their partially filled f shells. In a free atom, the quantum levels of each electron are characterized by its spin angular momentum $\boldsymbol{s}$, and orbital angular momentum $\boldsymbol{l}$. The total angular momentum of one electron $\boldsymbol{j}$ equals $\boldsymbol{l}+\boldsymbol{s}$. As for an atom as a whole, the total angular momentum ($\boldsymbol{J}$) is a good quantum number, which usually can be determined by the Russell-Saunder scheme. In this scheme, the total orbital angular momentum $\boldsymbol{L}=\sum_i \boldsymbol{l}_i$ and the total spin momentum $\boldsymbol{S}=\sum_i \boldsymbol{s}_i$ are also good quantum numbers. The total angular momentum and the total magnetic moment are given by $\boldsymbol{J}=\boldsymbol{L}+\boldsymbol{S}$ and $\boldsymbol{M}=g_J\mu_B\boldsymbol{J}$, respectively, where g_J is the Landè factor and μ_B is the Bohr magneton.

As well-known examples, the rare earth elements with partially filled $4f$ electronic shells usually manifest local moments magnetic behaviors. The rare earths are the seventeen elements from lanthanum (atomic number Z = 57) to lutetium (Z = 71). Scandium and Yttrium are often included because of their similar electronic structure. The Lanthanides correspond to the filling of the $4f$ electronic shell from 0 to 14 electrons, whereas Sc and Y have empty $4f$ shells and act as two more non-magnetic members of the family. In the free rare earth atoms, the normal electronic configuration is: $(\mathrm{Pd})^{46}\ 4f^n\ 5s^2\ 5p^6\ 5d^1\ 6s^2$. Having one $5d$ electron, the rare earth elements are at the beginning of the series of $5d$ transition elements and are homologous to scandium and yttrium.

Figure 2.1 shows the radial extent of different shells for a free gadolinium atom. The $4f$ shell has a small radial extent and is well shielded from outer perturbations by the full $5s$ and $5p$ shells. Therefore the $4f$ electrons remain well localized on the atom in the solid state, with negligible overlap between $4f$ wavefunctions centered on neighboring atoms. Thus the $4f$ electronic configuration can be described as an atomic shell with well-defined energy levels.

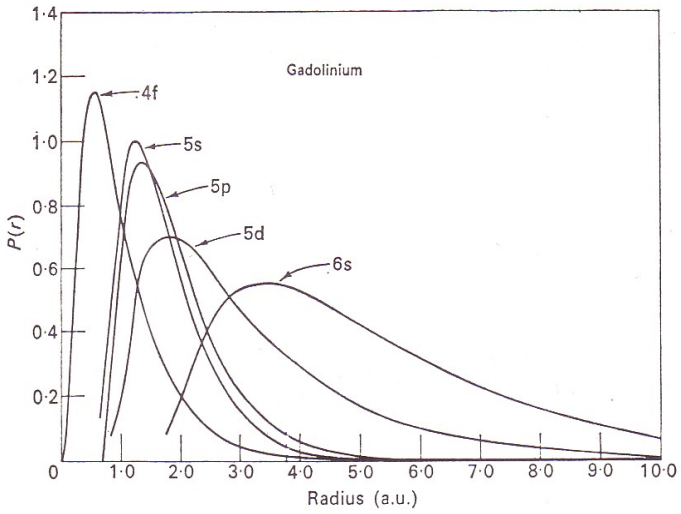

Figure 2.1 Radial extent of different shells in the free gadolinium ion [Freeman, 1972]. The radius unit is 1 atomic unit = 0.529 Å.

In the metallic state, the $5d$ and $6s$ valence electrons are delocalized and form the conduction electron band. Since the ionization energies of the $4f$ levels are slightly higher than those for $5d$ electrons, the rare earth atoms most frequently manifest the normal trivalent state in the metallic state. Therefore, a normal rare earth metal can be described as a lattice of rare earth ions with the $4f^n$ configuration immersed in a band of s or d electronic character. The properties governed by the valence electrons such as the bonding geometry and chemical properties are expected to vary smoothly across the rare earth series. A series of compounds can often be synthesized, which differ only in the choice of rare earth elements. This valuable ability allows for systematic studies of the physics of rare earth intermetallic compounds. In the series of isostructural compounds with only different rare earth elements in stable, trivalent states, the ionic radii of the lanthanides always decrease from La to Lu across the lanthanide period, which always leads to decreasing of the volumes of their unit cell. This is the so-called lanthanide contraction and is due to the increased Coulomb attraction between the nuclei and the $4f$ shell electrons across the lanthanide period. Particularly, with empty $4f$ shell, Y^{3+} usually manifest ionic radii size between Dy^{3+} and Ho^{3+}.

Sometimes, a $4f$ configuration with a 2+ or 4+ state will occur when the $4f$ shell is close to particularly stable, empty, full or half-filled state. For instance, the metallic elements europium and ytterbium are in divalent states with $4f^7$ and $4f^{14}$ configuration respectively. The interesting physics due to the valence change and/or the hybridizing of $4f$ electron and conduction electrons including the so-called heavy fermion physics will be discussed in section 2.4.

2.1.1 Hund's rules

The Russel-Saunders rule results in the total angular momentum $\boldsymbol{J}$ with a quantum number $|L+S|$, $|L+S-1|$,$\cdots$, $|L-S|$. For each J value, there is $2J+1$ degeneracy with $J_z = J$, $J-1$,$\cdots$,$-J$. The three Hund's rules can be used to determine the ground state electronic configuration of the total angular momentum $\boldsymbol{J}$ for a partially filled shell.

- The ground state has the largest value of total spin S that is consistent with the exclusion principle.
- For the maximum possible S value, the electrons are distributed between all possible states in accordance with the exclusion principle, and such that the resulting L value is maximum.
- For shells that are less than half-filled, the total angular momentum is given by $J = |L-S|$. For shells that are more than half-filled, $J = |L+S|$.

Using these rules, the ground state of the electronic configuration for rare earth ion can be determined. The calculated magnetic properties for the free, trivalent ions are shown in Table 2.1.

2.1.2 Magnetic moment and Curie law

In an applied magnetic field ($\boldsymbol{H}$), the n-folder degenerate, ground state of the $4f$ electronic configuration will be split to n levels with equal energy difference, which is the so-called Zeeman

Table 2.1 Components of the orbital angular momentum, L; the spin angular momentum, S; the total angular momentum, J; the calculated values of the Landè factor, $g_J = 1 + \frac{J(J+1)+S(S+1)-L(L+1)}{2J(J+1)}$; saturated moment, $\mu_{sat} = g_J J \mu_B$; effective moment, $\mu_{eff} = g_J[J(J+1)]^{1/2}\mu_B$; and de Gennes factor, $dG = (g_J - 1)^2 J(J+1)$ for the trivalent rare earth ions.

$4f$	R^{3+}	L	S	J	g_J	μ_{sat}	μ_{eff}	dG
0	La	0	0	0	-	-	-	-
1	Ce	3	1/2	5/2	6/7	2.14	2.54	0.18
2	Pr	5	1	4	4/5	3.20	3.58	0.80
3	Nd	6	3/2	9/2	8/11	3.27	3.62	1.84
4	Pm	6	2	4	3/5	2.40	2.68	3.20
5	Sm	5	5/2	5/2	2/7	0.71	0.84	4.46
6	Eu	3	3	0	-	-	-	-
7	Gd	0	7/2	7/2	2	7.00	7.94	15.75
8	Tb	3	3	6	3/2	9.00	9.72	10.50
9	Dy	5	5/2	15/2	4/3	10.00	10.64	7.08
10	Ho	6	2	8	5/4	10.00	10.61	4.50
11	Er	6	3/2	15/2	6/5	9.00	9.58	2.55
12	Tm	5	1	6	7/6	7.00	7.56	1.17
13	Yb	3	1/2	7/2	8/7	4.00	4.54	0.32
14	Lu	0	0	0	-	-	-	-

splitting. In the second-order perturbation theory, the magnetic field energy contribution to the system will be the Zeeman term:

$$\Delta E_n(H) = \mu_B H \langle n | \boldsymbol{L} + 2\boldsymbol{S} | n \rangle = g_J \mu_B H \langle n | \boldsymbol{J} | n \rangle , \tag{2.1}$$

where g_J is the Landè factor defined as:

$$g_J = 1 + \frac{J(J+1) + S(S+1) - L(L+1)}{2J(J+1)}. \tag{2.2}$$

plus a Van Vleck paramagnetic term.

The Van Vleck paramagnetic term is related to the excited state and is typically small in rare earth elements with partially filled $4f$ shell, except for Sm^{3+} and Eu^{3+} ions which have low excited energy levels, or for singlet ground states (non-magnetic ground states) such as found in crystalline electric field (CEF) split, non-Kramer's ions (e.g. Pr^{3+}). In general, the Van Vleck paramagnetic term is ignorable and the magnetic field induced energy can be expressed

as the interaction of the field with a magnetic moment $(-\boldsymbol{\mu} \cdot \boldsymbol{J})$,where

$$\boldsymbol{\mu} = -g_J \mu_B \boldsymbol{J}, \tag{2.3}$$

This allows the saturated magnetization of the local moment in the absence of other energy contributions such as the crystal electric field(CEF), to be expressed as:

$$\mu_{sat} = |\boldsymbol{\mu}| = g_J \mu_B J. \tag{2.4}$$

The temperature dependence of the magnetization can be derived by using simple statistical physics. The free energy of the system is given by:

$$F = -\frac{N}{\beta} \ln \sum_n \exp -\beta E_n(H), \tag{2.5}$$

where $\beta = 1/k_B T$, N is the number of magnetic ions. The magnetization is the derivative of the free energy with respect to magnetic field, given by:

$$M = -\frac{1}{V}\frac{\partial F}{\partial H} = -\frac{N}{V} g_J \mu_B J B_J(\beta g_J \mu_B J H), \tag{2.6}$$

where V is the volume, $B_J(x)$ is the well-known Brillouin function.

At high temperature ($k_B T \gg g_J \mu_B H$), the molar susceptibility can be determined as:

$$\chi = \frac{\partial M}{\partial H} = N_A \frac{(g_J \mu_B)^2}{3} \frac{J(J+1)}{k_B T} = \frac{C}{T}, \tag{2.7}$$

This variation of the susceptibility with respect to the inverse of temperature is known as Curie's law, where the Curie constant C can be written as a function of the effective moment (μ_{eff}):

$$C = N_A \frac{(g_J \mu_B)^2}{3} \frac{J(J+1)}{k_B} = N_A \frac{\mu_{eff}^2 \mu_B^2}{3 k_B}, \tag{2.8}$$

.

Comparison of the experimental determinations of the effective moment and saturated moment with the theoretical forms (summarized in Table 2.1) are useful in the analysis of new rare earth compounds, since it allows the theoretical value to be compared to the measured value. This comparison may be used to estimate the mass percentage of rare earth element presenting in an unknown compound. Furthermore, if rare earth intermetallic compound

manifests other magnetic properties (eg. the itinerant electronic magnetism) in addition to that associated with the local moment $4f$ electrons, then such a comparison of the theoretical values and the measured values can help us to identify the additional contribution.

2.1.3 Weiss Molecular field theory

The Curie's law has been derived within the hypothesis of negligible interactions between the magnetic moments, which is only strictly satisfied in few situations (eg. some paramagnetic salt containing very dilute magnetic ions). For materials having non-negligible magnetic interaction, a ferromagnetic(FM) or antiferromagnetic(AFM) ordered state may arise as the low temperature ground state. Weiss' molecular field theory provides a simple explanation for the FM behavior of local moment systems. Weiss assumed that the magnetic interactions can be taken into account by considering an effective field H_{eff} acting on each local moment, in addition to the external field H. Such an effective field arises from the thermal average of the surrounding moments, and is proportional to their magnetization: $H_{eff} = \alpha M$, where α serves as a coupling constant.

By using Eqn.2.6, the molar magnetization can be written as:

$$M = N_A g_J \mu_B J B_J(x), \tag{2.9}$$

where

$$x = \frac{J g_J \mu_B}{k_B T}(H + \alpha M). \tag{2.10}$$

Combining these two equations, the magnetization at an arbitrary temperature and external field can be found. Specifically, in zero external field ($H = 0$), the magnetization can have a non-zero value when:

$$T < \theta_{\mathrm{C}} = N_A \frac{\alpha \mu_{eff}^2 \mu_B^2}{3 k_B}, \tag{2.11}$$

which means that when the temperature is lower than θ_{C}, the system manifest spontaneous magnetization, the hallmark of a FM state. Therefore, θ_{C} is the FM ordering temperature T_{C}.

Above T_C, the system is in paramagnetic state. At sufficiently high temperature ($k_BT \gg g_J\mu_BH$ and $T > T_C$), the susceptibility can be expressed as the well-known Curie-Weiss law:

$$\chi = \frac{C}{T - C\alpha} = \frac{C}{T - \theta_C}. \tag{2.12}$$

The paramagnetic Curie temperature θ_C is same as T_C in Weiss's molecular field theory.

2.1.4 Arrott plot

Weiss's molecular field theory can be used to develop a criterion to determine the value of T_C for a local moment system by analysis of the isothermal magnetization data, which is the so-called Arrott plot [Arrott, 1957]. (In general, an Arrott plot is also suitable for any itinerant magnetic system based on the Landau theory.)

The difficulty in using Eqn. 2.12 to simply determine T_C is that, by definition, the system is FM if spontaneous magnetization exists within a single domain, and the susceptibility (χ) of the system tends to be infinite at T_C. Since the field dependent magnetization $M(H)$ tends to lose its linearity, even for a finite-small H, when the temperature approaches T_C, it is difficult to determine the divergent point of $\chi(T)$ in experiment (and thereupon T_C value) by analysis the temperature dependent magnetization data $M(T)$ under a fixed applied field. Instead, the Arrott plot provides a useful criterion for T_C value by analysis of $M(H)$ data sets at varied temperature in the vicinity of T_C.

Equation 2.9 and 2.10 can be written as:

$$M = M_0 B_J\left(\frac{M_0(H + \alpha M)}{N_A k_B T}\right), \tag{2.13}$$

where $M_0 = N_A g_J \mu_B J$ is the spontaneous magnetization at zero temperature. This equation can be rewritten as:

$$\frac{M_0(H + \alpha M)}{N_A k_B T} = B_J^{-1}\left(\frac{M}{M_0}\right). \tag{2.14}$$

The right-hand side of this equation can be expanded in a power series for values of $M \ll M_0$ giving

$$\frac{M_0(H + \alpha M)}{N_A k_B T} = \frac{M}{M_0} + \frac{1}{3}\left(\frac{M}{M_0}\right)^3 + \frac{1}{5}\left(\frac{M}{M_0}\right)^5 + \cdots . \tag{2.15}$$

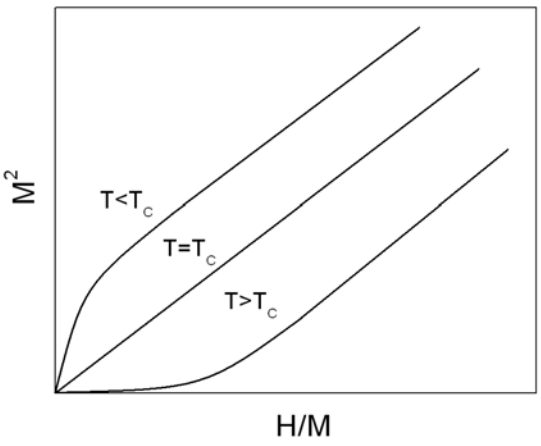

Figure 2.2 Schematic diagram of the Arrott's plot in the vicinity of $T_{\rm C}$.

This equation can be written as the form as:

$$H = a_1 M + a_3 M^3 + a_5 M^5 + \cdots , \tag{2.16}$$

where $a_1 = 1/\chi = (\frac{N_A k_B T}{M_0^2}) - \alpha$. At $T_{\rm C}$, $1/\chi = 0$, therefore $T_{\rm C} = \frac{\alpha M_0^2}{N_A k_B}$. Hence at $T_{\rm C}$

$$\frac{M_0 H}{N_A k_B T_{\rm C}} = \frac{1}{3}(\frac{M}{M_0})^3 + \frac{1}{5}(\frac{M}{M_0})^5 + \cdots . \tag{2.17}$$

This equation shows the cubic relation between the field and magnetization since $M \ll M_0$ in general.

Figure 2.2 shows a schematic diagram of the isothermal magnetization in the vicinity of $T_{\rm C}$ for the data plotted as M^2 with respect to H/M. In experiment, the values of H must be modified by subtracting the demagnetizing field (see Chapter 4). The curves linearly cross the origin point at $T_{\rm C}$. Experimentally, the data may show non-linear curves in Arrott plot due to CEF effect or other complications [Yeung et al., 1986, Neumann and Ziebeck, 1995, Brommer and Franse, 1990]. Nevertheless, the isothermal magnetization data crossing the origin is a criteria of the FM ordering based on the mean field theory.

2.1.5 RKKY interaction and de Gennes scaling

The magnetic interaction between the local moments occurs via various types of mechanisms for different systems. The simplest example is known as *direct exchange*, which is arises from the direct Coulomb interaction among electrons from the two ions. For rare earth intermetallic compounds, the overlap between the $4f$-orbitals of neighboring rare earth sites is usually small, which reduces the possibility of a direct exchange between the rare earth ions. The primary interaction of the magnetic moments is via the polarization of the conduction electrons, which is known as *indirect exchange*. Two mechanisms have been proposed in the indirect exchange interaction for rare earth intermetallic compounds. In the first one, known as RKKY (Ruderman-Kittel-Kasuya-Yosida) model, the magnetic coupling proceeds by means of spin polarization of conduction electrons. In the second mechanism, the spin polarization of the $5d$ electrons of the rare-earth atoms plays more important role.

The RKKY model was first proposed by Ruderman and Kittel [Ruderman and Kittel, 1954] and later extended by Kasuya [Kasuya, 1956] and Yosida [Yosida, 1957]. In this model, the exchange interaction energy between a conduction electron with spin $\boldsymbol{s}$ and a local moments with spin $\boldsymbol{S}$ is:

$$\Delta E = -2J_{sf}\boldsymbol{s}\cdot\boldsymbol{S}, \tag{2.18}$$

where J_{sf} is the exchange parameter.

For local moments submerged in a Fermi sea, the total exchange energy of the RKKY interaction between two local moments at position $\boldsymbol{R}_i$ and $\boldsymbol{R}_j$ is given by:

$$E = \frac{18\pi n^2}{E_F} J_{sf}^2 \boldsymbol{S}_i\cdot\boldsymbol{S}_j F(2k_F\left|\boldsymbol{R}_i-\boldsymbol{R}_j\right|) \tag{2.19}$$

where n is the average density of conduction electrons; E_F is the Fermi energy; k_F is the Fermi wavevector; and $F(x) = \frac{x\cos x - \sin x}{x^4}$ is a damped oscillatory function. This damped oscillatory behavior of the exchange energy with respect to the values of $2k_F\left|\boldsymbol{R}_i-\boldsymbol{R}_j\right|$, indicates that the magnetic ordering temperature usually drops with large R-R spacing and the ordering can be FM or AFM type, dependent on the values of k_F and $\boldsymbol{R}_i-\boldsymbol{R}_j$.

By using the molecular field approximation [Szytula and Leciejewicz, 1994], the T_{C} value for ferromagnet can be expressed as:

$$T_{\mathrm{C}} = -\frac{3\pi n^2}{k_B E_F} J_{sf}^2 (g_J - 1)^2 J(J+1) \sum_{i \neq o} F(2k_F R_{io}) \tag{2.20}$$

where o is the central ion and R_{io} is the distance between the central ion and the neighboring ith ion. This result is reminiscent to the one of Weiss's molecular field theory (Eqn. 2.11), but the term $\mu_{eff}^2 = g_J^2 J(J+1)$ in Eqn. 2.11 is replaced by the well-known de Gennes factor: $dG = (g_J - 1)^2 J(J+1)$. This difference comes from the assumption that only spin momentum contributes to the exchange interaction, which leads to the term of $S(S+1) = (g_J - 1)J(J+1)$, according to the well-known Wigner-Eckart theorem in quantum mechanics.

In AFM materials, the Néel temperature (T_{N}) can be derived in a similar manner by using the molecular field approximation [Mattis, 1965]. Therefore, the magnetic ordering temperatures are expected to scale with the de Gennes factor for isostructural rare earth intermetallic compounds within the RKKY model.

The second mechanism, first proposed by Campbell [Campbell, 1972], successfully explained the magnetic properties of binary rare earth transition metal intermetallic compounds, which manifest FM ordering without de Gennes scaling for isostructural compounds. In this model, the $5d$ electrons of the rare earth component play an important rule. The $4f$ local moments polarize the $5d$ electrons, and the later hybridize with the $3d$ electrons of transition metal. The overall indirect interaction between the $4f$ local moments is always FM. This mechanism proposes a short range, tight binding interaction and treats d and s electrons entirely separately, whereas the RKKY mechanism proposes a long range, free electron interaction and does not distinguish d and s electrons.

2.2 d electron and Itinerant magnetism

In rare earth intermetallic compounds, the magnetism contributed from the conduction electrons is usually weaker than the contribution from the unfilled $4f$ shells, except for some $3d$-rich transition metal-rare earth binary or ternary compounds. However, understanding

the susceptibility of the conduction electrons is important because they mediate the magnetic interaction between the $4f$ local moments, and they may hybridize with the $4f$ electrons to modify the local moment behavior in the cases of Ce and Yb based compounds. To approach this experimentally, the La, Lu and Y isostructural compounds with empty or full $4f$ shell are usually synthesized and the magnetic properties of the conduction electrons can be measured without the 'noise' of the $4f$, local moment magnetism.

In general, the local moment magnetism model is able to explain the magnetic properties of insulators and metals associated with $4f$ electrons successfully, but not the magnetic properties of conduction electrons. For example, the $3d$ transition metal elements (eg. Fe, Co and Ni) and some of their compounds or alloy manifest strong magnetic signals associated with the $3d$ itinerant electrons. Fe, Co and Ni elements have a FM ground state with non-integral, saturated moments equaling $2.21\mu_B$, $1.70\mu_B$ and $0.60\mu_B$ respectively. [Huang and Han, 1988] These values of saturated moments are less than the values corresponding to their Hund's ground states, or even the spin-only contribution.

On the other hand, a band model is able to successfully explain some magnetic properties of these conduction electron systems. It is well known that a non-interacting, conduction electron system can be treated as a Fermi sea and manifests Pauli paramagnetic behavior. For some d electron systems, the d electrons are more localized than normal s electrons, and the interaction between d-d electrons must be considered. The simple Stoner theory explains the ferromagnetism of d electron systems as the result of splitting between the spin-up and spin-down band due to the interaction between conduction electrons. To understand this theory, it is helpful to understand the paramagnetism of non-interaction conduction electron systems at first.

2.2.1 Pauli paramagnetism

In metals free electron paramagnetism mainly comes from the spin contributed magnetic moment of conduction electrons in an applied field. Since the conduction electrons are highly degenerate and obey the Fermi-Dirac distribution, the Pauli principle must be considered. As

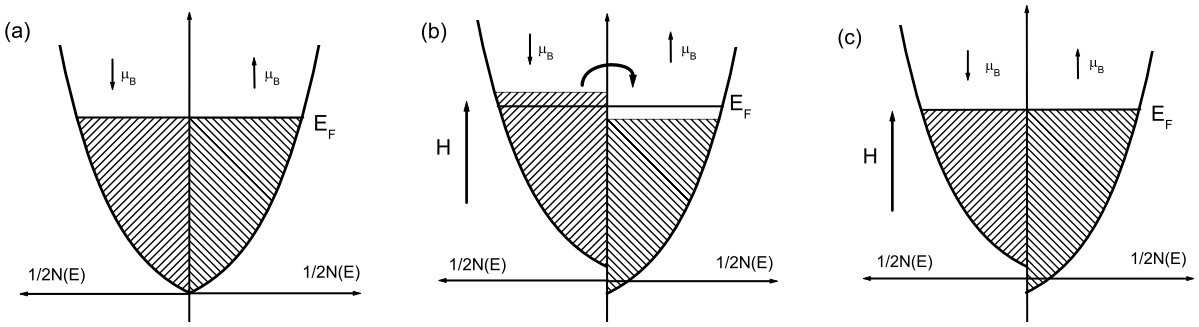

Figure 2.3 Diagram of Pauli paramagnetism. (a): No applied field. (b): No equilibrium state in an applied field H. (c): Equilibrium state in H.

we shall see below, only the electrons within a small range of the top of the Fermi distribution have a chance to flip spin in the applied field and contribute to the paramagnetic signal.

The expression for the paramagnetic susceptibility of a conduction electron gas at zero temperature is readily calculated. Figure 2.3 (a) shows the distribution of the spin-up and spin-down electrons with no applied magnetic field. The total density of states $[N(E)]$ is equally separated into the spin up and spin down parts. Below the Fermi energy (E_F), the shadow part is fully filled by the conduction electrons, and the area of the shadow part represents the number of the conduction electrons. Without an applied field, the numbers of the spin-up and spin-down electrons are equal and the total magnetization is zero. In an applied field H, the parallel and anti-parallel spin moment will gain additional energy $-\mu_B H$ and $+\mu_B H$, respectively. Therefore, the Fermi energy lever for the spin-up and spin-down electrons will have the difference as $2\mu_B H$ [Fig. 2.3 (b)]. Obviously, the electrons having higher E_F (spin-down part) in this hypothetical state will flow to the spin-up side so as to balance the Fermi energy level. In the equilibrium state, part of spin down electrons flip, from anti-parallel to parallel the magnetic field [Fig. 2.3 (c)]. The number of such electrons equals:

$$n = \frac{1}{2}\mu_B H N(E_F) \tag{2.21}$$

This leads to a magnetization that equals $\mu_B^2 H N(E_F)$ parallel to the applied field. Therefore, the magnetic susceptibility, which is called the Pauli paramagnetic susceptibility, is:

$$\chi = \mu_B^2 N(E_F). \tag{2.22}$$

When $T \neq 0$ K, the Pauli paramagnetic susceptibility will include a part from thermal excitation:

$$\chi = \mu_B^2 N(E_F)[1 - \frac{\pi^2}{12}(\frac{k_B T}{E_F})^2] \tag{2.23}$$

Since $\frac{k_B T}{E_F} \ll 1$, the Pauli paramagnetic susceptibility in this simple model is temperature independent and proportional to the density of states at Fermi level. It should be noted, though, that sharp features in the density of states (DOS) near E_F (sharp compared to $k_B T$) can lead to some temperature dependencies.

2.2.2 Stoner theory

The above derivation of Pauli paramagnetism assumes no interaction between the conduction electrons other than the Pauli exclusion effect. For the transition metals, the d band electrons, with their relatively large exchange interaction, mainly contribute the magnetization. Due to the exchange interaction, the band can spontaneously split for spin-up and spin-down electrons, which can lead to FM ordering.

The Stoner theory is based on the mean field approximation, which assumes an exchange interaction between the d-band electrons that independent with their wave vectors. This interaction causes an instability of the Fermi surface and then leads to a FM ground state. This theory successfully explains the observed, non-integral, saturated moments for $3d$ transition metal elements, but it is not able to explain the observed magnetic behavior of these itinerant electron systems at finite temperature successfully, specifically for $T \geq T_{\mathrm{C}}$. Nevertheless, the Stoner theory is useful to describe the ground state of correlated, itinerant electron systems and the study of it is the first step to understand the itinerant magnetism.

Diagrams illustrating the key ideas associated with the Stoner model at zero temperature are shown in Fig. 2.4. Assuming the exchange energy I between the d-band electrons is independent of their wave vectors, then the total exchange energy of the system with N electrons and magnetization M (in unit of μ_B) is given by

$$E_{ex} = I N_\uparrow N_\downarrow = \frac{1}{4} I N^2 - \frac{1}{4} I M^2, \tag{2.24}$$

$$N = N_\uparrow + N_\downarrow, M = N_\uparrow - N_\downarrow, \tag{2.25}$$

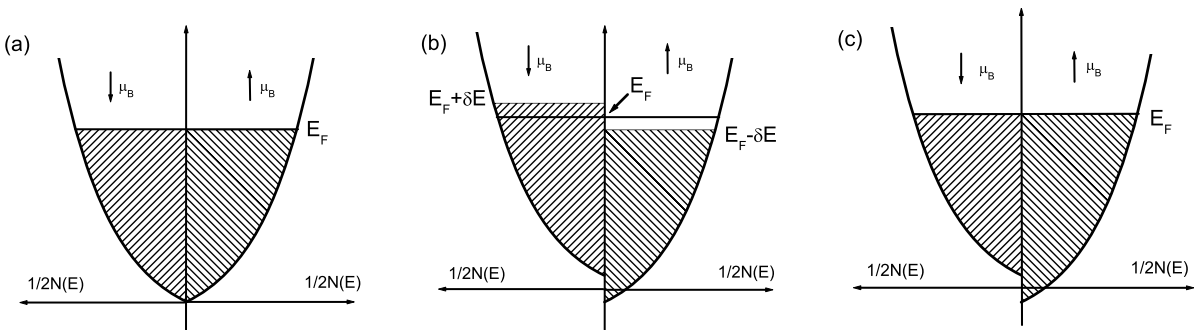

Figure 2.4 Diagram of Stoner theory. (a): Spin-up spin-down balance state with an exchange interaction. (b): Non-equilibrium state. (c): Ferromagnetic equilibrium state.

where N_σ is the number of electrons with spin σ.

As shown in Fig. 2.4 (a), when the number of the spin-up and spin-down electrons is equal, the magnetization equals zero, the total exchange energy has the maximum value equaling $\frac{1}{4}IN^2$, and the kinetic energy of the electrons equals zero. If, on the other hand, we assume that $\frac{1}{2}N(E_F)(\delta E)$ electrons from the spin-down band are moved to the spin-up band [Fig. 2.4 (b)], then the kinetic energy increases by ΔE_1

$$\Delta E_1 = \frac{1}{2}N(E_F)(\delta E)^2, \tag{2.26}$$

and the total exchange energy will decrease by ΔE_2

$$\Delta E_2 = \frac{1}{4}IM^2 = \frac{1}{4}IN^2(E_F)(\delta E)^2. \tag{2.27}$$

The total energy difference then is

$$\Delta E = \Delta E_1 - \Delta E_2 = \frac{1}{2}N(E_F)[1 - \frac{IN(E_F)}{2}](\delta E)^2. \tag{2.28}$$

Therefore, as the spin-down electrons within the range δE of the Fermi level are moved to the spin-up band, the energy difference is proportional to $(\delta E)^2$.

When $\frac{IN(E_F)}{2} > 1$, $\Delta E < 0$, the magnetic state is stable, and the system will manifest spontaneous magnetization [Fig. 2.4 (c)]. The saturated moment of the system in FM ground state may assume non-integral values, corresponding to the band filling. When $\frac{IN(E_F)}{2} < 1$, $\Delta E > 0$, the non-magnetic state is stable, and the system will manifest paramagnetic magnetization. The paramagnetic susceptibility χ can be derived as following.

Assuming an applied field H is along the spin up direction, the parallel and anti-parallel spin moment will gain additional energy $IN_\downarrow - \mu_B H$ and $IN_\uparrow + \mu_B H$, respectively. The difference

$$2\delta E = IN_\uparrow + \mu_B H - (IN_\downarrow - \mu_B H) = I(N_\uparrow - N_\downarrow) + 2\mu_B H = IN(E_F)\delta E + 2\mu_B H. \quad (2.29)$$

Therefore, the energy range of field induced spin flip is

$$\delta E = \frac{\mu_B H}{1 - \frac{IN(E_F)}{2}}, \quad (2.30)$$

and the total magnetic moment is

$$2\mu_B \frac{1}{2} N(E_F)\delta E = \mu_B^2 \frac{N(E_F)}{1 - \frac{IN(E_F)}{2}} H, \quad (2.31)$$

and the magnetic susceptibility is

$$\chi = \mu_B^2 \frac{N(E_F)}{1 - \frac{IN(E_F)}{2}}. \quad (2.32)$$

Although ferromagnetism is not realized for $\frac{IN(E_F)}{2} < 1$, the Pauli paramagnetic susceptibility (Eqn. 2.22) is enhanced by the factor $\frac{1}{1-\frac{IN(E_F)}{2}}$. The factor

$$Z = \frac{IN(E_F)}{2}. \quad (2.33)$$

is known as Stoner enhancement factor and the condition

$$Z = \frac{IN(E_F)}{2} = 1 \quad (2.34)$$

is known as Stoner criteria.

Three $3d$ transition metal elements (Fe, Co and Ni), with high T_C values are typically characterized as strong itinerant FM materials, in which $Z > 1$. More interesting magnetic behavior may appear when the system is close to the Stoner criteria. These systems, typically characterized as nearly FM materials ($Z < 1$ but close to 1), such as elemental Pd or Pt, or as weakly FM materials ($Z > 1$, both $N_\uparrow(E_F)$ and $N_\downarrow(E_F) \neq 0$), such as $ZrZn_2$ or Sc_3In with low T_C values, manifest strongly correlated, electronic behavior. In the view of the quantum phase transition theory, these systems are close to a so-called, quantum critical point (QCP), meaning

the paramagnetic to ferromagnetic phase transition can be tuned at zero temperature by some parameters such as pressure, doping, or applied field. Such nearly FM systems and weakly FM systems allow for studies of quantum criticality and possibly even novel superconducting state.

2.3 Crystalline Electric field

When rare earth ions are placed within a crystalline lattice, the interaction with their surroundings (neighboring atoms or conduction electrons) can be modeled as an electrostatic field, which is known as crystalline electric field (CEF). As the $4f$ electrons are screened by the full $5s$ and $5p$ shells (see Fig. 2.1), the CEF effect is relatively small compared with the spin-orbital coupling and can be treated as a perturbation of the free ion $4f$ electronic configuration. This perturbation lifts the Hund's rule ground state degeneracy of the free ion.

Assuming that the CEF is produced by an array of point charges surrounding the central free ion, or spatially extended charges that do not overlap with the electrons of the free ion, the CEF potential, V_{CEF}, must satisfy the Laplace equation:

$$\nabla^2 V_{CEF} = 0. \tag{2.35}$$

The solution of the Laplace equation can be expanded in terms of spherical harmonic function $Y_n^m(\theta, \varphi)$ as:

$$V_{CEF} = \sum_{n=0}^{\infty} \sum_{m=-n}^{n} A_n^m r^n Y_n^m(\theta, \varphi). \tag{2.36}$$

For the $4f$ configuration with total angular momentum J, there are $2J+1$ degenerate state $|JM_i\rangle$ before the perturbation associated with the CEF effect. Then the matrix elements due the CEF energy has the form:

$$\langle JM_i \left| A_n^m r^n Y_n^m(\theta, \varphi) \right| JM_k \rangle = A_n^m \langle R \left| r^n \right| R \rangle \langle \Phi_i \left| Y_n^m(\theta, \varphi) \right| \Phi_k \rangle . \tag{2.37}$$

The radial electron wave function $|R\rangle$ can be obtained from a non-relativistic or relativistic Hartree-Fock calculation and is the same for all states of a given electron configuration. The angle dependent, electron wave function $|\Phi\rangle$ can be expanded in terms of spherical harmonic functions up to the order of $n = 3$ for f electrons. Therefore, all of the terms of

$\langle \Phi_i | Y_n^m(\theta, \varphi) | \Phi_k \rangle$ with $n > 6$ will be vanished. Furthermore, all the terms with odd n will vanish because the electronic charges are equivalent contained in the crystal. The number of parameters can be further reduced by higher point symmetries associated with the R-site.

2.3.1 Steven's equivalent operators

For the rare earth ions, the above calculation method is very difficult. But if only the ground state J is considered, a much simpler method, associated with introducing the Steven's equivalent operators, [Stevens, 1952] may be applied. The main idea is to replace the spatial coordinate operators x_i, y_i and z_i in Eqn. 2.37 with the corresponding products of the angular momentum operators $\hat{J}_x$, $\hat{J}_y$ and $\hat{J}_z$. It has been shown that the matrix elements of the CEF Hamiltonian are proportional to a set of operators containing components of the angular momentum J. In this representation, the CEF Hamiltonian can be expressed in general form as:

$$\mathcal{H}_{CEF} = \sum_{n,m} A_n^m \langle r^n \rangle \theta_n O_n^m \tag{2.38}$$

Where O_n^m are Steven equivalent operators; θ_n is a multiplicative factor and often called α_J, β_J and γ_J for $n = 0$, 2 and 4 respectively; A_n^m are the CEF parameters. This CEF Hamiltonian are also often written as:

$$\mathcal{H}_{CEF} = \sum_{n,m} B_n^m O_n^m, \tag{2.39}$$

where $B_n^m = A_n^m \langle r^n \rangle \theta_n$. The energy splitting of the Hund's rule multiplet and the corresponding eigenfunctions can be calculated by applying the operators and diagonalizing the matrix elements.

2.3.2 Cubic symmetry

The simplest example is the CEF Hamiltonian in cubic point symmetry group, which have been well studied by Lea *at el.*[Lea et al., 1962]. In this case, the CEF Hamiltonian is reduced by the high symmetry to:

$$\mathcal{H}_{CEF} = B_4^0(O_4^0 + 5O_4^4) + B_6^0(O_6^0 - 21O_6^4), \tag{2.40}$$

where the fourfold axis in the cubic coordination has been chosen as the quantization axis.

In order to keep the eigenvalues in the same numerical range for all ratios of the fourth and sixth degree terms, for all of the possible J values, this expression is written as:

$$\mathcal{H}_{CEF} = W[\frac{x}{F4}(O_4^0 + 5O_4^4) + \frac{1-|x|}{F6}(O_6^0 - 21O_6^4)], \tag{2.41}$$

where $F4$ and $F6$ are normalizing parameters depending on the J value; W and x, as two unknown parameters represents the energy scale of CEF effect and the relative importance of the 4th and 6th order terms, respectively.

In rare earth intermetallic compounds, the single-ion Hamiltonian for a well-defined, local moment, associated with a R^{3+} ion, is assumed to be the sum of the CEF term, an exchange interaction term and an external field term:

$$\mathcal{H} = \mathcal{H}_{CEF} + \mathcal{H}_{exc} + \mathcal{H}_{ext}. \tag{2.42}$$

where $\mathcal{H}_{ext} = g_J \mu_B \boldsymbol{J} \cdot \boldsymbol{H}$. If the exchange interaction term is ignorable, thermodynamic properties of rare earth ions can be easily calculated by diagonalizing the Hamiltonian of the CEF term and the external field term.

As an example, Fig. 2.5 shows the calculated magnetization at 2 K and specific heat at zero applied field for a well-defined, local moment associated with Yb^{3+} ion ($J = 7/2$) as $x = 0.9$ and $W = 1$. With the Yb^{3+} in a cubic point symmetry group, its Hund's rule ground state is split to two doublets (Γ_6 and Γ_7) and one quartet (Γ_8), which have energy levels as shown in Fig. 2.5 (c). The specific heat anomaly due to the CEF splitting, known as 'Schottky anomaly', manifests itself as a broad peak with $C_p \sim T^{-2}\exp(-\frac{1}{T})$ below the maximum C_p and $C_p \sim T^{-2}$ above the maximum. It is worth noting that the magnetization at 2 K manifest a step-like behavior for $H//[100]$. In large enough external field ($\mathcal{H}_{ex} \gg \mathcal{H}_{CEF}$), the magnetization along all three principle axes are close to the value of the saturated moment associated with the Hund's rule ground state ($4\mu_B$).

In real systems, the exchange interaction is usually not small, and affects the magnetic properties dramatically. Unfortunately, the exchange interaction Hamiltonian, $\mathcal{H}_{exc}$, is difficult to address even by using the simple, molecular field approximation. In order to analyze the

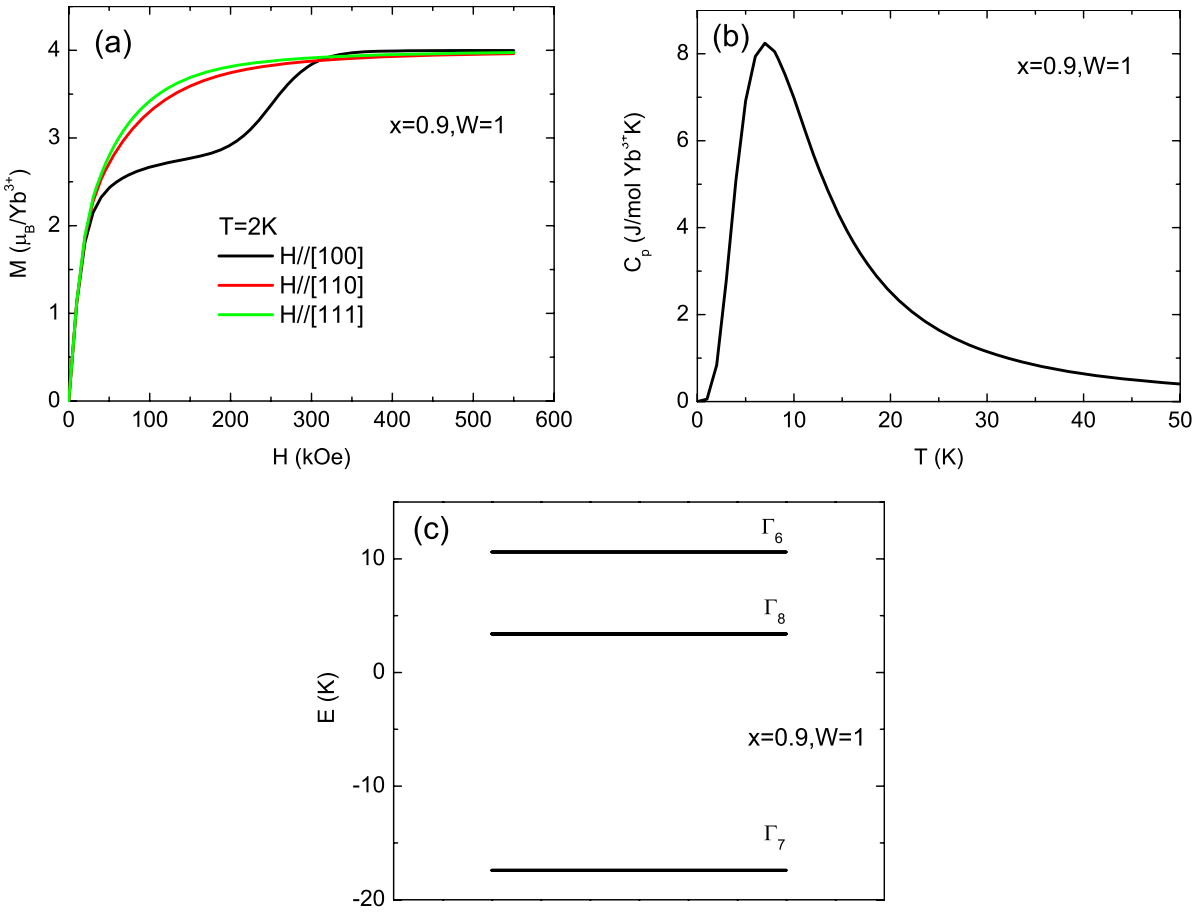

Figure 2.5 Calculated results of CEF induced magnetic properties of a well-defined, local moment associated with Yb^{3+} single ion in cubic symmetry as $x = 0.9$ and $W = 1$. (a) Magnetization versus applied field along the three principle axes at 2 K. (b) Specific heat versus temperature at zero field. (c) The energy splitting at zero field.

CEF effect without this complication, dilution-compounds, containing R_xY_{1-x} or R_xLu_{1-x}, are usually synthesized. As the magnetic rare earth ions are diluted to approach the single-ion limit, the interaction is ignorable. Therefore, the CEF parameters can be determined by fitting the zero field specific heat data and the magnetization data in varied applied field and varied temperature.

In principle, the CEF parameters can also be calculated by a simple point-charge model. In this model, the CEF is assumed to be mainly from the nearest neighbor ions with identified charges. The results with the rare earth coordination being either a tetrahedron, octahedron or cube have been given, for cubic point symmetry [Hutchings, 1964]. However, it is not unusual that the calculated results based on the point charge model show as large as a one order of magnitude difference compared with the experimental fitting results. Such difference may partially come about as the result of the influence of the conduction electron screening on the CEF.

2.4 Heavy fermion compounds

The term 'heavy fermion' are usually used to describe a subset of rare earth or actinide intermetallic compounds containing multivalent f electron ions (like Ce, Yb and U) and manifesting large electronic specific heat (γ). An arbitrary definition of a 'heavy fermion' system given by Stewart [Stewart, 1984b] is that $\gamma > 400$ mJ/mol$f$atom K^2, although many rare earth intermetallic compounds with lower γ values have also been characterized as heavy fermion materials. Nevertheless, all the heavy fermion compounds manifest anomalous f electronic behavior different from that observed for well-defined, local moment compounds. In 'normal' local moment, intermetallic compounds, the f band lie far below the Fermi level and the f electrons are localized. The interaction between the f electrons and the conduction electrons is a Heisenberg exchange interaction. This interaction leads to an intersite exchange interaction between the local moments by means of conduction electrons polarization, which is the so-called RKKY interaction and may be FM or AFM depending on the Fermi surface and the local moments spacing. In 'anomalous' rare earth compounds, the f levels lie near the Fermi

level and the hybridization between the conduction electrons and f electrons is significant. This anomaly usually happens as the $4f$ shell of rare earth ion is close to empty, full or half filled (like Ce, Yb or Eu), since the empty, full and half filled $4f$ shell are more stable, leading to the instability of $4f$ electronic configuration of the Ce^{3+}, Yb^{3+} and Eu^{3+} ions. Compounds containing these rare earths can, in the cases where they hybridize, be described as the so-called 'Kondo lattice' systems [Hewson, 1993], in which the hybridization with the conduction electrons leads to an AFM exchange interaction between the f electrons and conduction electrons. This AFM exchange interaction modifies the f electronic states in the region of the Fermi level and leads to anomalous low temperature behavior. In heavy fermion systems, the f electrons manifest local moment magnetic behaviors in the high temperature region, in the vicinity of a characteristic temperature, the so-called Kondo temperature (T_{K}), they start to lose their local moment behavior, and at the temperatures well below T_{K} the local moments are partially or totally compensated, and the system manifests a highly correlated, high-effective-mass electronic state.

2.4.1 Anderson Model

In order to understand the physics of heavy Fermion systems, it is necessary to start from a basic question: how does, or when can, an unfilled d or f electron shell survive in a metallic environment. Experimentally, when small amounts of transition metal elements are dissolved in a non-magnetic metal, the resulting alloys display varied magnetic properties. For example, local moment survives when Fe is dissolved in Cu, but not when Ni is dissolved in Cu. The Anderson model [Anderson, 1961] explains the variety as the result of a hybridization between the d or f electron of the impurity and the conduction electrons of the host. In this model, the unfilled d or f electron shell forms a so-called virtual bound state (vbs) in the conduction electron band of the host. The Hamiltonian for the Anderson model describes the d (or f) electron of the impurity hybridized with the conduction electrons (s electrons) plus the Coulomb interaction between the d electrons in the impurity ion. For the simplest non

degenerate d orbital this gives:

$$\mathcal{H} = \sum_{\sigma} \epsilon_d n_d + \sum_{\boldsymbol{k},\sigma} \epsilon_k c^{\dagger}_{\boldsymbol{k},\sigma} c_{\boldsymbol{k},\sigma} + U n_{d,\uparrow} n_{d,\downarrow} + \sum_{\boldsymbol{k},\sigma} (V_{\boldsymbol{k}} c^{\dagger}_{d,\sigma} c_{\boldsymbol{k},\sigma} + V^{*}_{\boldsymbol{k}} c^{\dagger}_{\boldsymbol{k},\sigma} c_{d,\sigma}). \tag{2.43}$$

The first two terms represent the individual kinetic energies of d electrons and s electrons. The third term gives the intra-atomic Coulomb repulsion of the lowest d orbitals of opposite spin. The final term is the hybridization interaction between the s and d electrons. Finding the solution of this Hamiltonian is a long and tedious task. Simple, intuitive diagrams shown in Fig. 2.6 illustrate some of the more salient physics.

Figure 2.6 (a) shows that a localized d (or f) impurity is embedded in the conduction electron host and the energy level of the d electron is lower than the Fermi level (E_F) of conduction electrons. If only the kinetic energy of s electron and d electron are considered, the d electron will form a bound state with the binding energy ϵ_d and a δ function anomaly in the density of states. If the hybridization effect and the intra-atomic Coulomb effect are included, the d electron will form virtual bound state (vbs) in each of the sub-bands, spin-up and spin-down. The hybridization energy broadens the density of states for d electron with the width $2\Delta = \pi V_{\boldsymbol{k}} V^{*}_{\boldsymbol{k}} N(E_F)$. The Coulomb energy causes an energy shift U between the spin-up level and spin-down level. Figure 2.6 (b) shows the case $|V_{\boldsymbol{k}}| \ll |U|$, where the spin-up vbs is fully occupied and the spin-down vbs is empty. In this case a well-defined local moment is formed. In the other extreme case $|V_{\boldsymbol{k}}| \gg |U|$, the spin-up vbs is equally occupied as the spin-down vbs [Fig. 2.6 (d)]. The d electron is effectively dissolved in the sea of conduction electrons and the impurity lose its magnetism. In the intermediate case, $|V_{\boldsymbol{k}}|$ is comparable to $|U|$, the spin-up and spin-down vbs are both partially, unsymmetrically occupied [Fig. 2.6 (c)]. The local moment is partially compensated and may manifest any value. The strict mathematical deviation leads that a local moment forms in the parameter regime $U + \epsilon_d > E_F$ and $\epsilon_d < E_F$ in the Anderson model.

Another important conclusion of Anderson model is that the hybridization of the d electron and the conduction electron will lead to an AFM exchange interaction between the local moment and conduction electrons in the local moment regime. Figure 2.7 shows the schematic diagram of the vbs close to the Fermi level, which makes the hybridization or covalent mix-

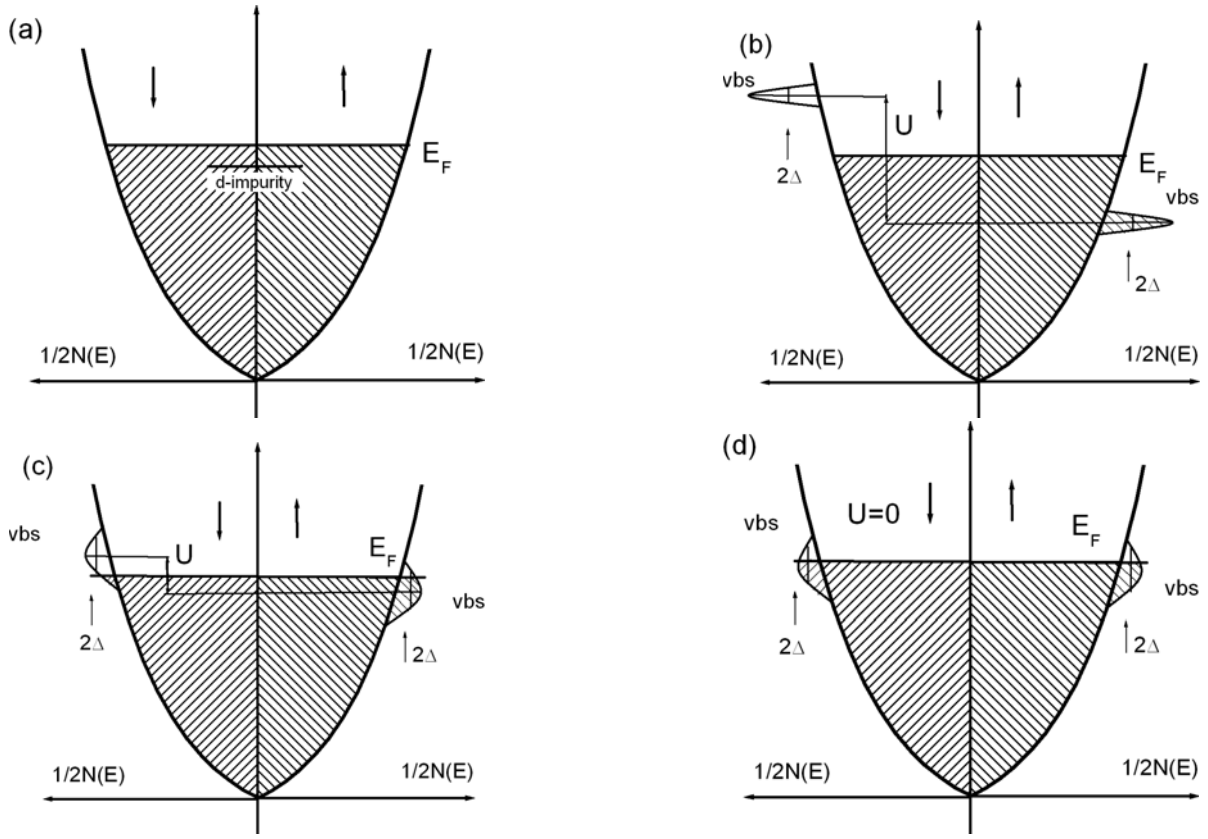

Figure 2.6 Schematic diagram of Anderson model. (a) d (or f) impurity immersed in conduction electron host. (b) The formation of the vbs. An occupied spin-up vbs with width 2Δ is attached below the Fermi energy E_F. A similar, but unoccupied vbs split by energy U above E_F occurs with spin-down sub-band. This diagram illustrate formation of a local moment with large U. (c) Partially occupied magnetic vbs with small U. The magnetic moment forming due to the different filling of the spin-up and spin-down vbs can be any spin value. (d) The symmetric case of equal spin-up and spin-down occupancies ($U = 0$) and thereupon no net magnetic moment.

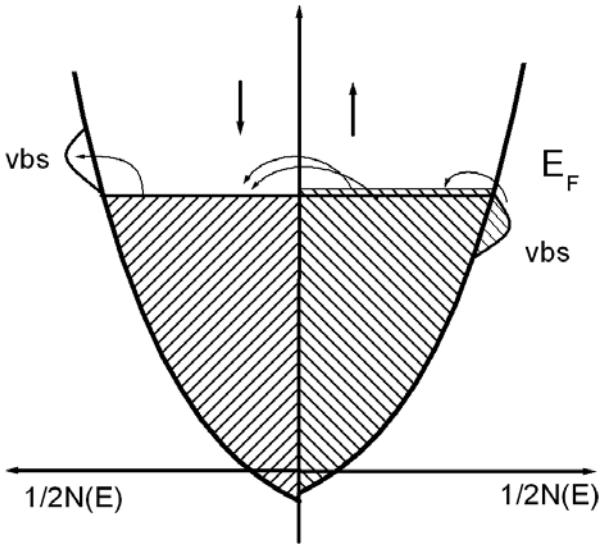

Figure 2.7 Schematic diagram of the AFM exchange interaction formation in Anderson model.

ing possible. Due to the hybridization, electrons will transfer from the occupied vbs to the spin-up sub-band as well as from the spin-down sub-band to the empty vbs. This electronic hop will induce a non-equilibrium state between the spin-up and spin-down sub-band, which makes the up-spin electrons flow into the spin-down sub-band. The net result of this whole process is to produce slightly more down-spin conduction electrons than up-spin conduction electrons hopping from the vbs. That means that small amount of conduction electrons will be polarized oppositely by the local moment due to their hybridization. This AFM coupling can be described as the so called *s-d* exchange Hamiltonian and is indeed the origin of the Kondo effect.

2.4.2 Single ion Kondo effect

A local minimum in the temperature dependent resistivity in certain dilute magnetic alloy [Wilson, 1953] (e.g. Cu, Ag, Au with unfilled, *d*-band, magnetic impurity such as Fe, Mn, Mo) has been observed experimentally since 1930. Figure 2.8 shows the schematic diagram of the resistivity minimum. After the lattice vibration contributed scattering resistance

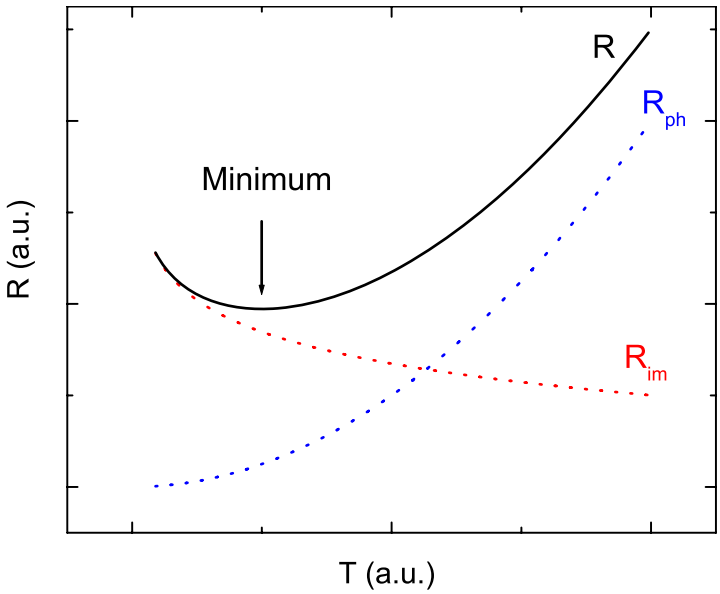

Figure 2.8 Schematic diagram of the resistivity Kondo minimum. The total resistivity equals the sum of phonon contribution (R_{ph}) and magnetic impurity contribution (R_{im}): $R = R_{ph} + R_{im}$.

(R_{ph}) is subtracted, the magnetic impurity contributed scattering resistance (R_{im}) increases as temperature decrease. The experimental data show that R_{im} manifests a clear temperature dependence:

$$R_{im} = a - b \ln T, \tag{2.44}$$

in the vicinity of the minimum, where a and b are temperature independent constants.

J. Kondo [Kondo, 1964] explained this resistivity minimum by using perturbation theory on the s-d exchange Hamiltonian [Zener, 1951],

$$\mathcal{H}_{sd} = -\frac{J}{N} \sum_{\boldsymbol{k},\boldsymbol{k'}} (\boldsymbol{S}^{+} c^{\dagger}_{\boldsymbol{k},\downarrow} c_{\boldsymbol{k'},\uparrow} + \boldsymbol{S}^{-} c^{\dagger}_{\boldsymbol{k},\uparrow} c_{\boldsymbol{k'},\downarrow} + \boldsymbol{S}_z (c^{\dagger}_{\boldsymbol{k},\uparrow} c_{\boldsymbol{k'},\uparrow} - c^{\dagger}_{\boldsymbol{k},\downarrow} c_{\boldsymbol{k'},\downarrow})) \tag{2.45}$$

where $\boldsymbol{S}_z$ and $\boldsymbol{S}^{\pm}$ are the spin operators for a state of spin $\boldsymbol{S}$. Kondo's calculation shows that the R_{im} have the form as:

$$R_{im} = R_0[1 - 4J\rho_F \ln \frac{k_B T}{D}], \tag{2.46}$$

where J is exchange coupling constant, ρ_F is the average density of states at Fermi level per electron, D is the half width of the conduction band. When $J < 0$, which means the s-d

coupling is AFM, the impurity resistivity increases with respect to $-\ln T$. Kondo's calculation successfully explain the minimum of temperature dependent resistivity in dilute magnetic alloys. However, the $-\ln T$ term diverges as $T \to 0$, which is inconsistent with the experimental observed finite resistivity at the base temperature.

In the calculations of thermodynamic properties, the perturbation theory lead to a divergent susceptibility and specific heat at a finite temperature T_{K},

$$k_B T_{\mathrm{K}} \sim D \exp^{-\frac{1}{2}J\rho_F} \tag{2.47}$$

known as the Kondo temperature. [Hewson, 1993] Experimentally, the susceptibility manifested Curie-Weiss behavior when $T \gg T_{\mathrm{K}}$, which is same as the result of the perturbation theory, but clearly deviates from the Curie-Weiss law below T_{K} [Fig. 2.9 (a)]. The specific heat manifested a broad peak about T_{K}, with the magnetic part of entropy associated with the impurity equaling $R\ln(2S+1)$ for the magnetic impurity with spin S. These experimental results indicated that the perturbation theory result was not applicable in the low temperature limit ($T \ll T_{\mathrm{K}}$). The problem of finding a solution valid in the low temperature regime was known as the 'Kondo problem'.

Solving the Kondo problem led to important developments in the region of theoretic physics. However, without any mathematic complication, the ground state of the impurity can be intuitively known by the entropy associated with the impurity in the experiments. The result $R\ln(2S+1)$ indicates that the ground state can only be a singlet, known as Kondo singlet, due the compensation of the local moment by the anti-parallel conduction electrons. The Kondo singlet ground state at $T = 0$ was firstly proved by Wilson by using renormalization group theory [Wilson, 1975]. The exact solutions to the s-d model with $S = \frac{1}{2}$ were discovered by Andrei [Andrei, 1980] and Wiegmann [Wiegmann, 1980] by using the Bethe ansatz method.

2.4.3 Physical properties of heavy Fermions

Heavy Fermion systems, usually described as Kondo lattices, manifest some characteristics different to dilute Kondo alloys. At first, unlike the pure, spin contributed magnetic moment for the d electron impurity, the magnetic moment of the f electron associated with its Hund's

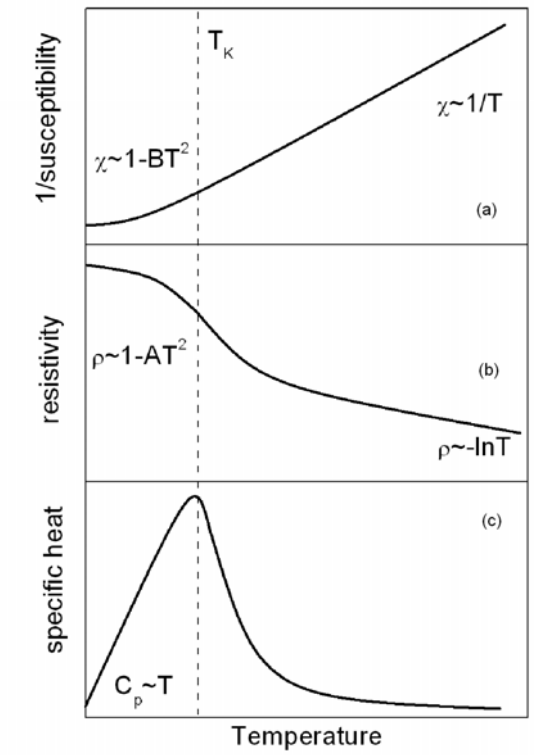

Figure 2.9 Low-temperature magnetic behavior of (a) susceptibility, (b) resistivity and (c) specific heat of a diluted Kondo system.

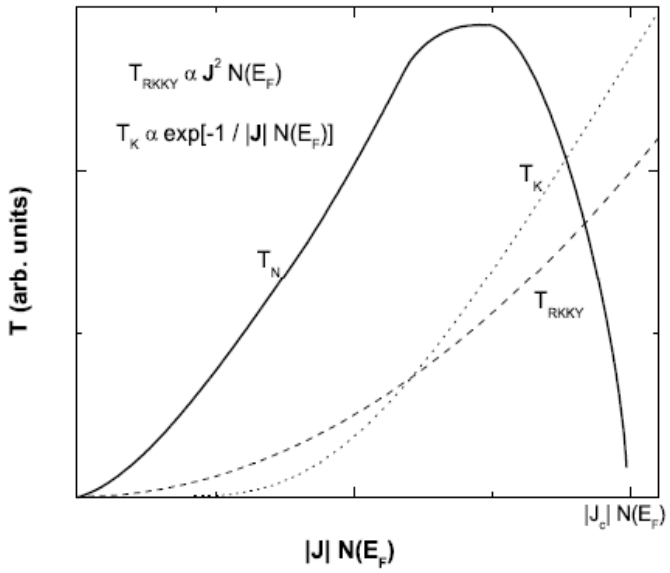

Figure 2.10 Doniach's phase diagram.

rule ground state usually consists of spin and orbital contribution, leading to a large degeneracy. For example, the Hund's rule ground states for Ce^{3+} and Yb^{3+} have $J = 5/2$ and $7/2$, leading to degeneracies $N = 6$ and 8 respectively, some of which may have been lifted by the CEF effect. Secondly, in a Kondo lattice, the f moments keep their periodicity, leading to $T < T_{\rm K}$ coherent, electronic behaviors. Indeed, a prominent signature of a Kondo lattice state is the fact that, below $T_{\rm K}$, the resistivity starts to rapidly decreases below a 'coherence temperature' T^*. Thirdly, the f moments in the heavy Fermion system are usually concentrated with a small spacings of about $4 - 5$ Å. For such concentrated impurities, the conduction electron screening clouds overlap and the inter-impurity interaction must be important.

Due to these complications, the magnetic properties of heavy Fermion compounds may show varied behaviors, dependent on varied systems as well as chemical or thermodynamic conditions, such as substitution, pressure and applied magnetic field. For example, a competition is anticipated between long-range magnetic ordering of the uncompensated moments and the low temperature Kondo screened state, as the value of $JN(E_F)$ varies [Doniach, 1977]. As illustrated in Fig. 2.10, the exchange interaction between the magnetic moments is char-

acterized by the RKKY temperature $T_{\mathrm{RKKY}} \propto J^2 N(E_F)$; the Kondo effect is characterized by the Kondo temperature T_{K}. When the parameter $JN(E_F)$ increase, T_{K} increases faster than T_{RKKY}, resulting in a local maximum in the ordering temperature T_{N}, followed by a drop in T_{N} around a critical value $J_C N(E_F)$. This may lead to a quantum phase transition at $T = 0$ K, with the possibility of tuning the parameter $JN(E_F)$ via a number of control parameters (chemical substitution, pressure, magnetic field). Experimentally, via tuning the parameters, the ground state of a heavy Fermion compound may vary from magnetic ordering, to non Fermi liquid (NFL) state in the vicinity of the quantum critical point (QCP), to an enhanced electronic mass, Fermi liquid state. The NFL behaviors usually involves logarithmic divergence of the specific heat $C_p/T \sim -\ln T$, and linear temperature dependence of the resistivity $\rho \sim T$ [Stewart, 2001, Stewart, 2006]. In the FL state, the resistivity manifests a quadratic temperature dependent behavior, $\rho = \rho_0 + AT^2$; the specific heat divided by temperature follows $C_p/T = \gamma + \beta T^2$, the magnetic susceptibility also becomes independent of temperature.

The so-called 'Wilson ratio' (WR) [Wilson, 1975] and 'Kadowaki-Woods ratio' (KWR) [Kadowaki and Woods, 1986] are useful for establishing correlation between the resistivity, specific heat and magnetic susceptibility in the FL state of heavy Fermion systems. In Landau's FL theory, $\sqrt{A} \sim m^*$, $\gamma \sim m^*$ and $\chi(T = 0) \sim m^*$, where $m^\star$ is the effective mass of the quasiparticle. The Wilson ratio and Kadowaki-Woods ratio are defined as:

$$WR = \frac{\pi^2 k_B^2 \chi(T=0)}{g_J^2 \mu_B^2 \gamma J(J+1)} \tag{2.48}$$

$$KWR = \frac{A}{\gamma^2} \tag{2.49}$$

respectively. Experimentally, the Wilson ratio usually manifests values between 1 and 2 for varied systems, whereas the calculated result of the Coqblin-Schrieffer model shows that $WR = \frac{N}{N-1}$ [Hewson, 1993]. However, the Kadowaki-Woods ratio can manifest values from the order of $10^{-5}\mu\Omega\mathrm{cm(K\ mol/mJ)}^2$ to the order of $10^{-7}\mu\Omega\mathrm{cm(K\ mol/mJ)}^2$ for varied heavy Fermion systems [N Tsujii and Kosuge, 2003]. Tsujii *et al.* generalized the concept of a fixed Kadowaki-Woods ratio to one dependent on the degeneracy of the f electronic configuration when the

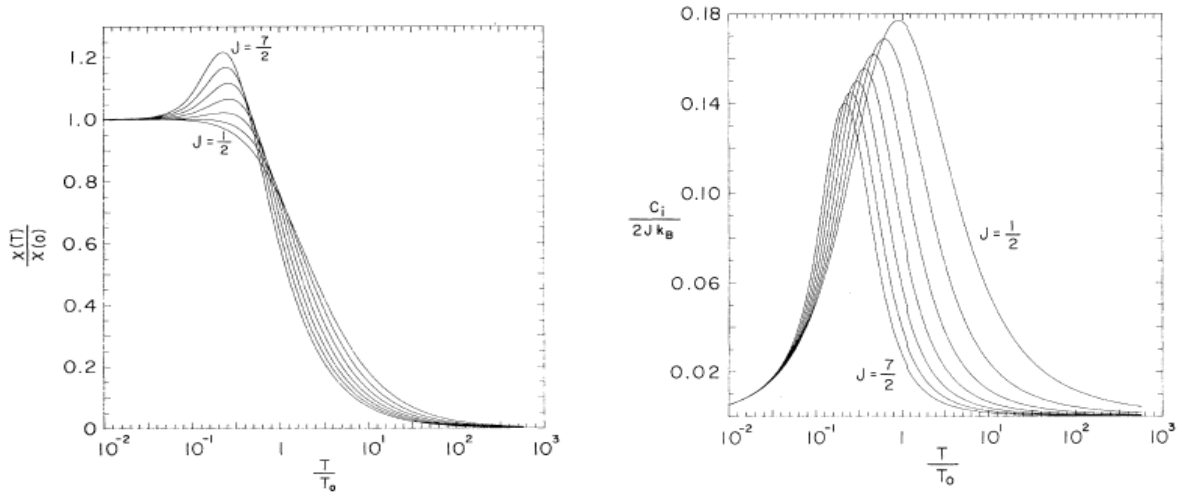

Figure 2.11 Rajan's results of magnetic susceptibility and specific heat of the Coqblin-Schrieffer model with $J = 1/2, 1, \ldots, 7/2$.

system enters the Kondo screen state [Tsujii et al., 2005]. Their calculated result for the Kadowaki-Woods ratio

$$KWR = \frac{A}{\gamma^2} = \frac{1 \times 10^{-5}}{1/2N(N-1)} \mu\Omega \text{ cm(K mol/mJ)}^2 \tag{2.50}$$

depends on the degeneracy N, which can be 2, 4, 6 and 8 for the Yb^{3+} ion due to the CEF splitting of the Hund's rule ground.

Although the heavy Fermion ground state is associated with many complications, theoretical analysis based on a single ion Hamiltonian is still useful. The so-called Coqblin-Schrieffer model [Coqblin and Schrieffer, 1969] describes an impurity with total angular momentum J dissolved in a free-electron metal. This model is a generalization of the basic s-d model:

$$\mathcal{H}_{CS} = \sum_{\boldsymbol{k},m} \epsilon_{\boldsymbol{k}} c^\dagger_{\boldsymbol{k},m} c_{\boldsymbol{k},m} - 2J \sum_{\boldsymbol{k},m} \sum_{\boldsymbol{k'},m'} c^\dagger_{\boldsymbol{k'},m'} c_{\boldsymbol{k},m} a^\dagger_m a_{m'} \tag{2.51}$$

where $-J < m < J$. The first term describes the kinetic energy and the second term describes the interactions between electrons and impurity.

Rajan [Rajan, 1983] calculated magnetic susceptibility and specific heat by using the Bethe Ansatz method on the Coqblin-Schrieffer model. Figure 2.11 shows the results for varied J

values. The characteristic temperature

$$T_0 = \frac{NT_{\mathrm{K}}}{2\pi\omega_N} \tag{2.52}$$

where ω_N is Wilson number [Rasul and Hewson, 1984]. The broad peak appearing in the temperature dependent susceptibility [2.11 (a)] is usually called as 'Kondo peak' and observed in many heavy Fermion systems. By using Rajan's results to fit the experimental data, the Kondo temperature as well as degeneracy of the local moment, which may be lifted by CEF effect, can be obtained.

CHAPTER 3. Crystal structure of RT_2Zn_{20} compounds

The RT_2Zn_{20} series of compounds were discovered in polycrystalline form in 1997 by Nasch *et al.* [Nasch et al., 1997]. These compounds assume the isostructural, cubic, $CeCr_2Al_{20}$ structure [Kripyakevich and Zarechnyuk, 1968, Thiede et al., 1998, Moze et al., 1998], in which the R and T ions each occupy their own single, unique crystallographic site with cubic and trigonal point symmetry respectively, and the Zn ions have three unique crystallographic sites (Fig. 3.1). The coordination polyhedra for R and T are fully comprised of Zn, meaning that there are no R-R, T-T or R-T nearest neighbors and the shortest R-R spacing is ~ 6 Å. The nearest-neighbor (NN) and next-nearest-neighbor (NNN) shells of the R are all Zn, forming an all Zn Frank-Kasper-like polyhedron around, and isolating the site [Fig. 3.1 (b)]. RT_2Zn_{20} compounds had been found to form for T = Fe, Ru, Co and Rh, but no thermodynamic or transport property measurements were reported. We have extended the range of known RT_2Zn_{20} compounds to T = Os and Ir series, and been able to grow most of these compounds in the single crystalline form. Furthermore, single crystals of six new, isostructural Yb compounds (YbT_2Zn_{20}, T = Fe, Co, Ru, Rh, Os and Ir) were synthesized for the first time.

The results of the attempts to grow single crystals of RT_2Zn_{20} systems are summarized in Table 3.1. For T = Fe, only the heavy rare earth (R = Gd - Lu) and Yttrium compounds can be synthesized. For T = Co, the successively grown compounds extend to include R = Nd and Sm. All the rare earth elements are though to be able to form RT_2Zn_{20} structure with T = Ru, Rh, Os and Ir, expect for R = Eu. The physical properties of the isostructural, T = Ni column compounds have not been well-studied and will also be presented in current work. Only limited rare earth elements (R = Y, Dy - Tm and Lu) were found to form the isostructural compounds with T = Ni and Pt. These results are consisted with the previous

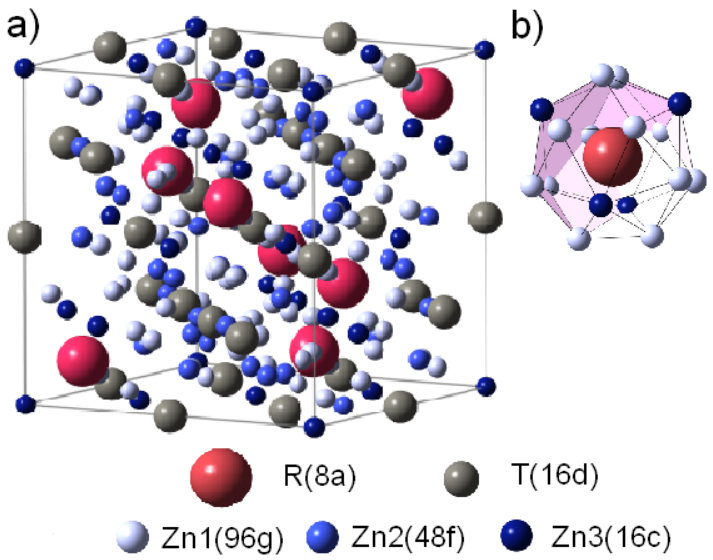

Figure 3.1 (a) The cubic unit cell of RT_2Zn_{20}. (b) The CN16 Frank-Kasper polyhedron of rare earth ions.

study for T = Fe, Co, Ni, Ru and Rh [Nasch et al., 1997].

Figure 3.2 shows the lattice parameters for GdT_2Zn_{20} and YT_2Zn_{20} (T = Fe, Co, Ru, Rh, Os and Ir) versus the Goldschmidt radius of the transition metal. The lattice parameters, determined by the refinement of powder X-ray diffraction, increase as the transition metal varies from $3d$ to $5d$ for both of GdT_2Zn_{20} and YT_2Zn_{20}. The error bars, smaller than the symbols in the plot, were estimated from the standard variation of multiple measurement results on one batch of sample. In addition to the refinement of powder X-ray diffraction, the crystallographic atomic site occupancies and positions were refined using single crystal X-ray data on the crystals of $GdFe_2Zn_{20}$ and $GdRu_2Zn_{20}$. Shown in Table 3.2, both compounds were found to be fully or very close to fully stoichiometric. The atomic site positions are very close to the isostructural compounds reported before [Nasch et al., 1997]. It should be noted, though, that the similar atomic number values for Zn and Fe made it difficult to resolve possible mixed site occupancies.

Figure 3.3 shows the lattice constants for RFe_2Zn_{20} (R = Y, Gd - Lu) and RCo_2Zn_{20} (R = Y, Nd, Sm, Gd - Lu)compounds, obtained by using the Rietica Rietveld refinement

Table 3.1 Summary of attempted growth of RT_2Zn_{20} compounds. +: single crystals obtained; − phase failed to be obtained; ⊕: un-attempted but expected to be obtained; ⊖: un-attempted, not expected to be obtained.

T	Y	La	Ce	Pr	Nd	Sm	Eu	Gd	Tb	Dy	Ho	Er	Tm	Yb	Lu
Fe	+	−	−	−	−	−	−	+	+	+	+	+	+	+	+
Co	+	−	−	−	+	+	−	+	+	+	+	+	+	+	+
Ni	+	⊖	−	⊖	⊖	⊖	−	−	−	+	+	+	+	−	+
Ru	+	+	+	+	+	+	−	+	+	+	+	+	+	+	+
Rh	+	+	+	+	+	+	−	+	+	+	+	+	+	+	+
Pd	−	⊖	−	⊖	⊖	⊖	−	−	⊖	⊖	⊖	⊖	−	−	⊖
Os	+	+	+	⊕	⊕	+	⊖	+	⊕	⊕	⊕	⊕	⊕	+	+
Ir	+	+	+	+	+	+	−	+	+	+	+	+	+	+	+
Pt	+	⊖	⊖	⊖	⊖	⊖	−	−	−	+	+	+	+	−	+

program, with respect to the effective radius of R^{3+} with CN = 9 [Shannon, 1976], since the data is absent for larger CN. The variation of the lattice constant illustrates the well-known lanthanide contraction for R = Gd - Lu with no evident deviation for R = Yb. However, the relatively larger lattice constants for YFe_2Zn_{20} and YCo_2Zn_{20} may indicate that, with this large CN, the effective ionic radii of Y^{3+} is different from the values for the small CN case. Nevertheless, this deviation for Y^{3+} ions is not unprecedented in the isostructural compounds RRu_2Zn_{20} [Nasch et al., 1997] and $RMn_2In_xZn_{20-x}$ [Benbow and Latturner, 2006], as well as the similar structure compound RCo_2 [Villars and Calvert, 1996]. Additional single crystal X-ray diffraction measurements were preformed on R = Gd, Tb, Er and Lu samples and demonstrated full occupancy on all crystallographic sites (within the detection limits) and the same lattice as the powder X-ray values.

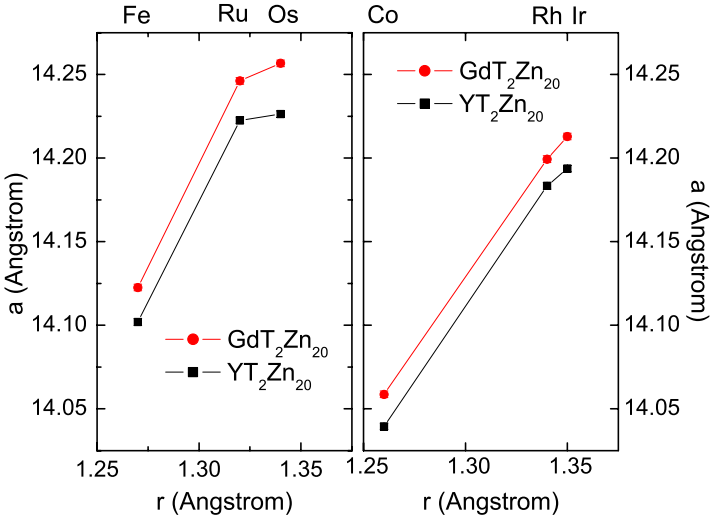

Figure 3.2 The lattice constants (a) of GdT_2Zn_{20} and YT_2Zn_{20} versus the Goldschmidt radius of the transition metal (r) [Schubert, 1964].

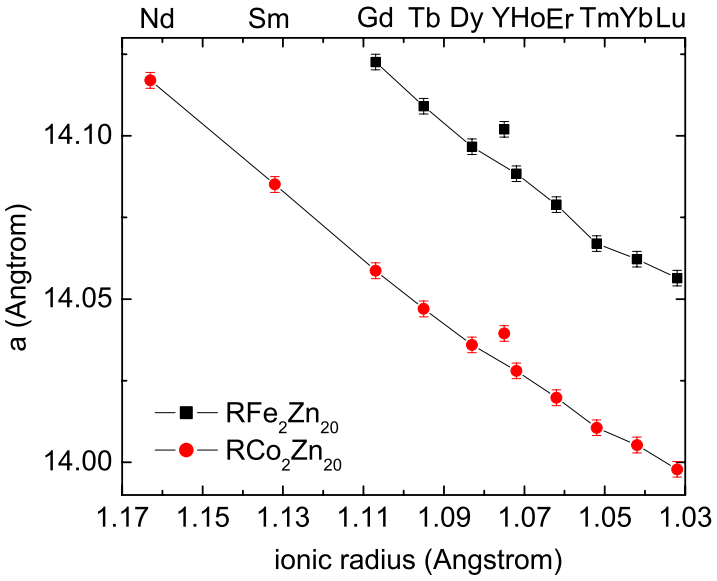

Figure 3.3 The lattice constants (a) for RFe_2Zn_{20} and RCo_2Zn_{20} versus the radius of the trivalent rare earth ion with CN = 9 [Shannon, 1976]. The error bars were estimated from the standard variation of four times measurement results on one batch of sample.

Table 3.2 Atomic coordinates and refined site occupancies for $GdFe_2Zn_{20}$ and $GdRu_2Zn_{20}$; each of the unique crystallographic sites were refined individually.

Atom	Site	Occupancy	x	y	z
		$GdFe_2Zn_{20}$			
Gd	8a	1.013(12)	0.125	0.125	0.125
Fe	16b	1.01(2)	0.5	0.5	0.5
Zn1	96g	0.993(7)	0.0587(1)	0.0587(1)	0.3266(1)
Zn2	48f	0.997(9)	0.4893(1)	0.1250	0.1250
Zn3	16c	1.006(18)	0	0	0
		$GdRu_2Zn_{20}$			
Gd	8a	1.026(9)	0.125	0.125	0.125
Ru	16b	1.030(11)	0.5	0.5	0.5
Zn1	96g	0.988(5)	0.0589(1)	0.0589(1)	0.3260(1)
Zn2	48f	1.000(8)	0.4888(1)	0.1250	0.1250
Zn3	16c	0.962(15)	0	0	0

CHAPTER 4. Experiment methods

4.1 Crystal Growth

Although polycrystalline samples can be used for preliminary measurements of the thermodynamic and transport properties of novel materials, high quality, single crystals are essential for any detailed analysis. The measurements on the single crystal materials can easily provide the anisotropic information about the magnetic properties and electronic structure. Whereas in polycrystalline materials, the random orientation of the microscopic grains can average out any anisotropies in their properties. In addition, the quality of single crystals is generally superior to polycrystalline materials, since the polycrystalline materials possess grain boundaries at which impurities are often present.

Numerous techniques are presently employed for the growth of single crystals. Reviews of many of these methods, including the Czochralski, Bridgeman and zone refining methods, can be found in ref. [Pamplin, 1980] and the references therein. However, most of these method require the composition of the melt to be equal or close to the desired product, which constrains these methods to the synthesis of only congruently or near-congruently melting compounds. Furthermore, the starting components must be heated above the melting temperature of the target compound, which may easily be above the working range of available furnaces and crucibles. Finally, the vapor pressures of the constituent elements may be appreciable at these high temperatures.

One of the most versatile methods for growing single crystals which avoids many of the above problems, is growth from high-temperature solutions, also known as flux growth. (see [Fisk and Remeika, 1989, Canfield and Fisk, 1992, Canfield and Fisher, 2001]) At high temperature, all of the constituent elements are dissolved in the flux. As the temperature of

the melt decreases, the solubility of the target compounds decreases, forcing the desired compound to precipitate (crystallize) out of the solution. One simple example of flux growth is the growth of binary intermetallic compounds from a 'self-flux', for which a binary phase diagram of the constituent elements presents as a very useful tool to determine the growth temperature and concentrations. The growth of $NdSb_2$ single crystals from Sb flux presents as a detailed example [Myers, 1999]. The growth of ternary compounds is similar to the growth of binary compounds. However, because the ternary phase diagram of the constituent elements is usually absent, the growth attempt is typically based on an analysis of the binary phase diagrams of the constituent elements, as well as on trial-and-error initial growths. As examples, more details for the growth of ternary $RAgSb_2$ and RAgGe compounds can be found in ref. [Myers, 1999] and [Morosan, 2005] respectively.

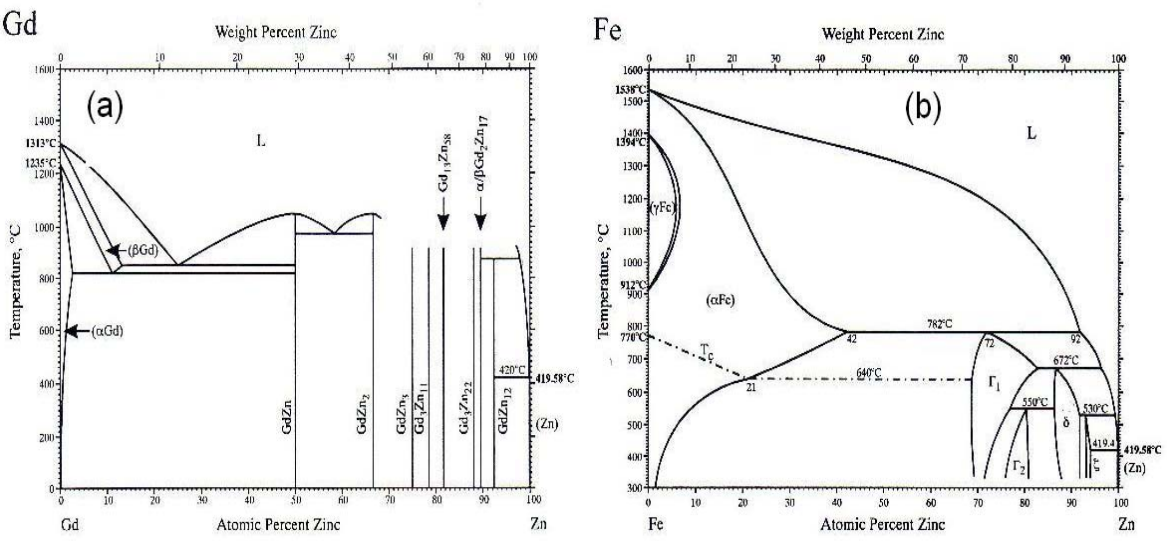

Figure 4.1 Binary phase diagram of (a) Gd - Zn, (b) Fe - Zn.

The very Zn rich composition of the RT_2Zn_{20} compounds and the low melting temperature of Zn (420 °C) motivated us to grow the single crystals from excess Zn. With an absence of the information about the ternary R-T-Zn systems, the analysis of the binary phase diagrams of the constituent elements helps us to make informed guesses for the initial growth concentrations and the temperatures. In order to illustrate the details of these growths, the growth of $GdFe_2Zn_{20}$ single crystals is chosen as an example. Figure 4.1 shows the binary phase diagrams

for Fe-Zn and Gd-Zn. Both of them show the melting point of Zn as the lowest eutectic point. Also, at 1000 °C, the Fe and Gd can be dissolved into Zn at 20% and 5% levels respectively. This analysis indicates that Zn is potentially viable for growing $GdFe_2Zn_{20}$. However, zinc was not considered as an ideal flux due to its relative high vapor pressure. At 1000 °C, the vapor pressure of zinc is higher than one atm, which would cause liquid zinc boil out in a container open to air. If zinc is sealed in a small quartz ampule, the ampule will be damaged by the pressure inside when the temperature is above 1150 °C since the quartz starts to be soften. As shown below, taking the high vapor pressure of zinc into account, we employed several strategies to mitigate vapor pressure related problems.

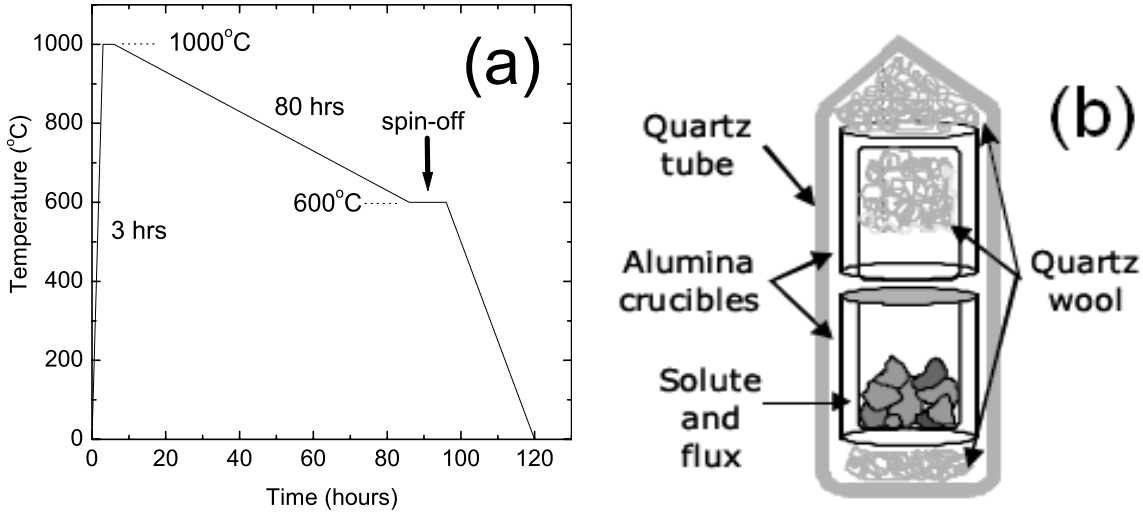

Figure 4.2 (a): Temperature profile for the growth of single crystals of RFe_2Zn_{20} from Zn flux. At about 90 hours, the ampule is removed from the furnace and the remaining flux is decanted from the crystallized material. (b): diagram of the ampule used for crystal growth.

High purity, constituent elements with the concentration Gd:Fe:Zn = 2: 4: 96 were placed inside a 2 ml alumina crucible, called the 'growth crucible' [Fig. 4.2 (b)]. Another crucible, called the 'catch crucible', is filled about two-third full with quartz wool and placed, inverted, on top of the growth crucible. The crucibles were subsequently sealed in a quartz ampule under approximately 1/3 atmosphere of high purity argon. (This partial-pressure of argon produced a pressure larger than one atmosphere at 1000 °C and helped to reduce the migration of Zn out of

the growth crucible.) The quartz ampule was elevated in the furnace by about one inch to make the top of the ampule closer to the heating elements, which produced a temperature gradient from the top to the bottom. Such a temperature gradient helps make the zinc vapor liquefy inside the growth crucible other than out of the crucible during the cooling down process and therefore helps to reduce the zinc loss. The ampule was then heated up to 1000 °C, and slowly cooled down to 600 °C, at which point the remaining liquid was decanted from the growth crucible. This was done by quickly removing the ampule from the furnace and inserting it, inverted, into a centrifuge. During the spin, the quartz wool in the catch crucible acted as a strainer allowing the excess flux to flow to the bottom of the catch where is solidified, and held separate any crystals that may have detached from the growth crucible.

It is worth noticing though, that for the local moments bearing members (R = Gd - Tm) in Fe series, single crystals obtained from different ratios of starting element concentrations manifest detectably different magnetic ordering temperatures. These differences, tentatively associated with very subtle variations of element occupancy on the crystallographic sites, are related to an extremely sensitivity to the small disorder for compounds with such a strongly correlated conduction electron background. A detail discussion of this is presented in Appendix A.

Similar procedures were used for growing other RT_2Zn_{20} compounds with the transition metal elements other than iron. For the T = Ru, Rh, Os or Ir, based on the analysis of the respective binary phase diagrams with Zn, and the results of initial growth attempts, we found that their solubility into Zn was much less than those of Fe and Co. Therefore, the growths of these compounds were made with lower transition metal concentrations. For R not equaling Yb, the initial concentration of starting elements (R:T:Zn) were 2: 4: 96 (T = Fe and Co), 1: 2: 97 (T = Ru, Rh), 1: 0.5: 98.5 (T = Os), and 0.75: 1.5: 97.75 (T = Ir). For R equaling Yb, the initial concentration of Yb:T:Zn were 2: 4: 96 (T = Fe and Co), 2: 2: 96 (T = Ru, Rh), 1: 0.5: 98.5 (T = Os), and 0.75: 1.5: 97.75 (T = Ir). The ampules were heated up to 1000 °C (T = Fe and Co), 1150 °C (T = Ru), 1100 °C (T = Rh), 1150 °C (T = Os and Ir), and cooled down to 600 °C, 850 °C, 700 °C, 750 °C respectively, at which point the remaining liquid was

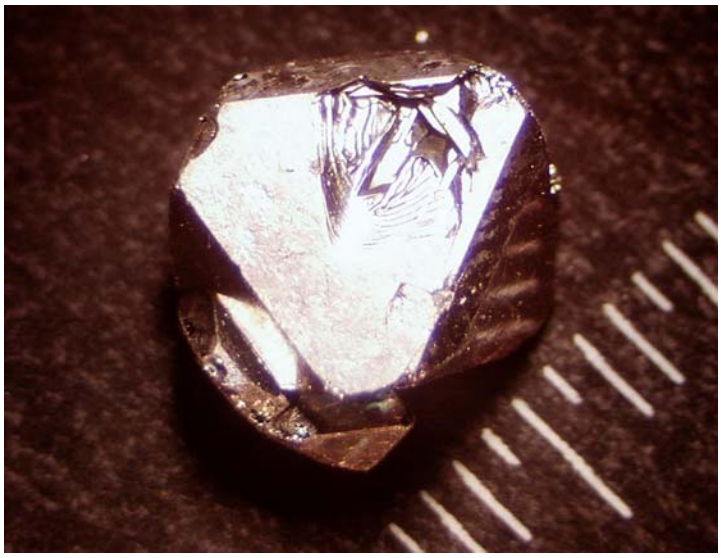

Figure 4.3 Single crystal of YFe_2Zn_{20}, with approximate dimensions $1 \times 1 \times 1$ cm^3.

decanted. The cooling rates were 5 °C/hr (T = Fe, Co, Ru, Rh), 4 °C/hr (T = Os), and 2.5 °C/hr (T = Ir).

Growths such as these often had only 2–3 nucleation sites per crucible and yielded crystals with typical dimensions of $7 \times 7 \times 7$ mm^3 (Fig. 4.3) or larger except for the Os compounds, which were significantly smaller (1–2 mm on one side). Residual flux and/or oxide slag on the crystal surfaces was removed by using diluted acid (0.5 vol. % HCl in H_2O for T = Fe, Co or 1 vol. % acetic acid in H_2O for T = Ru, Rh, Os and Ir), submerged in an ultrasonic bath.

4.2 Measurement methods

4.2.1 X-ray diffraction measurements

4.2.1.1 Powder X-ray diffraction measurements

Powder X-ray diffraction patterns were taken at room temperature in a Rigaku Miniflex powder diffractometer on pulverized single crystals to verify whether any impurity phases were present in the samples and to determine the unit cell dimensions. A conventional tube source was used to obtain the patterns in flat plate geometry using Cu K_α radiation. In order to

reduce the measurements errors of the unit cell dimensions, silicon powder ($a = 5.43088$ Å) was added to the pulverized samples and used as an internal standard. The mixed powder was then attached on the low background, silicon (510) crystal holders. Typical measurements consisted of scans of 2θ from 20° to 90°, data being recorded every 0.01°. The collected data was subsequently analyzed using the Rietica, Rietveld refinement program.

4.2.1.2 Single Crystal X-ray diffraction measurements

Room temperature, single crystal X-ray analysis were performed by collaborators on selected RT_2Zn_{20} compounds by employing a STOE image plate diffractometer with Mo K_α radiation and using the supplied STOE software [Stoe, 2002]. The data were adjusted for Lorentz and polarization effects, and a numerical absorption correction was preformed. The structural solutions were refined by full-matrix least-squares refinement using Bruker SHELXTL 6.1 software package [Sheldrick and SHELXTL, 2000]. The atomic disorder in the crystals was checked by refining site occupancies.

4.2.2 Magnetization measurement

Magnetic measurements were performed in a Quantum Design Magnetic Properties Measurement System (MPMS) with superconducting quantum interface device (SQUID) magnetometers in applied field $\leq$ 55 kOe or 70 kOe and in the temperature range from 1.85 K to 375 K. Additional magnetization measurements under hydrostatic pressure were preformed in a piston-cylinder clamp-type pressure cell, made out of non-magnetic Ni-Co alloy MP35N, in the SQUID magnetometers. Pressure was generated in a Teflon capsule filled with 50:50 mixture of n-pentane and mineral oil. The pressure dependent, superconducting transition temperature of 6-N purity Pb was employed to determine the pressure at low temperatures [Eiling and Schilling, 1981]. The pressure cell design allows for the routine establishment of pressures in excess of 8 kbar at low temperatures [Bud'ko et al., 2005].

In general, when making magnetization measurements on FM samples, some attention must be paid to the effects of demagnetizing fields [Chikazumi and Graham, 1997]. However,

this correction is small in the case of RT_2Zn_{20} because of the diluted nature of the magnetic moments. For example, in GdT_2Zn_{20} compounds, considering that the magnetization is mainly from the eight Gd^{3+} ions per unit cell, one estimates the maximum demagnetizing field as:

$$D_m = 4\pi \frac{8 \times 7\ \mu_B}{(14\ \text{Å})^3} = 2380\ \text{Oe}. \tag{4.1}$$

Experimentally, in the measurements of magnetization isotherms near T_C to create Arrott plots [Arrott, 1957] to be used in the determination of T_C, the demagnetizing field can introduce an error in this determination for plate-like shaped samples. To avoid this error, rod-like samples were measured with the magnetic field applied along their long axis. This minimized the demagnetization factor and thereby the demagnetizing field.

4.2.3 Resistivity measurement

Measurements of the electrical resistivity were made by using a standard AC, four-probe technique. The samples were cut as bars, which typically had lengths of 2–3 mm, parallel to the crystallographic [110] direction. Platinum wires were attached to the bars with Epotek H20E silver epoxy, and cured at 120 °C for $\sim$ 50 minutes. In order to decrease the contact resistances (most likely come from some remained epoxy), $\sim$ 100 mA current flowed though the contacts to heat and vaporize the epoxy. Then the typical contact resistances were between 1 and 2 ohms. AC electrical resistivity measurements were taken on these bars with $f = 16$ Hz, $I = 0.5$–0.3 mA in Quantum Design Physical Properties Measurement System, PPMS-14 and PPMS-9 instrument ($T = 1.85$–310 K). The He-3 option of the Quantum Design PPMS-14 and PPMS-9 units allowed us to extend the transport measurements down to $T = 0.4$ K when necessary. For the six Yb compounds, (YbT_2Zn_{20}, T = Fe, Co, Ru, Rh, Os and Ir), additional transport data (AC and/or triangular wave current) were taken for T down to 20 mK at the National High Magnetic Field Laboratory, Tallahassee, FL, using an Oxford dilution refrigerator.

4.2.4 Specific heat measurement

Temperature dependent specific heat measurements were performed using the heat capacity option of the Quantum Design PPMS-14 and PPMS-9 instruments. Specific heat data was often collected for temperature down to 2 K, but in some cases the He-3 option of the PPMS systems was used to reach ~ 0.4 K. A relaxation technique was used for the specific heat measurements, in which the sample was brifly heated and then allowed to cool. The thermal response of the samples was then fit over the entire temperature response using a model that accounts for the thermal relaxation of both the sample and the sample platform. The samples were attached to the heat capacity platform with Apiezon N grease. The thermal response of the platform and grease was measured separately for the appropriate field and temperature ranges, to allow for the subtraction of this component from the final measurement. For $YbCo_2Zn_{20}$, the specific heat data for 50 mK$\leq T \leq$2 K were taken in a dilution refrigerator insert for the Quantum Design PPMS system at Quantum Design Incorporated in San Diego.

CHAPTER 5. Nearly ferromagnetic Fermi-liquid behavior in YFe_2Zn_{20} and high-temperature ferromagnetism of $GdFe_2Zn_{20}$ *

5.1 Introduction

The field of condensed-matter physics has been interested in the effects of electron correlations from its inception [Moriya, 1985]. To this day, the properties of elemental Fe as well as Pd continue to present problems that interest both experimentalists as well as theorists [B Zellermann and Voitländer, 2004, Larson et al., 2004]. Materials such as Pd or Pt, that are just under the Stoner limit (often referred to as NFFL), or materials just over the Stoner limit, such as $ZrZn_2$ or Sc_3In on the ferromagnetic side, are of particular interest due their strongly correlated electronic behaviors [Moriya, 1985]. Of even greater interest are new examples of NFFLs that can be tuned with a greater degree of ease than the pure elements: that is, those that can accommodate controlled substitutions on a number of unique crystallographic sites in a manner that allows for (1) a tuning of the band filling/Fermi surface and (2) the introduction of local-moment-bearing ions onto a unique crystallographic site. Such a versatile system would open the field to a greater range of experimental studies of strongly correlated electronic states as well as potentially allowing for more detailed studies of quantum criticality and possibly even novel superconducting states.

In this chapter, I present the first results of an extensive study of the dilute, rare-earth-bearing, intermetallic compounds RT_2Zn_{20} (R = rare earth and T = transition metal in the Fe, Co and Ni columns of the periodic table). For these series of compounds, although the crystallography of this series was well detailed, so far, there have been no measurements of

*after "Nearly ferromagnetic Fermi-liquid behaviour in YFe_2Zn_{20} and high-temperature ferromagnetism of $GdFe_2Zn_{20}$", S. Jia, S. L. Bud'ko, G. D. Samolyuk and P. C. Canfield, *Nat. Phys.* **3** 334-338 (2007).

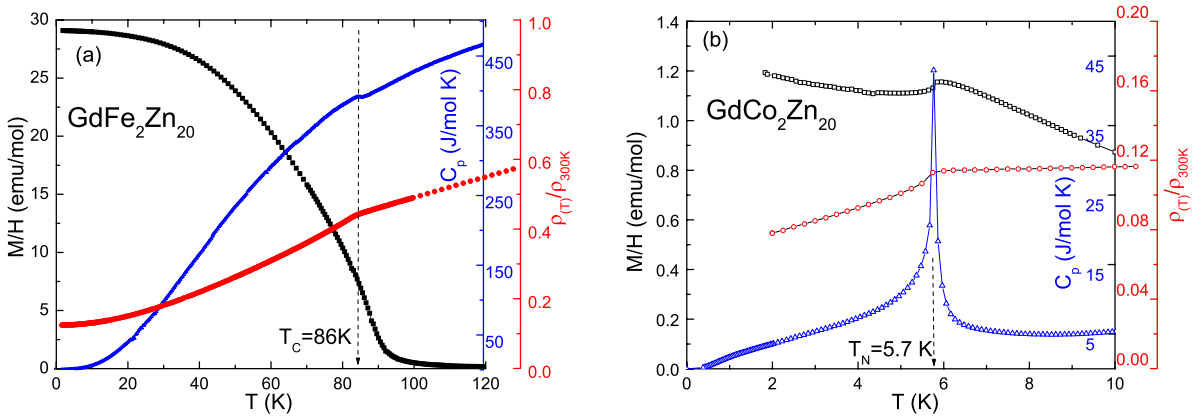

Figure 5.1 Temperature-dependent specific heat (blue), resistivity (red) and low-field ($H = 1000$ Oe) magnetization divided by applied field (black) for $GdFe_2Zn_{20}$ (a) and $GdCo_2Zn_{20}$ (b).

these compounds' physical properties. This, to some extent, is not unexpected because the limited data sets available on the isostructural RT_2Al_{20} compounds indicated very low magnetic ordering temperatures, consistent with the very low R concentrations [Thiede et al., 1998, Moze et al., 1998]. In particular, I will focus on the magnetic properties of YFe_2Zn_{20} and $GdFe_2Zn_{20}$, as well as their Co analogues. I will show how YFe_2Zn_{20} is an archetypical example of a NFFL and how, by embedding Gd ions into this highly polarizable medium, $GdFe_2Zn_{20}$ has a remarkably high ferromagnetic ordering temperature (T_C) of 86 K, even though it contains less than 5% atomic Gd and the Fe is not moment-bearing in the paramagnetic state.

5.2 Results and analysis

Figures 5.1 and 5.2 show temperature-dependent low-field magnetization, electrical resistivity and specific heat data, as well as anisotropic M(H) data, for $GdFe_2Zn_{20}$ and $GdCo_2Zn_{20}$. There are two conspicuous differences between the physical properties of these compounds: (1) $GdFe_2Zn_{20}$ orders ferromagnetically, whereas $GdCo_2Zn_{20}$ orders antiferromagnetically and (2) $GeFe_2Zn_{20}$ orders at a remarkably high temperature of $T_C = 86$ K, whereas $GdCo_2Zn_{20}$ orders at the more representative $T_N = 5.7$ K. From Fig. 5.2 a, the high-temperature Curie constant can be determined, giving effective moments ($7.9\mu_B$ and $8.2\mu_B$ for T = Fe and T = Co re-

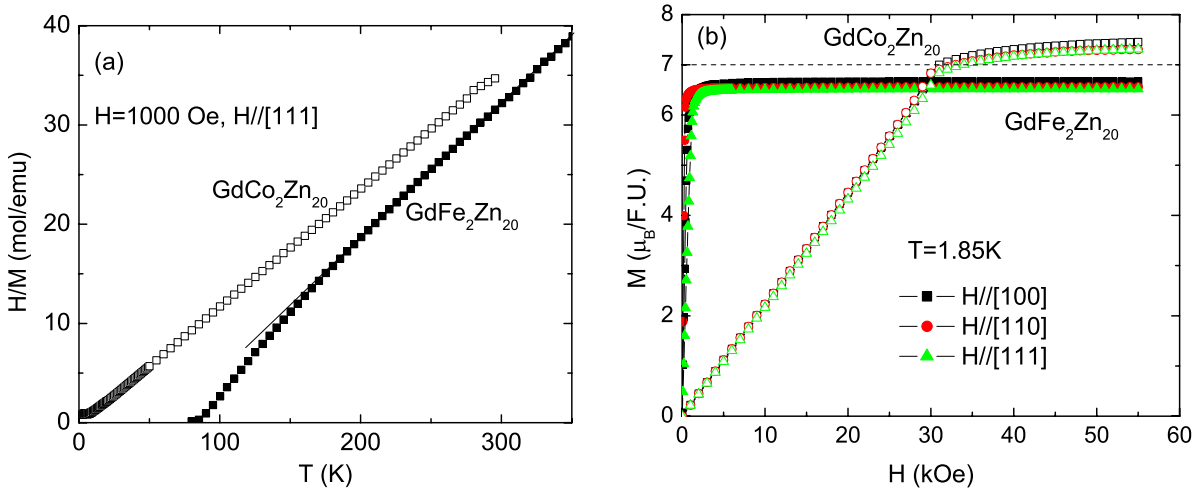

Figure 5.2 Magnetic properties of $GdFe_2Zn_{20}$ and $GdCo_2Zn_{20}$: (a) H/M as a function of temperature, (b) low temperature isothermal along three principle axises of cubic structure.

spectively) consistent with the effective moment of the Hund's rule ground state of Gd^{3+} ion ($7.94\mu_B$), indicating that, in the paramagnetic state, there is little or no contribution from the transition metal. The saturated moment deduced from the data in Fig. 5.2 b is close to that associated with Gd^{3+} ($7\mu_B$); slightly lower for $GdFe_2Zn_{20}$ and slightly higher for $GdCo_2Zn_{20}$.

To better understand this conspicuous difference in ordering temperatures, band-structure calculations were carried out by G. Samolyuk. Figure 5.3 shows the density of states as a function of energy for both $LuFe_2Zn_{20}$ and $LuCo_2Zn_{20}$. The upper curve in each panel shows the total density of states, whereas the lower curve shows the partial density of states associated with the transition metal. It should be noted that the difference between $LuFe_2Zn_{20}$ and $LuCo_2Zn_{20}$ density of states can be rationalized in terms of the rigid band approximation, with the Fermi level for $LuCo_2Zn_{20}$ being 0.3 eV higher than that for $LuFe_2Zn_{20}$, associated with the two extra electrons per formula unit. As will be shown in Chapter 6, calculations done on YFe_2Zn_{20} and $GdFe_2Zn_{20}$ as well as on YCo_2Zn_{20} and $GdCo_2Zn_{20}$ lead to similar density of states curves and further analysis of the $GdFe_2Zn_{20}$ and $GdCo_2Zn_{20}$ band-structural results leads to the prediction that for $GdFe_2Zn_{20}$ the ground state will be ferromagnetic(FM) with a total saturated moment of approximately $6.5\mu_B$ (with a small induced moment on Fe opposing

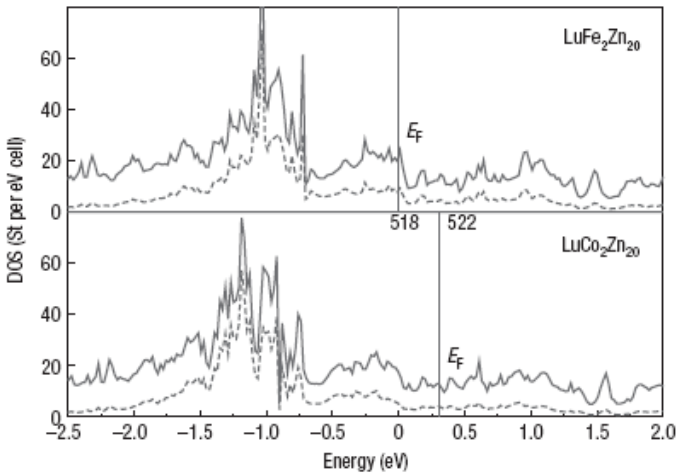

Figure 5.3 Density of states as a function of energy for $LuFe_2Zn_{20}$ and $LuCo_2Zn_{20}$: the upper curve shows total density, whereas the lower curve shows the partial density of states associated with Fe or Co.

the Gd moment) and for $GdCo_2Zn_{20}$ the saturated moment will be $7.25\mu_B$ (with practically no induced moment on Co). These results are consistent with the saturated values of the magnetization seen in Fig. 5.2 (b).

These calculations indicate that the RFe_2Zn_{20} compounds should manifest a higher electronic density of states at the Fermi level, $N(E_F)$, than the RCo_2Zn_{20} analogues and raise the question of whether or not this is the primary reason for the remarkably high T_C found for $GdFe_2Zn_{20}$. In addition, they raise the question of how correlated the electronic state is in these nominally nonmagnetic, Lu- and Y-based analogues. To address these questions, two substitutional series were grown: $Y(Fe_xCo_{1-x})_2Zn_{20}$ and $Gd(Fe_xCo_{1-x})_2Zn_{20}$. In order to check x, Energy Dispersive Spectra (EDS) measurements, a direct method to determine the elements concentrations, and powder X-ray diffraction measurements were employed. Figure 5.4 presents EDS measurement results for the Gd series, and the lattice constants for both series. The linear variation of lattice constants with x for both series is compliant with Vegard's law, which is consistent with the results of EDS. Due to these results, the nominal x value is used from this point onward.

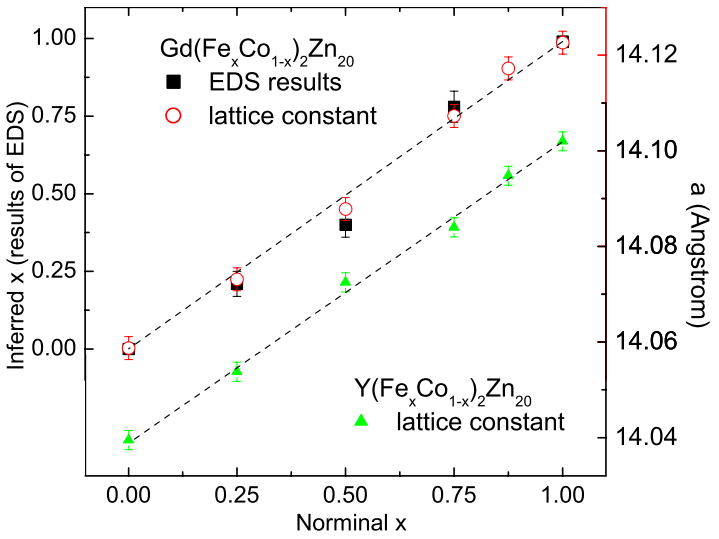

Figure 5.4 Lattice constants of the series of $Gd(Fe_xCo_{1-x})_2Zn_{20}$ (open circle) and $Y(Fe_xCo_{1-x})_2Zn_{20}$ (solid triangle). Fe concentration of $Gd(Fe_xCo_{1-x})_2Zn_{20}$ series inferred from EDS measurements (solid square).

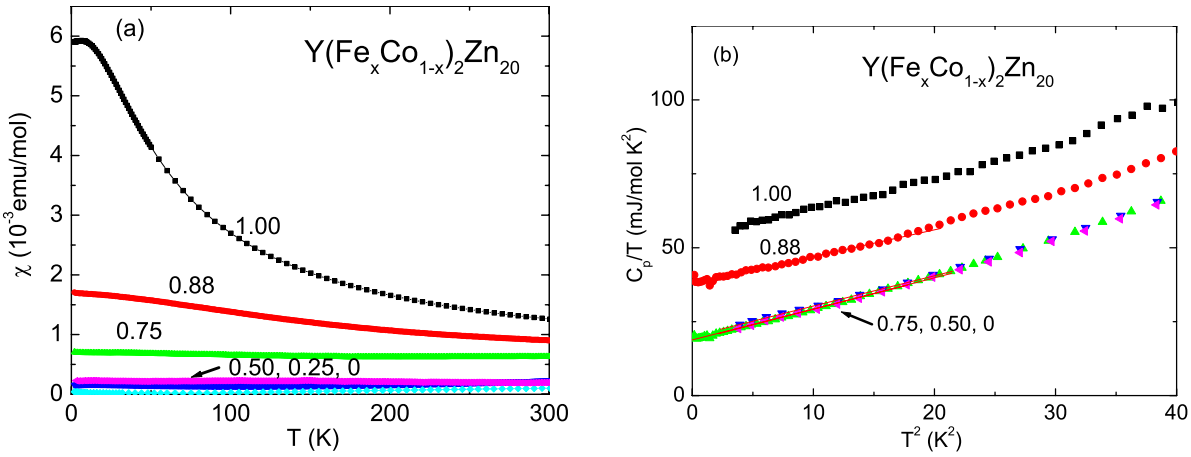

Figure 5.5 (a)Temperature-dependent magnetic susceptibility and (b) low temperature specific heat (plotted as C_p/T versus T^2) for $Y(Fe_xCo_{1-x})_2Zn_{20}$.

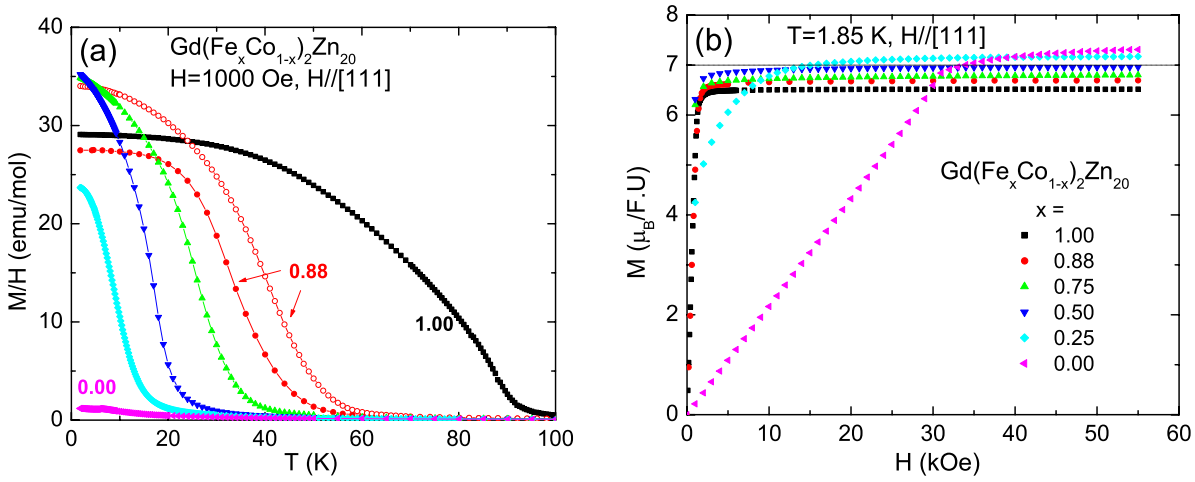

Figure 5.6 (a): M/H of $Gd(Fe_xCo_{1-x})_2Zn_{20}$ series versus temperature for $x = 1.00$, 0.88, 0.75, 0.50, 0.25 and 0 from right to left. Note data from two samples of $x = 0.88$ are shown. (b): Low temperature ($T = 1.85$ K) magnetization versus applied field for the series of $Gd(Fe_xCo_{1-x})_2Zn_{20}$.

Figure 5.5 shows thermodynamic data taken on the $Y(Fe_xCo_{1-x})_2Zn_{20}$ series. For $x = 0$, the low-temperature, linear component of the specific heat (γ) is relatively small (19 mJ mol^{-1}K^{-2}) and the susceptibility is weakly paramagnetic and essentially temperature independent. As x is increased, there is a monotonic (but clearly super-linear) increase in the samples paramagnetism as well as, for larger x values, an increase in the low-temperature γ values. For YFe_2Zn_{20} ($x = 1$), the value of γ has increased to over 250% of that for YCo_2Zn_{20} and the susceptibility has become both large and temperature dependent.

Figure 5.6 shows the temperature-dependent low-field magnetization as well as low temperature magnetization isotherms for $Gd(Fe_xCo_{1-x})_2Zn_{20}$. For $x \geq 0.25$, the ground state becomes FM and the transition temperature increases monotonically (but again in a super-linear fashion) with increasing x. The high-field, saturated magnetization decreases weakly, in a monotonic fashion with increasing x. For $x = 0.25$, the magnetization is not a typical FM one: the saturation appears ~ 10 kOe, much larger than the estimated, maximum demagnetizing field. Such anomaly may indicate the existence of an antiferromagnetic component to the long range order for $0 < x \leq 0.25$.

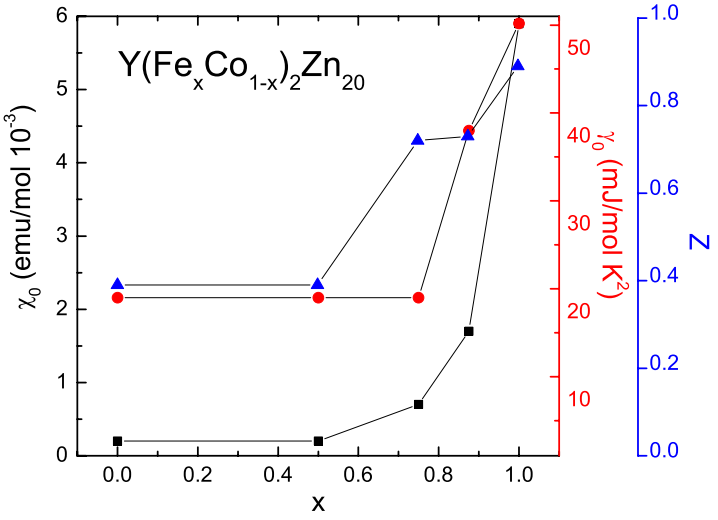

Figure 5.7 Linear coefficient of the specific heat, γ, magnetic susceptibility at based temperature (after core diamagnetism correction, subtracting $-2.3 \times 10^{-4} emu/mol$) [Mulay and Boudreaux, 1976], and Stoner enhancement factor, Z, as a function of x for $Y(Fe_xCo_{1-x})_2Zn_{20}$.

5.3 Discussion

Figures 5.7 and 5.8 demonstrate a clear correlation between x, the linear component of the electronic specific heat, the enhanced magnetic susceptibility of the Y-based series and the magnetic ordering temperature and the saturated magnetization of the Gd-based series. This correlation can be more clearly seen if the relation between the linear component of the specific heat and the low-temperature susceptibility of the Y-based series is placed in the context of a NFFL: that is, if the Stoner enhancement parameter, Z, for each member of the series can be determined [Ziman, 1979]. For such systems, the static susceptibility [corrected for the core diamagnetism [Mulay and Boudreaux, 1976]] is $\chi = \chi_0/(1-Z)$, where $\chi_0 = \mu_B N(E_F)$ (see Eqn. 6.1 from Chapter 6). Given that the linear component of the specific heat is given by $\chi_0 = (\pi k_B)^2 N(E_F)/3$, if both the low-temperature specific heat and magnetic susceptibility can be measured, then the parameter Z can be deduced [$Z = 1-(3\mu_B^2)/\pi^2 k_B^2)(\gamma_0/\chi_0)$], where k_B and μ_B are the Boltzmann constant and the Bohr magneton

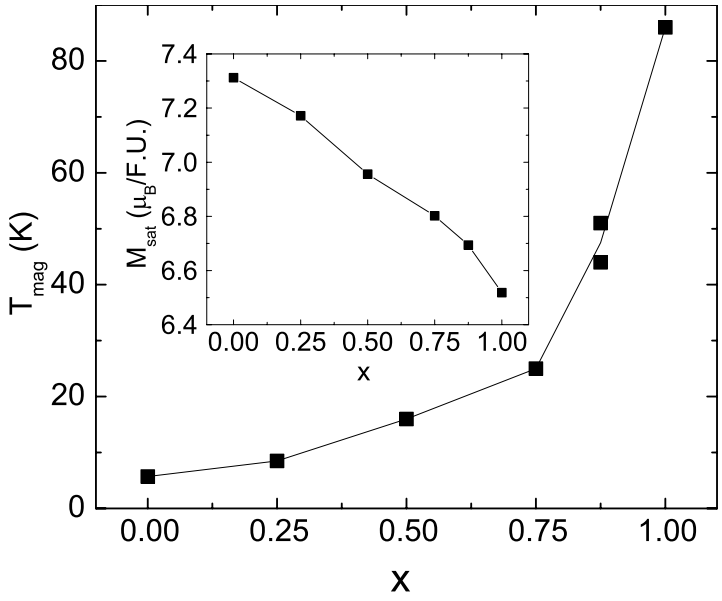

Figure 5.8 Magnetic ordering temperature for $Gd(Fe_xCo_{1-x})_2Zn_{20}$ as a function of x. Note that data from two samples of $x = 0.88$ are shown. Inset:saturated moment as a function of x.

respectively. The canonical example of such a system is elemental Pd for which, using data from ref. [Knapp and Jones, 1972, B Zellermann and Voitländer, 2004], $Z = 0.83$. For YFe_2Zn_{20}, $Z = 0.89$, a value that places it even closer to the Stoner limit than Pd. It should be noted that the temperature-dependent susceptibility of YFe_2Zn_{20} is also remarkably similar to that of Pd [see ref. [B Zellermann and Voitländer, 2004] and references therein]. (Detail analysis on the magnetic properties of YFe_2Zn_{20} as well as $LuFe_2Zn_{20}$ will be presented in Chapter 8.) The x dependence of the experimentally determined values of γ and $\chi(T = 0)$, as well as the inferred value of Z, for the $Y(Fe_xCo_{1-x})_2Zn_{20}$ series is plotted in Fig. 5.7. By choosing x, $Y(Fe_xCo_{1-x})_2Zn_{20}$ can be tuned from being exceptionally close to the Stoner limit to being well removed from it. Corrections to these inferred Z values coming from the difference between the measured electronic specific heat coefficient, γ, and the Sommerfeld coefficient, γ_0, where $\gamma = \gamma_0(1 + \lambda)$ only serves to slightly increase Z because λ, the electron mass enhancement parameter, is positive definite. By comparing the γ_0 inferred from the band structure to our

measured values of γ, we can estimate $\lambda = 0.85$ and 0.22 for $x = 1$ and $x = 0$ respectively, and this shifts Z to 0.94 for YFe_2Zn_{20} and to 0.50 for YCo_2Zn_{20}.

When the non-magnetic Y ion is replaced by the large Heisenberg moment associated with the $S = 7/2$ Gd^{3+} ion, as x is varied from zero to one in the $Gd(Fe_xCo_{1-x})_2Zn_{20}$ series, the Gd local moments will be in an increasingly polarizable matrix, one that is becoming a nearly ferromagnetic Fermi liquid. This results in an increasingly strong coupling between the Gd local moments as x is increased. Figure 5.8 shows the x dependence of magnetic ordering temperature T_{mag} and μ_{sat} for the $Gd(Fe_xCo_{1-x})_2Zn_{20}$. The value of T_{mag} increases in a monotonic but highly nonlinear fashion in a manner reminiscent of the behavior associated with the increasingly polarizability of $Y(Fe_xCo_{1-x})_2Zn_{20}$ seen in Fig. 5.7. The saturated moment extracted from the magnetization values, under 55 kOe applied field along the [111] crystallographic direction, varies monotonically from the slightly enhanced value of 7.3 μ_B for $GdCo_2Zn_{20}$ to the slightly deficient value of 6.5 μ_B for $GdFe_2Zn_{20}$.

One consequence of placing Gd ions into a matrix so close to the Stoner limit is an enhanced sensitivity to small sample-to-sample variations. This is most clearly illustrated by the data for the $Gd(Fe_{0.88}Co_{0.12})_2Zn_{20}$ samples shown in Fig. 5.6 and 5.8. Although the samples have the same nominal composition, there is a clear difference in their transition temperatures. However, this difference is not too significant given the large dT_C/dx slope seen in Fig. 5.8. On the other hand, measurements on four separate samples of $Gd(Fe_{0.25}Co_{0.75})_2Zn_{20}$ did not show any significant variations in T_C. Such sensitivity to the small disorder is not uncommon for the strongly correlated electronic system, particularly for the ones close to the Stoner criteria. For example, the different samples of $ZrZn_2$, the canonical example of weak ferromagnet, manifest $\sim$ 10% difference in their T_C [see ref. [Seeger et al., 1995, Pfleiderer et al., 2001, Yelland et al., 2005]].

5.4 Conclusion and Summary

YFe_2Zn_{20} is archetypical example of a NFFL with a Stoner enhancement factors of $Z \sim$ 0.88. The anomalously high FM ordering temperature (T_C = 86 K) of $GdFe_2Zn_{20}$ can be

understood as a result of embedding large, Heisenberg type moments associated with Gd^{3+} ions in this highly polarizable medium. In contrast, YCo_2Zn_{20} manifests non-correlated, normal metal behaviors and $GdCo_2Zn_{20}$ orders antiferromagnetically at $T_N = 5.7$ K. By tuning the band filling, the conduction electronic background of $Y(Fe_xCo_{1-x})_2Zn_{20}$ can be tuned from the edge of the Stoner limit to being well removed from it and the magnetic ordering temperature of $Gd(Fe_xCo_{1-x})_2Zn_{20}$ drops with a monotonic but highly nonlinear fashion.

The broader RT_2Zn_{20} family of compounds offers an even larger phase space for the study of correlated electron physics (for T = Fe and Ru as well as for R = Yb and Ce) and for the study of local moment physics, all in the limit of a dilute, rare-earth-bearing, intermetallic series. In this work , we study the local moment physics and the correlated electronic behavior associated with the transition metal for T = Fe and Ru as well as R = Gd - Tm in the following chapters. We will also study the effects of titrating very dilute local moments into a NFFL by tuning the Gd^{3+} concentration in $Gd_xY_{1-x}Fe_2Zn_{20}$. Finally, the study of the correlated electron physics associated with specific $4f$ electronic configuration (R = Yb) will be presented.

CHAPTER 6. Variation of the magnetic ordering in GdT_2Zn_{20} (T= Fe, Ru, Os, Co, Rh and Ir) and its correlation with the electronic structure of isostructural YT_2Zn_{20} *

6.1 Introduction

Magnetism of rare earth intermetallics, determined by the interaction between $4f$ local moments and conduction electrons, especially the d-band conduction electrons of transition metals, has been of interest to physicists for several decades [Franse and Radwanski, 1993, Szytula and Leciejewicz, 1994]. As shown in Chapter 5, initial studies of the dilute, rare earth bearing, intermetallic compounds, RT_2Zn_{20} (R = rare earth, T = transition metal in Fe, Co or neighboring groups), revealed varied, exotic magnetic properties. YFe_2Zn_{20} is an archetypical example of a NFFL with a Stoner enhancement factor of $Z = 0.88$ (where $\chi_{T=0} = \chi_{Pauli}/(1 - Z)$). By embedding large, Heisenberg type moments associated with Gd^{3+} ions in this highly polarizable medium, $GdFe_2Zn_{20}$ manifests highly enhanced ferromagnetic (FM) order. On the other hand, $GdCo_2Zn_{20}$ manifests ordinary, low temperature, antiferromagnetic (AFM) order ($T_N = 5.7$ K), correspondent to the 'normal metal' behavior of the conduction electron host, YCo_2Zn_{20}.

In rare earth containing series of intermetallic compounds, R = Gd members give the clearest indication of the strength and sign of the magnetic interaction, without any complications associated with crystalline electric field splitting of the Hund's rule ground state multiplet. In order to better understand the RT_2Zn_{20} series of compounds, in this paper we examine the thermodynamic and transport properties of six GdT_2Zn_{20} (T = Fe, Ru, Os, Co, Rh and Ir)

*after "Variation of the magnetic ordering in GdT_2Zn_{20} (T= Fe, Ru, Os, Co, Rh and Ir) and its correlation with the electronic structure of isostructural YT_2Zn_{20}", S. Jia, N. Ni, G. D. Samolyuk, A. Safa-Sefat, K. Dennis, Hyunjin Ko, G. J. Miller, S. L. Bud'ko, P. C. Canfield, *Phys. Rev. B* **77** 104408-14 (2008).

compounds as well as their R = Y analogues. We found FM transitions in the iron column members (with enhanced T_C values for T = Fe and Ru) and low temperature, AFM transitions in the cobalt column members. Consistent with these results, we also found enhanced paramagnetism in the T = Fe and Ru of YT_2Zn_{20} analogues. For $GdFe_2Zn_{20}$ and $GdRu_2Zn_{20}$, magnetization measurements under hydrostatic pressure indicated that their enhanced FM transitions are not primarily associated with a steric effect. A model of Heisenberg moments embedded in a NFFL can be proposed as a way to understand the enhanced FM transitions. Band structure calculations were employed to explain that the remarkable differences in magnetic ordering for different transition metal members are a result of different d-band filling.

6.2 Results and analysis

6.2.1 GdT_2Zn_{20}(T = Fe, Co, Ru, Rh, Os and Ir)

Before discussing each of the GdT_2Zn_{20} compounds separately, an overview of their temperature and field dependent magnetization serves as a useful point of orientation. In Fig. 6.1 the temperature dependent magnetization (M) divided by applied field (H) reveals the primary difference between the Fe column members of this family and the Co column members. For T = Fe, Ru and Os there is an apparent FM ordering (with remarkably high and moderately high values of T_C for T = Fe and Ru respectively), whereas for T = Co, Rh and Ir there is an apparent, low temperature AFM ordering.

The nature of the ordering is further confirmed by the low temperature, magnetization isotherms presented in Fig. 6.2. It should be noted that for each of the six GdT_2Zn_{20} compounds, the 1.85 K magnetization isotherms, measured with the applied field along [100], [110], [111] crystallographic directions, were found to be isotropic to within less than 5 %. This magnetic isotropy is not unexpected in the Gd-based intermetallics, in which the magnetism is mainly due to the pure spin contribution of the $4f$ shell of Gd^{3+}. For T = Fe, Ru and Os the magnetization is representative of a FM-ordered state with a rapid rise and saturation of the ordered moment in a field of the order of the estimated demagnetizing field (magnetic domain wall pinning being low in these single crystalline samples). For T = Co, Rh and Ir the

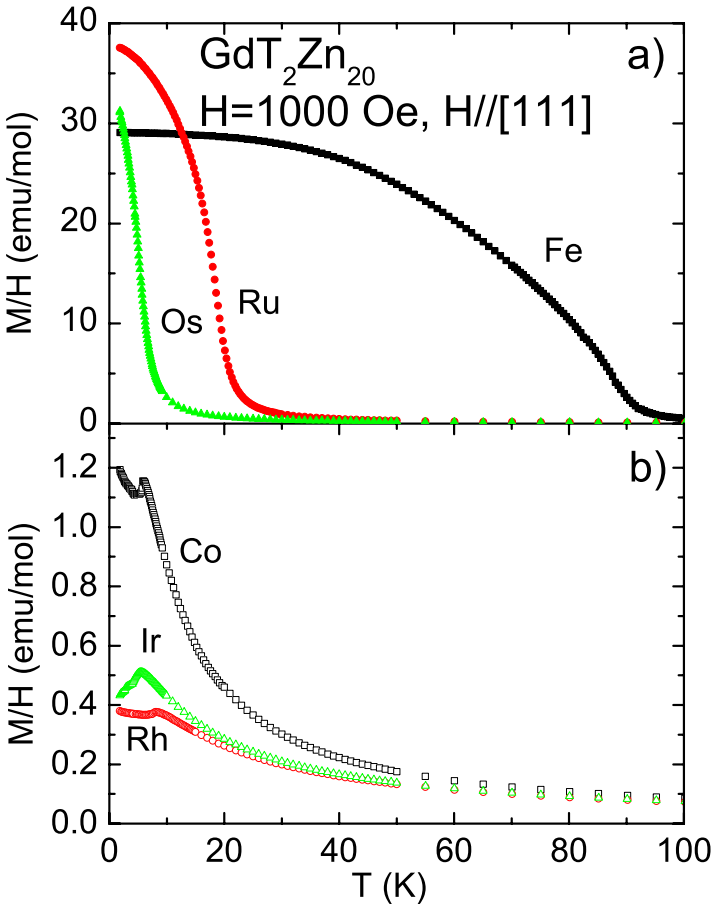

Figure 6.1 Temperature dependent magnetization of GdT_2Zn_{20}, divided by applied field $H = 1000$ Oe.

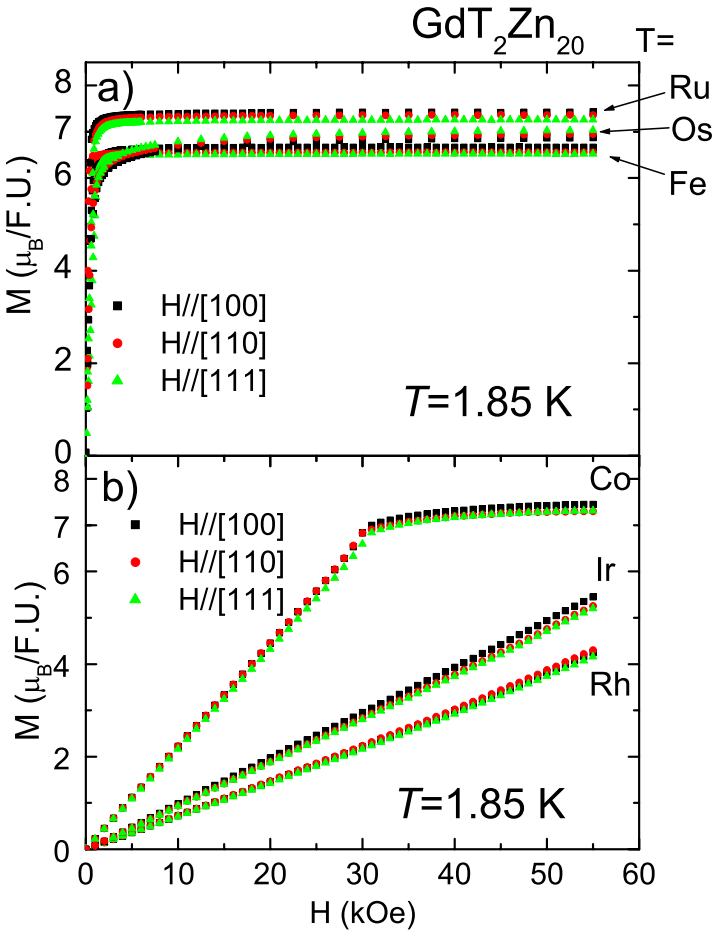

Figure 6.2 Field dependent magnetization of GdT_2Zn_{20} at 1.85 K.

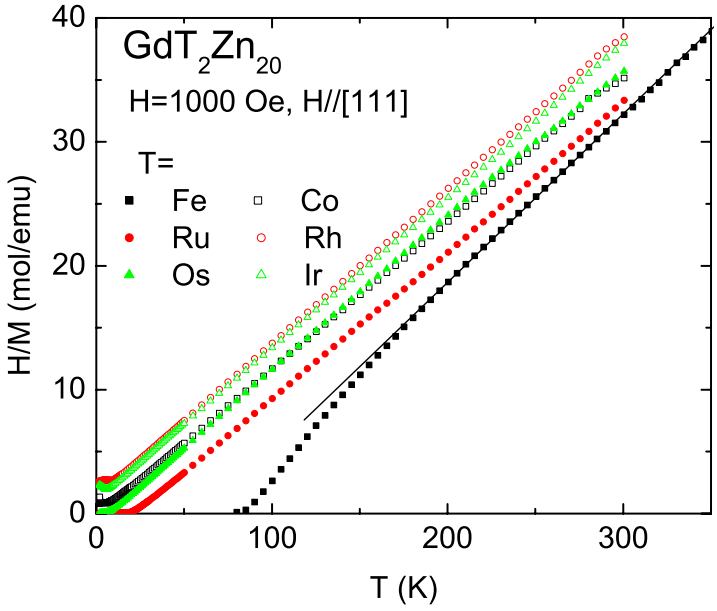

Figure 6.3 Applied field (H = 1000 Oe) divided by the magnetizations of GdT_2Zn_{20} as a function of temperature. The solid line represents the high-temperature CW fit for $GdFe_2Zn_{20}$.

field dependent magnetization data are consistent with AFM-ordered states that can be field stabilized to fully saturated states in large enough applied fields. This fully saturated state is observed for $GdCo_2Zn_{20}$ associated with a spin-flop transition near H = 31 kOe, whereas the maximum magnetic field in the equipment used (55 kOe) could not saturate the magnetic moment of the $GdRh_2Zn_{20}$ and $GdIr_2Zn_{20}$ samples. The field that can saturate the magnetic moment of Gd^{3+} ions was estimated as 95 kOe and 75 kOe for $GdRh_2Zn_{20}$ and $GdIr_2Zn_{20}$ respectively, from the linear extrapolations of their $M(H)$ data. These saturating field values are proportional to the values of their paramagnetic Curie temperature, θ_C (Table 6.1), which is not unexpected in the view of the molecular field approximation. The measured saturated moments for T = Fe, Ru, Os and Co samples are clustered around the Hund's rule ground state value of Gd^{3+}, 7 μ_B.

Figure 6.3 presents temperature dependent H/M data for the six Gd based compounds. For this low magnetic field, H/M approximately equals inverse susceptibility $[1/\chi(T)]$ in the

paramagnetic state. Except for $GdFe_2Zn_{20}$, the data sets of $1/\chi(T)$ of these compounds are essentially linear and parallel to each other over the whole temperature range of the paramagnetic state, manifesting Curie-Weiss (CW) behavior, $\chi(T) = C/(T - \theta_C)$, where C is Curie constant and θ_C is paramagnetic Curie temperature. The same C value is extracted from the parallel lines gives the same effective moments($\mu_{eff} \simeq 8\ \mu_B$), close to the value of Hund's rule ground state of Gd^{3+}(7.94 μ_B), without any apparent contribution from local moments associated with the transition metal. This is consistent with the low temperature saturated moments, being close to the theoretical value, $\mu_{sat} = 7\ \mu_B$ (Fig. 6.2). In contrast, $1/\chi(T)$ of $GdFe_2Zn_{20}$ obeys a simple CW law only above ~ 200 K and evidently deviates from it at lower temperatures (see discussion below). Nevertheless, its high-temperature CW behavior yields a μ_{eff} value close to the others. The sign of the θ_C values is consistent with their magnetic ordering type, except for $GdCo_2Zn_{20}$, which manifests AFM order but a positive, albeit small, θ_C (Table 6.1). This anomalous θ_C value for $GdCo_2Zn_{20}$ leads to a much larger susceptibility near the Néel temperature, T_N, than T = Rh and Ir members (Fig. 6.1).

$GdFe_2Zn_{20}$ is the most conspicuously anomalous in its behavior. Figure 6.4 presents a blow up of the low field M/H data as well as the results of measurements of temperature dependent specific heat (C_p) and electrical resistivity (ρ) in zero applied magnetic field. The specific heat data manifest a clear anomaly at $T_C = 85 \pm 1$ K [inset of Fig. 6.4(b)]. The resistivity data, although collected from a sample from different batch, show a clear break in slope (or maximum in $d\rho/dT$) at $T_C = 84 \pm 2$ K. Determination of the ordering temperature from magnetization data requires a more detailed analysis. Figure 6.5 presents a plot of M^2 versus H/M [an Arrott plot[Arrott, 1957]] from data collected on the same batch of sample used for C_p in the vicinity of T_C. The isotherm that most closely goes linearly through the origin is the one closest to T_C, giving a value 88 K. All of these measurements are consistent with transition temperature near 86 K. It should be noted though, that T_C values for different batch of samples can vary by as much as ± 3 K, even though the single-crystal X-ray measurements do not suggest evident crystallographic difference.

$GdRu_2Zn_{20}$ also manifests a relatively high FM ordering temperature (Figs. 6.1, 6.2 and

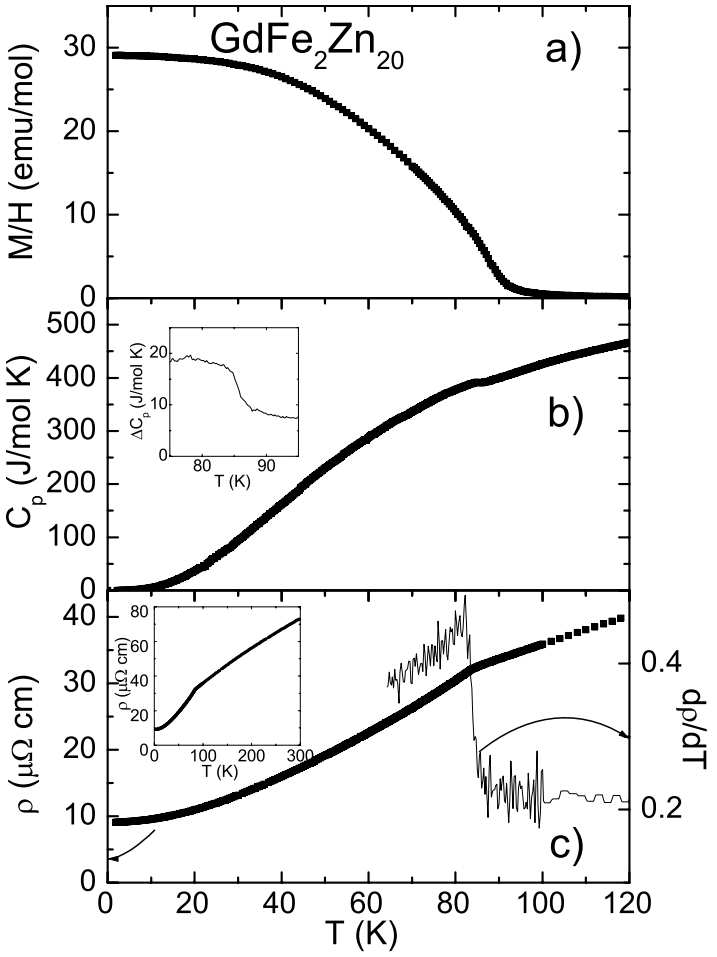

Figure 6.4 (a) Temperature dependent magnetization (M) of $GdFe_2Zn_{20}$ divided by applied field (H = 1000 Oe); (b) specific heat (C_p); (c) resistivity (ρ)and its derivative respect to temperature ($d\rho/dT$). Inset in (b): detail of C_p data near T_C. Inset in (c) ρ over whole temperature range, 2 K - 300 K.

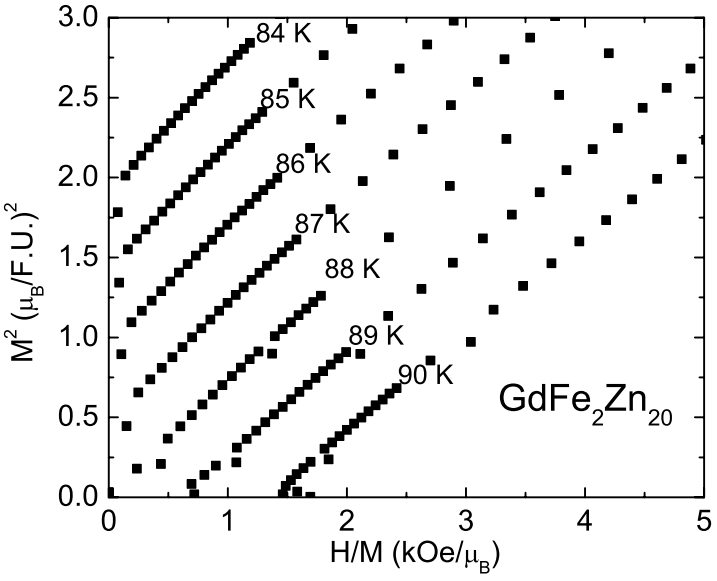

Figure 6.5 Arrott plot for $GdFe_2Zn_{20}$.

6.6 a). Figures 6.6(b, c) present temperature dependent specific heat and electrical resistivity measurements on $GdRu_2Zn_{20}$ in zero applied magnetic fields, both of which show clear evidence of ordering with $T_C = 20 \pm 1$ K. Figure 6.7 shows that, similar to $GdFe_2Zn_{20}$, the T_C of $GdRu_2Zn_{20}$ can be inferred from an Arrott plot analysis. These measurements were performed on samples from the same batch and the different methods for determining T_C agree to within ± 1 K.

$GdOs_2Zn_{20}$ appears to order ferromagnetically (Figs. 6.1, 6.2 and 6.8 a)at a T_C value as low as the Néel temperatures found for the Co column members of the GdT_2Zn_{20} family (see below). As shown in Fig. 6.8(b) and (c), the specific heat and resistivity data manifest features consistent with a magnetic phase transition near 4 K. However, the C_p data, with a broad shoulder above this temperature, does not manifest a standard λ-type of feature and may indicate a distribution of T_C values or multiple transitions. The Arrott plot for $GdOs_2Zn_{20}$, although having non-linear, isothermal curves, is also consistent with a FM transition between 4 K and 4.5 K (Fig. 6.9). Such a non-linear feature in the isothermal curves is also found in ref. [Brommer and Franse, 1990, Yeung et al., 1986], and may be associated with complex

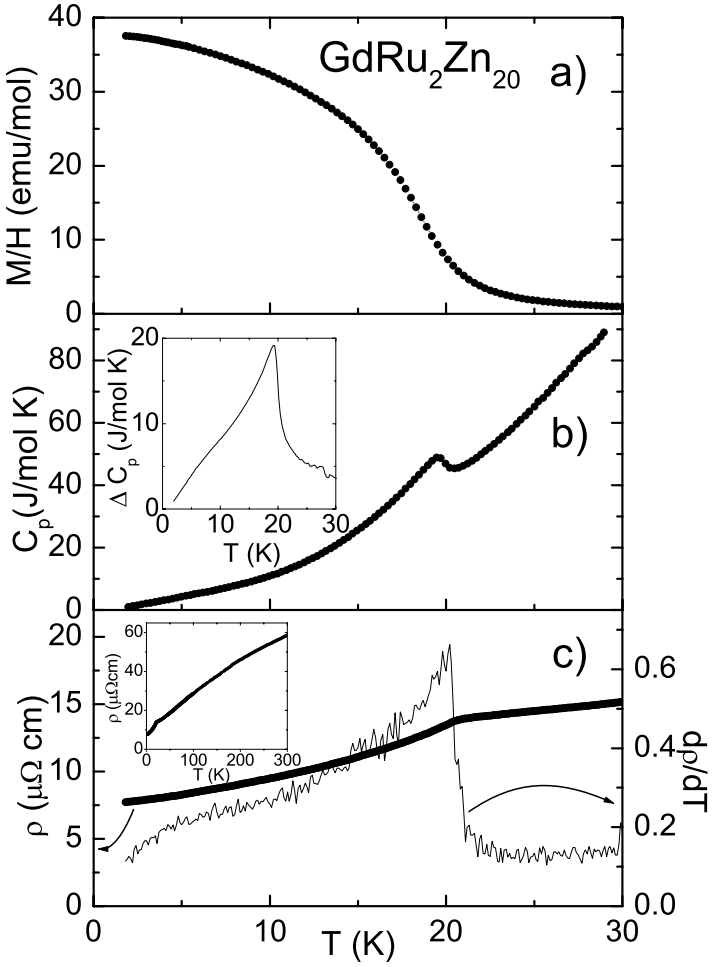

Figure 6.6 (a) Temperature dependent M/H for $GdRu_2Zn_{20}$ (H = 1000 Oe); (b) C_p; (c) ρ and $d\rho/dT$. Inset in (c): ρ over whole temperature range.

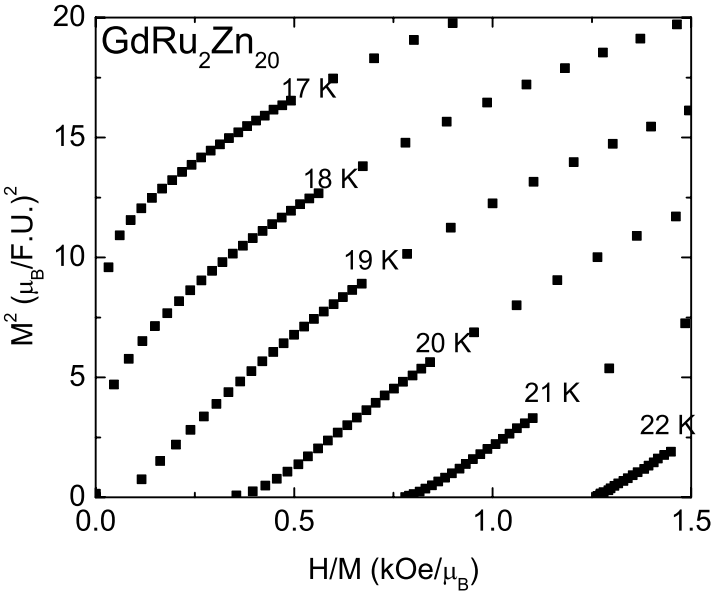

Figure 6.7 Arrott plot for $GdRu_2Zn_{20}$.

magnetic phenomenon in the critical region, rather than one simple, clearly defined, Landau type, 2nd order phase transition.

In contrast to the Fe column compounds, the Co column compounds all appear to order antiferromagnetically with the values of T_N between 4 and 7 K. Figures 6.10, 6.11 and 6.12 present the low temperature magnetic susceptibility, specific heat and electrical resistivity data for $GdCo_2Zn_{20}$, $GdRh_2Zn_{20}$ and $GdIr_2Zn_{20}$ respectively. In addition to these data, $d(\chi(T)T)/dT$ [Fisher, 1962] and $d\rho/dT$ [Fisher and Langer, 1968] have been added to the susceptibility and resistivity plots respectively. $GdCo_2Zn_{20}$ and $GdRh_2Zn_{20}$ manifest clear λ-type anomalies in their temperature dependent specific heat, with similar features appearing in their $d\rho/dT$ and $d(\chi(T)T)/dT$ data. From these thermodynamic and transport data we infer T_N of 5.7 K and 7.6 K for $GdCo_2Zn_{20}$ and $GdRh_2Zn_{20}$ respectively. $GdIr_2Zn_{20}$ shows a somewhat broader feature at $T_N = 4$ K and there may be a lower temperature transition near 2 K indicated in the magnetization data, although this is not clearly supported by corresponding features in either specific heat or resistivity data. A summary of the thermodynamic and transport measurements on the six GdT_2Zn_{20} compounds is presented in Table 6.1.

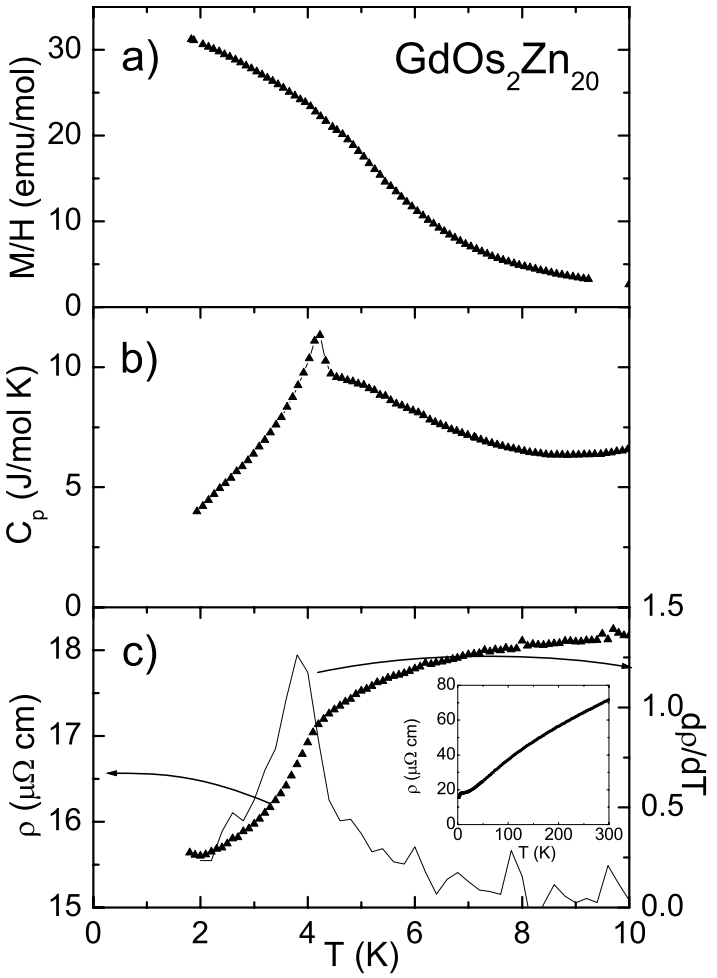

Figure 6.8 (a) Temperature dependent M/H for $GdOs_2Zn_{20}$ ($H = 1000$ Oe); (b) C_p; (c) ρ and $d\rho/dT$. Inset in (c): ρ over whole temperature range.

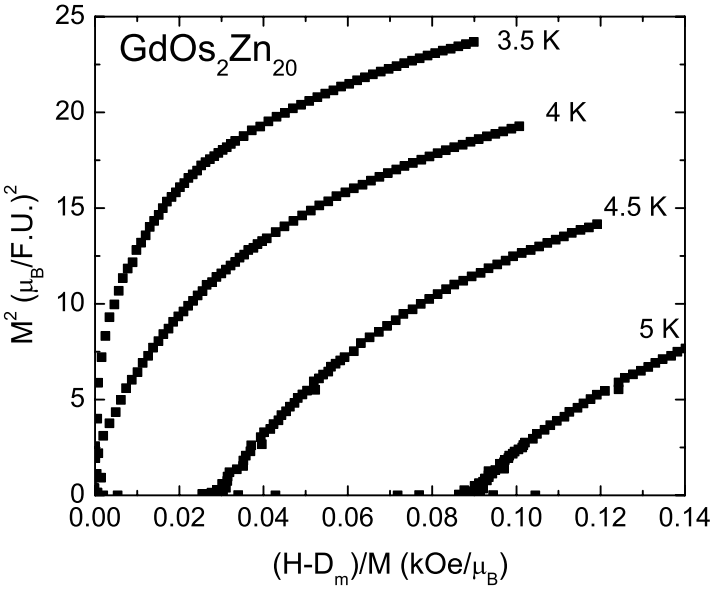

Figure 6.9 Arrott plot for $GdOs_2Zn_{20}$. The demagnetizing field D_m can not be ignored for this low T_C, and was estimated from the geometric factor of the sample ($D \sim 0.03$).

Table 6.1 Residual resistivity ratio, $RRR = \frac{R(300K)}{R(2K)}$; paramagnetic Curie temperature, θ_C and effective moment, μ_{eff} (from the CW fit of $\chi(T)$ from 100 K to 300 K, except for $GdFe_2Zn_{20}$; see text for details); magnetic ordering temperature, T_{mag}; and saturated moment at 55 kOe along [111] direction, μ_{sat} on GdT_2Zn_{20} compounds (T = Fe, Ru, Os, Co, Rh, Ir).

T	Fe	Ru	Os	Co	Rh	Ir
RRR	8.1	7.6	5	12.8	12.8	15.7
θ_C, K	46	23	3	3	-10	-8
μ_{eff}, μ_B	7.9	8.2	8.1	8.2	8.0	8.1
T_{mag}, K	86	20	4.2	5.7	7.7	4.2, 2.4[1]
μ_{sat}, μ_B	6.5	7.25	6.9	7.3		

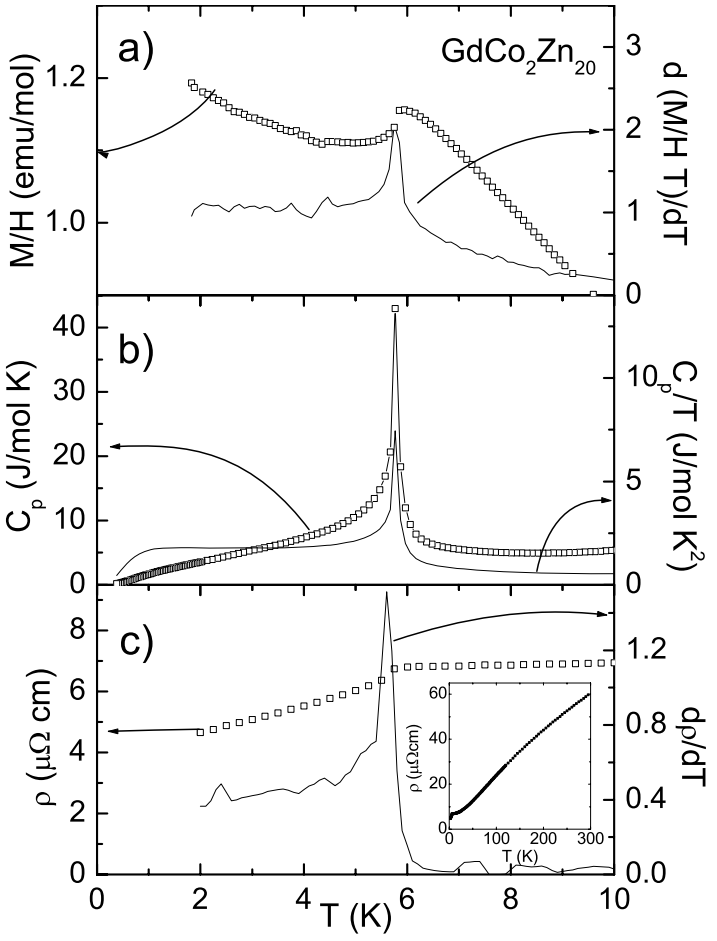

Figure 6.10 (a) Temperature dependent susceptibility (χ) and $d(\chi T)/dT$ of $GdCo_2Zn_{20}$; (b) C_p; (c) ρ and $d\rho/dT$. Inset in (c): ρ over whole temperature range.

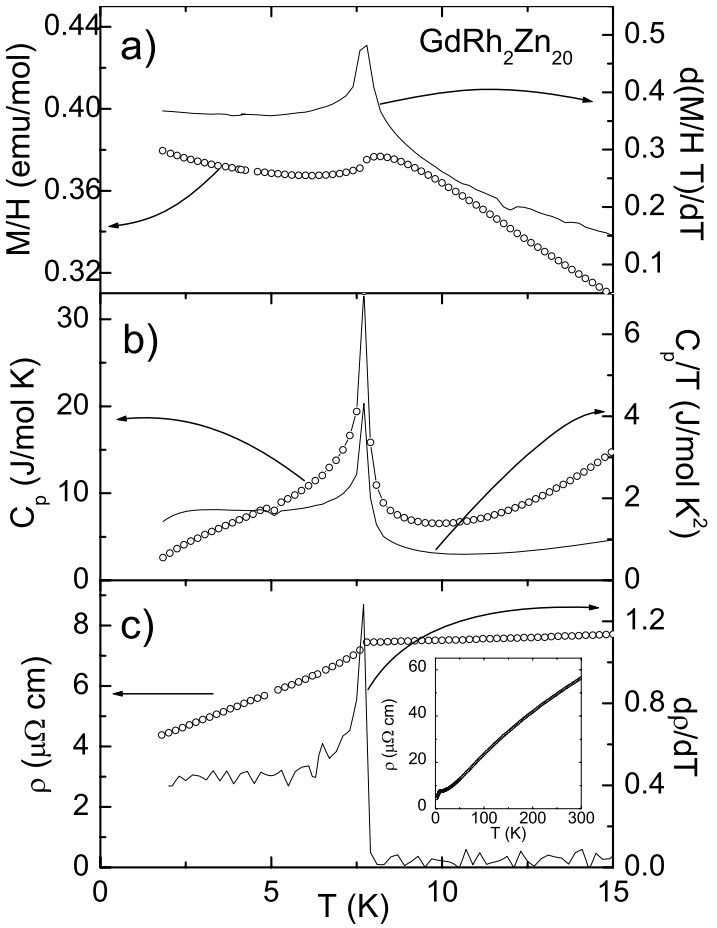

Figure 6.11 (a) Temperature dependent χ and $d(\chi T)/dT$ of $GdRh_2Zn_{20}$; (b) C_p; (c) ρ and $d\rho/dT$. Inset in (c): ρ over whole temperature range.

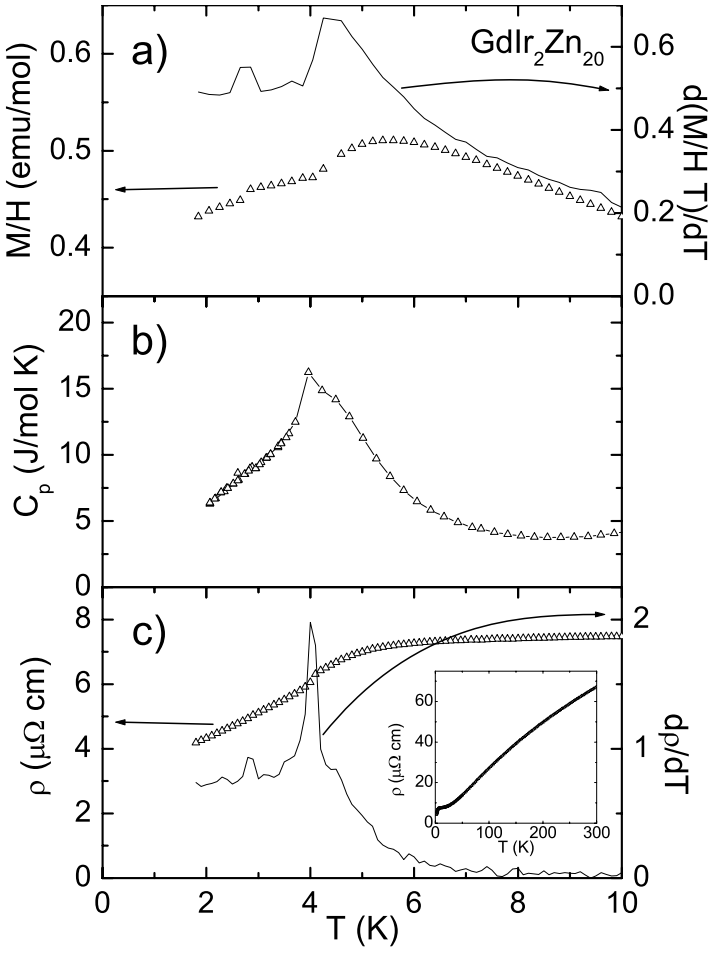

Figure 6.12 (a) Temperature dependent χ and $d(\chi T)/dT$ of $GdIr_2Zn_{20}$; (b) C_p; (c) ρ and $d\rho/dT$. Inset in (c): ρ over whole temperature range.

A logical question that comes to mind when comparing T_C for the Fe column members with the lattice parameter data shown in Fig. 3.2 is whether the drop in T_C as the transition metal moves down the column is associated with a steric effect. This can be addressed experimentally by measurements of T_C under hydrostatic pressure. Figure 6.13 presents low field magnetization for $GdFe_2Zn_{20}$ and $GdRu_2Zn_{20}$ under pressures up to 7 kilobar. The application of pressure suppresses the ferromagnetically ordered state in both compounds and the pressure dependence of $T_{10\%}$ (the temperature where the magnetization equals 10% of maximum magnetization and used as a caliper of T_C) of each compound is plotted in Fig. 6.14. The fact that both compounds manifest a suppression of T_C with increasing pressure indicates that the difference between $GdFe_2Zn_{20}$ and $GdRu_2Zn_{20}$ is not primarily a steric one. Approximating the bulk modulus of these compounds to be a generic 1Mbar, one can estimate that $GdRu_2Zn_{20}$ under 10 kbar hydrostatic pressure will have its lattice parameter reduced by 0.03 Å(25% of the difference between the lattice parameter of $GdFe_2Zn_{20}$ and $GdCo_2Zn_{20}$). If the cause of the T_C suppression was purely steric, such a change in lattice parameter should (at the very least) result in a dramatic increase in the T_C values of $GdRu_2Zn_{20}$ rather than the gradual suppression observed.

6.2.2 YT_2Zn_{20}(T = Fe, Co, Ru, Rh, Os and Ir)

In order to better understand the behavior of $GdFe_2Zn_{20}$ and $GdRu_2Zn_{20}$ with respect to the rest of the GdT_2Zn_{20} compounds, it is useful to examine the properties of the nonmagnetic analogues: the YT_2Zn_{20} compounds. The temperature dependent magnetization data (divided by applied field) and the low temperature magnetization isotherms for these six compounds are presented in Fig. 6.15 and Fig. 6.16, respectively. YFe_2Zn_{20} and YRu_2Zn_{20} have a greatly and intermediately enhanced paramagnetic signals respectively, whereas the rest of the materials manifest ordinary weak, either paramagnetic or diamagnetic, responses, as anticipated for non-moment bearing intermetallic compounds.

Measurements of low temperature specific heat (plotted as C_p/T versus T^2 in Fig. 6.17)

[1] two magnetic transitions were found

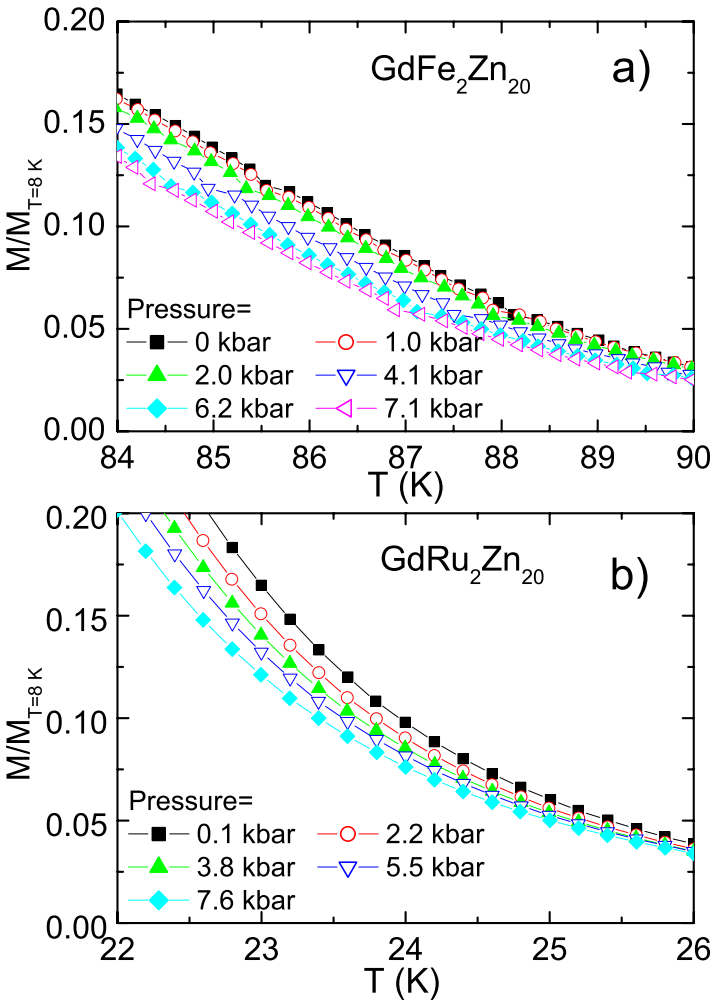

Figure 6.13 Magnetization of (a): $GdFe_2Zn_{20}$ and (b): $GdRu_2Zn_{20}$ in applied field ($H = 1000$ Oe) under different hydrostatic pressure.

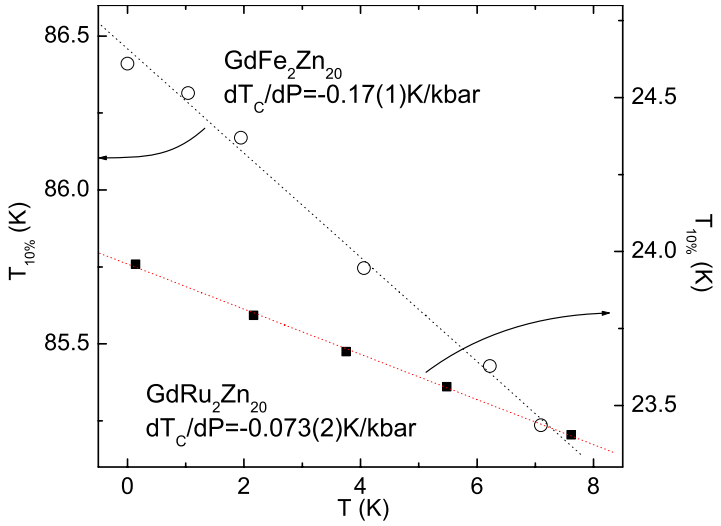

Figure 6.14 Pressure dependent $T_{10\%}$ (inferred as $T_{\rm C}$) of $GdFe_2Zn_{20}$ and $GdRu_2Zn_{20}$. The dash lines are the linear fits of the data.

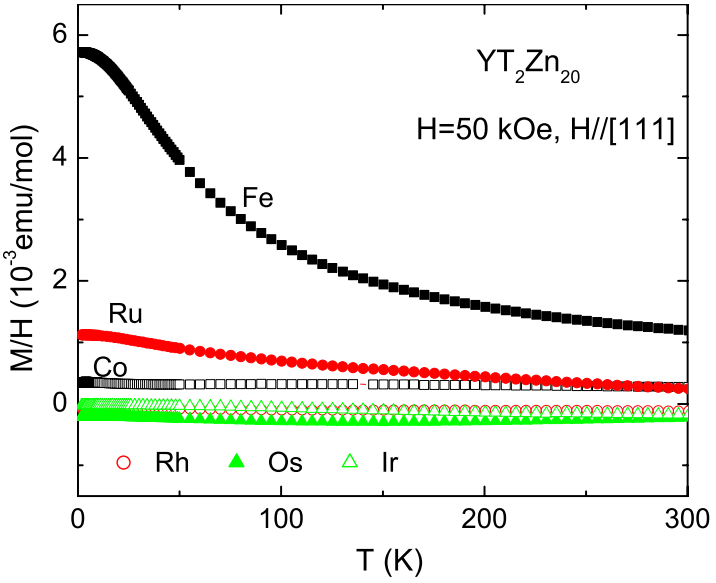

Figure 6.15 Temperature dependent magnetization of YT_2Zn_{20} under applied field $H = 50$ kOe.

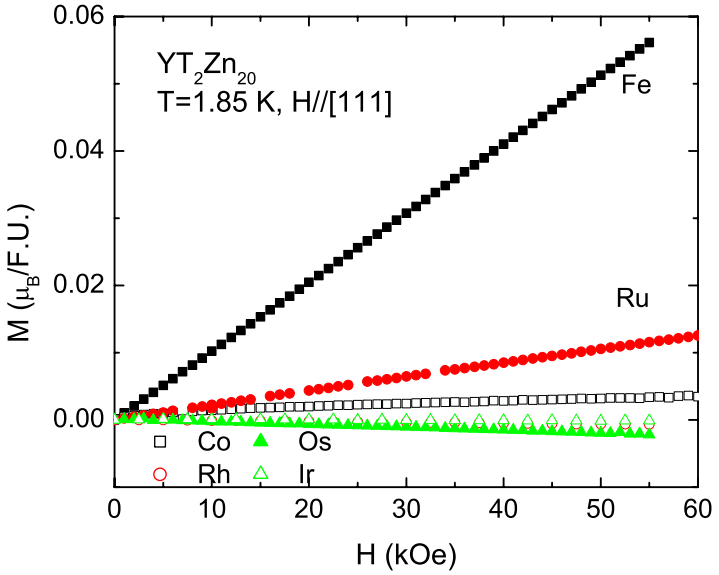

Figure 6.16 Field dependent magnetization of YT_2Zn_{20} at 1.85 K.

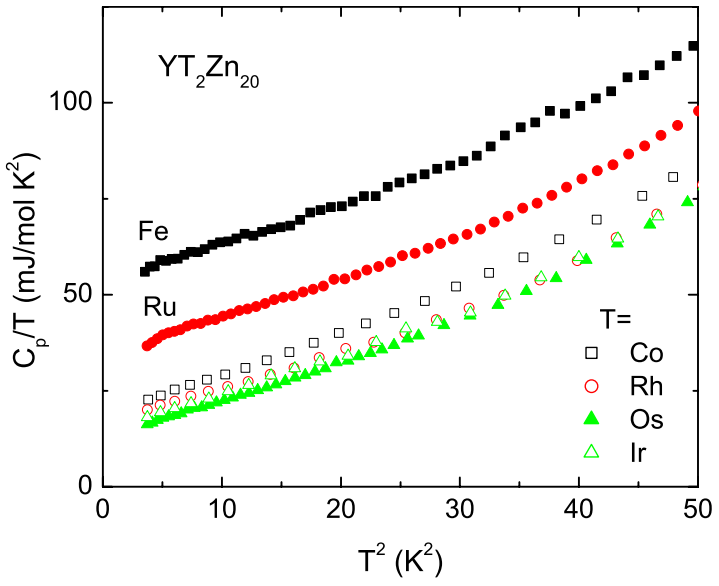

Figure 6.17 Low temperature specific heat of YT_2Zn_{20}.

also indicate a clear difference between YFe_2Zn_{20}, YRu_2Zn_{20} and the other members of the YT_2Zn_{20} series: enhanced values of the electronic specific heat being found for T = Fe and Ru. As shown in Chapter 5, YFe_2Zn_{20} can be thought of as being close to the Stoner limit. The simplest way to see this is to recall that, in this limit, whereas the Pauli paramagnetism is enhanced by a factor $(1-Z)^{-1}$, the electronic specific heat is not [Ziman, 1979]. This means that the term Z in the enhancement factor can then be inferred from the experimentally determined, low temperature values of γ_0 and χ_0. In common units

$$Z = 1 - 1.37 \times 10^{-2} \frac{\gamma_0(J/molK^2)}{\chi_{0-dia}(emu/mol)} \tag{6.1}$$

where χ_{0-dia} equals χ_0 with the core diamagnetism subtracted.

Giving the core diamagnetism values(-2.3×10^{-4}emu/mol for YFe_2Zn_{20} and YCo_2Zn_{20}, -2.5×10^{-4}emu/mol for YRu_2Zn_{20} and YRh_2Zn_{20}, and -2.9×10^{-4}emu/mol for YOs_2Zn_{20} and YIr_2Zn_{20})[Mulay and Boudreaux, 1976], Z can be inferred to be 0.88 and 0.67 for YFe_2Zn_{20} and YRu_2Zn_{20} respectively (Table 6.2). For reference, this can be compared to $Z = 0.83$ and 0.57 for elemental Pd and Pt respectively[†], which are thought to be canonical examples of NFFLs. These enhanced Z values indicate that YRu_2Zn_{20}, and particular YFe_2Zn_{20} are extremely close to the Stoner limit ($Z = 1$). In contrast, the Z values of the rest of the members are less than 0.5, which is comparable with the estimated value of the canonical example of 'normal metal', Cu, $Z = 0.29$ [‡]. It is worth noticing that, during the estimation of the Z values, the contribution from the Landau diamagnetism is ignored. Inversely proportional to the square of the effective mass of the conduction electrons[Ashcroft and Mermin, 1976], the Landau diamagnetic contribution becomes more significant for those members which have smaller γ_0 values. Thus, based on the thermodynamic measurements, the Pauli susceptibility values, even after the core diamagnetism correction, are still under-estimated. Due to this uncertainty, the Pauli susceptibility values after the core diamagnetism correction for YOs_2Zn_{20} and YRh_2Zn_{20}, albeit positive, are still less than the un-enhanced values ($Z = 0$) corresponding to their γ_0.

[†]The values of γ_0 and χ_{0-dia} are from ref. [Knapp and Jones, 1972, B Zellermann and Voitländer, 2004].
[‡]The values of γ_0 and χ_{0-dia} are from ref. [Kittel, 1996] and [Mulay and Boudreaux, 1976] respectively.

Table 6.2 Low temperature susceptibility, χ_0; and the values after core diamagnetism correction, χ_{0-dia}; linear coefficient of the specific heat, γ_0; and the Stoner enhancement factor, Z on YT_2Zn_{20} compounds (T = Fe, Ru, Os, Co, Rh, Ir).

T	Fe	Ru	Os	Co	Rh	Ir
χ_0[1],	5.73	1.14	-0.256	0.212	-0.076	-0.034
χ_{0-dia},	5.96	1.39	0.034	0.442	0.174	0.256
γ_0[2]	53	34	12.4	18.3	16.4	14.1
θ_D, K	123	124	125	121	127	124
Z[3]	0.88	0.67	-	0.43	-	0.24

6.2.3 Electronic Structure

Band structure calculations, performed on the representative, non-local moment members, YT_2Zn_{20} (T = Fe, Co and Ru), as well as their local moment analogues, GdT_2Zn_{20}, can help us to understand their diverse magnetic properties further. Figure 6.18 shows the result of the total and partial density of states (DOS) for each element for YFe_2Zn_{20}. At the Fermi level, E_F, the total DOS manifests a sharp peak, leading to the relatively large DOS at Fermi level ($N(E_F)$, see Table 6.3), and therefore large band contributed electronic specific heat, $\gamma_{band} = 30.6$ mJ/mol K^2. This result is consistent with the experimentally measured electronic specific heat, γ_0 with a large mass enhanced factor, $\lambda = 0.73$, if one assumes $\gamma_0 = (1 + \lambda)\gamma_{band}$. The peak-shape DOS at E_F is not unusual for the NFFL systems: similar calculation results have been obtained for Pd [Shimizu et al., 1963], YCo_2 [Tanaka and Harima, 1998] and Ni_3Ga [Hayden et al., 1986] by using similar techniques. The large peak at about -7 eV corresponds to totally filled d-states of Zn atoms. Figure 6.18 also shows significant contribution of Zn atoms' electronic states to the total DOS in the whole energy spectrum, whereas the Fe atoms' electronic states are mostly localized in the vicinity of E_F, although they are dilute in this compound (1/10 of Zn). Table 6.3 shows that the partial DOS of Fe at E_F is in between the values for elemental Pd and Fe (before band splitting), the canonical elemental

[1] Taken as $\frac{M(50\ \text{kOe}) - M(30\ \text{kOe})}{20\ \text{kOe}}$, in unit 10^{-3}emu/mol

[2] in unit mJ/molK^2

[3] Eqn. 6.1 is invalid for T = Os and Rh; see text

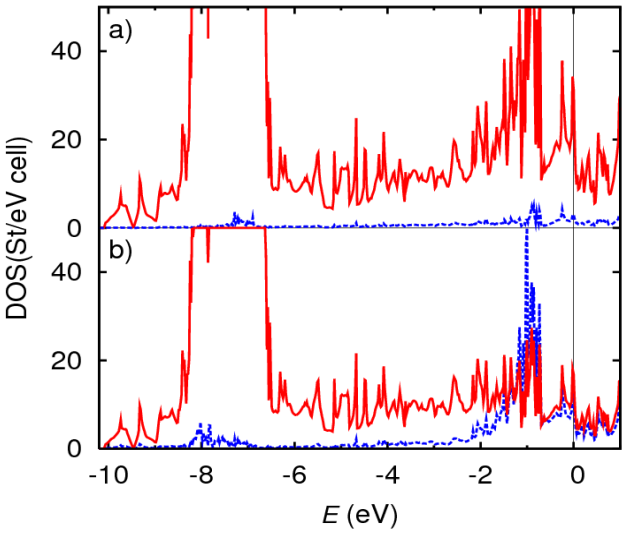

Figure 6.18 The DOS of YFe_2Zn_{20} (in St/eV cell) and partial DOS (in St/eV cell). E_F corresponds to zero energy. The red color solid line on (a) corresponds to total DOS and blue dashed - to Y atoms PDOS. The red color solid line on (b) corresponds to PDOS of Zn and blue dashed - to Fe atoms PDOS.

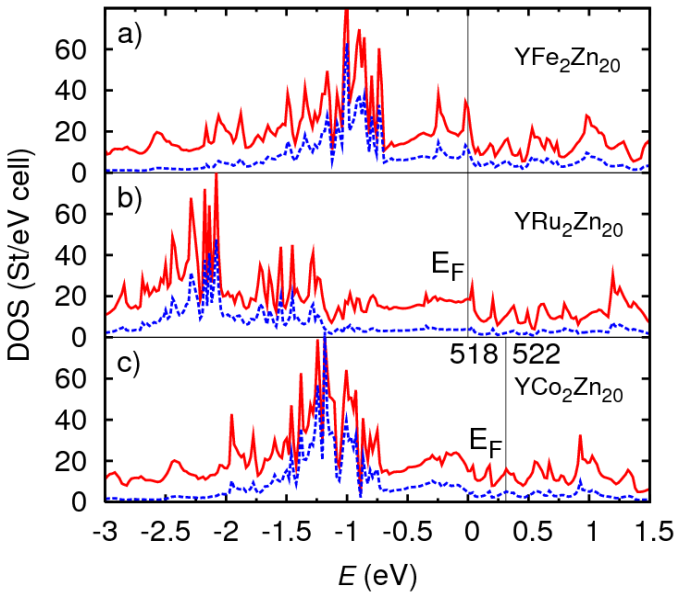

Figure 6.19 The DOS of YFe_2Zn_{20} (a), YRu_2Zn_{20} (b) and YCo_2Zn_{20} (c) near E_F (in St/eV cell) shown by red solid line and PDOS of Fe, Ru and Co atoms (blue dashed line) (in St/eV cell). E_F is shown by vertical lines. 518 and 522 corresponds to number of valence electrons in the unit cell calculated in the rigid band approximation from the DOS of YFe_2Zn_{20}.

examples of nearly ferromagnet and 'strong' ferromagnet systems. This result indicates that YFe_2Zn_{20} indeed may be even closer the Stoner criterion than Pd. The total DOS at E_F mainly corresponds to the hybridization of the $3d$-band of Fe and p-band of Zn; the $4d$-band of Y, although hybridized with the other two, contributes significantly less (Fig.6.18).

The dominant effect of the d-band filling on the magnetic properties of YT_2Zn_{20}, manifests itself clearer if one compares the electronic structure of the three YT_2Zn_{20} compounds: T= Fe, Co and Ru (Fig. 6.19). In Fig. 6.19, the total and Co-partial DOS of YCo_2Zn_{20} manifests a similar form as the YFe_2Zn_{20} analogue, but with E_F is shifted 0.3 eV higher due to adding 2 more valence electrons per formula unit. This similarity indicates that the difference in the electronic structure of YFe_2Zn_{20} and YCo_2Zn_{20} can be considered in terms of the rigid band approximation. On the other hand, the electronic structure of YRu_2Zn_{20} has the same Fermi

level position as YFe_2Zn_{20} because of the same valence electron filling. However, its total, and partial-Ru, DOS are lower than those for YFe_2Zn_{20}. This difference is not unexpected, since the $4d$ band is usually broader than the $3d$ band in the electronic structure of intermetallics. Calculated $N(E_F)$ of YCo_2Zn_{20} is half of the value of YFe_2Zn_{20}, whereas the value of YRu_2Zn_{20} is slightly larger than YCo_2Zn_{20} (Table 6.3).

The electronic structure calculation of the three GdT_2Zn_{20} analogues, based on the treatment of $4f$ electrons in core states, can help to understand the effect of submerging a Gd^{3+} local moment in these electronic backgrounds (Y analogues). Our calculations demonstrate that, in the ordered state, Gd and the transition metal carries a magnetic moment (see Table 6.3). The magnetic moment of the Gd atoms are about 7.4 μ_B for FM ordered compounds and 7.3 μ_B for AFM ordered compounds, significantly smaller compared to elemental Gd result [Perlov et al., 2000, I Turek and Blugel, 2003], 7.6 μ_B. The magnetic moment additional to the Hund's value (7 μ_B) comes from the polarization of Gd's p and d states by magnetic $4f$ electrons. The negative coupling between Gd and transition metals induces magnetic moments on these atoms in direction opposite to the Gd magnetic moment. In agreement with the high DOS of Fe atoms in YFe_2Zn_{20}, the induced magnetic moment on Fe atoms, -0.84 μ_B, is the largest among all series. The smaller DOS of Ru atoms in YRu_2Zn_{20} compound correlates with a smaller induced magnetic moment on Ru in $GdRu_2Zn_{20}$: -0.04 μ_B. The induced magnetic moment on Co is zero because of the compensation of interactions with Gd in AFM $GdCo_2Zn_{20}$. The calculated total magnetic moment, 7.25 μ_B, 6.53 μ_B and 7.30 μ_B for GdT_2Zn_{20} (T = Co, Fe and Ru respectively), are in good agreement with the experimental values, 7.3 μ_B, 6.5 μ_B and 7.25 μ_B (see Table 6.1). The DOS for $GdFe_2Zn_{20}$ [Fig. 6.20(a)] demonstrates a significant splitting between occupied and empty $3d$ states of Fe, in agreement with sizable Fe magnetic moments, whereas this splitting is almost negligible in case of Ru based compounds [Fig. 6.20(b)].

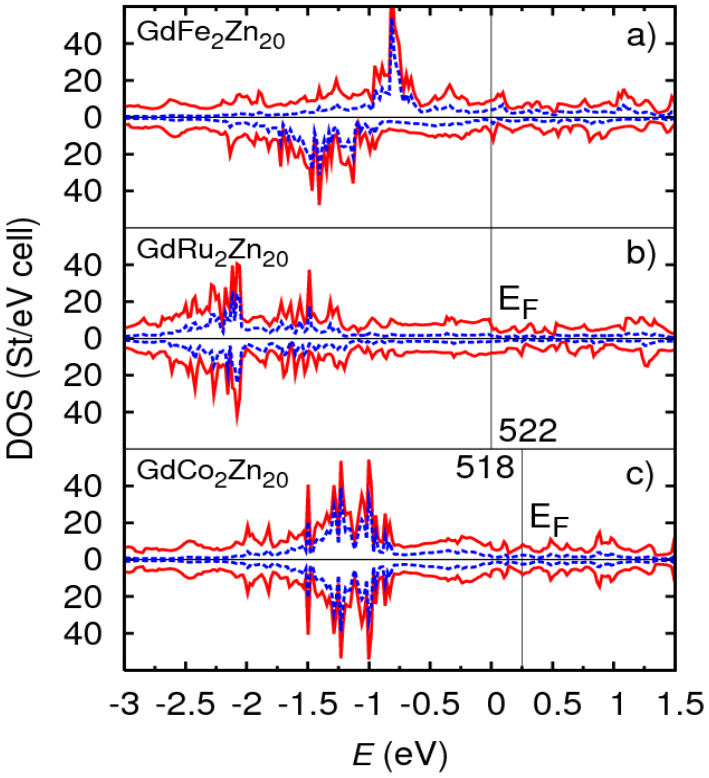

Figure 6.20 The red solid line corresponds to DOS of FM-ordered $GdFe_2Zn_{20}$ (a), FM-ordered $GdRu_2Zn_{20}$ (b) and AFM one $GdCo_2Zn_{20}$ (c) near E_F (in St/eV cell) and partial DOS of Fe, Ru and Co atoms (blue dashed line) (in St/eV atom). E_F is shown by vertical lines. 518 and 522 corresponds to number of valence electrons in the unit cell calculated in the rigid band approximation from the DOS.

Table 6.3 The calculated DOS in St/eV cell ($N(E_F)$), averaged DOS per one atom ($N(E_F)/N_{atoms}$), partial DOS at transition metal atom ($N_T(E_F)$) and magnetic moment in μ_B for Gd and transition metal, T, in GdT_2Zn_{20} compounds.

Compound	$N(E_F)$	$N(E_F)/N_{atoms}$	$N_T(E_F)$	Magnetic Moment	
				Gd	T
Pt (elemental)	2.2	2.2	2.2		
Pd (elemental)	2.6	2.6	2.6		
Fe (elemental)	3.5	3.5	3.5		
YCo_2Zn_{20}	16.32	0.35	1.28		
YFe_2Zn_{20}	31.35	0.68	2.86		
YRu_2Zn_{20}	18.72	0.41	1.0		
$GdCo_2Zn_{20}$	14.92			7.25	0.00
$GdFe_2Zn_{20}$	17.95			7.37	-0.84
$GdRu_2Zn_{20}$	17.15			7.34	-0.04

6.3 Discussion

The band structure calculation indicates that, with same structure and similar lattice parameters, the diverse magnetic properties of GdT_2Zn_{20} and YT_2Zn_{20} are mainly dependent on the d-band conduction electrons from the transition metal site. The different d-band filling of the Fe column members and the Co column members is associated with the different sign of the magnetic coupling of Gd^{3+} local moments, and thereupon the different type of magnetic ordering. Furthermore, the high and intermediately high $N(E_F)$ of $3d$ and $4d$ sub-bands of Fe and Ru, respectively, are associated with the strongly correlated electronic state of YFe_2Zn_{20} and YRu_2Zn_{20}, as well as the strong coupling between the Gd^{3+} local moments in $GdFe_2Zn_{20}$ and $GdRu_2Zn_{20}$, and therefore the high magnetic ordering temperatures. The negative induced moment on Fe site is not unexpected in intermetallic systems consisting of a heavy rare earth and a more than half-filled $3d$ transition metal [Franse and Radwanski, 1993, Brooks and Johansson, 1993], which can be understood in terms of the hybridization between the $3d$ electronic wavefunction of transition metal and the $5d$ electronic wavefunction of the rare earth [Campbell, 1972].

In addition to the electronic structure calculations, the remarkable high-temperature FM ordering of $GdFe_2Zn_{20}$ and $GdRu_2Zn_{20}$ can be understood in the conceptually simple context of large Heisenberg moments, associated with the Gd^{3+} ion ($S = 7/2$), being embedded in the NFFL associated with YFe_2Zn_{20} and YRu_2Zn_{20}. This framework has been employed to understand the anomalously high temperature FM ordering in some systems of local moments in NFFL hosts, such as dilute Fe, Co, or Gd in Pd or Pt [Nieuwenhuys, 1975, Crangle, 1964], or RCo_2(R = Gd - Tm) [Duc and Goto, 1999, Duc and Brommer, 1999]. In these systems, the itinerant electrons of the host (Pd, Pt or YCo_2) are polarized by the local moments (Fe, Co ions or R^{3+} ions), strongly couple them, and by doing so, result in high-temperature, local moment ordering.

As shown in Chapter 5, substitutional series of $Gd(Fe_xCo_{1-x})_2Zn_{20}$ and $Y(Fe_xCo_{1-x})_2Zn_{20}$ provide the versatility to study the correlation between the local moments and the high polarizable host. When x is varied from 0 to 1, by tuning the d-band filling, the inferred values of Z for the $Y(Fe_xCo_{1-x})_2Zn_{20}$ series, representing to some extent the polarizability, increase super-lineally from 0.43 to 0.88, giving rise to the highly nonlinear increase of the magnetic ordering temperature for the $Gd(Fe_xCo_{1-x})_2Zn_{20}$ series (see Figs. 5.7 and 5.8). This correspondence between the Z values and the magnetic ordering temperatures is even consistent with the T_C value for $GdRu_2Zn_{20}$, although the itinerant electrons of the transition metal are $4d$, not $3d$. Given $Z = 0.67$ for YRu_2Zn_{20}, a similar Z-value of the host is between $x = 0.5$ and 0.75 for $Y(Fe_xCo_{1-x})_2Zn_{20}$ (Fig. 5.7). The T_C value of $GdRu_2Zn_{20}$ is also between the T_C values for $x = 0.5$ and 0.75 for $Gd(Fe_xCo_{1-x})_2Zn_{20}$ (Fig. 5.8).

This conceptually simple framework can also help to understand the curious temperature dependence of the $1/\chi(T)$ data for $GdFe_2Zn_{20}$. Figure 6.21(a) shows the temperature dependent H/M in an applied field ($H = 1000$ Oe), with a dashed line representing the CW fit above 250 K. As shown before, the fit gives the value of the effective moment ($\mu_{eff} = 7.9\ \mu_B$), comparable with the effective moment of $4f$ electrons of Gd^{3+} in Hund's ground state. As T is decreased, the electronic background that the Gd^{3+} ion is immersed in becomes increasingly polarizable, leading to a temperature-dependent coupling that in turn leads to the nonlinearity

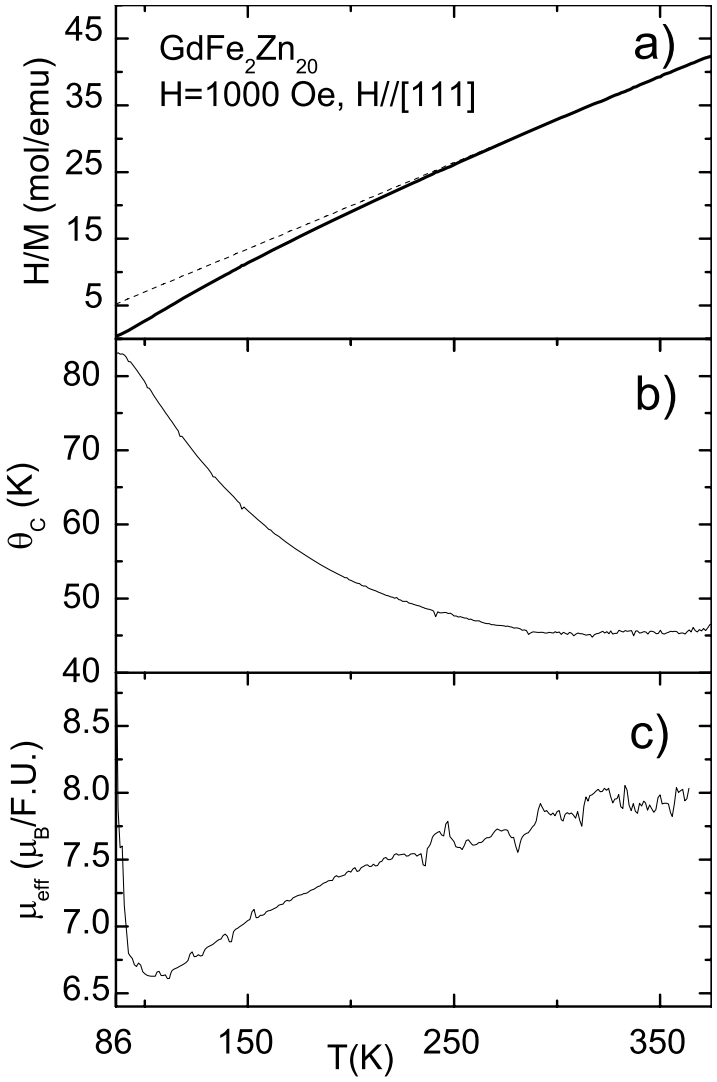

Figure 6.21 (a): H/M ($H = 1000$ kOe) of $GdFe_2Zn_{20}$ as a function of temperature. The dash line represents the Curie-Weiss fit above 250 K. (b): temperature varied θ_C. (c): temperature varied μ_{eff}. (See text)

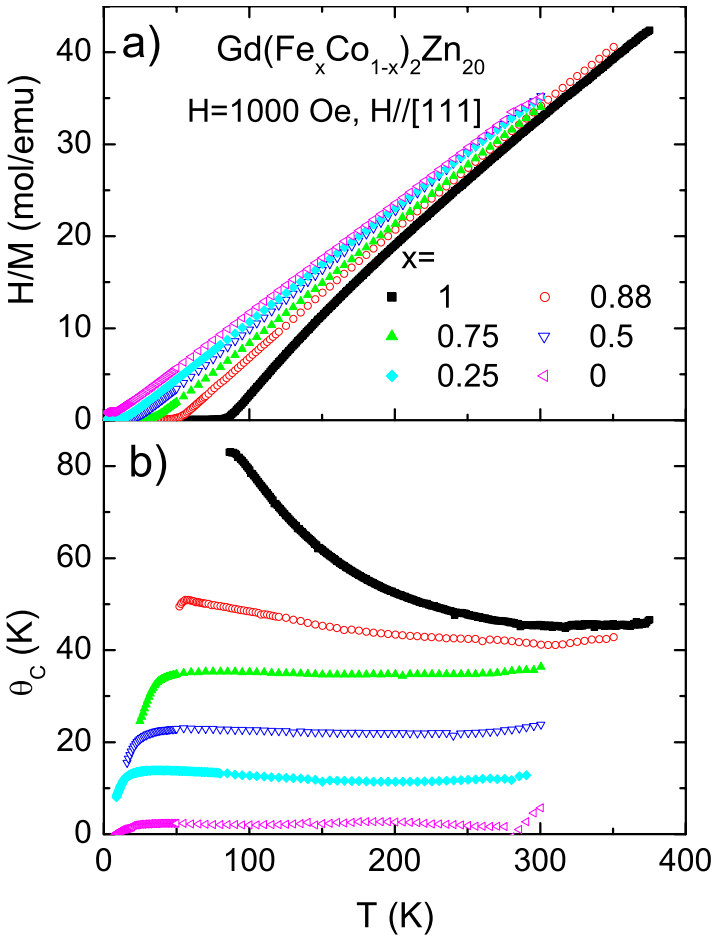

Figure 6.22 (a): H/M ($H = 1000$ kOe) of $Gd(Fe_xCo_{1-x})_2Zn_{20}$ as a function of temperature. (b): temperature varied θ_C. (See text)

of the $1/\chi$ versus T data. If a constant μ_{eff} for Gd^{3+} is assumed, then a temperature-dependent θ_C can be extracted from the $1/\chi$ data. As shown in Fig. 6.21(b), θ_C is essentially constant ($\sim$ 45 K) above 275 K; then increases monotonically as temperature decrease, tracking $\chi(T)$ of YFe_2Zn_{20} (Fig. 6.15).

The correlation of the temperature dependent χ and the polarizability of electronic background can also be seen in the susceptibility of $Gd(Fe_xCo_{1-x})_2Zn_{20}$ series. Figure 6.22(a) presents temperature dependent H/M under the applied field $H = 1000$ Oe. Linear and parallel to each other at high temperature region, the data sets start to deviate at lower temperature,

especially for large x. Similar to discussed before, the temperature dependent θ_C values were extracted with the assumption of invariant μ_{eff}. Figure 6.22(b) shows that θ_C varies strongly, much weakly and negligibly as $x = 1$, 0.88 and ≤ 0.75, respectively. For each x, the variation of θ_C tracks $\chi(T)$ of the $Y(Fe_xCo_{1-x})_2Zn_{20}$ series (Fig. 5.5).

An alternative method of analyzing the $\chi(T)$ data (shown in Fig. 6.21 a) assumes that some induced moment exists above T_C and is aligned, dynamically and locally, anti-parallel to the Gd moment (in essence forming a composite moment). Assuming an invariant θ_C, values of C can be inferred from:

$$1/C \approx \frac{d(\frac{T-\theta_C}{C})}{dT} = \frac{d(\frac{H}{M})}{dT}. \tag{6.2}$$

Shown in Fig. 6.21(c), μ_{eff} manifests a monotonic decrease with decreasing temperature down to 110 K, at which temperature it shows a minimum value 6.6 μ_B. From 100 K to T_C, μ_{eff} starts to rise in a highly nonlinear fashion. This rise of the μ_{eff} value is not unexpected in the vicinity of T_C in FM system, and could be due to the short range ordering or formation of magnetic clusters of the local moments [Mydosh, 1993]. The decrease of μ_{eff}, in this scenario, would be the result of the formation of magnetic droplets, consisting of the Gd^{+3} local moments and the oppositely polarized electron cloud from the highly polarizable host. Such magnetic droplets are not unprecedented in analogous systems, above T_C. For example, the 'giant moment' was observed in dilute Fe-Pd alloy [Clogston et al., 1962]; the deficient μ_{eff} of local moments was also found in RCo_2 series (R = Gd-Tm) [Stewart, 1984a] above T_C. Giving that the primary difference between these two alternative explanations is whether the itinerant electrons are polarized above T_C, measurements of Mössbauer spectra on the Fe sites at varied temperature should resolve this piont.

6.4 Summary

The six GdT_2Zn_{20} (T = Fe, Ru, Os, Co, Rh and Ir) compounds have magnetic properties that differ dramatically between the Fe column and the Co column members. The Fe column members order ferromagnetically with the enhanced transition temperatures for the T = Fe

and Ru members, whereas the Co column members all manifest low-temperature, AFM ordering. In a related manner, the T = Fe and Ru members of YT_2Zn_{20} family manifest typical properties associated with NFFLs. Band structure calculation results for the T = Fe and Ru members reveal that the large DOS at the Fermi level is correlated with the enhancement in the their magnetic properties. The conceptually simple framework of the Heisenberg moments embedded in the NFFL, was discussed to understand the enhanced transitions for $GdFe_2Zn_{20}$ and $GdRu_2Zn_{20}$ and the curious temperature dependence of the $1/\chi$ versus T data for $GdFe_2Zn_{20}$.

CHAPTER 7. Magnetic properties of $Gd_xY_{1-x}Fe_2Zn_{20}$: dilute, large, S-moments in a nearly ferromagnetic Fermi liquid *

7.1 Introduction

Materials that are just under the Stoner limit manifest large electronic specific heat and enhanced paramagnetism and are known as NFFLs [Moriya, 1985, Brommer and Franse, 1990]. Archetypical examples, such as Pd [Jamieson and Manchester, 1972], YCo_2 [Lemaire, 1966], $TiBe_2$ [Matthias et al., 1978], and Ni_3Ga [de Boer et al., 1967] have been studied for several decades. In addition to the interesting, intrinsic properties of these compounds, the introduction of local moments into these highly polarizable hosts has lead to both experimental and theoretic interest [Nieuwenhuys, 1975, Larkin and Mel'nikov, 1972, Maebashi et al., 2002]. In such highly polarizable hosts, local moment impurities can manifest long range, ferromagnetic order even for very low concentrations (0.5 at.% Fe in Pd [Mydosh et al., 1968] and 1 at.% Gd in Pd [Crangle, 1964]).

As shown in Chapter 5 and 6, YFe_2Zn_{20} was found to be a ternary example of a NFFL with a Stoner parameter $Z \sim 0.9$, as compared to $Z \sim 0.83$ for Pd, indicating strongly correlated electron behavior. When the large, **S** moment bearing, Gd^{3+} replaces the non-magnetic Y^{3+} ions, it was found that $GdFe_2Zn_{20}$ has a remarkably high ferromagnetic Curie temperature(T_C) of 86 K. Both of these compounds belong to the much larger, isostructural RT_2Zn_{20} (R = rare earth, T = transition metal such as Fe, Co, Ni, Ru, Rh, Os, Ir and Pt) [Nasch et al., 1997] family, in which the R and T ions each occupy their own unique, single, crystallographic sites. Motivated by these intriguing magnetic and structural properties, we focus, in this work, on

*after "Magnetic properties of $Gd_xY_{1-x}Fe_2Zn_{20}$: dilute, large, **S**-moments in a nearly ferromagnetic Fermi liquid", S. Jia, N. Ni, S. L. Bud'ko, P. C. Canfield, *Phys. Rev. B* **76** 184410 (2007).

the pseudo-ternary series $Gd_xY_{1-x}Fe_2Zn_{20}$, which can be used as a model for studying the effects of titrating very dilute local moments into a nearly ferromagnetic Fermi liquid. Given that RFe_2Zn_{20} is a dilute, rare earth bearing intermetallic, dilution of Gd onto the Y site (i) changes the lattice parameter by less than 0.2 %, (ii) does not change the band filling, (iii) does not change the all Zn local environment of either the Gd or Fe ions, and (iv) allows for the dilution of Gd in the system to be studied down to $x \approx 0.005$, i.e. down to approximately 200 *p.p.m.* Gd.

In this chapter, we report on the characterization of single crystals of $Gd_xY_{1-x}Fe_2Zn_{20}$ by X-ray diffraction, Energy Dispersive X-ray Spectroscopy (EDS), magnetization, resistivity and heat capacity measurements. These data reveal ferromagnetic order of the Gd^{3+} local moment above 1.80 K for Gd concentration above $x = 0.02$. These results will be discussed within the framework of the so-called *s-d* model [Shimizu, 1981a], based on the mean field approximation, and used to explain the variation of T_C across the series with respect to x.

7.2 Experimental Methods

As described in Chapter 4, single crystals of $Gd_xY_{1-x}Fe_2Zn_{20}$ were grown from a Zn-rich self flux [Canfield and Fisk, 1992]. For $x > 0.02$, high purity elements were combined in a molar ratio of $(Gd_xY_{1-x})_2Fe_4Zn_{94}$. For x less than 0.02, a $Y_{0.9}Gd_{0.1}$ master alloy was made via arc melting and appropriate amounts of this alloy were added to elemental Y. This was done to reduce the uncertainties associated with weighing errors. The samples were characterized by room temperature powder X-ray diffraction measurements [Fig. 7.1(a)]. The lattice constants varied linearly for $0 \leq x \leq 1$. This shift can be seen in the (117) peak position for selected x values [see Fig. 7.1(b)]. EDS measurements were made in a JEOL model 5910lv-SEM with a Vantage EDS system on representative samples.

DC magnetization was measured in a Quantum Design superconducting quantum interference device (SQUID) magnetometer, in a variety of applied fields ($H \leq 55$ kOe) and temperatures (1.85 K $\leq T \leq$ 375 K). In some crystals, the magnetization with respect to magnetic field measurements at 300 K showed a slight non-linearity with a small slope change around 3

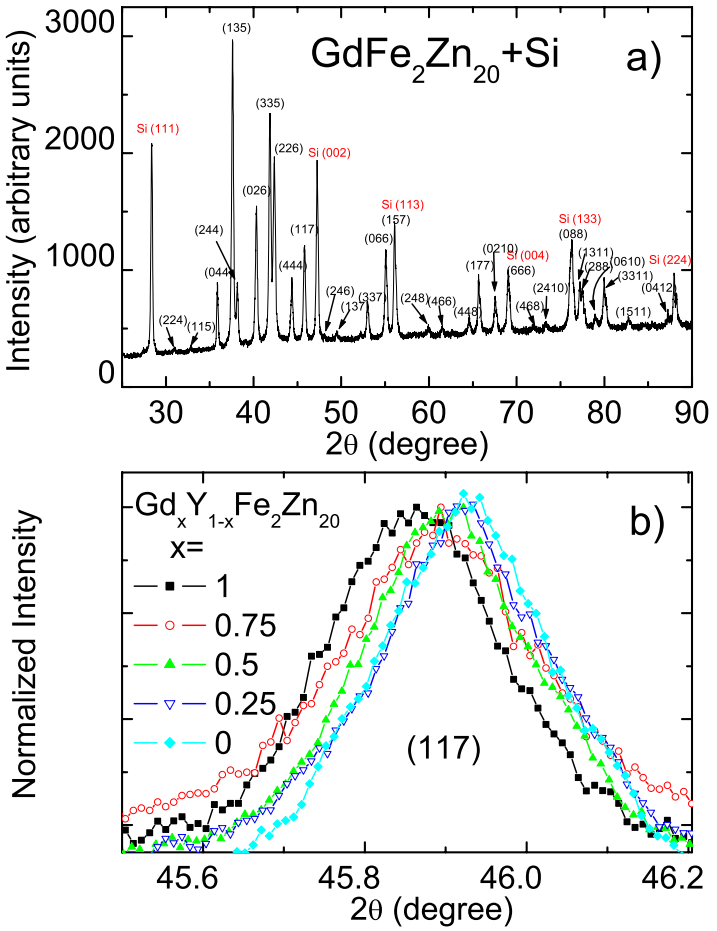

Figure 7.1 (a): Powder X-ray diffraction pattern of $GdFe_2Zn_{20}$ with a Si internal standard (using Cu K_α radiation) with main peaks indexed. (b): The normalized intensity of the (117) peak of $Gd_xY_{1-x}Fe_2Zn_{20}$ for representative x values, with the positions calibrated by the nearby Si(002) peak.

kOe (Fig. 7.2). This specific behavior is believed to be due to a small amount of ferromagnetic impurity, possibly Fe or FeO_x (2×10^{-5} μ_B/mol to 2×10^{-3} μ_B/mol) on the crystal. This feature is most likely extrinsic because the extent of the slope change is sample-dependent: some samples showing no feature at all. This feature is most clearly seen when two samples from the same batch (one with feature, one without) are compared (Fig. 7.2, inset a) or even subtracted from each other (Fig. 7.2, inset b). Given that this small, extrinsic ferromagnetic contribution saturates by $H \approx 10$ kOe (Fig. 7.2, inset b), the high temperature susceptibility can be determined by $\chi(T) = \frac{\Delta M}{\Delta H} = \frac{M_{(H=50\text{kOe})} - M_{(H=20\text{kOe})}}{30\text{kOe}}$. In this temperature region the intrinsic magnetization is a linear function of applied magnetic field for 20 kOe $\leq H \leq$ 50 kOe (Fig. 7.2). At lower temperatures, closer to T_C, the sample's intrinsic magnetization become large enough that we can measure $\chi(T)$ directly as M/H for $H = 1$ kOe.

7.3 Experiments Results

The size of the cubic unit cell, as determined by powder X-ray diffraction measurements, shows a linear dependence on x as it is varied from 0 to 1 (Fig. 7.3). The error bars of the lattice constants were estimated from the standard deviation determined by measurements on three samples from the same batch. These data are compliant with Vegard's law and imply that the nominal x is probably close to the actual x.

In order to check this further, EDS was used. This is a direct method of determining x, although it loses some of its accuracy because of the low, total rare earth concentration (< 5 at.%). Nevertheless, several representative members of the $Gd_xY_{1-x}Fe_2Zn_{20}$ series were measured and the inferred x values are close to the nominal x values within the fairly large error bars (Fig. 7.3).

Another way to estimate the concentration of gadolinium in the grown crystals is based on the analysis of the high temperature magnetic susceptibility data, which can be expressed as:

$$\chi_{Gd_xY_{1-x}Fe_2Zn_{20}} = \chi_{Gd^{3+}} + \chi_{YFe_2Zn_{20}} \tag{7.1}$$

Experimentally, $\chi_{Gd^{3+}}$ obeys the Curie-Weiss law above 150 K (Fig. 7.4a), from which the paramagnetic Curie temperature θ_C and Curie constants C can be extracted. The value of x

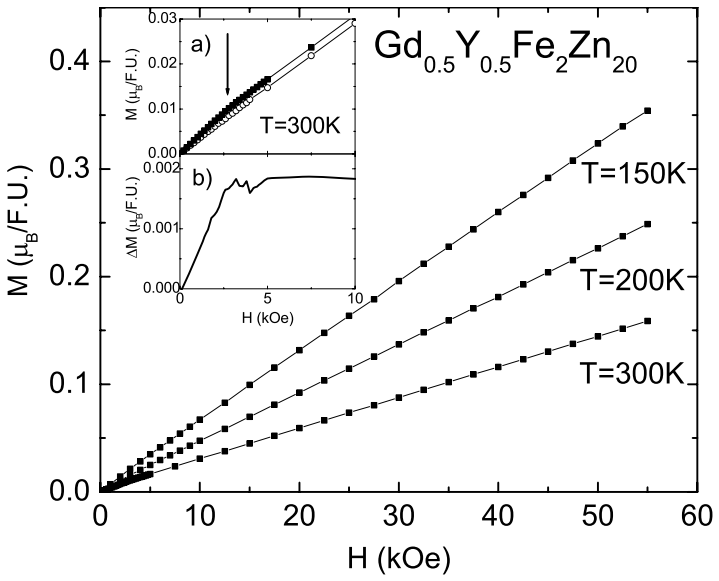

Figure 7.2 Magnetization M with respect to applied field H for a sample of $Gd_{0.5}Y_{0.5}Fe_2Zn_{20}$ at 150 K, 200 K and 300 K. The solid lines are guides to the eye. Inset a: detailed magnetization of two samples of $Gd_{0.5}Y_{0.5}Fe_2Zn_{20}$ at 300 K. The data set shown as solid squares (same data as in main figure) has slope change feature (indicated by an arrow); while the data set shown as open circles does not. Inset b: the difference of the two data sets reveals the saturation of ferromagnetic impurity above 5 kOe.

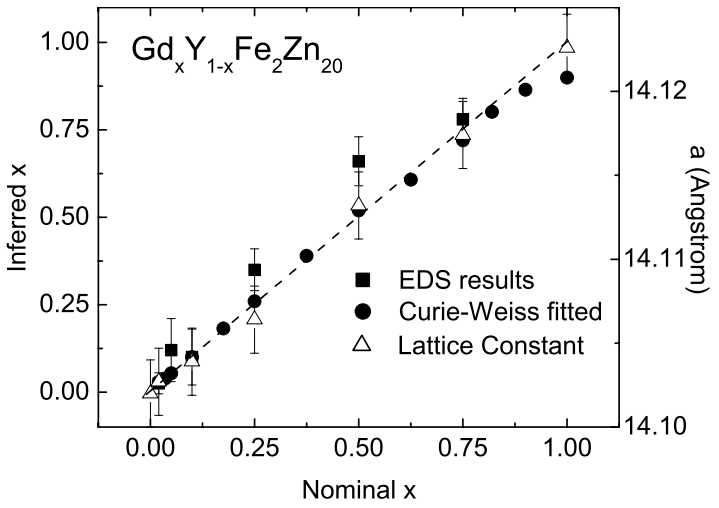

Figure 7.3 Gd concentration inferred from EDS (solid squares with the error bars determined by statistic errors) and high temperature magnetic susceptibility (solid circles). The open triangles represent lattice constants. The dash line is location where inferred x equals nominal x and also represents a linear dependence of the lattice parameter.

can be inferred by fixing the effective moment of Gd^{3+} as 7.94 μ_B. These values of inferred x are also plotted in Fig. 7.3. The agreement between each of these three different methods of determining inferred x and the nominal x value is good and for the rest of this paper nominal values will be used to estimate actual Gd content.

Another aspect of Fig. 7.4 that is noteworthy is that all $\chi_{Gd^{3+}}$ data sets deviate from their high temperature Curie-Weiss behaviors as the system approaches the magnetic ordering temperature. Since high fields can shift and broaden the features associated with ferromagnetism, at lower temperatures a field of 1 kOe was used (Fig. 7.4b). Whereas this deviation cannot be associated with the formation of superparamagnetic clusters above T_C (this would cause a slope change toward the horizontal rather than toward the vertical), it can be understood in terms of an increasing coupling between the Gd^{3+} local moments associated with the strongly temperature dependent, polarizable electronic background of the YFe_2Zn_{20} matrix (see discussion below).

Figure 7.5 shows the temperature dependent magnetization in an external field $H = 1000$ Oe for the whole range of x values. Ferromagnetic ordering can be clearly seen below 90 K for $x = 1$. The ordering temperature decreases monotonically as x decreases, although the exact values of T_C can not be unambiguously inferred from these plots. For $x \leq 0.035$, it becomes difficult to determine whether the compounds manifest ferromagnetism above the base temperature (1.85 K) based on the $M(T)$ curves alone. Even at 1000 Oe, for $x \geq 0.25$, the low-temperature magnetization is just slightly below the Hund's ground state value 7 μ_B/Gd at the base temperature (Fig. 7.5a). For $x < 0.25$ the low temperature, $H = 1000$ Oe, magnetization decreases with decreasing x (Fig. 7.5b).

Field-dependent magnetization measurements were made for each sample at base temperature (Fig. 7.6). For compounds with $x \geq 0.035$, the magnetization rapidly saturates as the magnetic field increases, consistent with a ferromagnetic ground state at 1.85 K. For $x \leq 0.01$, the $M(H)$ curves vary more smoothly with H and are more consistent with a paramagnetic state at 1.85 K. The $x = 0.02$ data are more ambiguous and require a still more detailed analysis.

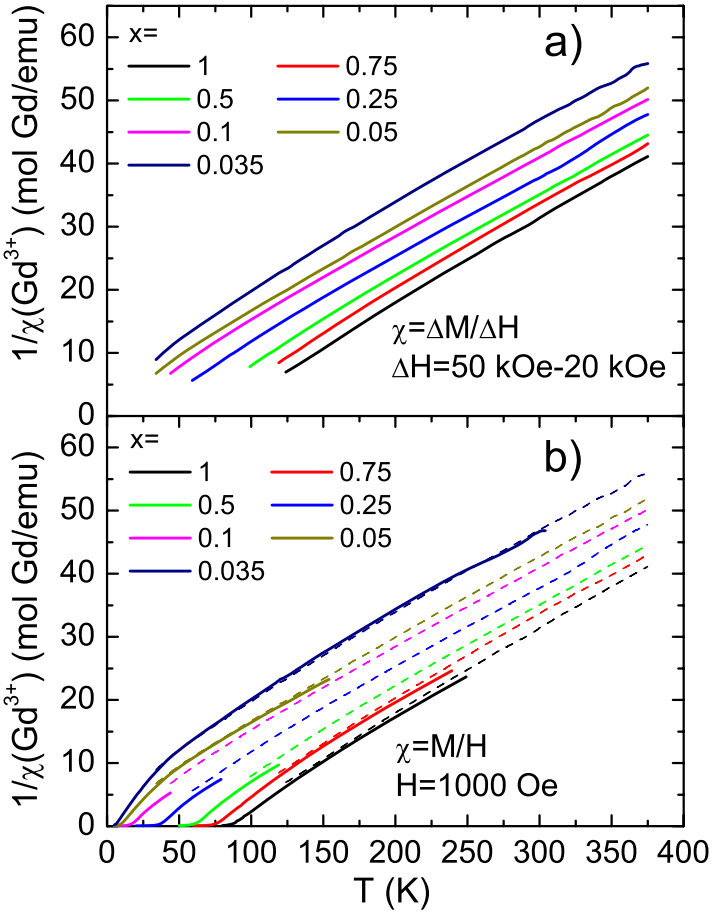

Figure 7.4 $1/\chi_{Gd^{3+}}$ vesus temperature for representative members of the $Gd_xY_{1-x}Fe_2Zn_{20}$ series. Note: data is normalized to mole Gd using x inferred from high-temperature data. From right-down to left-up: $x = 1, 0.75, 0.5, 0.25, 0.1, 0.05$ and 0.035. (a): obtained under high magnetic field. (b) Solid lines: obtained under 1 kOe applied field; dash lines: under high magnetic field.

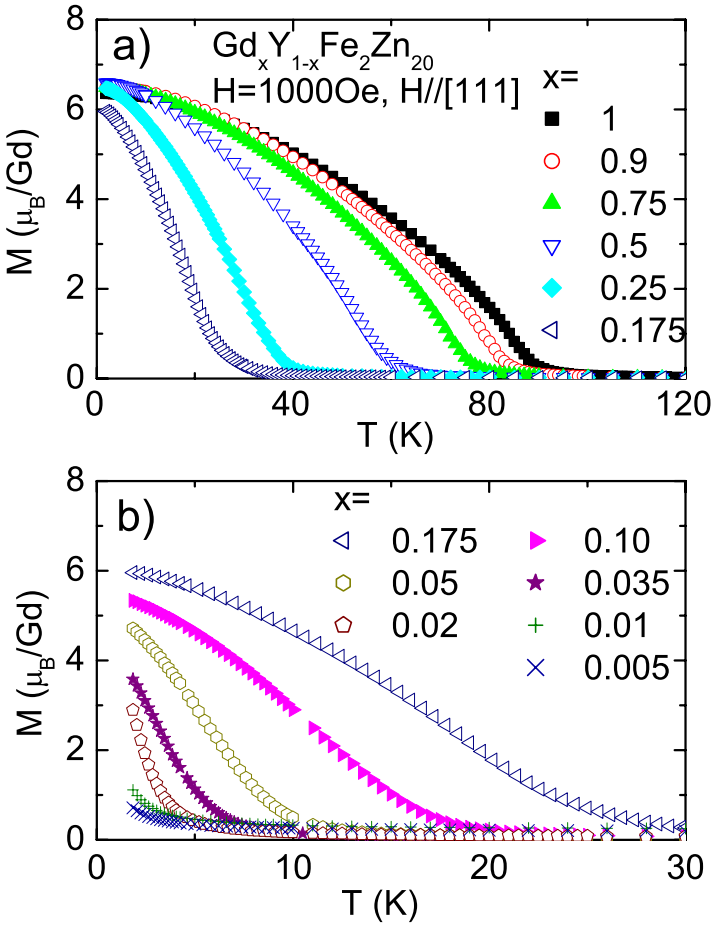

Figure 7.5 Temperature dependent magnetization of $Gd_xY_{1-x}Fe_2Zn_{20}$, H = 1000 Oe, for (a) $1.0 \geq x \geq 0.175$, (b) $x \leq 0.175$.

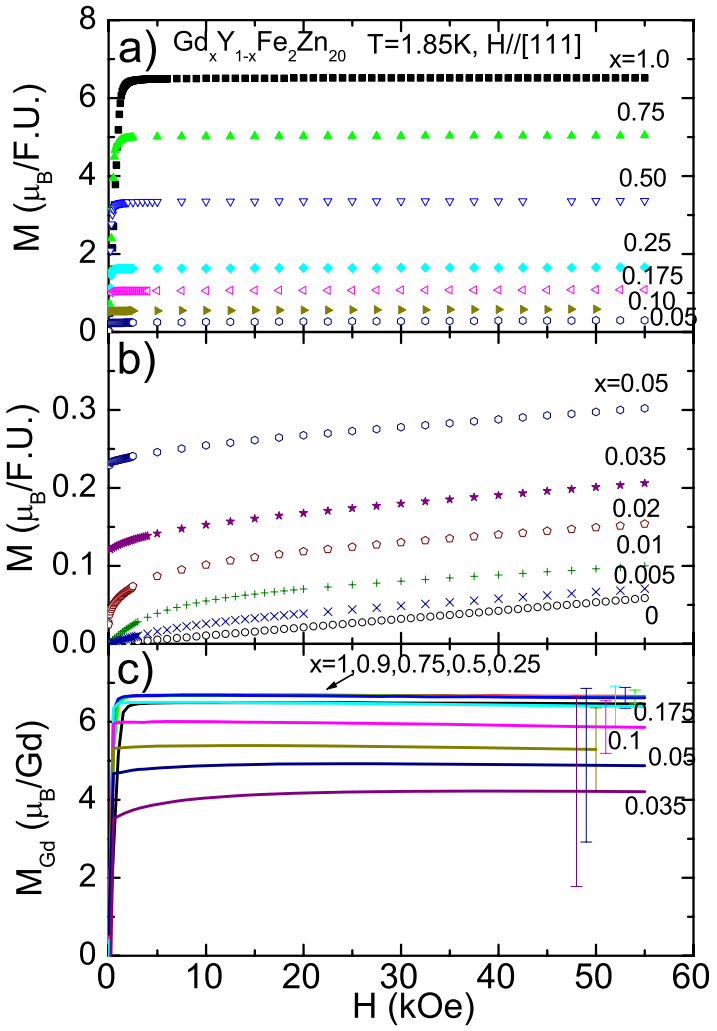

Figure 7.6 (a) and (b) Field dependent magnetization of $Gd_xY_{1-x}Fe_2Zn_{20}$ at 1.85 K. (c) Field dependent magnetization of $Gd_xY_{1-x}Fe_2Zn_{20}$ at 1.85 K, normalized to Gd^{3+} content (see text).The error bars were estimated by allowing for a ± 0.02 variation of x.

For $H > 10$ kOe the $M(H)$ data for $x \leq 0.05$ vary approximately linearly with H and have slopes comparable to that of YFe_2Zn_{20}, $x = 0$ (Fig. 7.6b). For all x values the magnetization can be thought of as a combination of the magnetization of Gd^{3+} ions and the highly polarizable background. In order to extract the magnetization of the Gd^{3+} ions, a background of $M_{YFe_2Zn_{20}}$ was subtracted from the $M(H)$ data. The $M_{Gd}(H)$ data are plotted in Fig. 7.6c normalized to the nominal x values. For $x \geq 0.25$ the saturated magnetization is essentially constant with a value slightly less than 7 μ_B/Gd. For $x < 0.25$ there is an apparent decrease in the saturated magnetization with decreasing x, but it should noted that the error bars, coming from the estimated ± 0.02 uncertainty of x, increase with decreasing x. These increasing error bars make it unclear whether the saturated moment of the Gd impurities is constant or decreasing in the small x limit.

A fuller analysis of $M(H)$ data, particularly the analysis of magnetization isotherms known as Arrott plots [Arrott, 1957], at a set of temperatures near T_C has been found to be a useful, and for $x < 0.25$ samples was actually the best method to determine T_C. The method is based on the mean field theory, in which M^2 is linear in I/M with zero intercept at the critical temperature T_C, where I is the internal field, equal to the difference between the external, applied field H and the demagnetizing field D_m. For an ellipsoid of $Gd_xY_{1-x}Fe_2Zn_{20}$, the demagnetizing field equals [Chikazumi and Graham, 1997]:

$$D_m = 4\pi M D \frac{N}{a^3 N_A} = 0.061 M D \tag{7.2}$$

where M is the magnetization (emu/mol), D is a geometric factor that can range from 1 to 0, N is the number of formula units per cell ($N = 8$), a is the cubic lattice constant (~ 14Å), and N_A is Avogadro number. Thus I/M, in units of kOe/μ_B, is:

$$\frac{I}{M} = \frac{H - D_m}{M} = \frac{H}{M} - 0.34D. \tag{7.3}$$

Using H, instead of I, in Arrott plots will shift the data along H/M axis in the positive direction by $0.34D$. That would experimentally introduce an error in the value of T_C for a flat shaped sample ($D \sim 1$) of $GdFe_2Zn_{20}$. Nevertheless, even in this extreme case, this error drops as x decreases due to reduction of the samples' magnetization as Gd^{3+} is diluted out

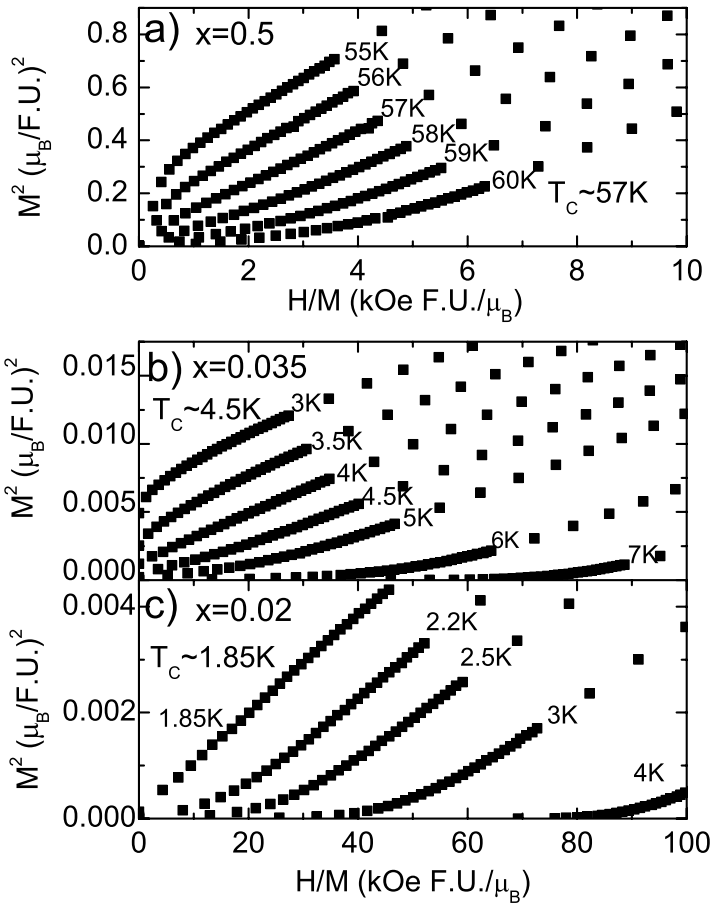

Figure 7.7 Arrott plots for representative members of the $Gd_xY_{1-x}Fe_2Zn_{20}$ series: x = (a) 0.5, (b) 0.035 and (c) 0.02.

(notice the different scale of the M axis for $x < 0.05$ in Fig. 7.7). Due to these concerns, rod-like-shape samples were measured along their long axis for the magnetization isotherms for samples with $x > 0.5$. This shape ensures D is minimized. Figures 7.7a and b show $T_C = 57 \pm 0.5$ K for $x = 0.5$ and $T_C = 4.5 \pm 0.5$ K for $x = 0.035$ respectively. For $x = 0.02$, Fig. 7.7c shows $T_C = 1.85$ K, a result that helps explain the difficulty experienced in determining the base-temperature magnetic state based on the $M(T)$ and $M(H)$ data discussed above. The T_C values determined for the Arrott plot analysis for all x are shown below in Fig. 7.13.

The temperature dependent electric resistivity data, $\rho(T)$ (measured in zero applied magnetic field), of the $Gd_xY_{1-x}Fe_2Zn_{20}$ compounds are shown, for representative x values, in Fig.

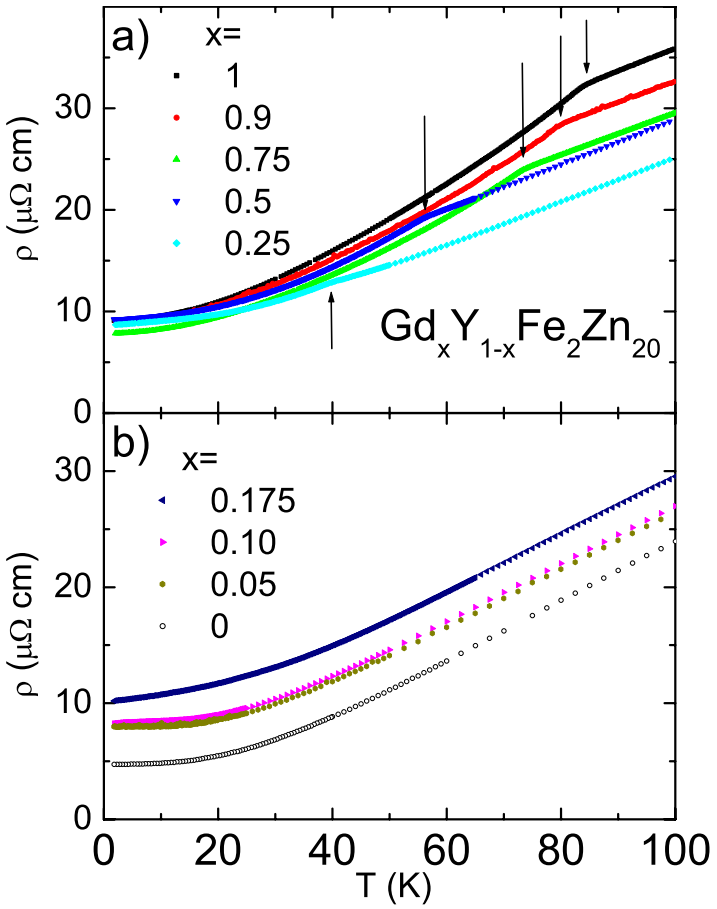

Figure 7.8 Zero-field resistivity for current along the [110] direction. The arrows represent T_C determined from Arrott plot analyses.

7.8. For $x \geq 0.25$, $\rho(T)$ curves show a kink at T_C due to the loss of spin disorder scattering below this temperature. In contrast, for $x \leq 0.175$, no clear kink can be detected. T_C values deduced from the maximum of $d\rho/dT$ for $x \geq 0.25$ (not shown here) are compatible with the values obtained from the Arrott plots (see Fig. 7.13b below).

Further information can be extracted from the $Gd_xY_{1-x}Fe_2Zn_{20}$ $\rho(T)$ data by assuming that the total resistivity of the compound can be written as:

$$\rho(T) = \rho_0 + \rho_{ph}(T) + \rho_{mag}(T), \tag{7.4}$$

where ρ_0 is a temperature independent, impurity scattering term, ρ_{ph} is the scattering from phonons and ρ_{mag} is the scattering associated with the interaction between conduction elec-

trons and magnetic degrees of freedom. In this series of pseudo-ternary compounds, the high temperature ($T \gg T_{\rm C}$) phonon contribution, ρ_{ph}, should be essentially invariant (due to the very dilute nature of the R ions). The magnetic contribution to the resistivity, ρ_{mag}, will be the combination of contributions from conduction electron scattered by (i) the $4f$ local moments and (ii) the spin fluctuations of $3d$ electrons (from Fe sites), both of which should saturate in the high temperature limit. Based on the analysis above, the high temperature resistivity of the whole series should be similar (modulo an offset) and manifest similar slopes due to the electron-phonon scattering. This is indeed the case: the data show linearity of $\rho(T)$ above 250 K with the slopes differing by less than 8%; less than the estimated dimension error (10%) of these bar-like-shape samples.

The magnetic and disorder contributions to the resistivity can be estimated by (i) removing the geometric error by normalizing the high temperature slope of all $\rho(T)$ plots to that of YFe_2Zn_{20} and then (ii) subtracting the $\rho_Y(T)$ data from the ρ normalized data.

The normalized ρ is given as:

$$\rho_{{\rm Gd}_x normalized} = \rho_{{\rm Gd}_x} \cdot \frac{\frac{d\rho_{{\rm Gd}_x}}{dT} \mid_{275{\rm K}}}{\frac{d\rho_{\rm Y}}{dT} \mid_{275{\rm K}}} \tag{7.5}$$

and

$$\Delta\rho = \rho_{{\rm Gd}_x normalized} - \rho_{\rm Y}. \tag{7.6}$$

The resulting $\Delta\rho$ will not only show the conduction electron scattering from the $4f$ local moments, but will also include scattering associated with the interaction between the $4f$ local moment and $3d$ electrons, especially near $T_{\rm C}$. The temperature dependent $\Delta\rho$ curves for the ${\rm Gd}_x{\rm Y}_{1-x}{\rm Fe}_2{\rm Zn}_{20}$ compounds are presented in Fig. 7.9. A pronounced upward cusp is centered about $T_{\rm C}$ for $x \geq 0.25$. For $x < 0.25$ the loss of the spin disorder feature becomes harder (or even impossible) to resolve, but the enhanced scattering above $T_{\rm C}$ persists. The decrease of $\Delta\rho$ with T below $T_{\rm C}$ is a common in ferromagnetic systems and can be explained as the result of a loss of spin disorder scattering of conduction electrons. On the other hand, the behavior of $\Delta\rho$ above $T_{\rm C}$ must come from a different conduction electron scattering process. A similar feature in $\Delta\rho$ is found in RFe_2Zn_{20} (R = Tb - Er) for $T > T_{\rm C}$ (shown in Chapter 8), but not in the isostructural $GdCo_2Zn_{20}$, which orders antiferromagnetically at a much lower temperature.

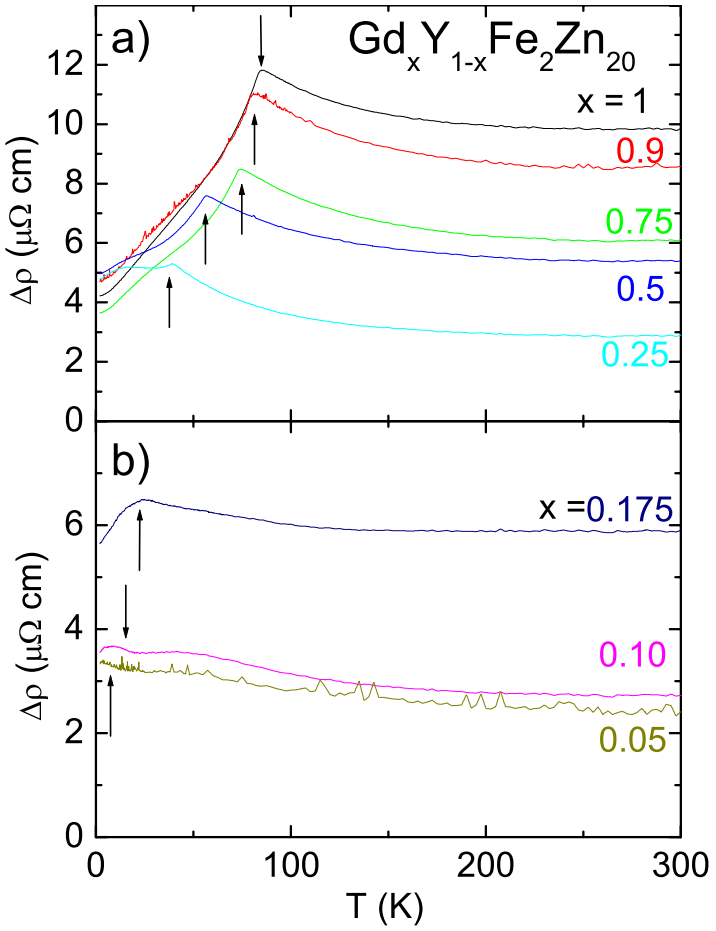

Figure 7.9 Temperature variation of $\Delta\rho$ (see text). The arrows represent T_C determined from Arrott plot analysis of magnetization measurements.

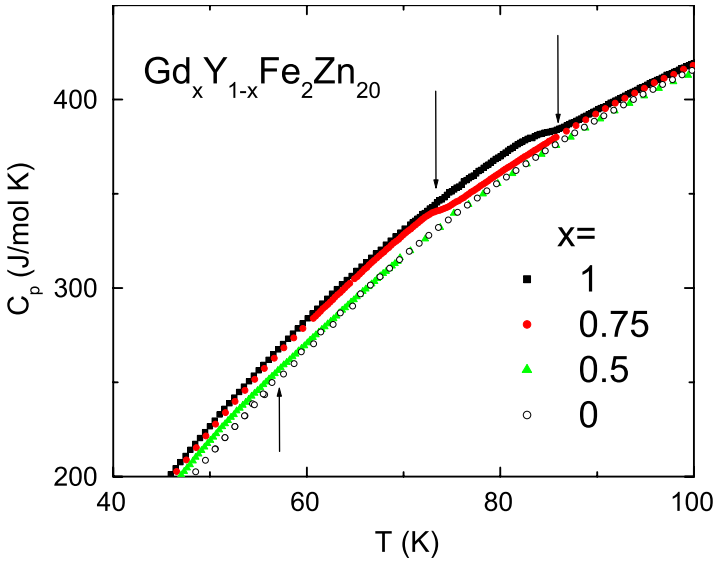

Figure 7.10 Temperature variation of specific heat C_p of the $Gd_xY_{1-x}Fe_2Zn_{20}$ series for $x = 1$, 0.75, 0.5 and 0. The arrows represent T_C determined from Arrott plot analyses.

The specific heat of the $Gd_xY_{1-x}Fe_2Zn_{20}$ compounds (Fig. 7.10) can be thought of as the sum of the contributions from electronic, vibrational and magnetic degrees of freedom. To remove the vibrational and electronic parts (at least approximately), the specific heat of YFe_2Zn_{20} and $LuFe_2Zn_{20}$ were used to estimate the background. The assumption that YFe_2Zn_{20} and $LuFe_2Zn_{20}$ closely approximate the non-magnetic C_p of the $Gd_xY_{1-x}Fe_2Zn_{20}$ series is supported by the fact that the difference between the measured C_p of YFe_2Zn_{20}, $LuFe_2Zn_{20}$ and $Gd_xY_{1-x}Fe_2Zn_{20}$ in the temperature region 20 K higher than T_C is on the order of one percent. Since $LuFe_2Zn_{20}$ has a molar mass closer to that of $GdFe_2Zn_{20}$ than YFe_2Zn_{20}, the combination of $(x)C_{LuFe_2Zn_{20}} + (1-x)C_{YFe_2Zn_{20}}$ is thought to be even closer to the non-magnetic background of $C_{Gd_xY_{1-x}Fe_2Zn_{20}}$.

Figure 7.11 shows

$$\begin{aligned} \Delta C &= C_{Gd_xY_{1-x}Fe_2Zn_{20}} \\ &- (x)C_{LuFe_2Zn_{20}} - (1-x)C_{YFe_2Zn_{20}} \end{aligned} \tag{7.7}$$

for $x \geq 0.175$ (a) and $x \leq 0.175$ (b), where the arrows indicate the T_C values determined from

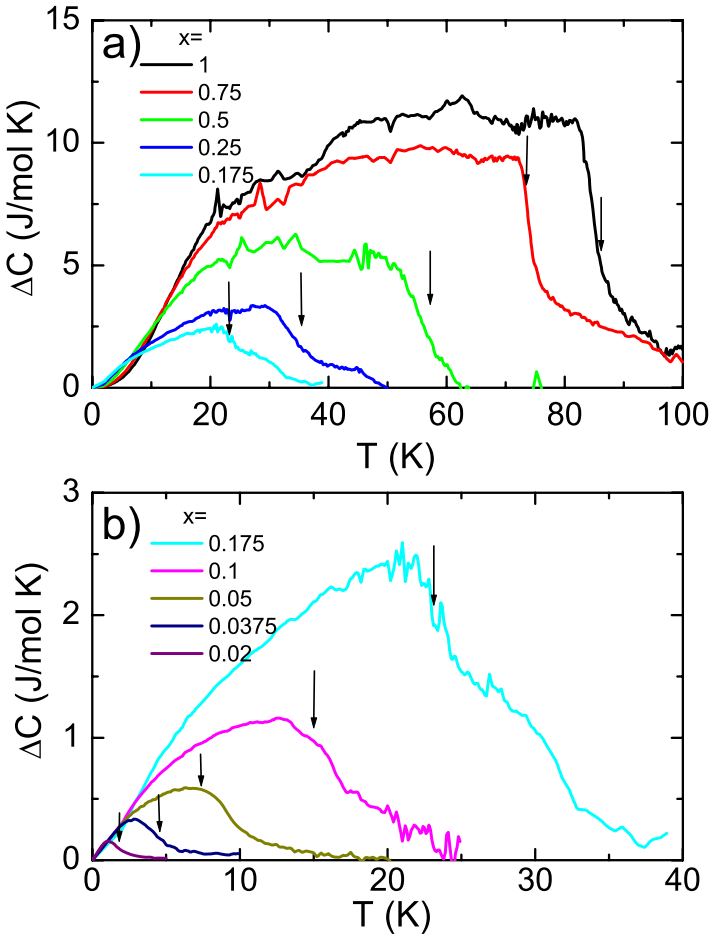

Figure 7.11 Temperature variation of ΔC. (a): From right to left, $x = 1, 0.75, 0.5, 0.25$ and 0.175. (b): From right to left, $x = 0.175, 0.1, 0.05, 0.0375$ and 0.02. The arrows represent T_C values determined from the Arrott analysis of magnetization measurements.

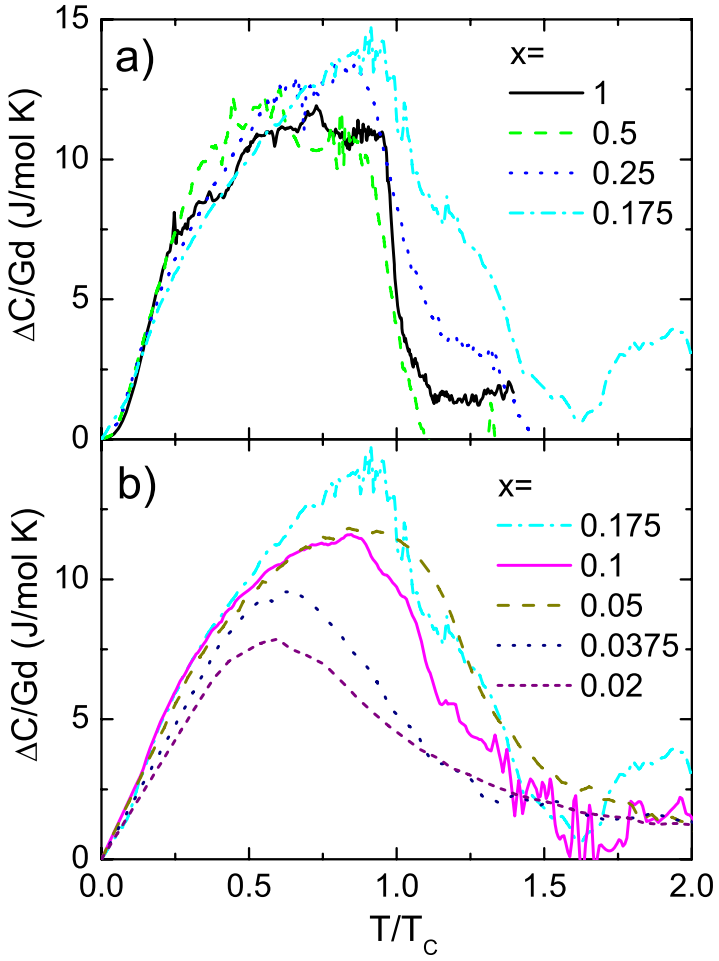

Figure 7.12 $\Delta C/x$ versus T/T_{C} for representative x values.

the Arrott plot analyses. The magnetic ordering manifests itself as a broad feature in ΔC with T_{C} occurring at, or near, the position at the maximum slope. Figure 7.12 shows that this feature persists, relatively unchanged in shape, down to $x = 0.1$. For values of $x < 0.1$ the feature broadens further, but is still distinct. This shape of ΔC is not unusual for Gd-base intermetallics with ferromagnetic order; for example, a similar feature is seen in GdPtIn [$T_{\mathrm{C}} \sim 68$ K see[Morosan et al., 2005]]. It should be noted that this ΔC feature is distinct from that associated with a spin-glass freezing: the maxima all occur at or below T_{C}, whereas a spin glass manifests a broad peak above the freezing temperature [Binder and Young, 1986].

The x dependence of the paramagnetic Curie temperature (θ_C), ferromagnetic ordering

temperature ($T_{\rm C}$) and saturated moments per Gd (μ_{Sat}) for each x are shown in Fig. 7.13a, b and c respectively. The values of the magnetic entropy, estimated by $S_M = \int \frac{\Delta C}{T} dT$, are shown in Fig. 7.13d. Both θ_C and $T_{\rm C}$ decrease monotonically with x. At first glance, the negative values of θ_C for $x < 0.25$ are unexpected and seem to be in contradiction with the existence of ferromagnetic ground state. However, these are high-temperature, θ_C values and ignore the increasingly strong, polarizable background associated with the near Stoner limit conduction electrons at intermediate temperatures. Furthermore, as shown in Fig. 7.4b, this low temperature effect becomes even more pronounced for small x. Although, as discussed earlier, the uncertainty of x makes the x-variation of μ_{Sat} ambiguous for small x, even the large x members of the $Gd_xY_{1-x}Fe_2Zn_{20}$ series manifest reduced saturated moments. This is attributed to the induced moment on the $3d$ electrons, which is anti-parallel to the Gd moment. The magnetic entropy, shown in Fig. 7.13d, associated with the ordered state is equal to, or slightly larger than, the magnetic entropy associated with the Hund's ground state of $Gd^{3+}(\mathbf{S} = 7/2)$. This fact indicates that the main part of the magnetic specific heat of the series of $Gd_xY_{1-x}Fe_2Zn_{20}$ is the contribution from the magnetic degrees of freedom of the Gd^{3+} local moments. The contribution to the magnetic specific heat from the itinerant electrons probably exists, but is, at most, comparable with the measurement uncertainty.

7.4 Analysis and Discussion

For rare earth bearing intermetallics, the interaction between $4f$ local moments is primarily mediated by means of polarization of the conduction electrons. Regardless of the details of the mechanism involved in this interaction [Ruderman and Kittel, 1954, Kasuya, 1956, Yosida, 1957, Campbell, 1972], we propose that the $3d$ electrons from Fe sites act as important mediators of the Gd-Gd interaction in $Gd_xY_{1-x}Fe_2Zn_{20}$ system. In YFe_2Zn_{20}, the interaction between $3d$ electrons is not sufficient to split the conduction band but is large enough to make the compound exhibit strongly enhanced paramagnetism. When Y^{3+} ions are fully replaced by Gd^{3+} ions, these $3d$ electrons are polarized by the Gd^{3+} local moments. The interaction between $3d$ electrons assists in stabilizing the splitting of the conduction electron band and

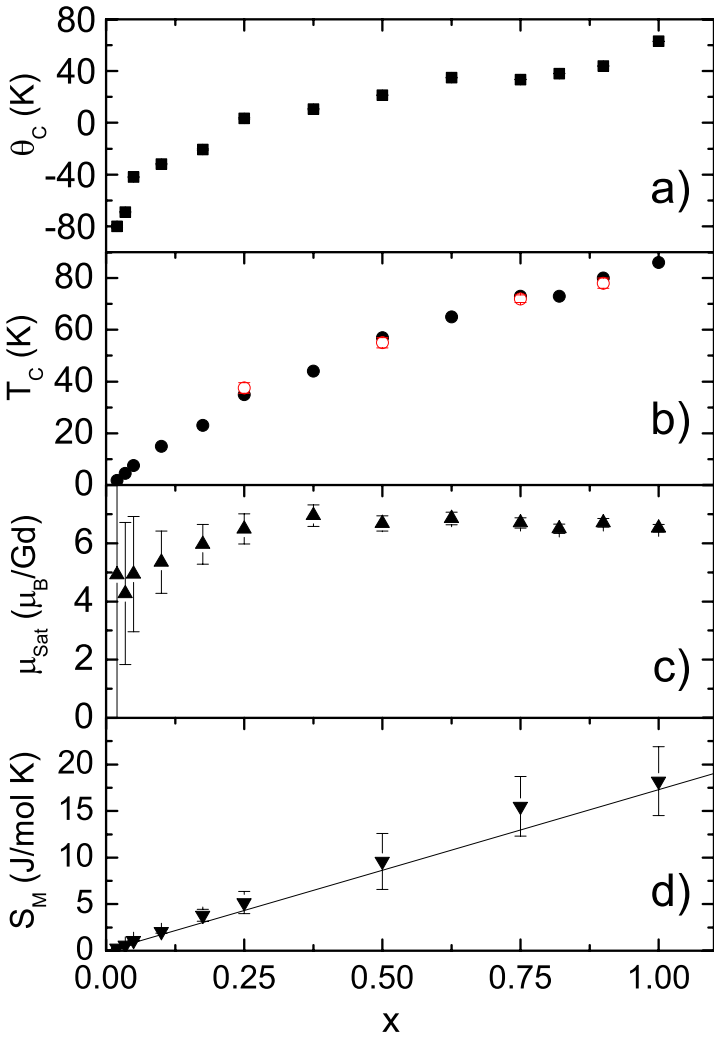

Figure 7.13 (a) Paramagnetic Curie temperature, θ_C, (b) ferromagnetic ordering temperature, T_C [The values of T_C in (b) were determined by Arrott plot analyses (black circle) and the resistivity measurements(open circle).], (c) saturated moment per Gd, μ_{Sat} and (d) magnetic entropy, S_M with respect to x for the $Gd_xY_{1-x}Fe_2Zn_{20}$ series. The solid line in (d) represents $S_M = xRln8$ (R is gas constant), the magnetic entropy of Gd^{3+} Hund's ground state. The error bars are estimated as 1 % of the total entropy, $S = \int_0^{T_C} \frac{C_p}{T} dT$.

enhances the magnetic interaction between Gd^{3+} local moments, resulting in the remarkably high, ferromagnetic transition temperature for $GdFe_2Zn_{20}$. This physical picture is consistent with the results of the band structure calculation which predicts the Fe induced moment as $0.34\mu_B$/Fe in the ground state of $GdFe_2Zn_{20}$ (shown in Chapter 6).

In order to perform further analysis on the magnetic properties of $Gd_xY_{1-x}Fe_2Zn_{20}$, a comparison with the binary RCo_2 (R = rare earth) intermetallics is useful. YCo_2 and $LuCo_2$ show nearly ferromagnetic behavior while the series of compounds, (Gd-Tm)Co_2, with $4f$ local moments manifest a ferromagnetic ground state [Duc and Brommer, 1999, Duc and Goto, 1999]. In addition to these magnetic similarities, the resemblance between the crystal structure of RT_2Zn_{20} and the so-called C-15 Laves structure of RCo_2 [Gschneidner and Pecharsky, 2006] is noticeable: both rare earth and transition metal ions occupy same unique, single crystallographic sites in the same space group: $Fd\bar{3}m$. The unit cell of the RT_2Zn_{20} compounds can be thought of as an expansion of the C-15 Laves phase unit cell via the addition of a large number(160) of Zn ions.

Well-studied for several decades, the series of (Gd-Tm)Co_2 has been treated as an example of $4f$ local moments embedded in a nearly ferromagnetic host: YCo_2 or $LuCo_2$. The so-called *s-d* model has been employed by Bloch and Lemaire [Bloch and Lemaire, 1970] and Bloch et. al. [Bloch et al., 1975] to explain their magnetic properties. This model was first introduced by Takahashi and Shimizu [Takahashi and Shimizu, 1965] to understand the magnetic properties of alloys of the nearly ferromagnetic transition metal, Pd, with dilute Fe or Co local moment impurities. In this model, the polarization effect of the local moments on the itinerant electrons is considered in terms of a molecular field. Motivated by the similarity of the magnetic properties and the crystal structure of RFe_2Zn_{20} and RCo_2, we applied the *s-d* model to the $Gd_xY_{1-x}Fe_2Zn_{20}$ series.

This model considers one magnetic system consisting of two types of spins: one local moment, and the other one giving rise to an exchange-enhanced, paramagnetic susceptibility. [Bloch and Lemaire, 1970] For $Gd_xY_{1-x}Fe_2Zn_{20}$ system, under an applied field H, for $T > T_C$,

the magnetization of the Gd local moments and the conduction electrons are:

$$M_{\mathrm{Gd}} = (xC_{\mathrm{Gd}}/T)(H + n_{\mathrm{Gd}-e}M_e) \tag{7.8}$$

$$M_e = \chi_{e,0}(H + n_{e-e}M_e + n_{\mathrm{Gd}-e}M_{\mathrm{Gd}}) \tag{7.9}$$

where C_{Gd} is the Curie constant of the Gd^{3+} local moments; $n_{\mathrm{Gd}-e}$, n_{e-e} are molecular-field coefficient representing the interaction between itinerant electrons and Gd^{3+} local moments, and itinerant electrons with themselves, respectively; $\chi_{e,0}$ is the paramagnetic susceptibility without exchange enhancement. The total magnetization of $Gd_xY_{1-x}Fe_2Zn_{20}$ is the sum of M_{Gd} and M_e. It should be noted that when $x = 0$, the total susceptibility reduces to the exchange-enhanced susceptibility:

$$\chi_e = \chi_{\mathrm{YFe_2Zn_{20}}} = \frac{M_e}{H} = \frac{\chi_{e,0}}{1 - n_{e-e}\chi_{e,0}} \tag{7.10}$$

which is simply the Stoner enhanced susceptibility of YFe_2Zn_{20}.

Assuming that the electronic structure of the conduction band and the position of the Fermi level in the paramagnetic state are the same across the whole $Gd_xY_{1-x}Fe_2Zn_{20}$ series, from Eqs. 7.8–7.10, one gets the total susceptibility of $Gd_xY_{1-x}Fe_2Zn_{20}$

$$\begin{aligned} \chi_{\mathrm{Gd}_x\mathrm{Y}_{1-x}\mathrm{Fe_2Zn_{20}}} &= \frac{xC_{\mathrm{Gd}}}{T - \chi_{\mathrm{YFe_2Zn_{20}}} n^2_{\mathrm{Gd}-e} xC_{\mathrm{Gd}}} \\ &+ \frac{\chi_{\mathrm{YFe_2Zn_{20}}}(T + 2n_{\mathrm{Gd}-e}xC_{\mathrm{Gd}})}{T - \chi_{\mathrm{YFe_2Zn_{20}}} n^2_{\mathrm{Gd}-e} xC_{\mathrm{Gd}}}. \end{aligned} \tag{7.11}$$

If one assumes the coupling between the pure spin moment ($\mathbf{S} = 7/2$) of the Gd^{3+} and the conduction electron spin σ ($\sigma = 1/2$) to be a Heisenberg exchange interaction, $2J_0\vec{S}\cdot\vec{\sigma}$, where J_0 is the exchange parameter, then the molecular field coefficient can be written as:

$$n_{Gd-e} = -J_0/(2\mu_B^2 N) \tag{7.12}$$

where N is the number of rare earth ions per volume.

The $Gd_xY_{1-x}Fe_2Zn_{20}$ system will become ferromagnetic when $\chi_{\mathrm{Gd}_x\mathrm{Y}_{1-x}\mathrm{Fe_2Zn_{20}}}$ diverges. Thus,

$$\begin{aligned} T_{\mathrm{C}} &= \chi_{\mathrm{YFe_2Zn_{20}}}(T_{\mathrm{C}}) n^2_{\mathrm{Gd}-e} xC_{\mathrm{Gd}} \\ &= x\chi_{\mathrm{YFe_2Zn_{20}}}(T_{\mathrm{C}}) \frac{J_0^2 S(S+1)}{3k_B N \mu_B^2} \end{aligned} \tag{7.13}$$

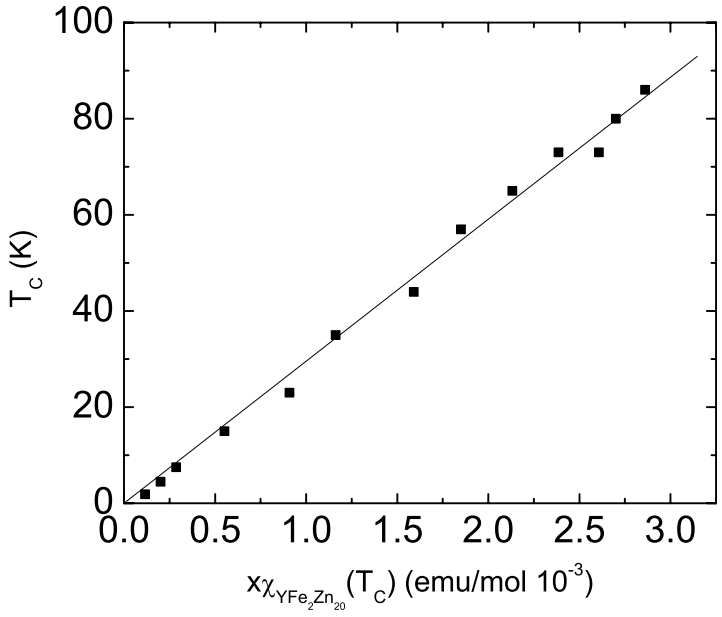

Figure 7.14 $T_{\rm C}$ of $Gd_xY_{1-x}Fe_2Zn_{20}$ versus $x\chi_{YFe_2Zn_{20}}(T_{\rm C})$. The solid line is linear fit through the origin point (associated with no detected $T_{\rm C}$ for YFe_2Zn_{20}).

where k_B is the Boltzmann constant.

Equation 7.13 reveals that $T_{\rm C}$ depends on the product of x and $\chi_{YFe_2Zn_{20}}(T_{\rm C})$, rather than just x. This is consistent with Fig. 7.13b showing a nonlinear dependence of $T_{\rm C}$ on x. Figure 7.14 shows that the values of $T_{\rm C}$ depend linearly on the product $x\chi_{YFe_2Zn_{20}}(T_{\rm C})$ across the whole series. From Fig. 7.14 the slope equals $2.955 \pm 0.0037 \times 10^4$ K mol/emu and thus J_0 can be extracted as 3.96 ± 0.05 meV.

In addition to the magnetic ordering, this model can also explain the curious temperature dependence of the $1/\chi$ versus T data for the $Gd_xY_{1-x}Fe_2Zn_{20}$ series. Setting $J_0 = 3.96$ meV, one obtains the temperature dependent, total susceptibility of $Gd_xY_{1-x}Fe_2Zn_{20}$. The results of $1/\chi_{Gd_xY_{1-x}Fe_2Zn_{20}}$ for representative x values are shown as the solid lines in Fig. 7.15; whereas the dotted lines and the dash lines present the experimental results under 1 kOe and high magnetic field, representatively. These calculated results qualitatively reproduce the experimental, temperature dependent susceptibilities, especially their deviation from the

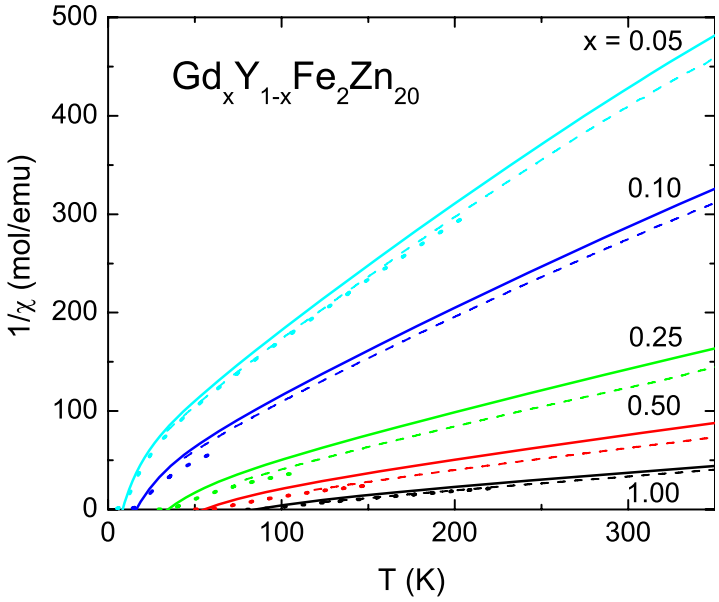

Figure 7.15 $1/\chi$ of $Gd_xY_{1-x}Fe_2Zn_{20}$ versus T for representative x values. Dotted lines: measured under 1 kOe applied filed; dash lines: obtained under high magnetic field; solid lines: calculated results. (See text)

Curie-Weiss law close to T_C. It should be noted that the χ data in Fig. 7.15 is the full χ without any subtraction of "non-magnetic" background. In this sense Fig. 7.15, and the *s-d* model, appear to treat the magnetization data more fully than the simple assumption behind Eqn. 7.1.

In addition to the thermodynamic properties discussed above, the feature in $\Delta\rho$ above T_C (Fig. 7.9) is also worth discussing further. The upward-pointing cusp at T_C of $\Delta\rho(T)$ is associated with the sign change of $d\Delta\rho/dT$, from negative to positive as the temperature decreases. This feature is absent from simple models of $\rho(T)$ [Craig et al., 1967, Fisher and Langer, 1968], based on the models assuming a single lattice of magnetic ions and a single band of conduction electrons. This theoretical model is over-simplified for $Gd_xY_{1-x}Fe_2Zn_{20}$, a strongly correlated electron system. Similar unusual upward cusps in $\Delta\rho(T)$ at T_C were found in the electric transport measurements of RCo_2 [Gratz et al., 1995]. They were explained by invoking an increasing, non-uniform fluctuating f-d exchange interaction, which provides an

increase of spin fluctuations of the $3d$-electron subsystem as the temperature approaches T_C in the paramagnetic state, which in turn leads to increased conduction electron scattering. Recently, a resistivity peak in $\rho(T)$ at T_C has been found in diluted magnetic semiconductors [Matsukura et al., 1998], and motivated further theoretical study beyond the simple model [Timm et al., 2005]. On the other hand, as "good" metals, the $Gd_xY_{1-x}Fe_2Zn_{20}$ system (and indeed the other RFe_2Zn_{20} compounds. See Chapter 8) present another, clear example of this interesting behavior.

7.5 Summary

We presented a set of data including magnetization, electrical transport and specific heat, measured on flux-grown single crystals of $Gd_xY_{1-x}Fe_2Zn_{20}$. We found that the series order ferromagnetically above 1.85 K for $x \geq 0.02$. The variation of T_C with respect to x, as well as the curious temperature dependent magnetic susceptibilities, are well explained by a modification of the s-d model based on molecular field approximation.

CHAPTER 8. Magnetic properties of RFe_2Zn_{20} and RCo_2Zn_{20}(R = Y, Nd, Sm, Gd - Lu)

8.1 Introduction

Intermetallic compounds consisting of rare earth and transition metals, as well as metalloids, have versatile magnetic properties. [Szytula and Leciejewicz, 1994] Compounds with itinerant d electrons are of particular interest when they are in the vicinity the Stoner transition: such systems, characterized as nearly or weakly ferromagnet, manifest strongly correlated electronic properties.[Moriya, 1985] On the other hand, heavy rare earth ions manifest magnetic versatility associated with the $4f$ electrons: null magnetism (Y^{3+} or Lu^{3+}), pure spin, local moment magnetism (Gd^{3+}), potentially anisotropic, crystal electric field (CEF) split, local moment magnetism (Tb^{3+} - Tm^{3+}), and more exotic magnetism: Yb ions may hybridize with conduction electrons and manifest so-called heavy fermion behavior. Needless to say, series of examples that combine these interesting versatilities have attracted the attention of physicists. For example, the binary RCo_2 (R = rare earth) compounds, with the nearly ferromagnetic (FM) end members YCo_2 and $LuCo_2$, and the local moment, FM members (R = Pr, Nd, Gd - Tm), have been studied for more than 35 years[Franse and Radwanski, 1993, Duc and Goto, 1999, Duc and Brommer, 1999].

As shown in Chapter 5 - 7, the series of intermetallic compounds RT_2Zn_{20} have varied magnetic behavior. YFe_2Zn_{20} and $LuFe_2Zn_{20}$ are archetypical examples of nearly ferromagnetic Fermi liquid (NFFL) with Stoner enhancement factors of $Z = 0.88$ (where $\chi_{T=0} = \chi_{Pauli}/(1-Z)$). By embedding large, Heisenberg type moments associated with Gd^{3+} ions in this highly polarizable medium, $GdFe_2Zn_{20}$ manifests highly enhanced FM order. On the other hand, $GdCo_2Zn_{20}$ manifests ordinary, low temperature, antiferromagnetic (AFM) order,

correspondent to the 'normal metal' behavior of the conduction electron host, YCo_2Zn_{20}. In addition to these interesting, 3*d* electron and local moment properties, six related YbT_2Zn_{20} compounds (T = Fe, Co, Ru, Rh, Os and Ir) show heavy fermion ground states, associated with different Kondo temperatures (T_K) and Yb ion degeneracies. (will be shown in Chapter 9).

Given the similarities and differences between the RFe_2Zn_{20} and RCo_2Zn_{20} (R = Gd, Y, Lu) series, it becomes important to study all of the R = Y, Gd - Lu members in detail. A comparative study of the RFe_2Zn_{20} and RCo_2Zn_{20} series will help to further understand the magnetic interaction between the local moments by means of the strongly polarizable medium, particularly with the crystal electronic field (CEF) effect associated with non-zero orbital angular momentum. Furthermore, given the very similar CN-16 Frank-Kasper polyhedron for R ions, as well as the less than 2% difference of lattice constants for the whole RT_2Zn_{20} families, the study of the CEF effect on these local moment members will also help in the understanding of the varied heavy fermion states of YbT_2Zn_{20}, which were thought to be due to the competition between temperature scales associated with the CEF splitting and the Kondo effect. (will be shown in chapter 9).

In this chapter, we present the results of magnetization, heat capacity and resistivity measurements on RFe_2Zn_{20} and RCo_2Zn_{20} (R = Y, Nd, Sm, Gd - Lu) compounds. Compare with the 'normal metal' behaviors for YCo_2Zn_{20} and $LuCo_2Zn_{20}$, YFe_2Zn_{20} and $LuFe_2Zn_{20}$, manifest clear, NFFL behaviors associated with the spin fluctuation of the itinerant electrons. For the RFe_2Zn_{20} compounds (R = Gd - Tm), the well-defined local moment members all manifest enhanced FM ordering with T_C values that roughly scale with the de Gennes factor. Their anomalous, temperature dependent susceptibility and resistivity can be explained as the result of local moments embedded in a NFFL. In contrast, for the RCo_2Zn_{20} series, only Gd and Tb members manifest AFM ordering above 2 K, and the magnetic properties for R = Dy - Tm clearly manifest features associated with single ion CEF effects on the R ions in the cubic symmetry coordination. For the R = Tb - Tm members in the Co series, the CEF parameters can be determined from the magnetic anisotropy and the specific heat data, and are roughly

consistent with calculation results using the point charge model. For the Fe series, the R = Tb - Tm members show moderate magnetic anisotropy in their ordered state, mainly due to the CEF effect on the R ions, which is consistent with the magnetic anisotropy for the Co members. These results, as well as the analysis on the heat capacity and resistivity, indicate that the FM state emerges from the fully degenerate Hund's rule ground state for RFe_2Zn_{20} (R = Gd - Ho), whereas $ErFe_2Zn_{20}$ and $TmFe_2Zn_{20}$ manifests CEF splitting above their Curie temperatures.

8.2 Experiments and Results

We start characterizing the compounds with the non-magnetic rare earth ions of the series: Y(Lu)Fe_2Zn_{20} and Y(Lu)Co_2Zn_{20}. Without any $4f$ electronic magnetism, these compounds manifest the itinerant electronic magnetic properties associated with the conduction electron background of each series. Next, we will introduce the two series of compounds with well-defined $4f$ local moments: R = Gd - Tm. We will introduce the magnetization and specific heat data for the Co series at first. Then an overview of the magnetic properties for the Fe series will be presented next. After that, the magnetization, specific heat and resistivity data will be presented for each Fe member separately. Finally, similar data for the R = Yb heavy fermion compounds, $YbFe_2Zn_{20}$ and $YbCo_2Zn_{20}$ will be presented.

8.2.1 Y(Lu)Fe_2Zn_{20} and Y(Lu)Co_2Zn_{20}

Temperature dependent magnetization data (divided by the applied field) for Y(Lu)Fe_2Zn_{20} and Y(Lu)Co_2Zn_{20} are shown in Fig. 8.1 (a). The Fe members manifest similar, strongly enhanced, temperature-dependent paramagnetic signals, whereas the Co members manifest temperature-independent Pauli paramagnetic signals. Low temperature features for the two Fe compounds are shown in the inset of Fig. 8.1. In the applied field of 10 kOe, the magnetization signals of both Fe members show a faint maximum below 10 K, whereas the high magnetic field (50 kOe) suppresses the lowest temperature M/H values, as well as the maximum. In our experience on the measurements of different batch of samples, these low temperature features

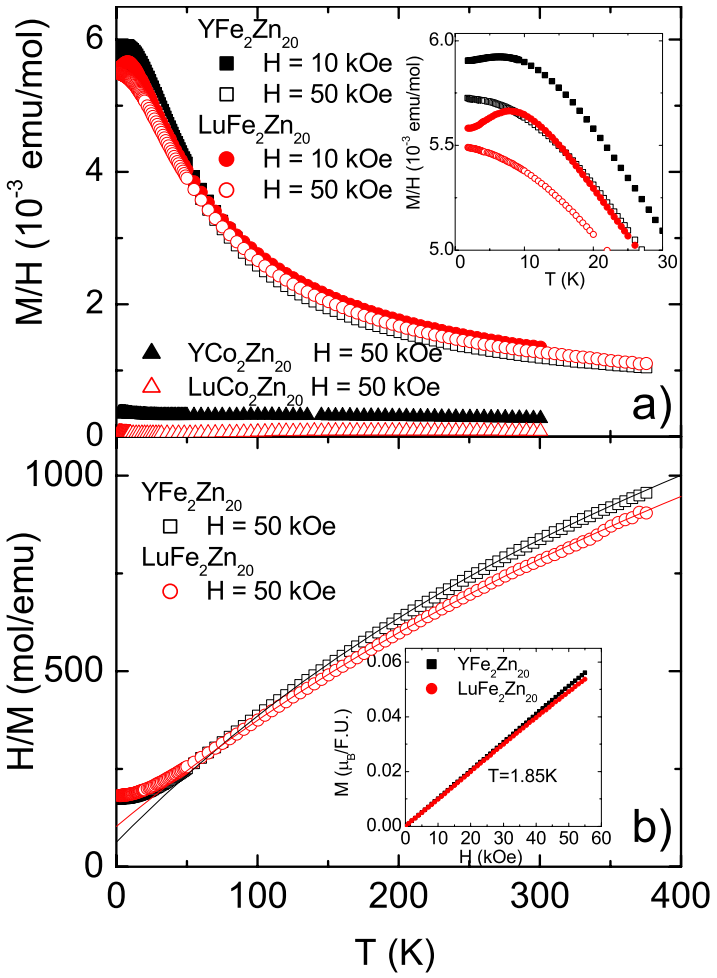

Figure 8.1 (a) Temperature dependent magnetization M divided by the applied field H for YFe_2Zn_{20} and $LuFe_2Zn_{20}$ as well as their Co analogues for $H = 10$ kOe and 50 kOe. Inset: a blow-up plot at low temperature. (b) H/M for YFe_2Zn_{20} and $LuFe_2Zn_{20}$. The solid lines present the modified Curie-Weiss $[\chi(T) = C/(T - \theta_C) + \chi_0]$ fit for the data above 100 K. Inset: field dependent magnetization at 1.85 K.

are moderately sample-dependent (different samples may show 20% different magnetization signal and 2–3 K difference in the temperature of the maximum, T_{max}). Nevertheless, the maximum of the temperature dependent susceptibility, $\chi(T)$, is a common feature in the NFFLs, such as Pd [Gerhardt et al., 1981], YCo_2 and $LuCo_2$ [Burzo et al., 1993], as well as $TiBe_2$ [Gerhardt et al., 1983], although quantitative calculation of $\chi(T)$ still presents a challenge even for the simplest case of Pd [B Zellermann and Voitländer, 2004, Larson et al., 2004]. The field suppression of the magnetization (and T_{max}) at low temperature is not attributed to the possible existence of a paramagnetic impurity contribution (which would contribute more to the value of M/H at lower temperature and lower field, and therefore suppress the maximum of M/H in lower field), but, as discussed below, to the intrinsic variation of $\chi = dM/dH$ with respect to H at different temperatures.

Figure 8.1 (b) shows that above a characteristic temperature ($T^* \sim 50$ K), the susceptibility of YFe_2Zn_{20} and $LuFe_2Zn_{20}$ can be approximately fitted by a Curie-Weiss (CW) term [$\chi(T) = C/(T-\theta_C)$] plus a temperature-independent term (χ_0). The values of effective moment (μ_{eff}), θ_C and χ_0 are extracted as 1.0 μ_B/Fe, -16 K, 3.8×10^{-4}emu/mol and 1.1 μ_B/Fe, -33 K, 3.4×10^{-4}emu/mol for YFe_2Zn_{20} and $LuFe_2Zn_{20}$, respectively. These values of μ_{eff} are significantly larger than the estimated induced moment of Fe site in the FM ground state of $GdFe_2Zn_{20}$, $\sim 0.35\mu_B$/Fe. Such apparent CW-like behavior was also observed in other NFFL systems. [Shimizu, 1961, Burzo et al., 1993] In the context of the spin fluctuation model [Moriya, 1985], itinerant electronic systems can manifest CW-like behavior with a Curie constant related to the local amplitude of the spin fluctuation. The magnetization data at the base temperature (1.85 K) show nearly linear dependent with the applied field [Inset in Fig. 8.1 (b)], which is distinct from the Brillouin function type of magnetization curves associated with local moments.

In order to better understand the variation of the maximum in temperature dependent M/H data for YFe_2Zn_{20} and $LuFe_2Zn_{20}$, $M(T)$ and $M(H)$ measurements were performed on $LuFe_2Zn_{20}$ for varied applied field and temperature respectively. Figure 8.2 shows that the magnetic field suppresses the values of M/H, as well as the maximum of M/H, which disappears when $H \geq 20$ kOe. Figure 8.3 shows $\Delta M/\Delta H$ at varied temperature, which values were

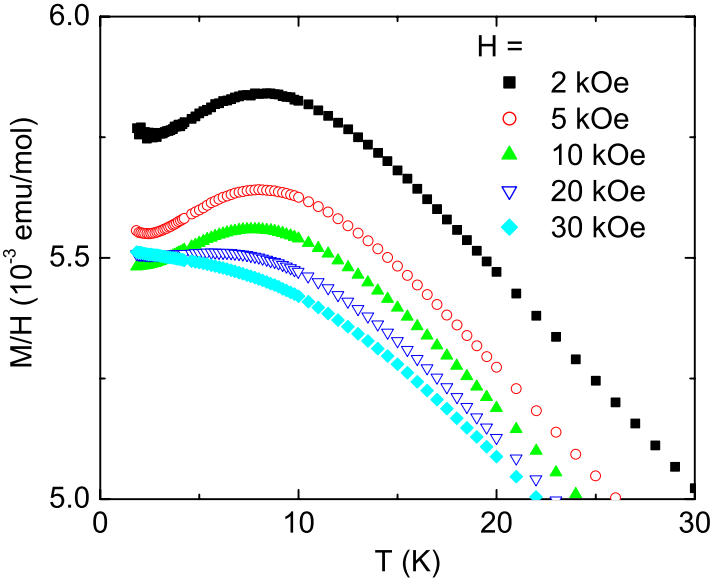

Figure 8.2 Temperature dependent M/H for $LuFe_2Zn_{20}$. From right to left: $H = 2$ kOe, 5 kOe, 10 kOe, 20 kOe and 30 kOe.

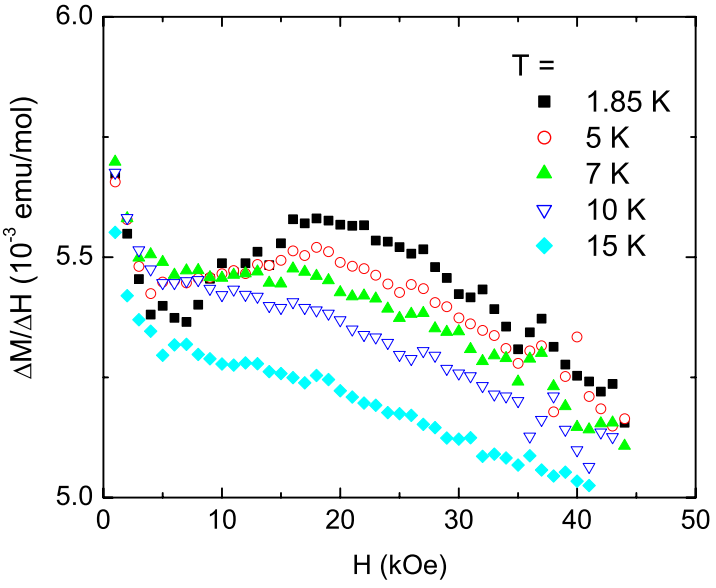

Figure 8.3 $\Delta M/\Delta H$ for $LuFe_2Zn_{20}$ at varied temperature.

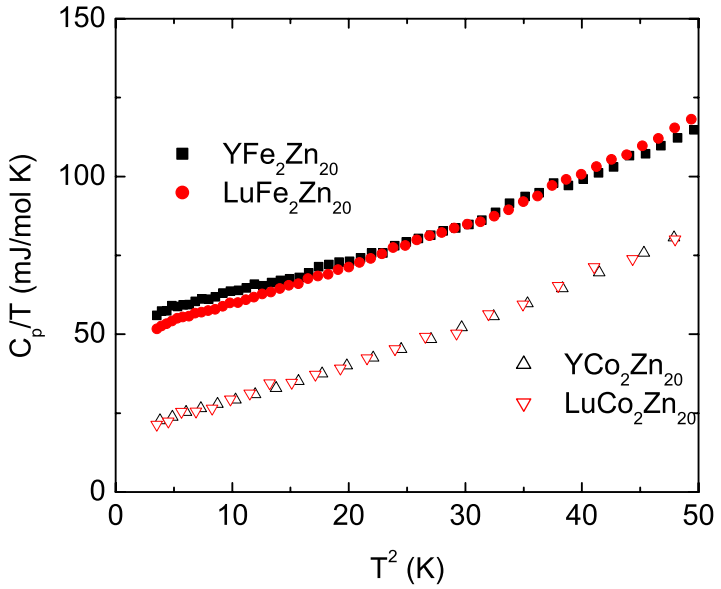

Figure 8.4 Low temperature specific heat data of YFe_2Zn_{20} and $LuFe_2Zn_{20}$ (plotted as C_p/T versus T^2), as well as the Co analogues.

extracted from the $M(H)$ data. For $T \geq 10$ K, the values of $\Delta M/\Delta H$ monotonically decrease with increase H, whereas a local maximum appears around 20 kOe in the data sets as $T \leq 7$ K. This critical temperature (~ 7 K) is close to the T_{max}; the maximum of $\Delta M/\Delta H$ (20 kOe) is also close to the suppression field determined by Fig. 8.2. This curious, field dependent, susceptibility at varied temperature is reminiscent to the one of $TiBe_2$, albeit the amplitude of local maximum in $\Delta M/\Delta H$ is much smaller. [Gerhardt et al., 1983, Acker et al., 1981] In the case of $TiBe_2$, the reason of anomalous field-dependent magnetization is still not clear. [Jeong et al., 2006]

Figure 8.4 presents the low temperature specific heat data for YFe_2Zn_{20} and $LuFe_2Zn_{20}$, as well, as for the Co analogues, plotted as C_p/T versus T^2. All four compounds manifest clear Fermi liquid behavior ($C_p = \gamma T + \beta T^3$). The similar β values (represented as the slopes of the data sets in the plot, ~ 1.2mJ/molK^4) indicate the similar Debye temperatures for these 4 compounds (~ 340 K), consistent with their similar molar mass, similar composition and similar lattice parameters. On the other hand, the over 2.5 times larger values of electronic

specific heat (γ) of the Fe members indicate a larger density of states at Fermi level [$N(E_f)$], compared to the Co analogues (consistent with the band structure calculation results). The values of the electronic specific heat can be employed to estimate the Stoner enhancement factor, Z, in the context of the Stoner theory: that is, the static susceptibility is enhanced by $\frac{1}{1-Z}$, whereas the electronic specific heat is not. The estimated Z values of YFe_2Zn_{20} and $LuFe_2Zn_{20}$ are 0.88, 0.89, respectively, comparable with the estimated values of the canonical NFFL systems: Pd: 0.83, and YCo_2: 0.75.[†]

The temperature dependent electrical resistivity data for YFe_2Zn_{20} and $LuFe_2Zn_{20}$ are larger than that for the Co analogues over the whole temperature range (Fig. 8.5). This is not unexpected for a NFFL since the spin fluctuations will affect the scattering process of the conduction electrons, which leads to an additional contribution to the resistivity. In order to study the spin fluctuation contribution to the resistivity, the total electrical resistivity $\rho(T)$ is assumed to be:

$$\rho(T) = \rho_0 + \rho_{ph}(T) + \rho_{sf}(T), \tag{8.1}$$

where the first, second and third terms represent residual, phonon and spin fluctuation scattering, respectively. Assuming the phonon scattering contribution, $\rho_{ph}(T)$, is essentially same for the Fe and Co analogues, then, the spin fluctuation scattering contribution, $\rho_{sf}(T)$, can be estimated as:

$$\rho_{sf}(T) = (\rho - \rho_0)_{\mathrm{Y/LuFe_2Zn_{20}}} - (\rho - \rho_0)_{\mathrm{Y/LuCo_2Zn_{20}}}. \tag{8.2}$$

Shown in Fig. 8.5b, $\rho_{sf}(T)$ for these two compounds increase with temperature and is close to a saturated value (10 $\mu\Omega$cm) at 300 K, within the accuracy of the measurements.

The analysis of the low temperature resistivity data reveals a quadratic, standard Fermi liquid, behavior [$\rho(T) = \rho_0 + AT^2$] for all 4 compounds (Fig. 8.6). The A values of the Fe compounds are about 7 times larger than the two Co analogues. This result is consistent with the 2.5 times larger γ values of the Fe compounds, in the context of the Fermi liquid theory, meaning A is proportional to the square of the effective mass of the quasi-particles due to the

[†]The values of γ and χ for YCo_2 are from ref. [Burzo et al., 1993, Ikeda et al., 1984]

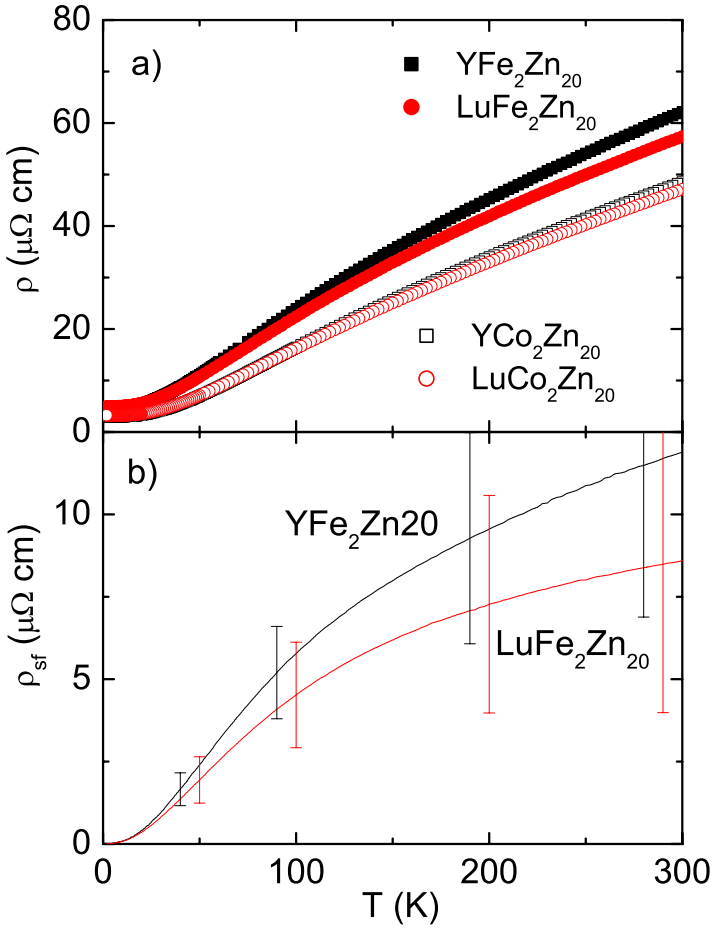

Figure 8.5 (a): Temperature dependent resistivity of YFe_2Zn_{20} and $LuFe_2Zn_{20}$, as well as their Co analogues. (b): estimated spin fluctuation contribution to the resistivity for YFe_2Zn_{20} and $LuFe_2Zn_{20}$. The error bars were estimated as $\pm 10\%$ of the values of the resistivity for YCo_2Zn_{20} and $LuCo_2Zn_{20}$ respectively.

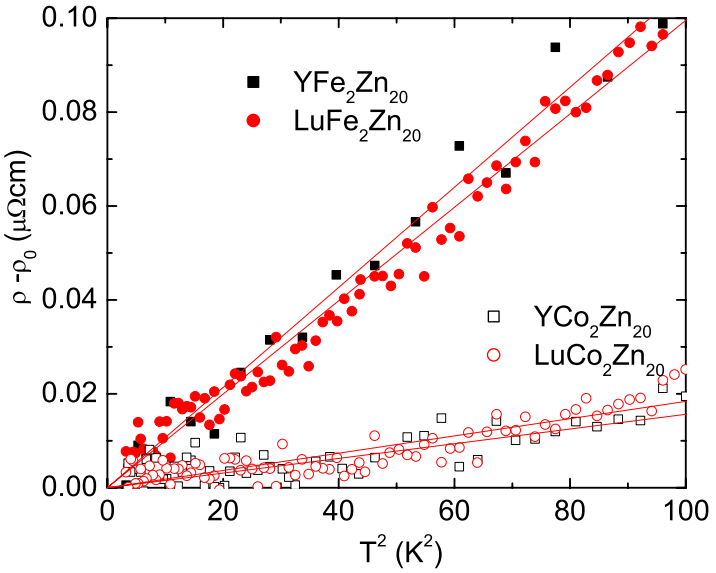

Figure 8.6 ρ versus T^2 for YFe_2Zn_{20} and $LuFe_2Zn_{20}$, as well as their Co analogues. The solid lines present the linear fit of the data sets from 2 K to 9 K.

strong correlation effect, whereas γ is proportional to the effective mass. In the point of view of spin fluctuation theory, nearly FM metals manifest Fermi liquid behaviors at low temperature region with enhanced A values by spin fluctuations [Moriya, 1985].

8.2.2 RCo_2Zn_{20} (R = Nd, Sm, Gd - Tm)

Before to discuss the heavy rare earth compounds (R = Gd - Yb), the results of thermodynamic measurement on $NdCo_2Zn_{20}$ and $SmCo_2Zn_{20}$ are briefly presented. Figure 8.7 shows the temperature magnetization data (divided by the applied field H = 1000 Oe) for $NdCo_2Zn_{20}$ and $SmCo_2Zn_{20}$. Neither of them manifest any sign of magnetic ordering above 2 K. The temperature dependent H/M for $NdCo_2Zn_{20}$ shows a CW behavior $[\chi(T) = C/(T - \theta_C) + \chi_0]$ with $\mu_{eff} = 3.7\mu_B$, $\theta_C = -2.3$ K and $\chi_0 = 6.8 \times 10^{-4}$ emu/mol. The value of the effective moment is close to the theoretical values for the Hund's rule ground state of the $4f$ electrons of Nd^{3+} ion ($3.6\mu_B$). On the other hand, the magnetization of $SmCo_2Zn_{20}$ drop with increase temperature, but in a distinctly non-CW manner. This behavior is not unexpected in Sm

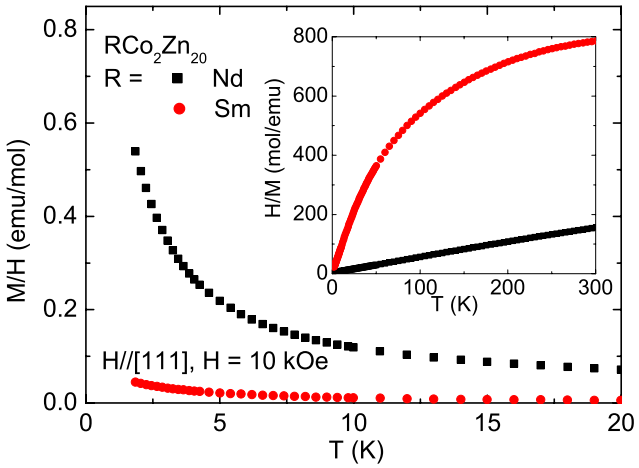

Figure 8.7 Temperature dependent magnetization of RCo_2Zn_{20} (R = Nd and Sm) compounds, divided by applied field $H = 10000$ Oe. Inset: applied field ($H = 10000$ Oe) divided by the magnetizations of RCo_2Zn_{20} (R = Nd and Sm) as a function of temperature.

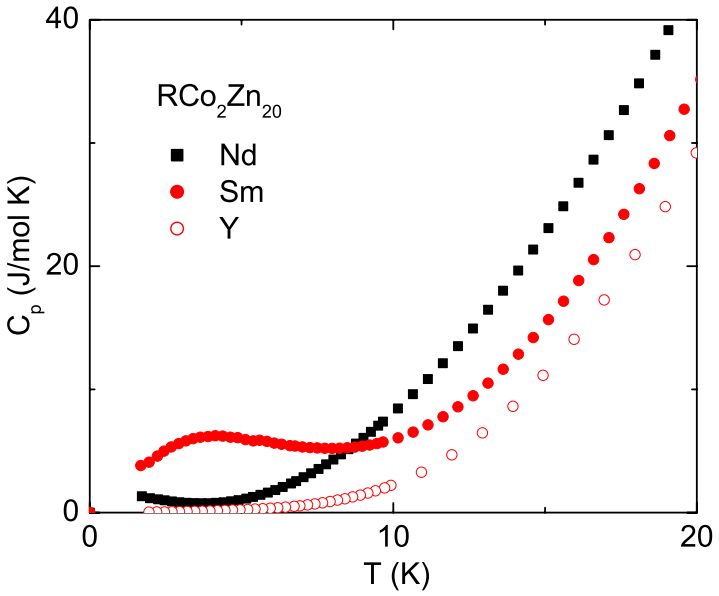

Figure 8.8 Temperature dependent specific heat for RCo_2Zn_{20} (R = Nd, Sm and Y).

containing compounds [Myers et al., 1999], and is most likely due to the thermal population of the first excited Hund's rule multiplet.

Specific heat data for $NdCo_2Zn_{20}$ and $SmCo_2Zn_{20}$ are shown in Fig. 8.8 along with data for YCo_2Zn_{20} for comparison. The low temperature upturn in the $NdCo_2Zn_{20}$ data below 2 K may be due to a lower temperature magnetic ordering or a Schottky anomaly due to the CEF splitting. The specific heat data for $SmCo_2Zn_{20}$ manifest a broad peak around 4 K, which is most likely due to the CEF splitting of the Hund's rule ground state of Sm^{3+}. Both $NdCo_2Zn_{20}$ and $SmCo_2Zn_{20}$ data increase much faster above 10 K, and keep more than 10 J/mol K larger above 25 K (not shown here), compared with the data for the non-magnetic analogue YCo_2Zn_{20}. On the other hand, the calculated results of the CEF splitting for the Hund's rule ground state of Nd^{3+} ion in a point charge model show the splitting energy levels within 25 K (see Table 8.2). This large deference indicates that, at this point, the magnetic part of C_p for $NdCo_2Zn_{20}$ and $SmCo_2Zn_{20}$ cannot be well estimated, since the C_p data of YCo_2Zn_{20} is not a good subtraction background and their Lanthanum analogues is absent.

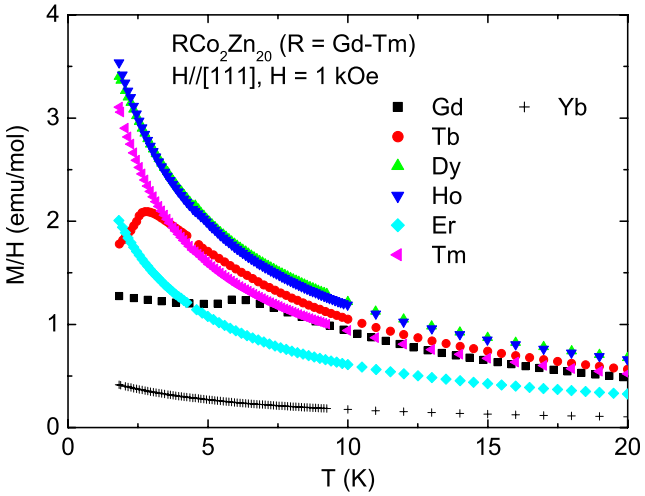

Figure 8.9 Temperature dependent magnetization of RCo_2Zn_{20} (R = Gd - Yb) compounds, divided by applied field $H = 1000$ Oe.

Temperature dependent magnetization data (divided by the applied field $H = 1000$ Oe) for RCo_2Zn_{20} (R = Gd - Yb) are presented in Fig. 8.9. In addition to the previously reported, AFM ordered $GdCo_2Zn_{20}$ with the Neél temperature $T_N = 5.7 \pm 0.1$ K, $TbCo_2Zn_{20}$ also shows AFM ordering with $T_N = 2.5 \pm 0.1$ K, which also clearly manifests itself in the specific heat data (shown below in Fig. 8.11). The rest of the members (R = Dy - Yb) do not show magnetic ordering above 2 K. Due to the relatively low density of state at Fermi level $[N(E_F)]$ for the Y and Lu analogues and large R-R separation, such low temperature magnetic ordering for the $4f$ local moments coupled via the Ruderman-Kitter-Kasaya-Yosida (RKKY) interaction is not unexpected.

Figure 8.10 shows the temperature dependent H/M for R = Gd - Tm and Yb members of the RCo_2Zn_{20} series. All the members, including $YbCo_2Zn_{20}$, manifest CW behavior $[\chi(T) = C/(T - \theta_C) + \chi_0]$ with negligible small χ_0 ($\leq 2 \times 10^{-3}$emu/mol) and the values of μ_{eff} close to the theoretical values for the Hund's ground state of the $4f$ electronic configurations; all the values of θ_C are close to 0, consistent with the low magnetic ordering temperatures (Table 8.1).

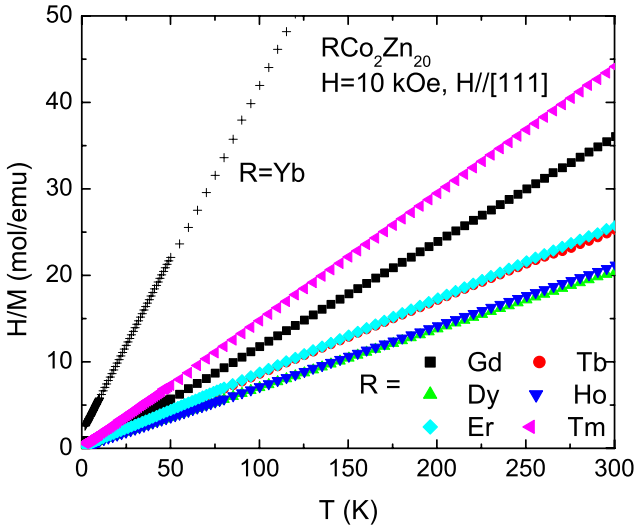

Figure 8.10 Applied field (H = 10000 Oe) divided by the magnetizations of RCo_2Zn_{20} (R = Gd - Yb) as a function of temperature.

Table 8.1 Paramagnetic Curie temperature, θ_C (with ±0.1 K errors) and effective moment, μ_{eff} [from the CW fit of $\chi(T)$ from 50 K to 300 K]; Neél temperature, T_N for RCo_2Zn_{20} compounds (R = Nd, Gd - Yb).

	Nd	Gd	Tb	Dy	Ho	Er	Tm	Yb
θ_C, K	-2.3	3.3	-2.6	-3.7	1.4	-2.1	-0.03	-5.2
μ_{eff}, μ_B	3.7	8.1	9.8	10.9	10.7	9.7	7.4	4.5
T_N, K		5.7	2.5					

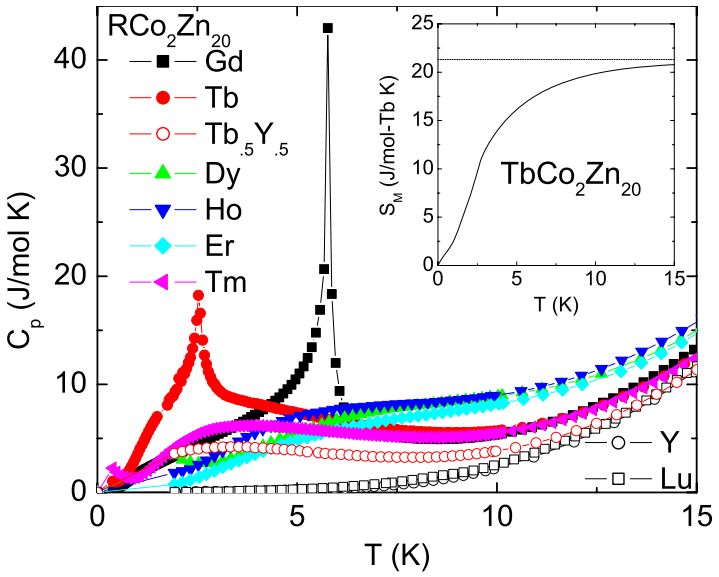

Figure 8.11 Temperature dependent specific heat for RCo_2Zn_{20} (R = Gd - Tm, Y and Lu), as well as $Tb_{0.5}Y_{0.5}Co_2Zn_{20}$. Inset: temperature dependent magnetic entropy for $TbCo_2Zn_{20}$. The dashed line presents the entropy of the full Hund's ground state of Tb^{+3}.

The specific heat data for RCo_2Zn_{20} (R = Gd - Tm , Y and Lu), as well as the pseudo-ternary compound $Tb_{0.5}Y_{0.5}Co_2Zn_{20}$ are presented in Fig. 8.11. In addition to the previously studied $GdCo_2Zn_{20}$, the specific heat data for $TbCo_2Zn_{20}$ manifests a λ-type of anomaly with a peak position at 2.5 K, the AFM ordering temperature. In addition to this peak, the C_p data also show a broad shoulder above 2.5 K, which is due to the CEF splitting above the magnetic ordering temperature. This anomaly, associated with CEF splitting of the $4f$ electronic configuration of Tb^{3+}, manifests itself more clearly in the C_p data for $Tb_{0.5}Y_{0.5}Co_2Zn_{20}$: when T_N is suppressed to well below 2 K, the C_p data show a Schottky anomaly with a peak position $\sim$ 3 K. The magnetic part of entropy for $TbCo_2Zn_{20}$ is shown in the inset to Fig. 8.11. Approximately 50 % of the total magnetic entropy is recovered by T_N, and by 15 K the full $S = R \ln 13$ is recovered (R is gas constant). This is consistent with a very small, total CEF splitting in the these compounds, associated with the highly symmetric environment of the R ions. For the rest of the members, R = Dy - Tm, the specific data show broad, Schottky-type of anomaly below 10 K, as shown in the insets of Fig. 8.14, 8.15, 8.16 and 8.17 (shown below). The increasing tendency for $DyCo_2Zn_{20}$ below 2 K may indicate a magnetic ordering below, whereas the increasing tendency for $TmCo_2Zn_{20}$ below 0.7 K may be due to a magnetic ordering at very low temperature and/or a nuclear Schottky anomaly.

The released, magnetic part of entropy above 2 K (above 0.4 K for the $TmCo_2Zn_{20}$) are shown in Fig. 8.12. For R = Dy - Tm, there is an obvious deficit of magnetic entropy compared with the value associated with fully degenerated Hund's ground state, which indicates unaccounted entropy below 2 K (0.4 K for $TmCo_2Zn_{20}$) associated with low lying CEF levels and magnetic ordering.

In order to better understand the magnetic properties for R = Tb - Tm members, the CEF effect acting on the R ions is evaluated by thermodynamic measurements. The single-ion Hamiltonian for the R^{3+} is assumed to be the sum of the CEF term, an exchange interaction term and an external field term:

$$\mathcal{H} = \mathcal{H}_{CEF} + \mathcal{H}_{exc} + \mathcal{H}_{ext}. \tag{8.3}$$

where $\mathcal{H}_{ext} = g_J \mu_B \vec{J} \cdot \vec{H}$, g_J is Lande factor, $\vec{J}$ is the total angular momentum, and $\vec{H}$ is the

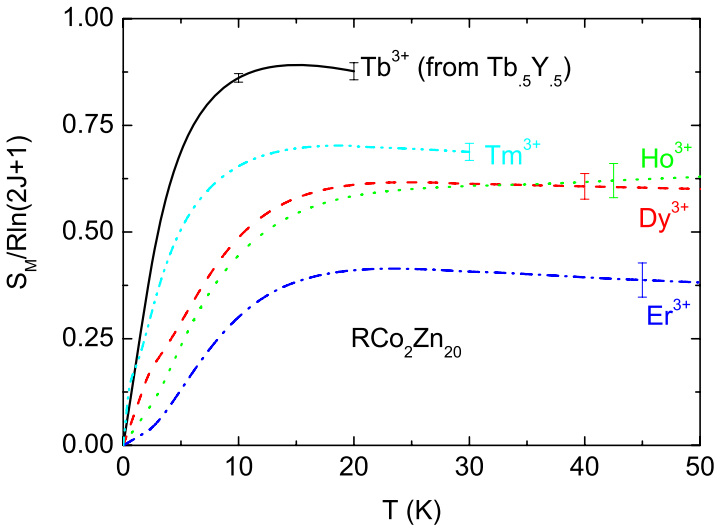

Figure 8.12 Normalized magnetic part of entropy for RCo_2Zn_{20} (R = Dy - Tm) as well as for $Tb_{0.5}Y_{0.5}Co_2Zn_{20}$ (in units of per mole R^{3+}). The error bars were estimated from the ±1 % of the total entropy.

.

external magnetic field.

Since the rare earth ions are located in a cubic point symmetry, the CEF term, H_{CEF}, can be written as:

$$\mathcal{H}_{CEF} = B_4^0(O_4^0 + 5O_4^4) + B_6^0(O_6^0 - 21O_6^4). \tag{8.4}$$

where O_l^m operators are the well-known Stevens operators [Stevens, 1952], and B_4^0 and B_6^0 are CEF parameters [Lea et al., 1962]. If one follows the work of Lea *et al.* [Lea et al., 1962], this expression can be written as:

$$\mathcal{H}_{CEF} = W[\frac{x}{F4}(O_4^0 + 5O_4^4) + \frac{1-|x|}{F6}(O_6^0 - 21O_6^4)]. \tag{8.5}$$

where $F4$ and $F6$ are factors introduced by Lea *et al.* [Lea et al., 1962] and dependent with J, W is the energy scale, and x represents the relative importance of the 4th and 6th order terms.

Noticing that the possible magnetic ordering temperatures are below 2 K for RCo_2Zn_{20} (R = Dy - Tm), as well as for $Tb_{0.5}Y_{0.5}Co_2Zn_{20}$, the exchange interaction term will be approximated

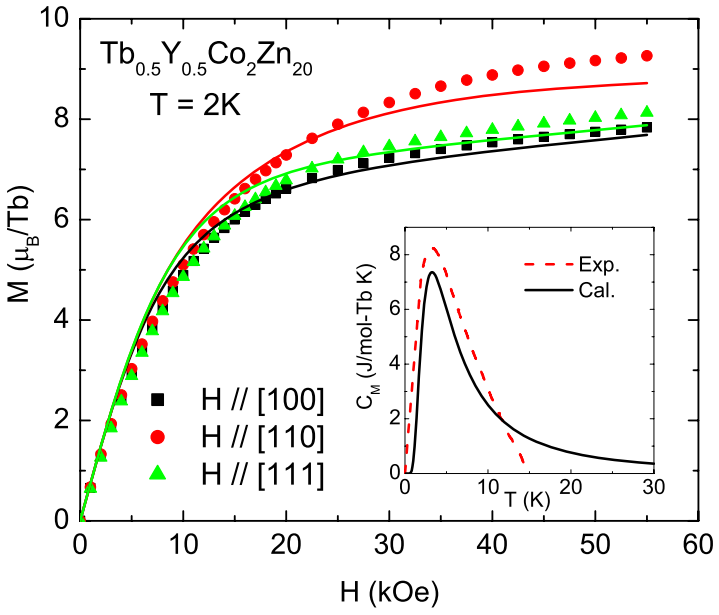

Figure 8.13 Field dependent magnetization for $Tb_{0.5}Y_{0.5}Co_2Zn_{20}$ along three principle axes. The solid lines present the fitting results. Inset: magnetic part of specific heat. The solid and dashed line present the experimental and calculated result respectively.

as zero, an approximation that will be better for R = Tm than for R = Dy. Thus, the CEF parameters for different R ions were determined by fitting the magnetization at 2 K and the temperature dependent specific heat data.

Figure 8.13–8.17 show the CEF fitting results of the magnetization at 2 K and the magnetic part of specific heat with the single ion Hamiltonian (ignoring the interaction term) for $Tb_{0.5}Y_{0.5}Co_2Zn_{20}$ and RCo_2Zn_{20} (R = Dy - Tm). The specific heat data for all members are less than the one of YCo_2Zn_{20} at high temperature range, which is likely due to the errors associated with resolving the difference between the sample's total C_p and the relatively large nonmagnetic contribution. Therefore, the fittings of C_p were performed below 20 K. For R = Dy - Tm, the experimental magnetization data were slightly less than the calculated results. Such phenomena, more significant for R = Dy and Ho, are most likely due to the still relevant AFM-type of interaction between the local moments. As shown in table 8.2, the inferred W and x values for all 5 compounds are clustered in a narrow range: $|W| < 0.1$, $|x| < 0.25$.

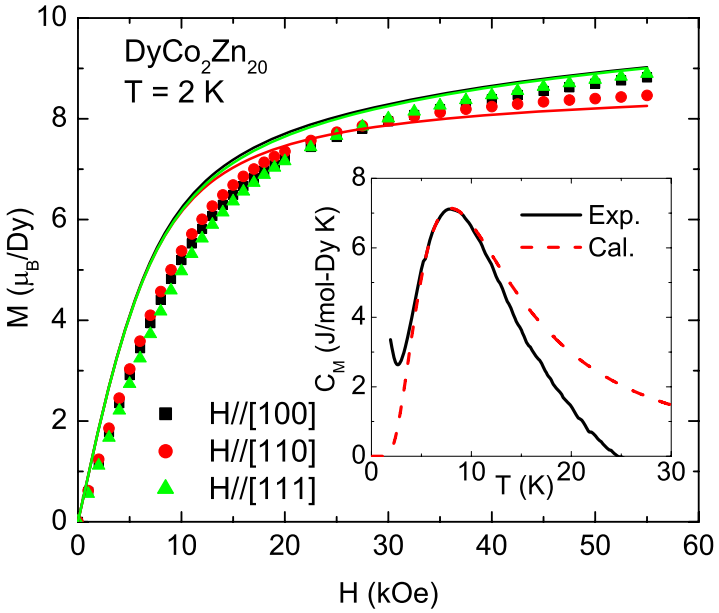

Figure 8.14 Field dependent magnetization for $DyCo_2Zn_{20}$ along three principle axes. The solid lines present the fitting results. Inset: magnetic part of specific heat. The solid and dashed line present the experimental and calculated result respectively.

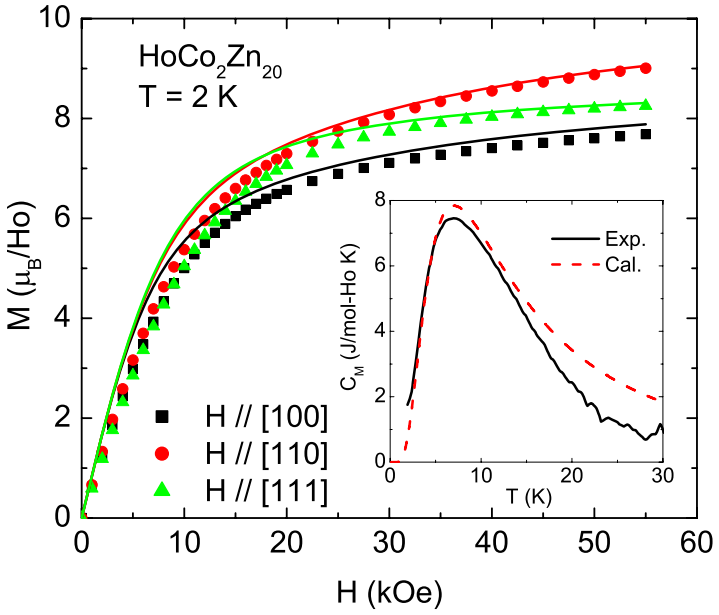

Figure 8.15 Field dependent magnetization for $HoCo_2Zn_{20}$ along three principle axes. The solid lines present the fitting results. Inset: magnetic part of specific heat. The solid and dashed line present the experimental and calculated result respectively.

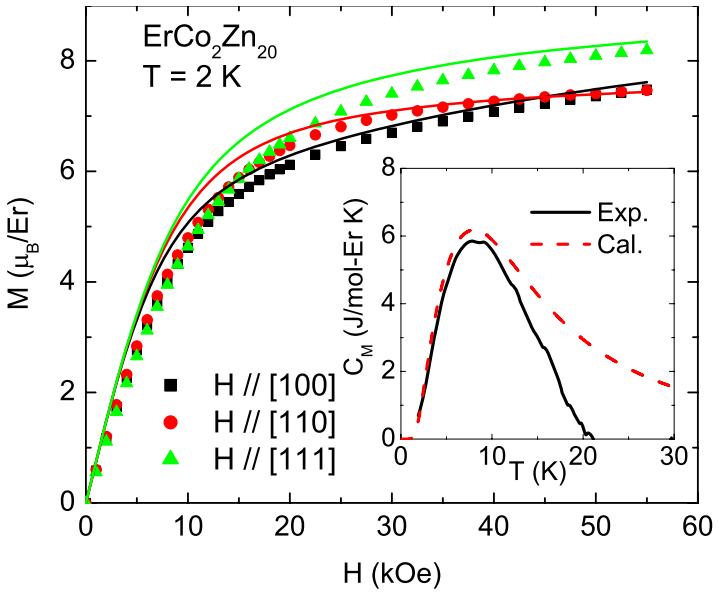

Figure 8.16 Field dependent magnetization for $ErCo_2Zn_{20}$ along three principle axes. The solid lines present the fitting results. Inset: magnetic part of specific heat. The solid and dashed line present the experimental and calculated result respectively.

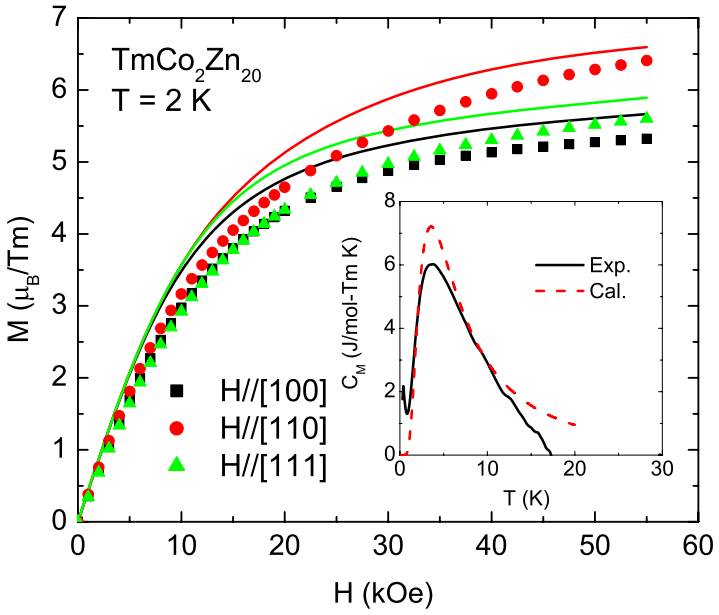

Figure 8.17 Field dependent magnetization for $TmCo_2Zn_{20}$ along three principle axes. The solid lines present the fitting results. Inset: magnetic part of specific heat. The solid and dashed line present the experimental and calculated result respectively.

Table 8.2 Comparison of the CEF parameters of RCo_2Zn_{20} compounds (R =Nd, Tb - Yb), determined from magnetization measurements to those calculated in a point charge model.

		Nd	Tb	Dy	Ho	Er	Tm	Yb
W (K)	exp.		0.084	-0.073	0.067	-0.077	0.07	
	cal.	0.28	0.026	-0.021	0.018	-0.025	0.044	-0.28
x	exp.		0.2	0.1	0.22	-0.1	-0.15	
	cal.	0.26	-0.68	-0.41	0.23	-0.22	-0.41	-0.64
B_4^0 (10^{-4} K)	exp.		2.8	-1.2	2.5	1.3	1.75	
	cal.	12.2	-3.0	1.4	0.7	-0.9	-3.0	29.6
B_6^0 (10^{-6} K)	exp.		8.9	-4.7	3.8	-5	7.9	
	cal.	81.2	1.1	-0.9	1.0	-1.4	3.5	-81.4

This result, indicating small energy scales of the CEF effect and relatively large B_6^0 terms, are roughly consistent with the calculated results based on the point charge model (see Appendix B). Furthermore, it should be noted that the signs of the B_6^0 terms for the calculated results are all consistent with the experimental ones; this is not the case for the B_4^0 terms. This behavior is not difficult to understand, as shown in the Appendix B, the contributions to the CEF splitting are mainly from the CN-16 Frank-Kasper polyhedron formed by 4 NN and 12 NNN Zn neighbors. For the B_4^0 term, the contributions cancel each other by the two sets of neighbors, whereas the contributions for the B_6^0 terms is the sum. Therefore, the B_6^0 terms are relatively large and the calculated results are more reliable.

8.2.3 RFe_2Zn_{20} (R = Gd - Tm)

Before discussing each of the well-defined, local moment compounds in this series separately, an overview of their temperature dependent magnetization data serves as a useful point of orientation. Figure 8.18 shows M/H versus T (the applied field H = 1000 Oe) for R = Gd - Tm members. In contrast to the Co series compounds, the Fe series compounds all manifest FM ground states with enhanced T_C values, which systematically decrease as R varies from Gd to Tm. Such enhanced FM ordering has been explained as the result of local moments embedded in the NFFL host, most clearly seen in YFe_2Zn_{20} and $LuFe_2Zn_{20}$. This systematic

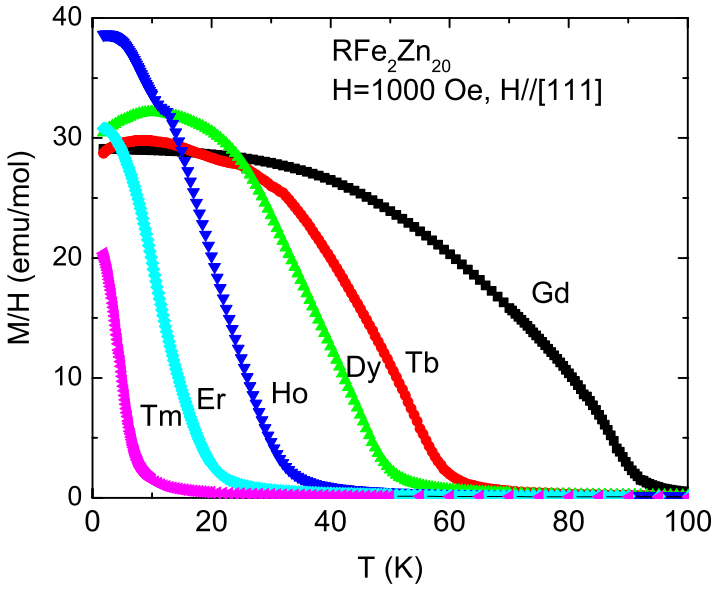

Figure 8.18 Temperature dependent magnetization of RFe_2Zn_{20} (R = Gd - Tm), divided by applied field $H = 1000$ Oe.

variation of T_C on R is not unexpected for such heavy rare earth compounds when the magnetic interaction between the R ions are associated with the spin part of the Hund's ground state of $4f$ electrons.

The temperature dependent H/M data, approximately equaling inverse susceptibilities $[1/\chi(T)]$ in the paramagnetic state, for R = Gd - Tm, as well as for $YbFe_2Zn_{20}$, are shown in Fig. 8.19. Similar to $GdFe_2Zn_{20}$ (see Chapter 6,7), the $1/\chi(T)$ data sets for R = Tb - Tm follow the CW law $[\chi(T) = C/(T - \theta_C) + \chi_0]$ at high temperatures, and deviate from the law when approaching their magnetic ordering. The effective moment (μ_{eff}) and the paramagnetic Curie temperature (θ_C) for these 6 compounds were listed in Table 8.3. All μ_{eff} values are close to the theoretical value for the Hund's ground state of the trivalent $4f$ electronic configuration.

8.2.3.1 $TbFe_2Zn_{20}$

Temperature dependent M/H, specific heat and resistivity data sets for $TbFe_2Zn_{20}$ are shown in Fig. 8.20. The $M(T)/H$ data are consistent with FM order below 60 K, and the

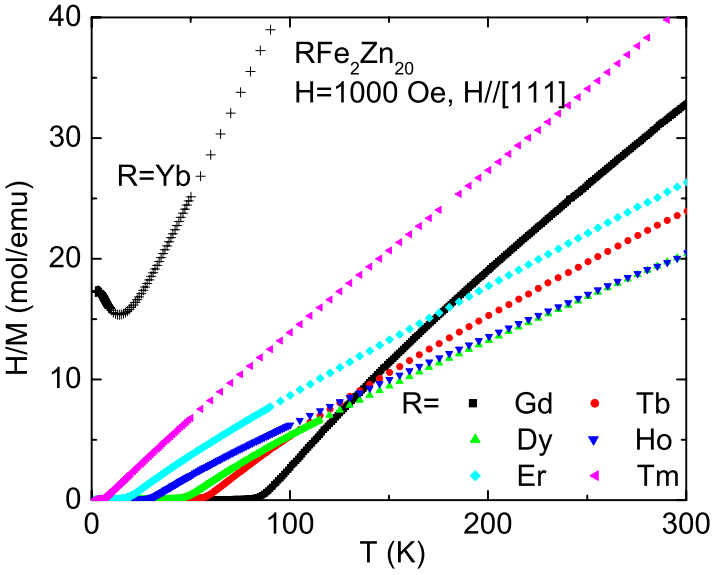

Figure 8.19 Applied field ($H = 1000$ Oe) divided by the magnetizations of RFe_2Zn_{20} (R = Gd - Tm) as a function of temperature.

Table 8.3 Residual resistivity ratio, $RRR = R(300K)/R(2K)$; paramagnetic Curie temperature, θ_C (with ± 0.5 K errors) and effective moment, μ_{eff} (from the CW fit of $\chi(T)$ from 100 K to 300 K, except for $GdFe_2Zn_{20}$, which was fitted from 200 K to 375 K; Curie temperature, T_C; and saturated moment at 55 kOe along the easy direction, μ_{sat} for RFe_2Zn_{20} compounds (R = Gd - Yb).

	Gd	Tb	Dy	Ho	Er	Tm	Yb
RRR	8.1	7.2	15.0	10.0	13.2	10.1	31.2
θ_C, K	46	30	20	9	0	-2	-23
μ_{eff}, μ_B	7.9	9.5	10.5	10.6	9.5	7.7	4.7
T_C, K	86	58	46	28	17	5.5	
μ_{sat}, μ_B	6.7	8.1	9.5	9.9	8.5	6.2	

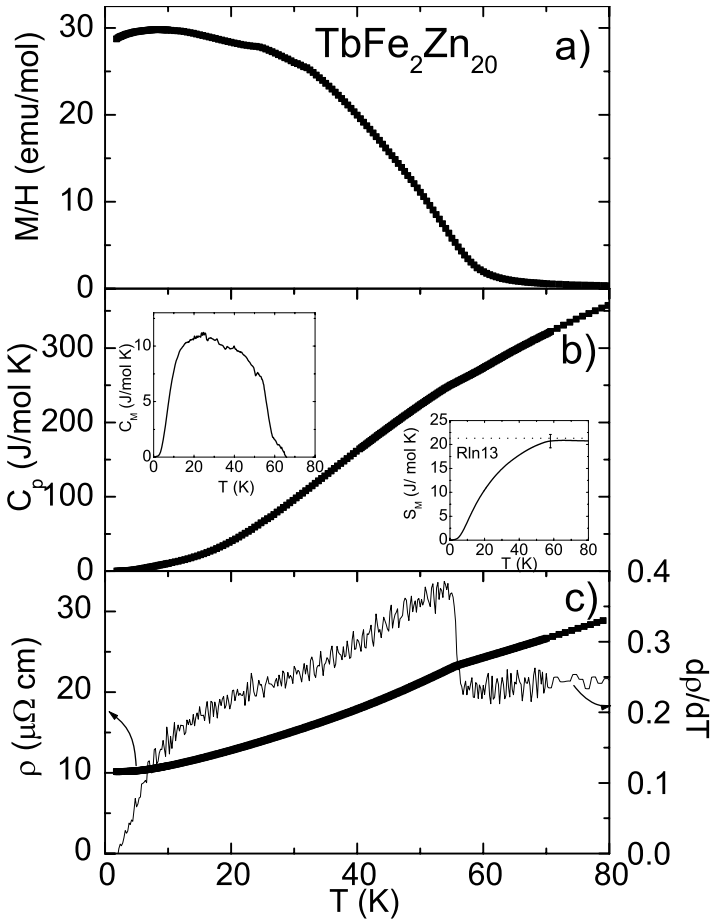

Figure 8.20 (a) Temperature dependent M/H for $TbFe_2Zn_{20}$ (H = 1000 Oe); (b) C_p; (c) ρ and dρ/dT. Upper inset : magnetic part of specific heat. Lower inset: magnetic entropy S_M.

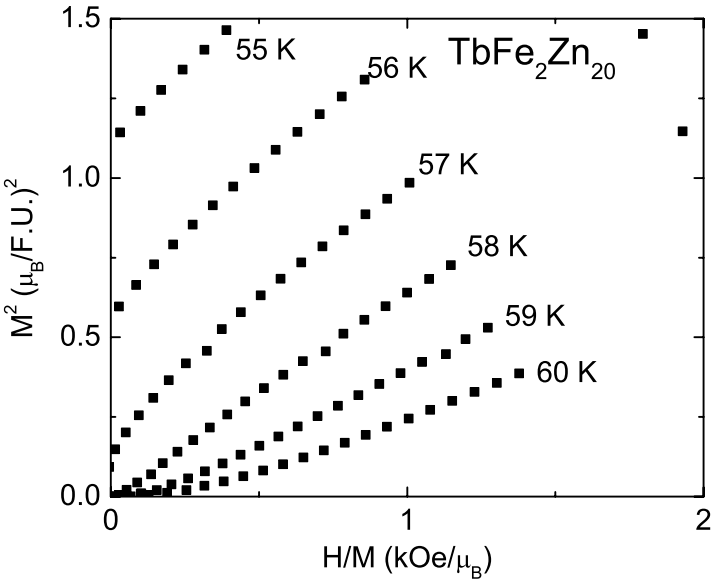

Figure 8.21 Arrott plot of magnetic isothermals for $TbFe_2Zn_{20}$.

magnetic phase transition manifests itself as a faint feature in C_p data, indicating $T_C = 56 \pm 3$ K. Such behavior associated with T_C appears as a broad feature with T_C occurring at the position of the maximum slope of the magnetic part of specific heat (Fig. 8.20 upper inset). As shown in the lower inset to Fig. 8.20 b, at T_C, the magnetic entropy is close to the value for the full degeneracy of the Hund's ground state of Tb^{3+}, $R \ln 13$. As we shall see for the rest of the local moment members (R = Dy - Tm), the released magnetic entropy at T_C for the respective rare earth ion, is close to the full degeneracy value for their Hund's ground state, except for R = Tm. The $\rho(T)$ data manifests a change in the slope, which could be seen even more clearly on in the $d\rho/dT$ data, consistent with a $T_C = 56 \pm 1$ K.

Figure 8.21 presents a plot of M^2 versus H/M (an Arrott plot) isotherms near T_C. The isotherm that most closely goes though the origin is the one closest to T_C, giving for this case a value of 58 K, consistent with the results of the C_p and $\rho(T)$ measurements. Figure 8.22 shows magnetization versus external field data along 3 different crystallographic directions: [100], [110] and [111], at 2 K. All of these data sets are consistent with a low temperature FM ground state with moderate anisotropy. The spontaneous longitudinal magnetic moment in

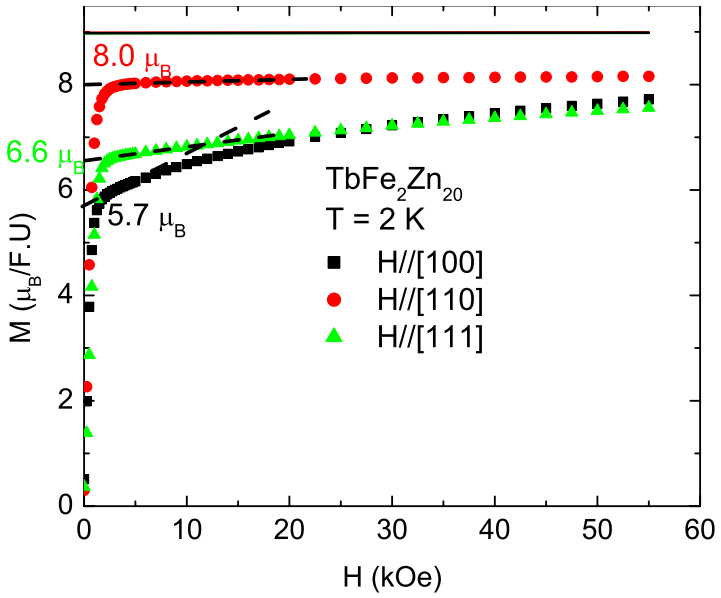

Figure 8.22 Field dependent magnetization of $TbFe_2Zn_{20}$ along three principle axes at 2 K. The three lines represent the calculated results based on molecular field approximation are all clustered near 9 μ_B and appear as a single line. The dashed lines and the values present the extrapolate of the magnetization curves and the estimated spontaneous magnetic moments along three directions.

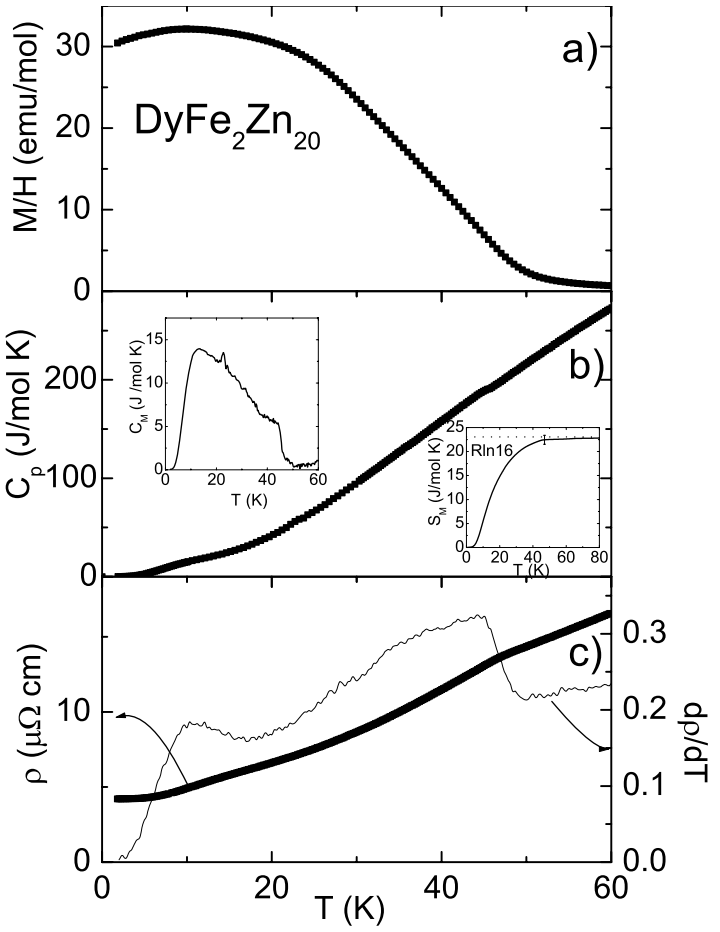

Figure 8.23 (a) Temperature dependent M/H for $DyFe_2Zn_{20}$ (H = 1000 Oe); (b) C_p; (c) ρ and $d\rho/dT$. Upper inset: magnetic part of C_p. Lower inset: magnetic entropy.

zero applied external field, estimated as the extrapolation of the magnetization curves back to $H = 0$, yield $M([110]) = 8.0\mu_B$, $M([111]) = 6.6\mu_B$, and $M([100]) = 5.7\mu_B$. The ratio of them is very close to $1 : \sqrt{2/3} : \sqrt{1/2}$. Such behavior indicates that the spontaneous magnetic moments along [111] and [100] directions can be understood as the projection of the one along the easy axis, [110]. At 2 K, the saturated moment at 55 kOe along the easy axis, [110], is $8.1\mu_B$, $0.9\mu_B$ less than the value associated with the Hund's ground state.

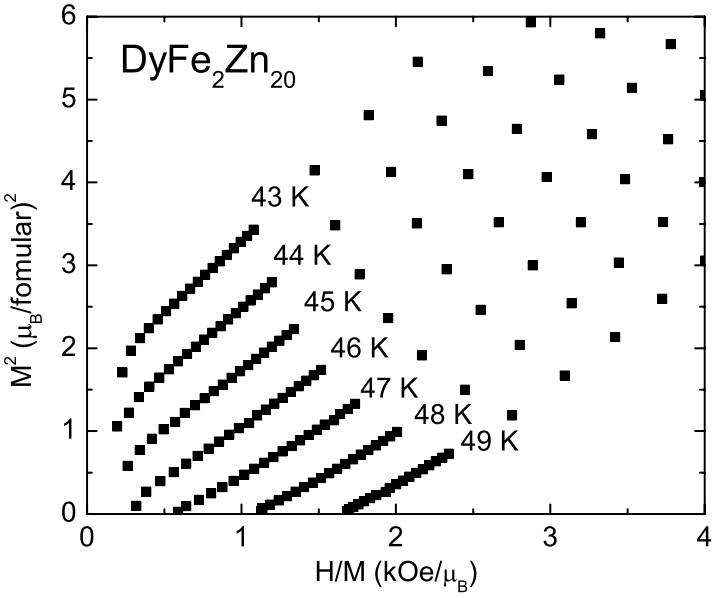

Figure 8.24 Arrott plot of magnetic isothermals for $DyFe_2Zn_{20}$.

8.2.3.2 $DyFe_2Zn_{20}$

The low field thermodynamic and transport properties of $DyFe_2Zn_{20}$ are shown in Fig. 8.23. The temperature dependent magnetization data (Fig. 8.23 a) suggest a FM transition below 50 K. The specific heat data show a kink associated with magnetic ordering (Fig. 8.23 b), which can be seen more clearly after the subtraction of the non-magnetic background (upper inset) and indicates $T_C = 45 \pm 1$ K. This FM transition temperature is further confirmed by a weak change in slope in $\rho(T)$ (associated with the low temperature loss of spin disorder scattering), indicating $T_C = 45 \pm 2$ K. Given that the loss of spin disorder scattering in intermetallics often scales with de Gennes parameter [Fournier and Gratz, 1993], the feature we find in $\rho(T)$ below T_C becomes fainter and fainter as R progresses from Gd to Tm. These values of T_C are consistent with the result of the Arrott plot analysis, from which a value of $T_C = 45 \pm 1$ K can be inferred(Fig. 8.24).

It is worth noticing that the specific heat data show a faint shoulder near 10 K, which appears to be a broad peak after the background subtraction, and is coincident with a slope

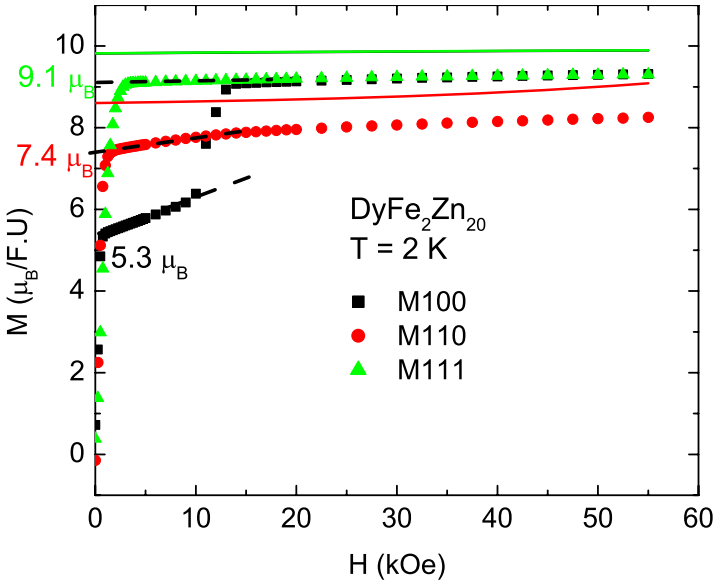

Figure 8.25 Field dependent magnetization of $DyFe_2Zn_{20}$ at 2 K along three principle axes. The solid lines represent the calculated result based on molecular field approximation (see data analysis part below). The dashed lines and the values present the extrapolate of the magnetization curves and the estimated spontaneous magnetic moments along 3 directions.

change feature in $\rho(T)$ data. As seen below, such anomaly below T_C in C_p and $\rho(T)$ data also appears for the members of R = Ho, Er and Tm. Those anomalies are likely due to the magnetic excitation energy spectrum associated with the Hund's rule multiplet of R^{3+} ions in their FM states. (Further discussion will be presented below.)

The 2 K field dependent, magnetization isotherms for $DyFe_2Zn_{20}$ are shown in Fig. 8.25. Compared to $TbFe_2Zn_{20}$, the magnetization curves for $DyFe_2Zn_{20}$ reveal a slightly more complicated, anisotropic behavior. The magnetization along [100] direction manifests one metamagnetic phase transition near 12 kOe. Above this transition, the magnetization along [100] direction is essentially the same as that for the field along the easy [111] axis. The spontaneous longitudinal magnetization along the three directions, $M([111]) = 9.1\mu_B$, $M([110]) = 7.4\mu_B$, and $M([100]) = 5.3\mu_B$, have a ratio very close to $1 : \sqrt{1/2} : \sqrt{1/3}$. These results indicate that $M([110])$ and $M([100])$ can be seen as the projection of $M([111])$. The metamagnetic phase

transition along [100] can be understood as the process of a classical spin reorientation in a cubic symmetry coordination. As in the case for $GdFe_2Zn_{20}$ and $TbFe_2Zn_{20}$, the saturated moment of $DyFe_2Zn_{20}$ at 55 kOe, $9.5\mu_B$, is slightly less than the value of the Hund's ground state value, $10\mu_B$.

8.2.3.3 $HoFe_2Zn_{20}$

Figure 8.26 presents the low field thermodynamic and transport data from measurements on $HoFe_2Zn_{20}$. The anomalies associated with the FM transition in $HoFe_2Zn_{20}$ in the specific heat and resistivity data are relatively weak. The specific heat anomaly can be associated with $T_C \sim 28$ K, and the $d\rho/dT$ data show faint anomaly at this temperature (Fig. 8.26). The T_C value is determined as 28 ± 1 K from C_p data, as well as 29 ± 1 K from $\rho(T)$ data. This determinate T_C value is consistent with the result of the Arrott plot analysis (Fig. 8.27), which gives $T_C = 28 \pm 1$ K.

The low temperature magnetic isotherms for $HoFe_2Zn_{20}$ manifest similar, but obviously larger, anisotropy to the ones for $TbFe_2Zn_{20}$ (Fig. 8.28). The ratio of the spontaneous magnetization, $M([110]) : M([111]) : M([100]) = 9.1\mu_B : 7.0\mu_B : 6.1\mu_B$ is close to the ratio of $1 : \sqrt{2/3} : \sqrt{1/2}$. This ratio is consistent with the projection of the local moment from the easy [110] axis onto the [111] and [100] axes. In the external field of 55 kOe, the magnetization along the easy axis, [110], reaches the value of $9.9\mu_B$, very close to the value of the Hund's ground state, $10\mu_B$.

8.2.3.4 $ErFe_2Zn_{20}$

The low field thermodynamic and transport properties of $ErFe_2Zn_{20}$ are shown in Fig. 8.29. The specific heat data show a kink near 18 K [Fig. 8.29 (b)], which can be seen more clearly after the background subtraction (upper inset) and indicates $T_C = 18 \pm 1$ K. The resistivity data show no clear anomaly at this temperature.(Fig. 8.29) The released magnetic entropy reaches 21 J/mol K at T_C, 90% of the one associated with the Hund's ground state of Er^{3+}, $R \ln 16$ (Fig. 8.29 lower inset). Although $\rho(T)$ data manifest no anomaly at T_C, we will see below that

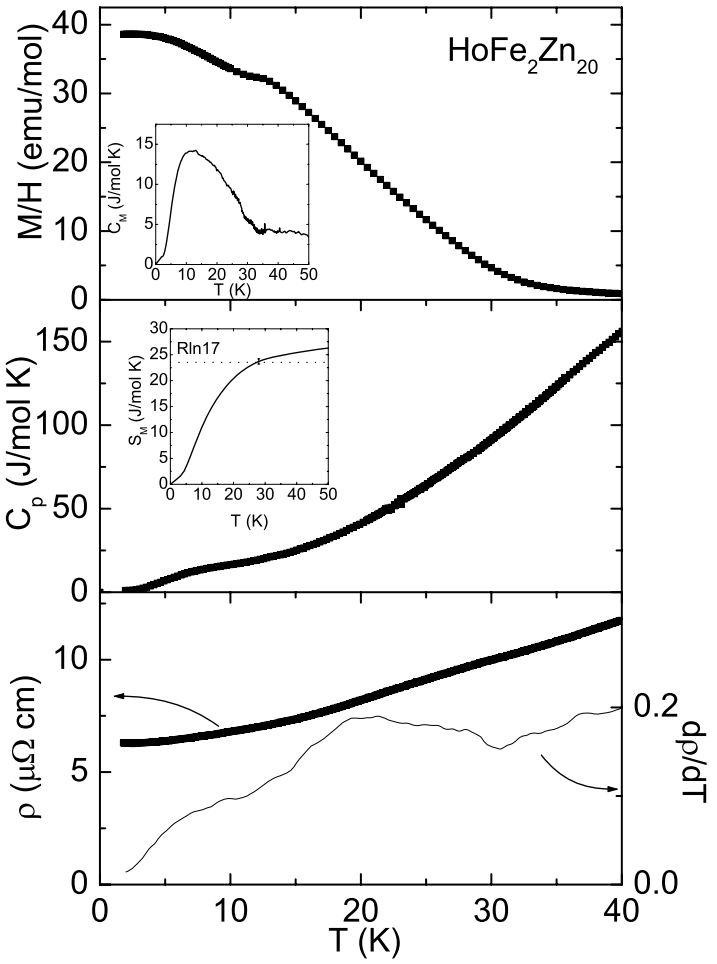

Figure 8.26 (a) Temperature dependent M/H for $HoFe_2Zn_{20}$ (H = 1000 Oe); (b) C_p; (c) ρ and dρ/dT. Upper inset: magnetic part of C_p data. Lower inset: magnetic entropy.

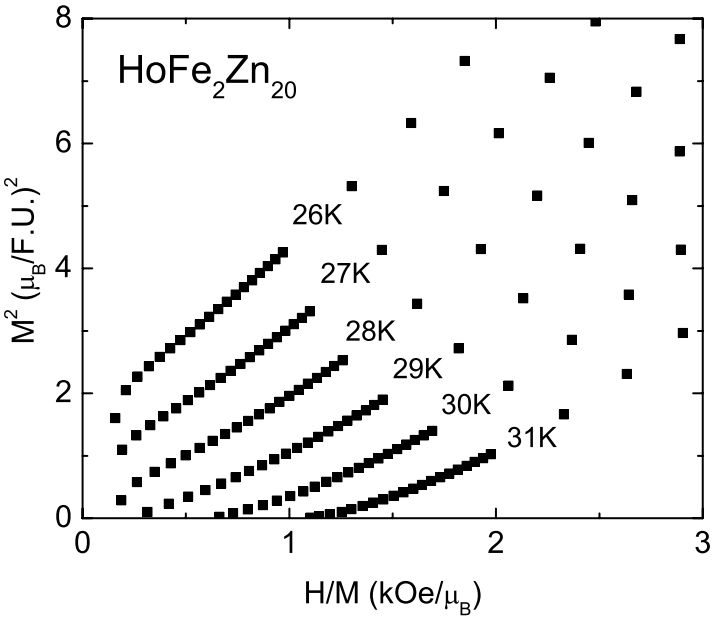

Figure 8.27 Arrott plot of magnetic isothermals for $HoFe_2Zn_{20}$.

the weak anomaly associated with magnetic ordering can be blow up after the background [$\rho(T)$ for $LuFe_2Zn_{20}$]subtraction. The Arrott plot for $ErFe_2Zn_{20}$ (Fig. 8.30), although showing non-linear, isothermal curves, demonstrates $T_C = 17 \pm 0.5$ K with no ambiguity. The non-linear feature is not unexpected for the $4f$ local moment systems associated with the CEF induced anisotropy. [Neumann and Ziebeck, 1995]

The magnetic anisotropy of $ErFe_2Zn_{20}$ is reminiscent of that of $DyFe_2Zn_{20}$: both have the same easy and hard magnetization orientations, [111] and [110] respectively, as well as the metamagnetic transition along the [100] direction (Fig. 8.31). The ratio of the spontaneous longitudinal magnetic moments, $M([111]) : M([110]) : M([100]) = 7.4\mu_B : 5.9\mu_B : 4.2\mu_B$ is also close to the ratio of $1 : \sqrt{2/3} : \sqrt{1/3}$.

8.2.3.5 $TmFe_2Zn_{20}$

The low field magnetization, specific heat and resistivity data for $TmFe_2Zn_{20}$ are shown in Fig. 8.32. The temperature dependent magnetization data suggest a FM transition below

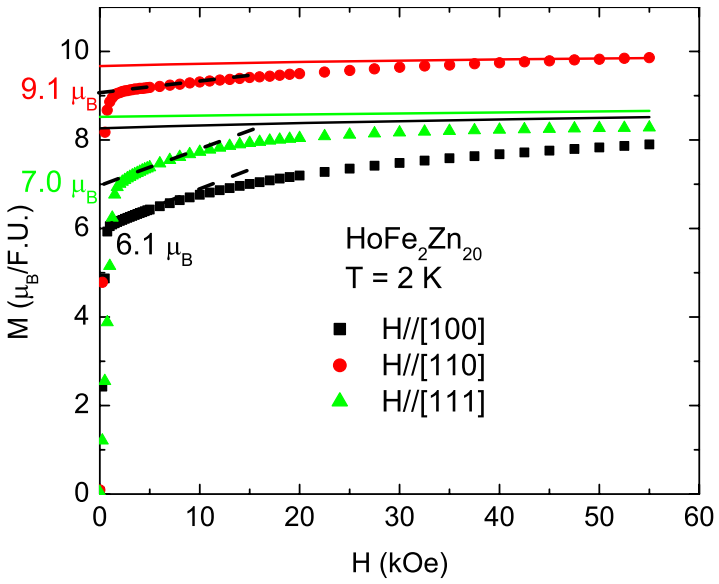

Figure 8.28 Field dependent magnetization of $HoFe_2Zn_{20}$ at 2 K along three principle axes. The solid lines represent the calculated result based on molecular field approximation (see data analysis part below). The dashed lines and the values present the extrapolate of the magnetization curves and the estimated spontaneous magnetic moments along 3 directions.

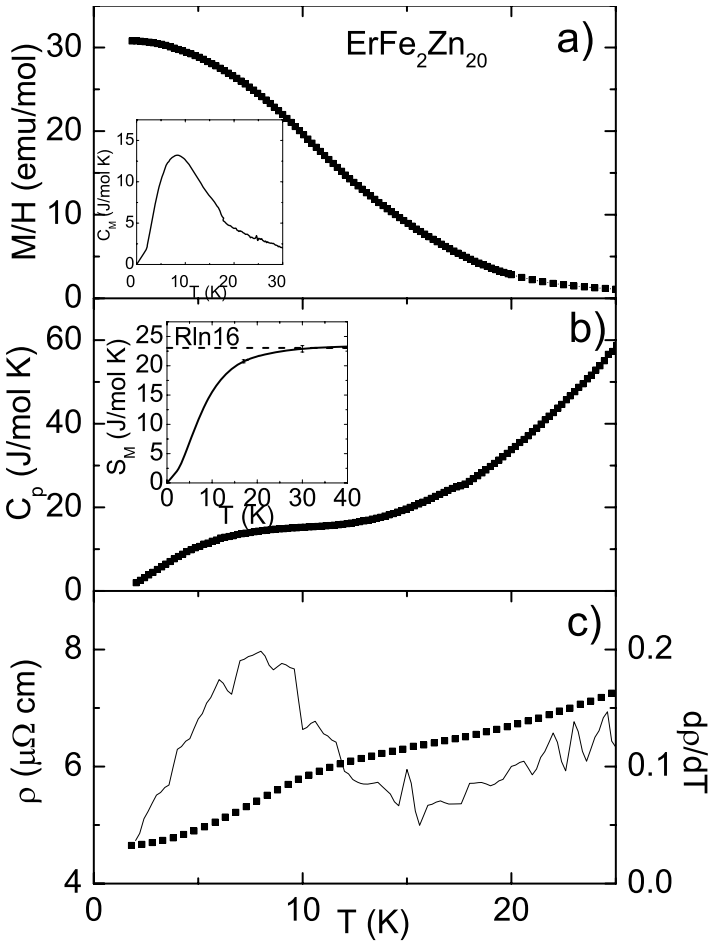

Figure 8.29 (a) Temperature dependent M/H for $ErFe_2Zn_{20}$ (H = 1000 Oe); (b) C_p; (c) ρ and dρ/dT. Upper inset: magnetic part of C_p data. Lower inset: magnetic entropy.

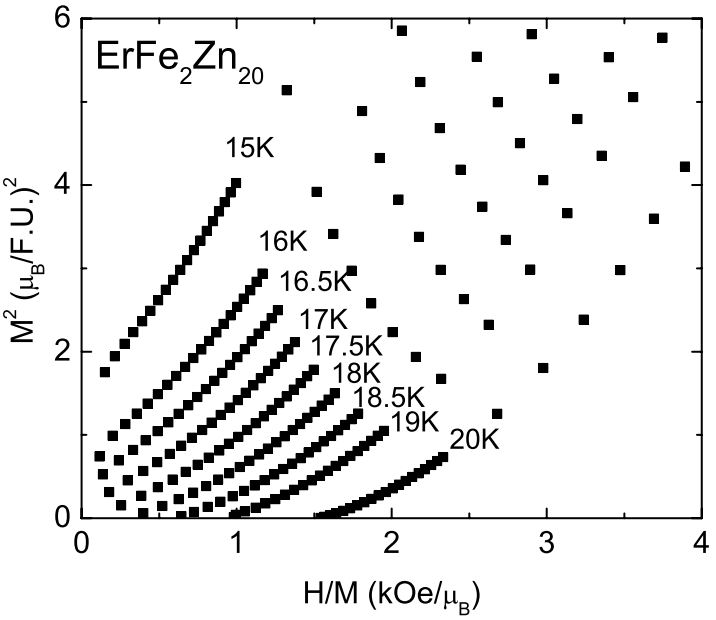

Figure 8.30 Arrott plot of magnetic isothermals for $ErFe_2Zn_{20}$.

10 K (Fig. 8.32 a). However, the specific heat data for $TmFe_2Zn_{20}$ only manifest one broad peak at 4.5 K (Fig. 8.32 b), which is less like the anomalies associated with T_C for R = Gd - Er, and more like a Schottky anomaly associated with a CEF splitting. The resistivity data also show anomaly below 5 K (Fig. 8.32 c). However, at this point, it is difficult to determine whether this anomaly is associated with the magnetic ordering or the CEF splitting of the $4f$ electrons of Tm^{3+} ions. As we can see below, after the subtraction of the nonmagnetic background, the anomaly associated with the loss of the spin disorder scattering can be seen more clearly.

For $TmFe_2Zn_{20}$, the Arrott plot analysis provides the reliable criterion for T_C determination. Figure 8.33 shows that T_C can be determined as 5.5 ± 0.5 K without any ambiguity. At this temperature, the magnetic entropy is 15 J/mol K, only 70% of the value of fully released entropy of Hund's ground state of Tm^{3+}, $R \ln 13$ (Fig. 8.32 upper inset).

The low temperature magnetic isotherms for $TmFe_2Zn_{20}$ manifest the same easy and hard axis as Tb and Ho members, [110] and [111], respectively (Fig. 8.34). The spontaneous

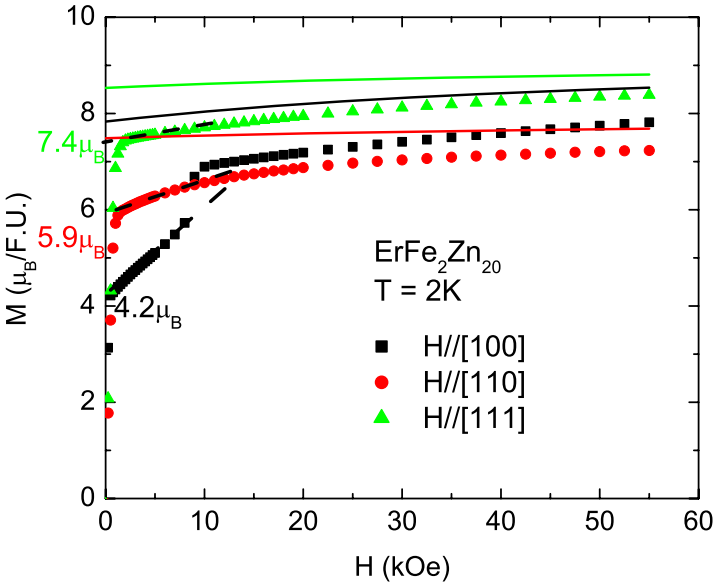

Figure 8.31 Field dependent magnetization of $ErFe_2Zn_{20}$ at 2 K along three principle axes. The solid lines represent the calculated result based on molecular field approximation (see data analysis part below). The dashed lines and the values present the extrapolate of the magnetization curves and the estimated spontaneous magnetic moments along 3 directions.

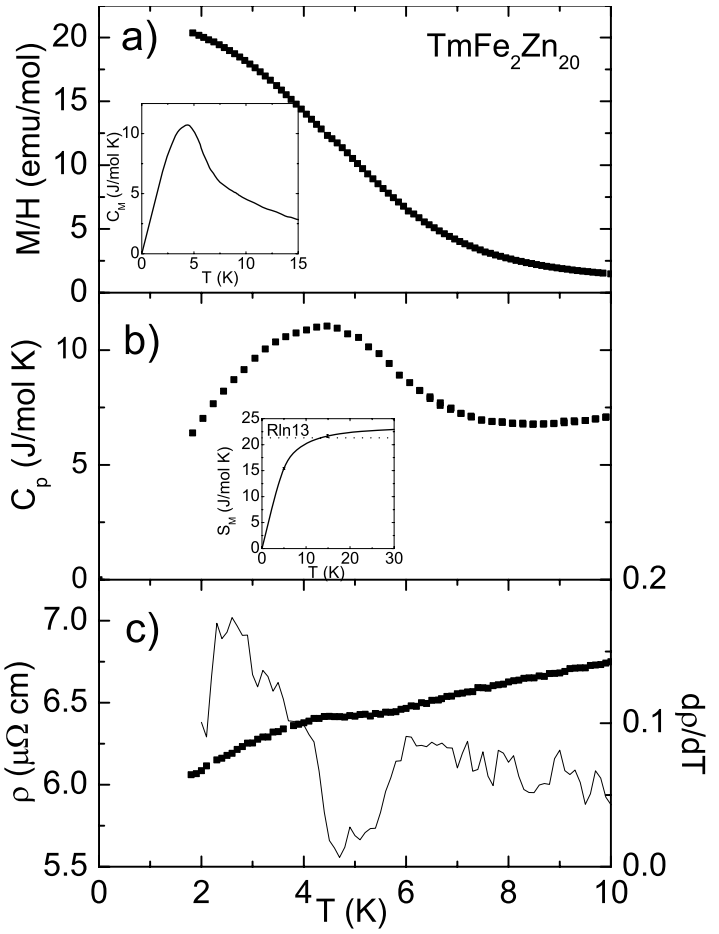

Figure 8.32 (a) Temperature dependent M/H for $TmFe_2Zn_{20}$ (H = 1000 Oe); (b) C_p; (c) ρ and $d\rho/dT$. Inset A: magnetic part of C_p data. Inset B: magnetic entropy.

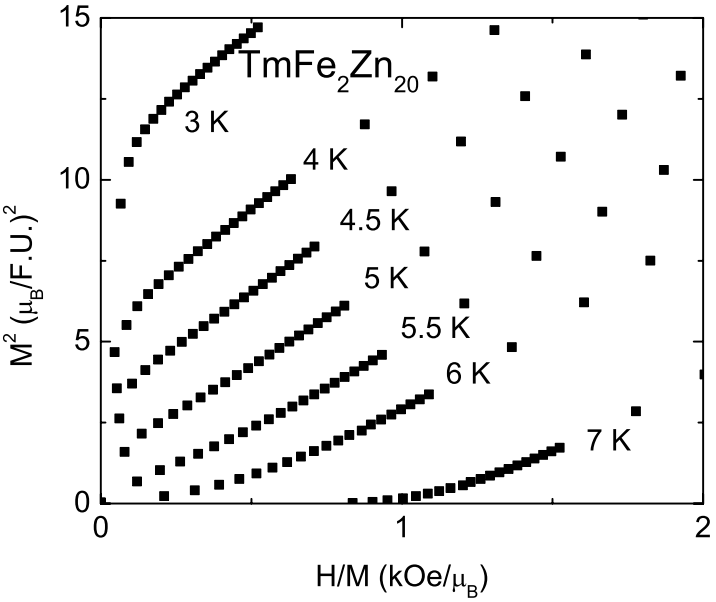

Figure 8.33 Arrott plot of magnetic isothermals for $TmFe_2Zn_{20}$.

longitudinal magnetic moments along the three principle axes are all close to $4\mu_B$. Such a result may be due to the relatively low value of T_C, which makes the spontaneous magnetic moment less anisotropic at 2 K. The saturated moment along the easy axis reaches $6.2\mu_B$ at 55 kOe, $0.8\mu_B$ less than the value of the Hund's ground state, $7\mu_B$.

8.2.4 $YbFe_2Zn_{20}$ and $YbCo_2Zn_{20}$

Figure 8.35 shows temperature dependent susceptibility and resistivity data for $YbFe_2Zn_{20}$ and $YbCo_2Zn_{20}$. The susceptibility data for $YbFe_2Zn_{20}$ manifest a broad, Kondo-type peak about 20 K, indicating a clear loss of local moment behavior, whereas the susceptibility for $YbCo_2Zn_{20}$ shows CW behavior down to 1.8 K (Fig. 8.10), associated with the effective moment value $\mu_{eff} = 4.5\mu_B$. Above $\sim$ 50 K, $\chi(T)$ for $YbFe_2Zn_{20}$ manifests a CW behavior with an effective moment of $4.7\mu_B$, close to the value of the Hund's ground state of Yb^{3+}, $4.5\mu_B$ (see Fig. 8.19). The resistivity data for $YbFe_2Zn_{20}$ show a broad shoulder about 30 K, whereas for $YbCo_2Zn_{20}$, the resistivity data shows a Kondo resistance minimum about 50 K and a clear coherent peak about 2 K. These apparently different behaviors for these two Yb-based heavy

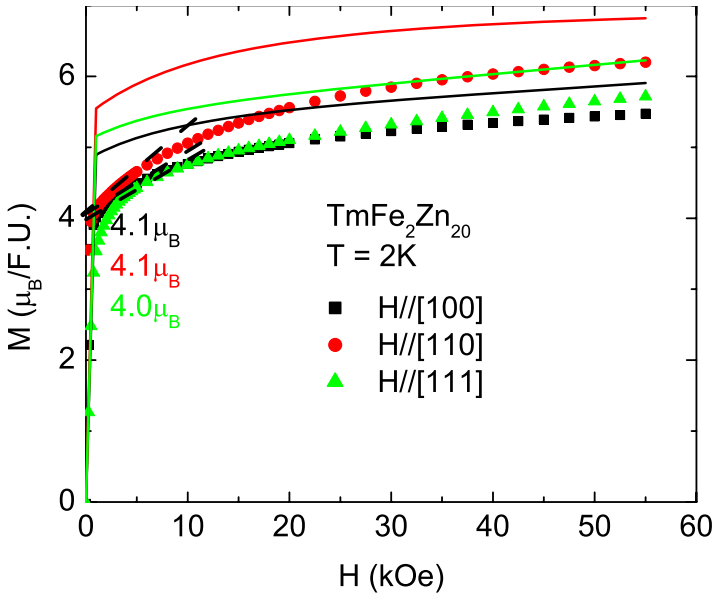

Figure 8.34 Field dependent magnetization of $TmFe_2Zn_{20}$ at 2 K along three principle axes. The solid lines represent the calculated result based on molecular field approximation (see data analysis part below). The dashed lines and the values present the extrapolate of the magnetization curves and the estimated spontaneous magnetic moments along 3 directions.

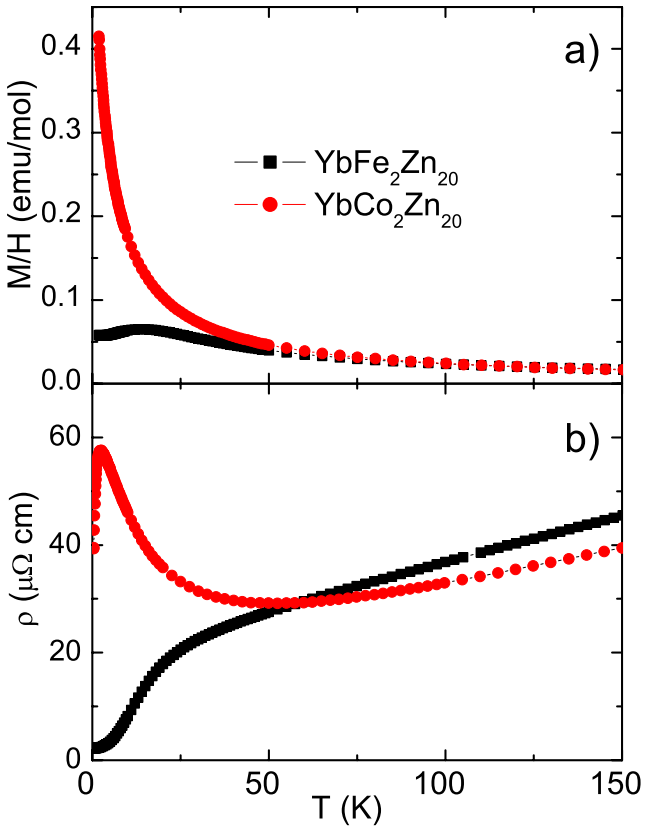

Figure 8.35 Temperature dependent M/H (a) and resistivity (b) for $YbFe_2Zn_{20}$ and $YbCo_2Zn_{20}$ ($H = 1000$ Oe).

fermion compounds with same structure can be explained as the result of significantly different Kondo temperatures: T_K = 33 K and 1.5 K for Fe and Co compounds, respectively. Detail analysis for these two compounds as well as YbT_2Zn_{20} (T = Ru, Rh, Os and Ir) compounds will be presented in Chapter 9.

8.3 Data Analysis and Discussion

As shown in Fig. 8.36 (a), the T_C values of RFe_2Zn_{20} compounds (R = Gd - Tm) scale fairly well with the de Gennes factor, $dG = (g_J - 1)^2 J(J + 1)$, which indicates a RKKY interaction. All of the θ_C values for each compounds are smaller than their respective T_C values (for R = Er and Tm, the values of θ_C are even negative). These small θ_C values are consistent with the deviation of $\chi(T)$ from the CW law (Fig. 8.19). As observed in the case of pseudo-ternary compounds $Gd_xY_{1-x}Fe_2Zn_{20}$, such deviation can be explained as a result of increasing coupling between the local moments embedded in the strongly temperature dependent, polarizable matrix, YFe_2Zn_{20} or $LuFe_2Zn_{20}$. (See Chapter 7)

Previous studies show that the magnetization of $GdFe_2Zn_{20}$ at base temperature are nearly isotropic with a deficient saturated moment ($\sim 0.5\mu_B$ less than the value of Hund's rule ground state of Gd^{3+}). For R = Tb - Tm, the magnetization anisotropy at base temperature is significant ,and correlates with the easy and hard axes of the respective RCo_2Zn_{20} analogue. Such behavior indicates the anisotropy of RFe_2Zn_{20} (R = Tb - Tm) may mainly be due to the CEF effect on the R^{3+} ions. The $M(H)$ curves at 2 K manifest divided behavior for R = Tb, Ho and Tm, compare with R = Dy and Er: for R = Tb, Ho and Tm, the magnetization process are gradual along all 3 principal axes; for R = Dy and Er, the magnetization data along [100] direction shows one metamagnetic transition. Both types of magnetization processes (gradual increase and metamagnetic transition) are common for the FM ordered $4f$ local moments with CEF anisotropy associated with the R in a cubic point symmetry, and can be understood in terms of the purification of the CEF split $4f$ electronic wave function due to the Zeeman effect of the external field, and the rotation of the local moment. [Pierre, 1982] Given that Tb^{3+} and Tm^{3+}, as well as Dy^{3+} and Er^{3+} ions have same total $4f$ electronic Hund's rule ground state

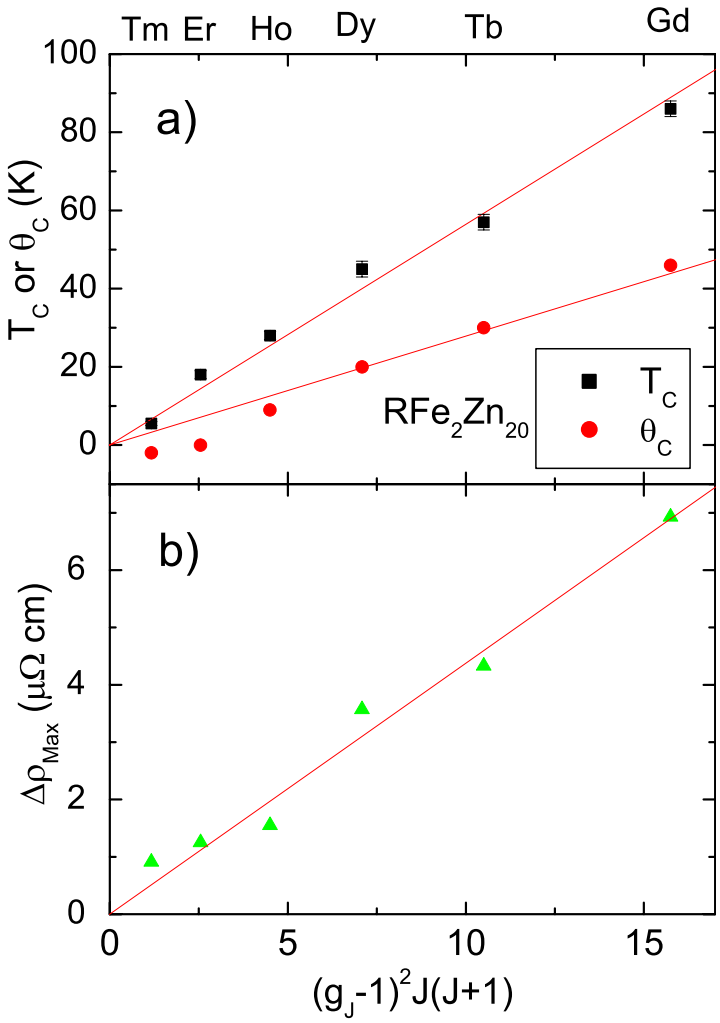

Figure 8.36 T_C and θ_C (a), the maximum value on $\Delta\rho$ (b) with respect to the de Gennes factor for RFe_2Zn_{20} (R = Gd - Tm).

quantum number ($\mathbf{J}$ = 6 and 15/2 respectively), the similar magnetic anisotropy indicates similar CEF effect for the two sets of rare earth ions, respectively.

In order to better understand the magnetic anisotropy of RFe_2Zn_{20} compounds (R = Tb - Tm), the CEF effect acting on the R ions must to be considered. However, multiple difficulties associated with the strongly polarizable back ground [Y(Lu)Fe_2Zn_{20}] as well as the strong magnetic interaction, make the determination of the CEF parameters hard. For example, in order to reduce the magnetic interaction, the magnetic R^{3+} ions were placed into a dilute coordination, $R_xY_{1-x}Fe_2Zn_{20}$ or $R_xLu_{1-x}Fe_2Zn_{20}$. A FM ground state has been found even for very dilute magnetic R concentration: it was found that $Tb_{0.05}Y_{0.95}Fe_2Zn_{20}$, $Dy_{0.05}Y_{0.95}Fe_2Zn_{20}$ as well as $Ho_{0.1}Y_{0.9}Fe_2Zn_{20}$ manifest FM ordering above 2 K. For such small x, the background subtraction (magnetization and/or specific heat of YFe_2Zn_{20} or $LuFe_2Zn_{20}$), as well as the uncertainty of x, make the fitting process unreliable.

On the other hand, due to the very similar R coordination and the lattice parameters for Fe and Co series, the CEF parameters determined from RCo_2Zn_{20} compounds should be close to those for the RFe_2Zn_{20} compounds, with respective R members. Figure 8.37 shows that the anisotropy of the pseudo-ternary Fe compounds, $Er_{0.1}Y_{0.9}Fe_2Zn_{20}$ and $Tm_{0.1}Y_{0.9}Fe_2Zn_{20}$, which still manifest a paramagnetic state at the base temperature, is close to the calculated results from the determined CEF parameters of the respective Co compounds. The calculated results also fairly well mimic the crossing behavior of the magnetization along [110] and [100] directions for R = Er, as well as along the [111] and [100] directions for R = Tm. For all three directions, the calculated results are slightly larger than the experimental ones, which is most likely due to the ± 0.02 uncertainty of the nominal x value. The larger magnetization for $Er_{0.1}Y_{0.9}Fe_2Zn_{20}$ than the calculated results below 10 kOe is consistent with residual FM interactions between the Er^{3+} local moments.

The magnetization along the three axes for the all Fe compounds were calculated based on the molecular field approximation in a self-consistent manner. In the single-ion Hamiltonian for the R^{3+} ions (Eqn. 8.3), with the molecular field approximation, the magnetic interaction

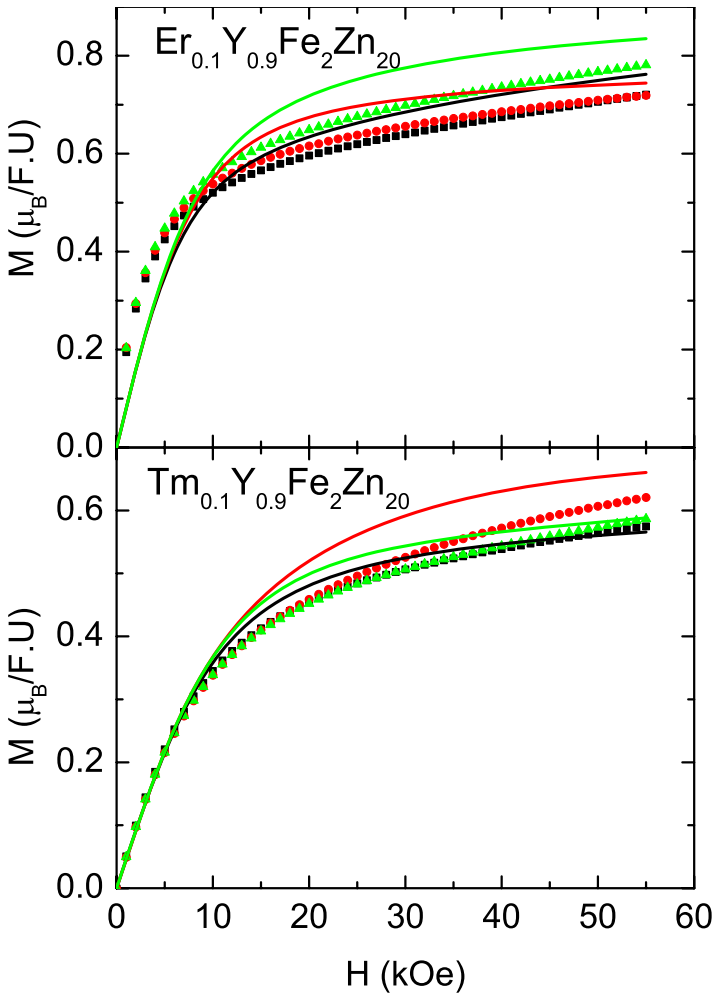

Figure 8.37 Field dependent magnetization for $Er_{0.1}Y_{0.1}Fe_2Zn_{20}$ (a) and $Tm_{0.1}Y_{0.1}Fe_2Zn_{20}$ (b) along three principle axes at 1.85 K. The solid lines present the calculated magnetization by using the single-ion Hamiltonian and the CEF coefficients determined from the respective Co members.

term is written as:

$$\mathcal{H}_{exc} = g_J \mu_B \vec{J} \cdot \vec{H}_M, \tag{8.6}$$

where H_M is the molecular field. It obeys the self-consistent condition:

$$H_M = \lambda g \mu_B \left\langle \vec{J} \right\rangle, \tag{8.7}$$

$$\left\langle \vec{J} \right\rangle = \frac{\sum_0 J_n \exp\left(-E_n/k_B T\right)}{\sum_0 \exp\left(-E_n/k_B T\right)}, \tag{8.8}$$

where J_n and E_n are the eigenvalues and eigenenergies of the nth eigenfunction; λ is the molecular field constant which can be obtained from the ordering temperature: $\lambda = \frac{3k_B T_C}{\mu_{eff}^2}$.

The calculated magnetizations were compared with the experimental results in Figs. 8.22, 8.25, 8.28, 8.31 and 8.34. All these calculated magnetization values are obviously larger than the experimental results. This difference is probably due to (i) the molecular field approximation over-estimating the molecular field constant as well as the internal field, and (ii) the induced moments from the Fe site aligning in an antiparallel manner with respect to the R^{3+} local moments (as in the case of $GdFe_2Zn_{20}$.

Figure 8.38 shows the magnetic part of specific heat as a function of T/T_C for RFe_2Zn_{20} (R = Gd - Tm). The magnetic ordering temperature (T_C) of R = Gd - Er members manifests itself as the position of maximum slope, with a decreasing sharpness as R varies from Gd to Er. $TmFe_2Zn_{20}$ does not appear to have any anomaly in the C_M data at T_C. Below T_C, the data sets for R = Dy - Tm show a broad peak, which shifts closer to its T_C as R varies from Dy to Tm, whereas the data for $GdFe_2Zn_{20}$ show no explicit peak. If the broad peaks are corresponding to the magnetic excitation energy spectrum associated with CEF effect, then the relative positions of these peaks to T_C, to some extend, indicate the ratio of the energy scales of the CEF splitting (for a single ion) to the magnetic interaction. The shift of the peak position as R varies from Dy to Tm indicates that the energy scale of the magnetic order relatively decreases compared with the CEF splitting. Such phenomena is consistent with the analysis on the magnetic part of entropy: as shown in the insets of Figs. 8.20, 8.23, 8.26, 8.29 and 8.32, Tb, Dy and Ho compounds manifest fully released S_M at their T_C; whereas Er and Tm compounds still release part of S_M above their T_C, which indicates that, unlike R = Gd -

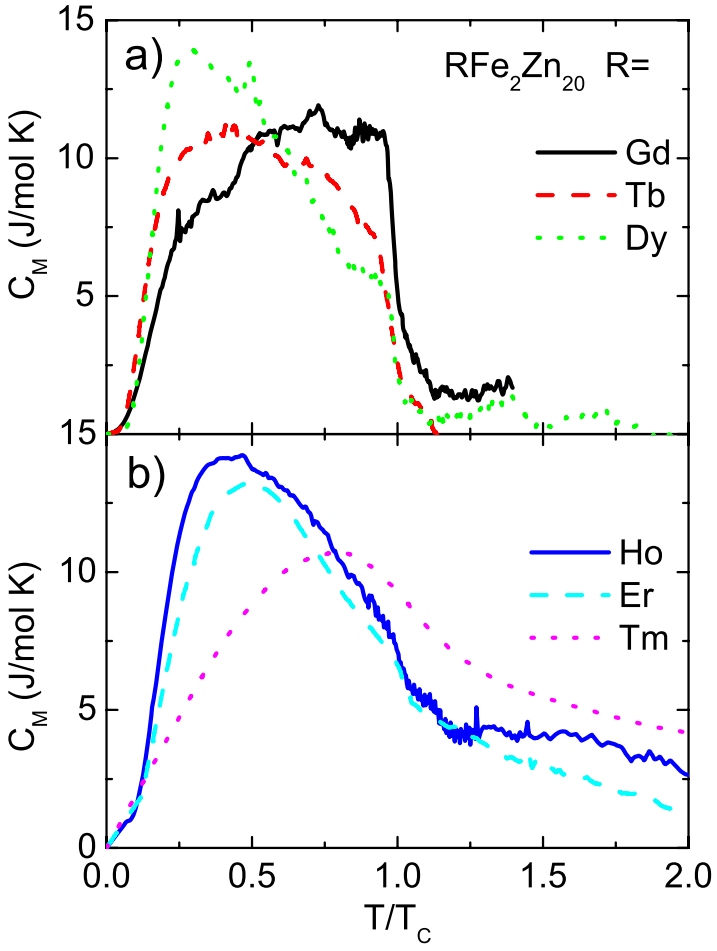

Figure 8.38 Magnetic part of specific heat versus T/T_{C} for RFe_2Zn_{20} (R = Gd - Tm).

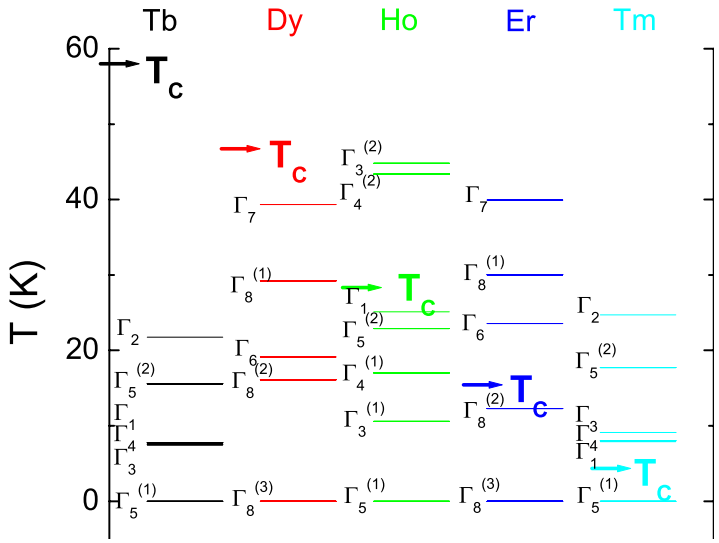

Figure 8.39 Single-ion CEF splitting energy levels for RCo_2Zn_{20} (R = Tb - Tm). The arrows present the T_C values for RFe_2Zn_{20} with respective R.

Ho members, the CEF splitting for the $4f$ electronic configuration of the Tm^{3+} and Er^{3+} may extend above magnetic ordering temperature.

Based on the assumption that the Fe and Co series manifest similar CEF splitting (for a single R ion), the comparison between the magnetic ordering temperature and the CEF splitting for different R ions is qualitatively diagrammatized in Fig. 8.39. The levels represent the single ion, CEF splitting of the Hund's ground state of $4f$ electronic configuration of R^{3+}, determined from RCo_2Zn_{20} and the arrows represent the T_C values of RFe_2Zn_{20}. The T_C value is comparable with the highest energy level of CEF splitting for R = Ho. For R = Er and Tm, the T_C values is about $\frac{1}{2}$ and $\frac{1}{5}$ of the highest CEF levels, respectively. This diagram, though it cannot be used to determine the precise energy splitting of the RFe_2Zn_{20} compounds (the CEF levels have been strongly modulated and mixed by the interaction energy), is qualitatively consistent with the specific measurements, and indicates that, at least for $TmFe_2Zn_{20}$, the CEF energy splitting already happens well above its T_C. In summary, is appears plausible that, due to extremely similar liganal environments, equivalent members of the RFe_2Zn_{20} and RCo_2Zn_{20}

series have similar CEF splitting schemes.

Further insight can also be gained from a careful revisiting of the transport data. The total resistivity of RFe_2Zn_{20} (R = Gd - Yb) can be written as:

$$\rho(T) = \rho_0 + \rho_{ph}(T) + \rho_{mag}(T), \tag{8.9}$$

where ρ_{mag} is scattering associated with the $4f$ moments and the spin fluctuation of itinerant electrons. As seen in Fig. 8.40 a, for the whole series above 250 K, the resistivity data sets show essentially linear behavior with slopes differing by less than 12%, within the estimated dimension error ($\pm$10%) of these bar-like-shape samples. These similar, high temperature behaviors indicate that, in the high temperature limit, the magnetic scattering is saturated, whereas the phonon scattering is essentially invariant for the whole series (due to the very dilute nature of the R ions). Therefore, the magnetic contribution to the resistivity can be estimated by (1) subtracting residue resistivity, ρ_0 (2) normalizing the high temperature slope of all $\rho(T)$ to that of $LuFe_2Zn_{20}$ and then (3) subtracting the $\rho_{Lu}(T) - \rho_{Lu0}$ data from the normalized data. The result is written as:

$$\Delta\rho(T) = (\rho_{\rm R} - \rho_{\rm R0})\frac{\frac{{\rm d}\rho_{|mathrmR}}{{\rm d}T}\,|_{275{\rm K}}}{\frac{{\rm d}\rho_{\rm Lu}}{{\rm dT}}\,|_{275{\rm K}}} - (\rho_{\rm Lu} - \rho_{\rm Lu0}). \tag{8.10}$$

As shown before, the subtraction background $\rho_{\rm Lu}(T)$ already includes the scattering associated with the spin fluctuation of itinerant electrons. Thus, $\Delta\rho$ will not only include the scattering from the $4f$ moments, but will also include scattering associated with the interaction between the $4f$ moments and itinerant electrons. Figure 8.40 (b) and (c) show $\Delta\rho$ versus temperature, as well as normalized temperature ($T/T_{\rm C}$) for R = Gd - Tm. For R = Gd - Er, a pronounced upward cusp, whose height decreases from Gd to Er, is centered about $T_{\rm C}$, whereas $TmFe_2Zn_{20}$ manifests a broad feature and only very weak anomaly around its $T_{\rm C}$ (see the blow-up inset of Fig. 8.40). As shown in Fig. 8.36 (b), the maximum values on the cusps for different R scale with the de Gennes factor, which indicates that the decrease of $\Delta\rho$ with T below $T_{\rm C}$ is the result of a loss of spin disorder scattering of conduction electrons, associated with the $4f$ local moment. However, as found in the pseudo-ternary compounds $Gd_xY_{1-x}Fe_2Zn_{20}$,

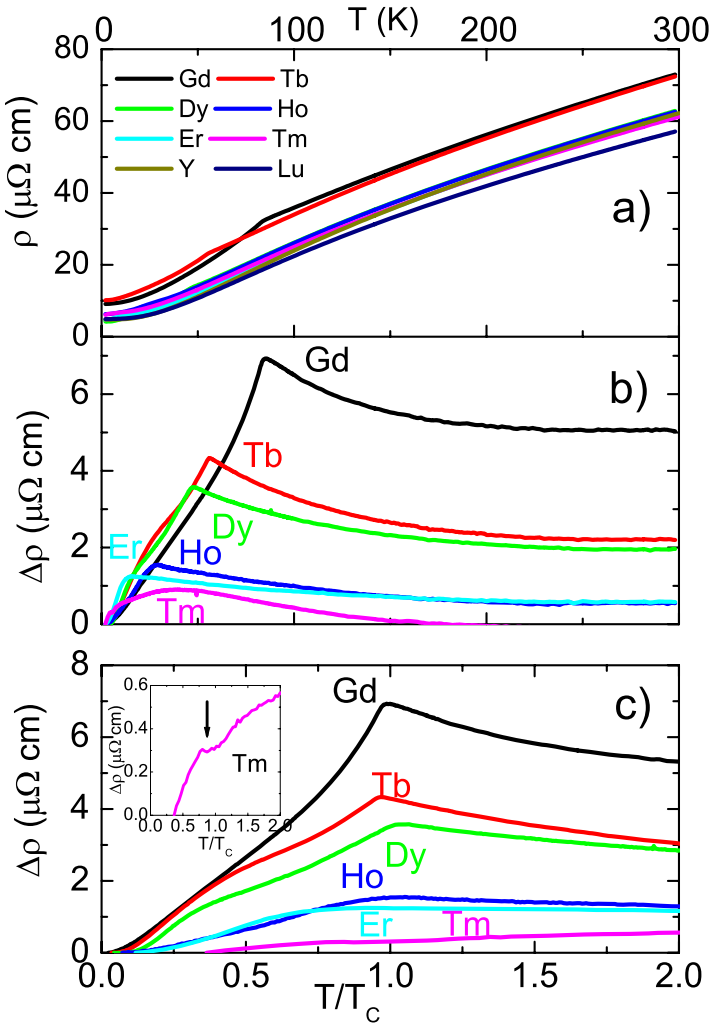

Figure 8.40 (a): ρ versus T, (b): $\Delta\rho$ versus T, (c): $\Delta\rho$ versus T/T_{C} for RFe_2Zn_{20} (R = Gd - Tm). Inset: the blow up $\Delta\rho$ data for $TmFe_2Zn_{20}$. The arrow presents the FM ordering temperature.

the decrease behavior of $\Delta\rho$ with increasing T above T_C is more conspicuous and must come from a different conduction electron scattering process [simple models of $\rho(T)$ due to magnetic scattering cannot explain this anomaly [Craig et al., 1967, Fisher and Langer, 1968]]. Giving that RT_2Zn_{20} compounds only manifest this behavior when the local moments are embedded in the highly polarizable background ($GdCo_2Zn_{20}$ does not show this behavior), this anomaly is thought to be associated with the spin fluctuation of the $3d$ electrons. Also appearing in the resistivity of RCo_2 (R = Gd - Tm) [Gratz et al., 1995], the decreasing behavior of $\Delta\rho$ with increasing T above T_C has been explained as the result of the increase of the spin fluctuation of $3d$ electrons, which is provided by the increasing, nonuniform fluctuating $4f$-d electron exchange interaction, as the temperature approaches T_C in the paramagnetic state. Since both Y(Lu)Co_2 and Y(Lu)Fe_2Zn_{20} are classical examples of NFFLs, such an anomaly could be associated with these strongly correlated electron systems. On the other hand, considering that the Hund's ground state of Tm^{3+} has been significantly split above FM ordering for $TmFe_2Zn_{20}$, it is not unexpected that the conduction electron scattering process manifests a different behavior associated with the CEF effect.

The nearly FM compounds: YFe_2Zn_{20} and $LuFe_2Zn_{20}$ are also merit further discussion. Shown in Fig. 8.1, the low field susceptibility (H = 10 kOe) manifests a maximum about 6 K and 8 K for YFe_2Zn_{20} and $LuFe_2Zn_{20}$ respectively. Such a maximum in the temperature dependent susceptibility also appears for other examples of nearly FM compounds. For example, Pd manifests $T_{max} \sim 70$ K [Gerhardt et al., 1981]; YCo_2 and $LuCo_2$ manifests $T_{max} \sim$ 100 K[Burzo et al., 1993]; and $TiBe_2$ manifests $T_{max} \sim 10$ K[Gerhardt et al., 1983]. Another interesting phenomena in nearly FM materials is the so-called itinerant electron metamagnetism (IEM), which is an applied magnetic field induced, first order, phase transition between a paramagnetic state and spin polarized state [Wohlfarth and Rhodes, 1962]. Experimentally, IEM has been observed for YCo_2 and $LuCo_2$ around 70 T. [Goto et al., 1989, Goto et al., 1990] Within the framework of Landau theory, the maximum in temperature dependent susceptibility is thought to be related to IEM.[Shimizu, 1981b] The magnetic part of the free energy ΔF

can be writen as the function of the magnetic moment M:

$$\Delta F = \frac{1}{2}aM^2 + \frac{1}{4}bM^4 + \frac{1}{6}cM^6 \ , \tag{8.11}$$

where a, b and c are the Landau expansion coefficients.

As shown by Shimizu [Shimizu, 1981b], the condition for the existence of IEM is: $a > 0$, $b < 0$, $c > 0$ and $\frac{3}{16} < \frac{ac}{b^2} < \frac{9}{20}$. Within the framework of the spin fluctuation theory, Yamada [Yamada, 1993] generalized this work by introducing a temperature dependent function of the mean square amplitude of spin fluctuations. These theoretical works demonstrated that the existence of IEM is associated with the maximum in $\chi(T)$ by means of the factor of $\frac{ac}{b^2}$, which can be estimated as:

$$\frac{ac}{b^2} = [1 - \frac{\chi(0)}{\chi(T_{max})}]^{-1}. \tag{8.12}$$

Furthermore, the IEM can only happen below T_{max}. These results seem to be consistent with the experimental results in various itinerant electronic systems. [Goto et al., 2001]

According to the Eqn. 8.12, the values of $\frac{ac}{b^2}$ can be estimated as 310 and 72 for YFe_2Zn_{20} and $LuFe_2Zn_{20}$ respectively ($M/H \sim \chi(T)$ at 10 kOe), which are much larger than the region of the existence of IEM, indicating that IEM may not exist. Indeed, recent measurements on a part of the $LuFe_2Zn_{20}$ sample used for the magnetization data in Fig. 8.1 in a pulse magnetic field up to 55 T at 0.3 K, show no evidence of metamagnetic transition. In nearly FM materials, no evidence of IEM appears for $TiBe_2$,[Yamada and Terao, 1998], which also manifests a relative low value of T_{max}. From these points of view, Y(Lu)Fe_2Zn_{20} and $TiBe_2$ may represent the examples of NFFLs different from YCo_2 and $LuCo_2$.

This lack of an IEM sheds further light on the magnetic properties of the local moment bearing, RFe_2Zn_{20} (R = Gd - Tm) compounds. As shown before, all the members manifest 2nd order paramagnetic to ferromagnetic phase transitions. This behavior is different from that seen in the RCo_2 (R = Gd - Tm) system: the magnetic phase transitions of R = Dy - Tm members for RCo_2 are 1st order whereas R = Gd and Tb members have 2nd order transitions [Duc and Brommer, 1999]. This difference is not difficult to explain in Landau theory: unlike Y(Lu)Co_2, the host of Y(Lu)Fe_2Zn_{20} lack of ability to show IEM and therefore can not be

induced to show metamagnetic transition by any molecular field associated with the $4f$ local moments.

8.4 Summery

RFe_2Zn_{20} and RCo_2Zn_{20} (R = Gd - Lu, Y) demonstrate diverse magnetic properties. The conspicuous differences are mainly associated with the conduction electron polarizability of the host (non-magnetic) compounds. YFe_2Zn_{20} and $LuFe_2Zn_{20}$ manifest similar,nearly ferromagnetic properties. When the $4f$ local moments are embedded in this highly polarizable medium, RFe_2Zn_{20} (R = Gd - Tm) series show highly enhanced FM ordering. In contrast, YCo_2Zn_{20} and $LuCo_2Zn_{20}$ manifest normal, Pauli paramagnetic behaviors. In a related manner, $GdCo_2Zn_{20}$ and $TbCo_2Zn_{20}$ show low temperature AFM ordering, and the magnetic properties for RCo_2Zn_{20} (R = Dy - Tm) are more strongly influenced by the CEF effect on the R ions. CEF coefficients determined for the Co series are consistent with the properties of the Fe series. On the other hand, $YbFe_2Zn_{20}$ and $YbCo_2Zn_{20}$ manifest different heavy Fermion behaviors.

CHAPTER 9. Thermodynamic and transport properties of YbT_2Zn_{20} (T= Fe, Ru, Os, Co, Rh and Ir) *

9.1 Introduction

Heavy fermion compounds have been recognized as premier examples of strongly correlated electron behavior for several decades.[Hewson, 1993] Ce- and U-based heavy fermion compounds have been well studied, and in recent years a small number of Yb-based heavy fermions have been identified as well.[Stewart, 1984b, Stewart, 2001, Stewart, 2006] Unfortunately, in part due to the somewhat unpredictable nature of $4f$ ion hybridization with the conduction electrons, it has been difficult to find closely related (e.g., structurally) heavy fermion compounds, other than of the $ThCr_2Si_2$ structure, especially Yb-based ones, that allow for systematic studies of the Yb ion degeneracy. Part of this difficulty is associated with the fact that the $4f$ hybridization depends so strongly on the local environment of the rare earth ion.

In this Chapter, I present thermodynamic and transport data on six strongly correlated Yb-based intermetallic compounds found in the RT_2Zn_{20} family for T = Fe, Co, Ru, Rh, Os, and Ir. Containing less than 5 at. % of rare earth ions which still fully occupy one unique crystallographic site, RT_2Zn_{20} intermetallic compounds offer the possibility of investigating $4f$ electronic magnetism in fully ordered compounds for relatively low rare earths concentration. For the case of R = Yb or Ce, these materials offer the possibility of preserving low temperature, coherent effects while more closely approximating the single ion, Kondo impurity limit. With the specific heat coefficient values of $\gamma > 400$ mJ/mol K^2, these six Yb compounds effectively

*after "Six closely related YbT_2Zn_{20} (T= Fe, Ru, Os, Co, Rh and Ir) heavy fermion compounds with large local moment degeneracy", M. S. Torikachvili, S. Jia, E. D. Mun, S. T. Hannahs, R. C. Black, W. K. Neils, Dinech Martien, S. L. Bud'ko, P. C. Canfield, *Proc. Natl. Acad. Sci. U. S. A.* **104** 9960 (2007).

double the number of known Yb-based heavy fermions [Stewart, 1984b].

As shown in the previous chapters, the rare earth ion is coordinated by a CN16 Frank-Kasper polyhedron consisted by Zn atoms in a cubic point symmetry. This near spherical distribution of neighboring Zn atoms gives rise to a relatively low crystal electric field (CEF) effect, which has been investigated for the isostructural, local moment members (R = Tb - Tm, T = Co and Fe). In addition the isolated and dilute Yb and T sites promise a large degree of similarity between the members of this isostructural group of Yb-based heavy fermions. These compounds provide a route to studying how the degeneracy of the Yb ion at Kondo temperature, $T_{\rm K}$, effects the low temperature-correlated state.

9.2 Result

Thermodynamic and transport data taken on the six YbT_2Zn_{20} compounds are presented in Figs. 9.1–9.3 and are summarized in Table 9.1. At first glance, the temperature dependent magnetic susceptibility, electrical resistivity and specific heat for T = Fe, Ru, Rh, Os, and Ir are qualitatively similar, whereas YCo_2Zn_{20} manifests somewhat different magnetic properties. Most conspicuously, instead of manifesting a clear loss of local moment behavior at low temperature, the temperature-dependent susceptibility of $YbCo_2Zn_{20}$ continues to be Curie-Weiss-like down to 2 K [Fig. 9.1 (a) Inset].

Focusing initially on the five, apparently similar, YbT_2Zn_{20} compounds (T = Fe, Ru, Rh, Os, Ir), Fig. 9.1 (b) demonstrates that each of these compounds appears to be an excellent example of a Yb-based heavy fermion with electronic specific heat, γ, values ranging between 500 and 800 mJ/mole K^2. These large γ values are consistent with a clear loss of local moment behavior for each compound below 20 K. The modest rise in the $C_p(T)/T$ data below 2 K is most probably associated with a nuclear Schottky anomaly and, for this work, is simply ignored. The low temperature magnetic susceptibility correlates well with the electronic specific heat values leading to the Wilson ratio for these five compounds having values between 1.1 and 1.3 (see Table 9.1). The temperature-dependent electrical resistivity data (Fig. 9.2) for these five compounds are also remarkably similar at high temperature and manifest clear T^2 temperature

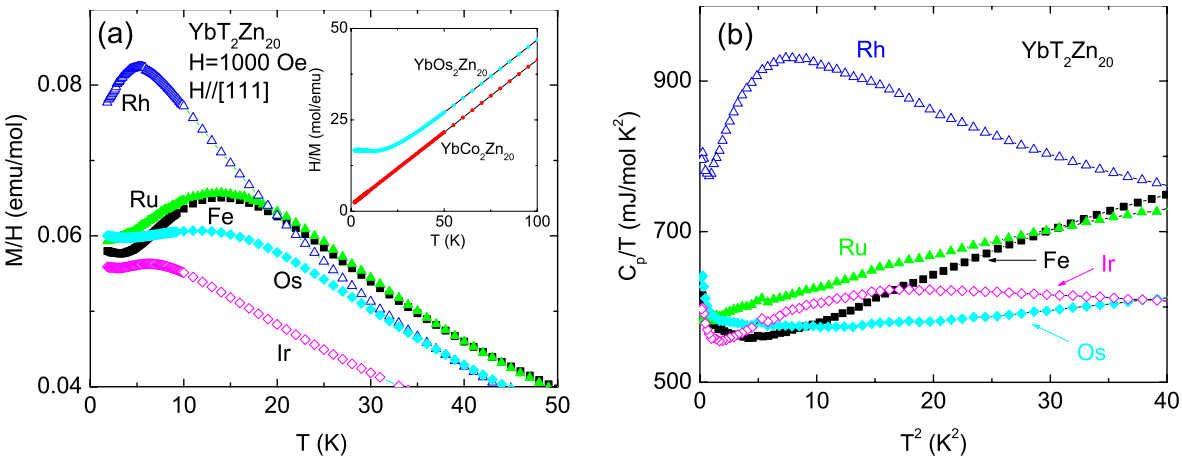

Figure 9.1 Low temperature thermodynamic properties of YbT_2Zn_{20} compounds (T = Fe, Ru, Rh, OS, Ir). (a) Magnetization (M) divided by the applied field (H = 1000Oe. Inset: H/M for $YbCo_2Zn_{20}$ and $YbOs_2Zn_{20}$. (b) Low temperature specific heat (C_p) divided by temperature, as a function of T^2.

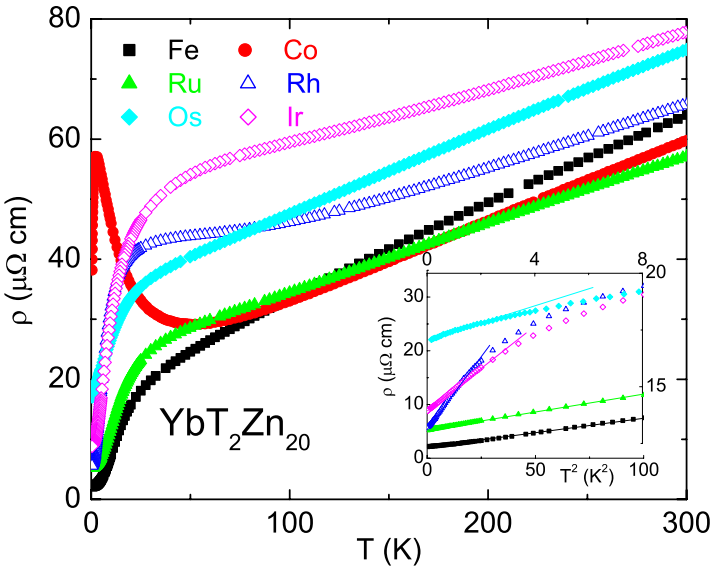

Figure 9.2 Temperature dependent electrical resistivity if YbT_2Zn_{20} compounds (T = Fe, Co, Ru, Rh, OS, Ir). Inset: Low temperature resistivity as a function of T^2 for T = Fe, Ru, Rh, Os, Ir; note separate axes for T = Os on top and right.

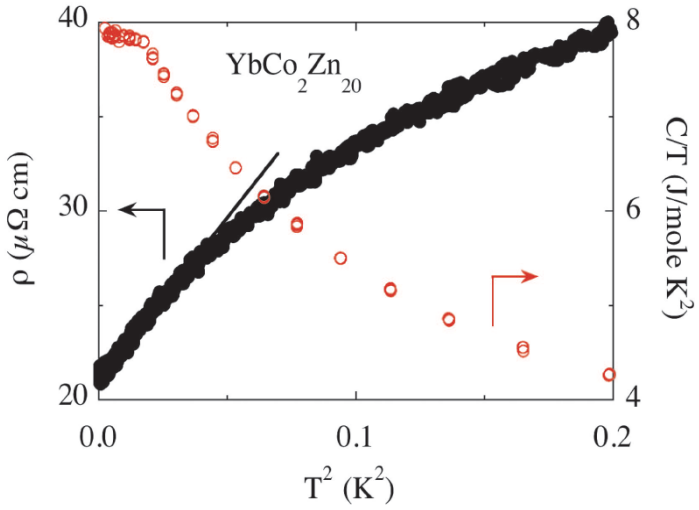

Figure 9.3 Low temperature electrical resistivity and C_p/T of $YbCo_2Zn_{20}$ as a function of T^2.

dependencies at low temperatures (see Inset of Fig. 9.2). Although resistivity data were taken down to 20 mK, no indications of either magnetic order or superconductivity were found for any of the YbT_2Zn_{20} compounds.

The thermodynamic and transport properties of $YbCo_2Zn_{20}$ are somewhat different from the other five compounds. $YbCo_2Zn_{20}$ does not manifest the clear loss of local moment behavior above 1.8 K, in the susceptibility data [see Fig. 9.1 (a) Inset] and the electrical resistivity and the specific heat only manifest Fermi-liquid-like behavior associated with $\rho \sim AT^2$ and $C_p(T)/T \sim \gamma$ for T less than 0.2 K (Fig. 9.3). Although the higher temperature electrical resistivity of $YbCo_2Zn_{20}$ is similar to the other five YbT_2Zn_{20} compounds, it manifests a much clearer example of a resistance minimum and lower temperature coherence peak about 2 K.

9.3 Data Analysis

The coefficient of the T^2 resistivity (A) is plotted as a function of the electric specific heat (γ) for these six Yb compounds in their Fermi liquid state in a Kadowaki-Woods (KW) [Kadowaki and Woods, 1986, Miyake et al., 1989] type plot along with other Yb-based com-

pounds that manifest varying degrees of hybridization (Fig. 9.4). The extremely large A and γ values for $YbCo_2Zn_{20}$ place its data point far away from the other five compounds and near to the point associated with the exceptionally heavy Fermion, YbPtBi [Fisk et al., 1991, Movshovich et al., 1994]. For the T = Fe, Ru, Rh, Os and Ir compounds, the A values vary by as much as one order of magnitude, whereas the γ values vary relatively little. This gives rise to a vertical spread of the KW data points, associated with the values of Kadowaki-Woods ratio (KWR) ranging from 2×10^{-7} to 15×10^{-7} $\mu\Omega\text{mol}^2\text{K}^2/\text{mJ}^2$.

Recent theoretical work [N Tsujii and Kosuge, 2003, Tsujii et al., 2005, Kontani, 2004] has generalized the idea of a fixed KWR ($\sim 1 \times 10^{-5}$ $\mu\Omega\text{mol}^2\text{K}^2/\text{mJ}^2$) to one that can vary by over an order of magnitude, depending on the value of the degeneracy of the Yb ion when it hybridizes. Fig. 9.4 shows, as solid lines, the KWR values for the four degeneracies possible for the Kramers, Yb^{3+} ion. The low KWR values for $YbFe_2Zn_{20}$ and $YbRu_2Zn_{20}$ indicate that for T = Fe, Ru the Yb ion has a significantly larger degeneracy upon entering the Kondo-screened state than is the case for the T = Rh, Os, Ir compounds.

As shown in Chapter 3, the sole Yb site is surrounded by 16 Zn NNs and NNNs in a cubic point symmetric coordination. Therefore, the Yb ion's Hund's rule ground state multiplet ($N = 8$) will split to a quartet and two doublets states will a small total splitting by the CEF effect. If, as Tsujii et al. suggested, the competition between the CEF splitting Δ and the Kondo temperature T_K is the primary factor giving rise to the varied values of the KWR, then there should be some indication of this in other data as well. In the light of the Coqblin-Schrieffer model [Coqblin and Schrieffer, 1969, Rajan, 1983], an examination of Fig. 9.1 indicates that the larger the ratio of the maximum susceptibility to the low temperature susceptibility, the larger is the degeneracy of the Yb system at T_K. The ratios of the maximum susceptibility to the low temperature susceptibility for T = Fe and Ru are 1.12 and 1.11, respectively, whereas the ratios for T = Rh, Os, and Ir are 1.06, 1.01, and 1.01, respectively. These values are consistent with a difference in degeneracy of at least $\Delta N = 2$ (see Fig. 9.4).

This analysis can be made even more thoroughly by performing a fit [Rajan, 1983] to the magnetic susceptibility [$\chi(T)$] and the magnetic part of specific heat (C_m) over a wide

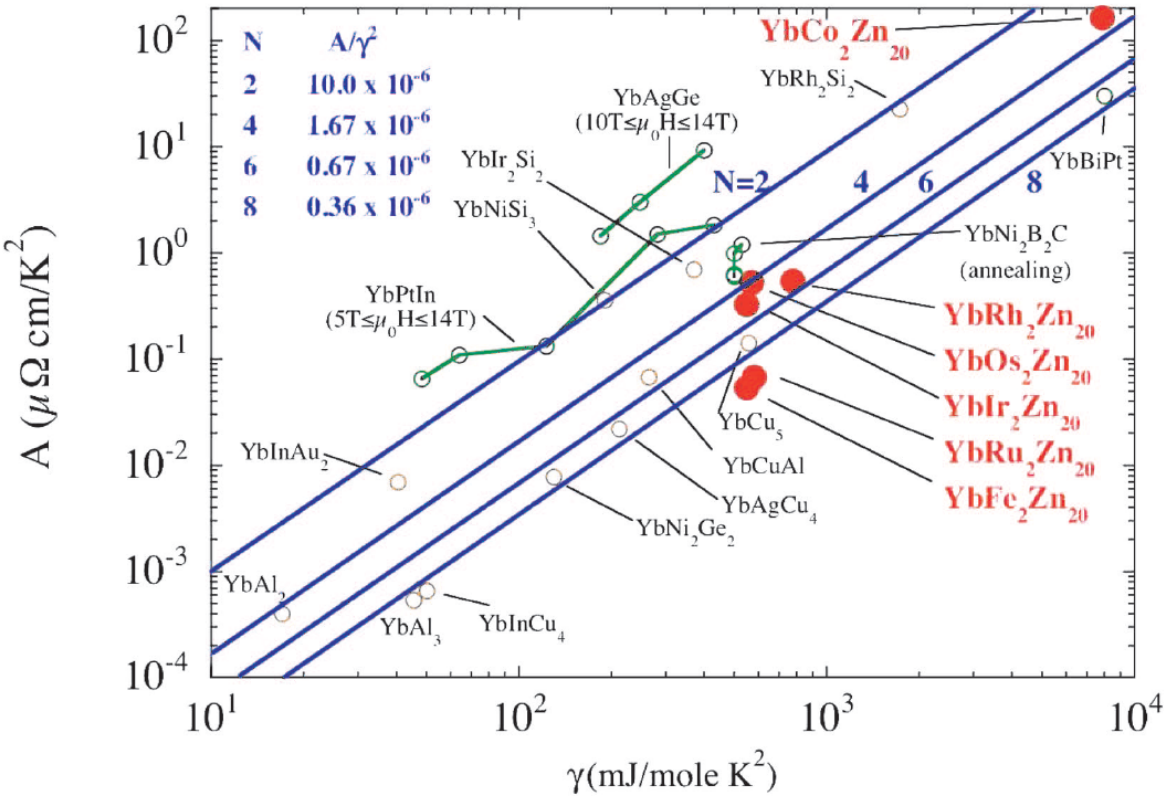

Figure 9.4 Loglog plot of A versus γ (KadowakiWoods plot) of six new YbT_2Zn_{20} heavy fermion compounds (T = Fe, Co, Ru, Rh, Os, Ir) shown with representative data from ref. [Tsujii et al., 2005] as well as data for YbBiPt [Fisk et al., 1991, Movshovich et al., 1994], $YbNi_2B_2C$ [Avila et al., 2004b], YbPtIn [Morosan et al., 2006],YbAgGe [Bud'ko et al., 2004], $YbNiSi_3$ [Avila et al., 2004a], and $YbIr_2Si_2$ [Hossain et al., 2005]. The solid lines for degeneracies $N = 2$, 4, 6, and 8 are taken from ref. [Tsujii et al., 2005].

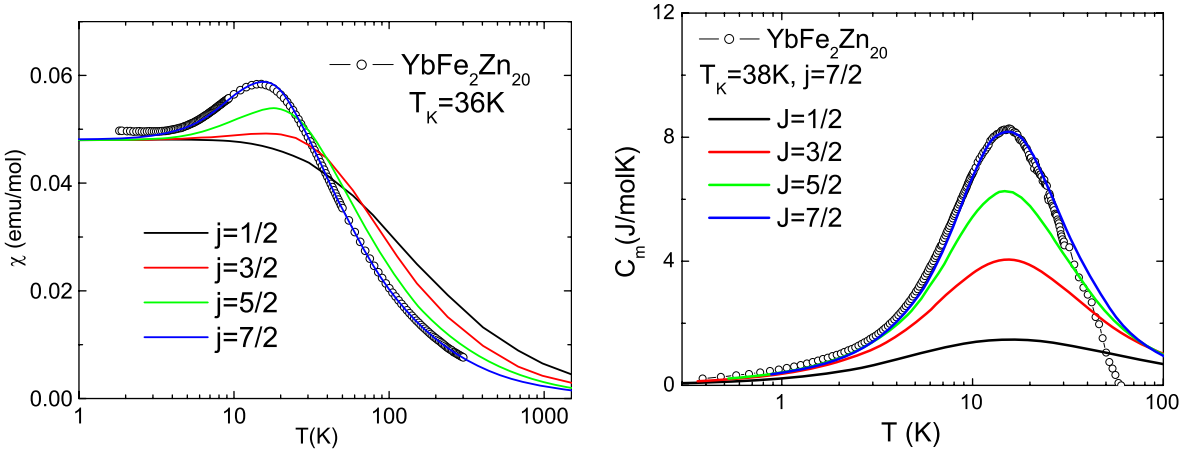

Figure 9.5 Coqblin-Schrieffer analysis of magnetic susceptibility (a) and specific heat data (after subtraction from the nonmagnetic analogues, $LuFe_2Zn_{20}$) (b) for $YbFe_2Zn_{20}$. Data are shown as open symbols and best fits to $J = 1/2$, $3/2$, $5/2$, $7/2$ using formalism described in ref. [Rajan, 1983] are shown in black, red, green, and blue lines, respectively. T_K values from these fits are $\simeq 36$ K and $\simeq 38$ K.

temperature range. This is shown in figs. 9.5 for $YbFe_2Zn_{20}$, the compound with the largest degeneracy ($N = 8$) inferred from the KW plot (Fig. 9.4). Both $\chi(T)$ and C_m data are best fit by the $J = 7/2$ ($N = 8$) curve. These data are particularly compelling because the height of the anomaly is not an adjustable parameter once N is chosen. This analysis further confirms the degeneracy inferred from Fig. 9.4 and confirms that the low temperature, greatly enhanced, electronic specific heat is due to Kondo screening of the large degenerate Yb ion.

Figures 9.6 presents similar data from $YbRh_2Zn_{20}$, one of the compounds that the KW analysis predicts to have a lower degeneracy at T_K. The susceptibility data are best fit by $J = 3/2$. The maximum in the magnetic specific heat data falls between the $J = 3/2$ and $J = 5/2$ values, indicating that the CEF splitting scheme will not allow the very simple type of analysis on which ref. [Rajan, 1983] is premised: i.e., one that has the CEF levels either at $T \ll T_K$ or $T \gg T_K$. These data can be well fit, though, by the addition of a Schottky anomaly associated with a $T \geq T_K$ CEF level. The low temperature part of the specific heat data can be well fit by assuming that a quadruplet is Kondo screened and that there is a doublet CEF

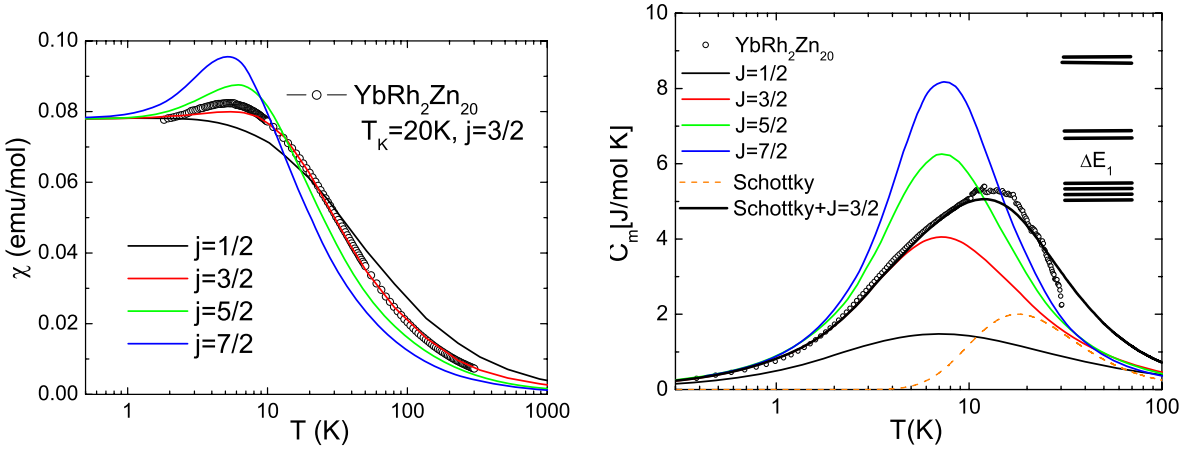

Figure 9.6 Coqblin-Schrieffer analysis of magnetic susceptibility (left panel) and specific heat data (after subtraction from the non-magnetic analogues, $LuRh_2Zn_{20}$) (right panel) for $YbRh_2Zn_{20}$. The Schottky contribution ($\Delta E_1 = 40$ K) is shown as a dashed red line; the sum of Schottky and Rajan ($J = 3/2$) terms is shown as a solid black line. T_K values from these fits are $\simeq 20$ K and $\simeq 15$ K.

level located at 40 K. The sum of the Kondo screened quadruplet and the Schottky anomaly associated with the 40 K doublet are shown as the solid line. Taken together, Figs. 9.4-9.6 indicate that the large electronic specific heat values shown in Fig. 9.1 are due to Kondo screening and that the degeneracies for the YbT_2Zn_{20} compounds are most probably $N = 8$ for T = Fe, Ru and $N = 4$ for T = Os, Co, Rh, Ir.

As the degeneracies of the Yb ions were inferred, by the analysis above, when they enter the Kondo screening states (see Table 9.1), the values of their T_K can be then inferred by using $T_K = (R \ln N)/\gamma$, a rough estimation from magnetic entropy [Fisk et al., 1988], or by using $T_K = (N-1)\pi^2 R\omega_N/3N\gamma$, the Bethe ansatz results of N-fold CoqblinSchrieffer model [Hewson, 1993] where ω_N is the so called Wilson number and that is a function of N as discussed in ref. [Rasul and Hewson, 1984]. These expressions produce T_K values that are within 5% of each other for $2 \leq N \leq 8$. It should also be noted that the T_K value estimated by this method is close to that found by fitting the thermodynamic data (see Fig. 9.5 and 9.6). As could be anticipated, T_K values for T = Fe and Ru are indeed larger than those found for T = Rh, Os, Ir.

Table 9.1 Summary of structural, thermodynamic and transport data on YbT_2Zn_{20} compounds (T = Fe, Co, Ru, Rh, OS and Ir). Shown are cubic lattice parameter, a; paramagnetic CurieWeiss temperature, θ_C, and effective moment, μ_{eff}, obtained from fit to inverse susceptibility between 100 and 300 K (after subtractions data from the nonmagnetic analogues, LuT_2Zn_{20}); low temperature magnetic susceptibility, χ_0 taken at 1.8 K; magnetic susceptibility at the maximum, χ_{max} and corresponding temperature, $T_{\chi max}$; residual resistivity, ρ_0, taken at $T \simeq 20$ mK; coefficient of the T^2 resistivity, A (with range of fit given below); residual resistivity ratio, RRR; linear coefficient of the specific heat, γ; Wilson ratio, WR; KadowakiWoods ratio, KWR; degeneracy, N; and estimated Kondo temperature, T_K.

T	a	θ_C	μ_{eff}	χ_0	χ_{max}	$T_{\chi max}$	ρ_0	A	RRR	γ	WR	KWR	N	T_K
	Å	K	μ_B	$\frac{10^{-3}\text{emu}}{\text{mol}}$	$\frac{10^{-3}\text{emu}}{\text{mol}}$	K	$\mu\Omega$cm	$\mu\Omega$cm K^{-2}		$\frac{\text{mJ}}{\text{mol K}^2}$		$\frac{\mu\Omega\text{cm mol}^2\text{K}^2}{\text{mJ}^2}$		K
Fe	14.062	-22.6	4.5	58.0	65.1	14.0	2.1	5.4×10^{-2} ($T \leq 11$ K)	31.2	520	1.2	2.0×10^{-7}	8	33
Co	14.005	-4.2	4.3	415.1			21	165 ($T \leq 0.2$ K)	2.8	7900		27×10^{-7}	4	1.5
Ru	14.193	-15.5	4.5	58.9	65.4	13.5	5.3	6.8×10^{-2} ($T \leq 11$ K)	10.9	580	1.1	2.0×10^{-7}	8	30
Rh	14.150	-15.9	4.4	77.7	82.4	5.3	5.6	54×10^{-2} ($T \leq 6$ K)	11.8	740	1.3	10.1×10^{-7}	4	16
Os	14.205	-19.2	4.5	60.0	60.7	11.5	17	53×10^{-2} ($T \leq 1$ K)	4.4	580	1.1	15×10^{-7}	4	20
Ir	14.165	-23.8	4.4	55.9	56.3	6.5	8.8	33×10^{-2} ($T \leq 5$ K)	8.9	540	1.2	11×10^{-7}	4	21

9.4 Discussion

Given that the studies of the RT_2Zn_{20} families in Chapter 5-8 have shown that T = Fe and Ru compounds manifest anomalously high-temperature, local moment ordering due to the fact that the Y and Lu host materials are close to the Stoner limit, it is noteworthy that for the YbT_2Zn_{20} materials it is the T = Fe and Ru compounds that appear to be significantly different from the T = Rh, Os, and Ir compounds. Although we currently do not have enough data to conclude that this Stoner enhancement of the host material (if it even persists in the Yb based members) is responsible for the higher ratio of T_K to the CEF splitting Δ , such an enhancement certainly could be responsible for increased T_K values. This question is the focus of an ongoing study of pseudo ternary $Yb(Fe_xCo_{1-x})_2Zn_{20}$ compounds.

Although at first glance the data for $YbCo_2Zn_{20}$ appear to be different from that of the other members of this family, at low enough temperatures, it also appears to enter into a Fermi liquid ground state and, as shown in Fig. 9.4, has an intermediate N value, similar to $YbOs_2Zn_{20}$. $YbCo_2Zn_{20}$ has a substantially lower T_K, and may be closer to a quantum critical point (QCP) than the other, T = Fe, Ru, Rh, Os, Ir members of the family: i.e., small perturbations to $YbCo_2Zn_{20}$ may lead to the onset of magnetic order, giving rise to a $T = 0$ phase transition controlled by a non-thermal (magnetic field, pressure, doping) tuning parameter. If $YbCo_2Zn_{20}$ is simply closer to a QCP, then, given that the unit cell dimensions for $YbCo_2Zn_{20}$ are the smallest of the family, this would imply that applications of modest pressure to other members of the YbT_2Zn_{20} family may lead to several new Yb-based compounds for the study of quantum criticality. Most recently, a magnetic transition in $YbCo_2Zn_{20}$ has been observed under the pressure larger than 1 GPa in electrical resistivity measurements. [Saiga et al., 2008]

CHAPTER 10. Summary and Conclusion

The study of the RT_2Zn_{20} system was part of an exploration of the magnetic properties of large unit cell intermetallic compounds with dilute rare earth ions that are still fully occupying a unique crystallographic site. Such compounds offer the possibility of studying local moment as well as hybridizing rare earth closer to the single ion limit, but still preserving periodicity.

Single crystals of RT_2Zn_{20} compounds were grown from Zn self-flux, and then identified by the X-ray diffraction measurements. Thermodynamic and transport measurements indicated that YFe_2Zn_{20} is closer to the Stoner criteria than element Pd, the canonical example of a nearly ferromagnetic Fermi liquid. As a result of local moments associated with Gd^{3+} being embedded in this highly polarizable Fermi liquid, remarkably high-temperature ferromagnetic ordering (T_C = 86 K) was found for $GdFe_2Zn_{20}$. By tuning the transition metal site, the pseudo-ternary compounds $Y(Fe_xCo_{1-x})_2Zn_{20}$ could be tuned from the edge of the Stoner limit to a 'normal metal' state. Dependent on the band filling, the magnetically ordered state of $Gd(Fe_xCo_{1-x})_2Zn_{20}$ range from high-temperature, ferromagnetic one to low-temperature, antiferromagnetic one. This relation between the conduction electronic background and the local moment ordering also manifests itself for the transition metal site is Ru, Rh, Os and Ir. Ferromagnetic ordering of the local moment was found in GdT_2Zn_{20} as T equaling the iron column members (with enhanced T_C values for T = Fe and Ru) and low temperature antiferromagnetic (AFM) ordering was found for the cobalt column members. Correspondingly, nearly ferromagnetic behaviors were found for the T = Fe and Ru members in YT_2Zn_{20} analogues.

So as to study the effects of T on R ions other than Gd, Y, and Lu, a thorough compound-by compound study of the R = Tb - Tm members in RFe_2Zn_{20} and RCo_2Zn_{20} series was made. For the RCo_2Zn_{20} series, only Gd and Tb members manifest AFM ordering above 2 K, and

the magnetic properties for R = Dy - Tm clearly manifest features associated with single ion CEF effects on the R ions. In contrast, for the RFe_2Zn_{20} series, the well-defined local moment members (R = Gd - Tm) all manifest enhanced ferromagnetic ordering with T_C values roughly scaling with the de Gennes factor. The R = Tb - Tm members show moderate magnetic anisotropy in their ordered state, mainly due to the CEF effect on the R ions.

As a model system of very dilute local moments in a NFFL, pseudo-ternary compounds $Gd_xY_{1-x}Fe_2Zn_{20}$ were studied for varied Gd concentrations (x). Ferromagnetic ordering of the local moments associated with Gd^{3+} ions was found above 1.80 K for $x > 0.02$. The measurement results were discussed within the framework of the so-called $s-d$ model[Shimizu, 1981a], based on the mean field approximation, and used to explain the variation of T_C across the series with respect to x.

In addition to these local moment bearing compounds, six Yb compounds (YbT_2Zn_{20} , T = Fe, Co, Ru. Rh, Os and Ir) proved to be heavy fermion compounds with electronic specific heat coefficients $\gamma > 500$ mJ/mol K^2. Thermodynamic and transport measurements revealed that $YbCo_2Zn_{20}$ is close to the quantum critical point and has a substantially lower $T_K \simeq 1$ K. The other five compounds manifest Fermi liquid states associated with different degeneracy of the Yb ion for T = Fe, Ru and T = Rh, Os and Ir. Such differences are due to the competition between the different T_K values and the similar CEF splitting of the Yb ions in these isostructural compounds.

Possessing a rich phase space that allows for tuning of the band filling, the local moment concentration as well as the hybridized $4f$ electronic state, the RT_2Zn_{20} family offer a model system for the study of local moment magnetism, itinerant electronic magnetism, and heavy Fermion physics. Future work should be devoted to investigating the pseudo-ternary Yb compounds with varied transition metal doping. Such studies will help lead to an understanding of how the hybridization of Yb's $4f$ electrons takes place as they are submerged in varied conduction electron backgrounds. Also, the study of the isostructural, RT_2Zn_{20} (R = Dy - Lu, T = Ni and Pt) compounds might further our understanding of the relation between the band filling and local moment magnetic ordering.

APPENDIX A. Sample dependent, magnetic transitions for $TbFe_2Zn_{20}$

Figure A.1 shows the magnetization (at H = 1000 Oe) and zero applied field resistivity for three batches of $TbFe_2Zn_{20}$, which were synthesized from different initial molar ratios of starting elements, Tb:Fe:Zn = 2:3:95, 2:4:94 and 2:5:93. The ferromagnetic ordering temperatures, determined as 52 ± 2 K, 56 ± 1 K and 67 ± 2 K for the three samples, increase as the growth concentration of Fe increases. Similar features were also found for R = Gd and Er, but the variation of the T_C values are less than in the Tb case. Comparative, Single crystal x-ray diffraction measurements performed on the samples, albeit inconclusive, indicated that the crystallographic differences are mainly associated with subtle (at the edge of resolution) variations of occupancy of the Fe site.[Ko et al., 2008] The main difficulty with x-ray diffraction measurements is related to the similar atomic number values for Zn and Fe. Recently, two carefully prepared, pieces of $TbFe_2Zn_{20}$ samples with same geometric form and dimension, from the starting elements, Tb:Fe:Zn = 2:3:95 and 2:5:93, were used for single-crystal neutron scattering.[Christianson, 2008] This measurement result found that the Fe site has $\sim 1\%$ deficiency for the 2:3:95 sample. All these crystallographic measurements indicate the sensitivity of the magnetic properties to the small disorder for RFe_2Zn_{20} compounds, which is not uncommon for the correlated electron systems (such as the NFFL background).

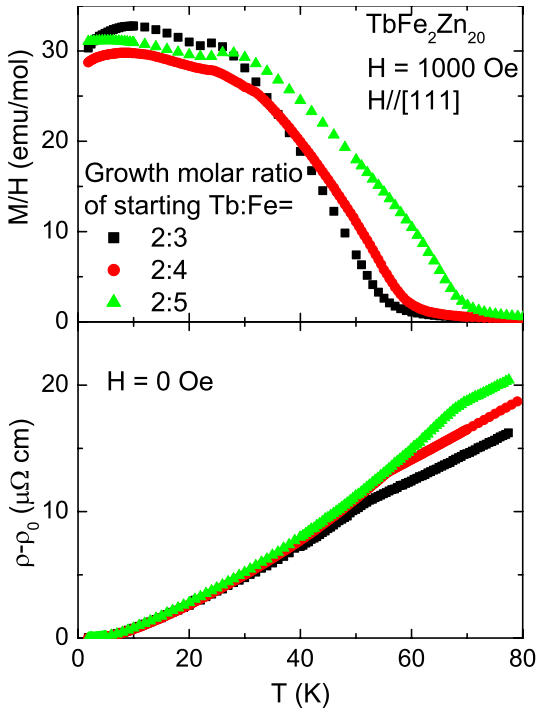

Figure A.1 (a): Temperature dependent M/H for $TbFe_2Zn_{20}$ (H = 1000 Oe) from different initial growth molar ratio of starting elements; (b) temperature dependent ρ in zero applied field.

APPENDIX B. Determination of CEF parameters of RT_2Zn_{20} system by point charge model

As shown in Fig. 3.1, the distance between the rare earth ion and NNs, as well as NNNs, is close to 3 Å; whereas the distance with the next next nearest neighbors (NNNN, 6 Zn in $48f$ site) is larger than 5 Å. Due to this isolated, cage-like coordinate of rare earth ions, the effect of the ions other than the CN-16 Frank-Kasper polyhedron is neglected in the calculation of the CEF coefficient, based on the point charge model.

The neighbors shell of rare earth ion in the C-15 Laves compounds (RNi_2) forms the same polyhedron, whose CEF coefficients have been calculated by B. Bleaney [Bleaney, 1963], based on the point charge model. Therefore, one can directly cite the results:

$$B_4^0 = -\frac{3}{2}\left(\frac{91e^2Z_1}{726R_1^5} - \frac{7e^2Z_2}{54R_2^5}\right)\left\langle r^4\right\rangle \langle J\|\beta\|J\rangle \tag{B.1}$$

$$B_6^0 = \frac{9}{16}\left(-\frac{8e^2Z_1}{363R_1^7} - \frac{8e^2Z_2}{81R_2^7}\right)\left\langle r^6\right\rangle \langle J\|\gamma\|J\rangle\,, \tag{B.2}$$

where Z_1e and Z_2e is the charge of the NN and NNN ions ($Z_1 = Z_2 = 2$ for Zn^{2+}), R_1 and R_2 is the distance between the R ion and the two sets of ions, $\left\langle r^4\right\rangle$ and $\left\langle r^6\right\rangle$ are the mean fourth and sixth powers of the electronic radius for the $4f$-electrons, and β and γ are the Steven multiplicative factors. Extracting the values of $\left\langle r^4\right\rangle$ and $\left\langle r^6\right\rangle$ from ref.[Freeman and Watson, 1962], β and γ values from ref.[Lea et al., 1962], and R_1 and R_2 values from single crystal X-ray diffraction result, one can calculate the B_4^0 and B_6^0 values.

BIBLIOGRAPHY

[Acker et al., 1981] Acker, F., Fisk, Z., Smith, J. L., and Huang, C. Y. (1981). Enhanced paramagnetism of $TiBe_2$ and ferromagnetic transitions in $TiBe_{2-x}Cu_x$. *Journal of Magnetism and Magnetic Materials*, 22:250–256.

[Anderson, 1961] Anderson, P. W. (1961). Localized magnetic states in metals. *Physical Review*, 124:41.

[Andrei, 1980] Andrei, N. (1980). Diagonalization of the kondo hamiltonian. *Physical Review Letters*, 45:379.

[Arrott, 1957] Arrott, A. (1957). Criterion for ferromagnetism from observations of magnetic isotherms. *Physical Review*, 108:1394.

[Ashcroft and Mermin, 1976] Ashcroft, N. W. and Mermin, N. D. (1976). *Solid state physics*. Saunders College Philadelphia, Pa.

[Avila et al., 2004a] Avila, M. A., Sera, M., and Takabatake, T. (2004a). $YbNiSi_3$: An antiferromagnetic kondo lattice with strong exchange interaction. *Physical Review B*, 70:100409.

[Avila et al., 2004b] Avila, M. A., Wu, Y. Q., Condron, C. L., Bud'ko, S. L., Kramer, M., Miller, G. J., and Canfield, P. C. (2004b). Anomalous temperature-dependent transport in $YbNi_2B_2C$ and its correlation to microstructural features. *Phys. Rev. B*, 69(20):205107.

[B Zellermann and Voitländer, 2004] B Zellermann, A. P. and Voitländer, J. (2004). The onsager reaction field concept applied to the temperature dependent magnetic susceptibility of the enhanced paramagnets Pd and Pt. *Journal of Physics: Condensed Matter*, 16(6):919–934.

[Benbow and Latturner, 2006] Benbow, E. M. and Latturner, S. E. (2006). Mixed-metal flux synthesis of quaternary $RMn_2Tr_xZn_{20-x}$ compounds with Tr=Al, In. *Journal of Solid State Chemistry*, 179:3989–3996.

[Binder and Young, 1986] Binder, K. and Young, A. P. (1986). Spin glasses: Experimental facts, theoretical concepts, and open questions. *Reviews of Modern Physics*, 58(4):801.

[Bleaney, 1963] Bleaney, B. (1963). Crystal field effects and the co-operative state. II. the cubic $LnNi_2$ compounds. *Proceedings of the Royal Society of London. Series A, Mathematical and Physical Sciences*, 276(1364):28–38.

[Bloch et al., 1975] Bloch, D., Edwards, D. M., Shimizu, M., and Voiron, J. (1975). First order transitions in ACo_2 compounds. *Journal of Physics F: Metal Physics*, 5(6):1217–1226.

[Bloch and Lemaire, 1970] Bloch, D. and Lemaire, R. (1970). Metallic alloys and exchange-enhanced paramagnetism. application to rare-earth & cobalt alloys. *Physical Review B*, 2(7):2648.

[Brommer and Franse, 1990] Brommer, P. E. and Franse, J. J. M. (1990). in *Ferromagnetic Materials* vol 5, edited by K.H.J. Buschow and E.P. Wohlfarth, pages 323–396. Amsterdam: North-Holland.

[Brooks and Johansson, 1993] Brooks, M. S. S. and Johansson, B. (1993). in *Handbook of Magnetic Materials* vol. 7 Edited by K.H.J. Buschow, pages 139–230. Amsterdam: Elsevier.

[Bud'ko et al., 2005] Bud'ko, S., Wilke, R., Angst, M., and Canfield, P. (2005). Effect of pressure on the superconducting transition temperature of doped and neutron-damaged MgB_2. *Physica C: Superconductivity*, 420:83–87.

[Bud'ko et al., 2004] Bud'ko, S. L., Morosan, E., and Canfield, P. C. (2004). Magnetic field induced non-fermi-liquid behavior in YbAgGe single crystals. *Physical Review B*, 69:014415.

[Burzo et al., 1993] Burzo, E., Gratz, E., and Pop, V. (1993). On the magnetic behaviour of ACo_2 ($A = Y, Lu, Zr, Sc$ and Hf) compounds. *Journal of Magnetism and Magnetic Materials*, 123:159–164.

[Campbell, 1972] Campbell, I. A. (1972). Indirect exchange for rare earths in metals. *Journal of Physics F: Metal Physics*, 2:L47–L50.

[Canfield and Fisher, 2001] Canfield, P. C. and Fisher, I. R. (2001). High-temperature solution growth of intermetallic single crystals and quasicrystals. *Journal of Crystal Growth*, 225:155–161.

[Canfield and Fisk, 1992] Canfield, P. C. and Fisk, Z. (1992). Growth of single crystals from metallic fluxes. *Philosophical Magazine Part B*, 65:1117–1123.

[Chikazumi and Graham, 1997] Chikazumi, S. and Graham, C. (1997). *Physics of Ferromagnetism*. Oxford University Press.

[Christianson, 2008] Christianson, A. D. (2008). private communication.

[Clogston et al., 1962] Clogston, A. M., Matthias, B. T., Peter, M., Williams, H. J., Corenzwit, E., and Sherwood, R. C. (1962). Local magnetic moment associated with an iron atom dissolved in various transition metal alloys. *Physical Review*, 125:541.

[Coqblin and Schrieffer, 1969] Coqblin, B. and Schrieffer, J. R. (1969). Exchange interaction in alloys with cerium impurities. *Physical Review*, 185:847.

[Craig et al., 1967] Craig, P. P., Goldburg, W. I., Kitchens, T. A., and Budnick, J. I. (1967). Transport properties at critical points: The resistivity of nickel. *Physical Review Letters*, 19:1334.

[Crangle, 1964] Crangle, J. (1964). Ferromagnetism in dilute solutions of gadolinium in palladium. *Physical Review Letters*, 13:569.

[de Boer et al., 1967] de Boer, F. R., Schinkel, C. J., and Biesterbos, J. (1967). High density of states and strong exchange interactions in Ni_3Ga. *Physics Letters A*, 25(8):606–607.

[Doniach, 1977] Doniach, S. (1977). The kondo lattice and weak antiferromagnetism. *Physica B+C*, 91:231–234.

[Duc and Brommer, 1999] Duc, N. H. and Brommer, P. E. (1999). in *Handbook of Magnetic Materials,* vol. 12, Edited by K.H.J. Buschow, pages 259–394. Amsterdam: Elsevier.

[Duc and Goto, 1999] Duc, N. H. and Goto, T. (1999). in *Handbook on the Physics and Chemistry of Rare Earths* vol. 26, edited by K.A. Gschneidner, Jr. and L. Eyring, pages 177–264. Amsterdam: Elsevier.

[Eiling and Schilling, 1981] Eiling, A. and Schilling, J. S. (1981). Pressure and temperature dependence of electrical resistivity of Pb and Sn from $1 - 300$ K and $0 - 10$GPa–use as continuous resistive pressure monitor accurate over wide temperature range; superconductivity under pressure in Pb, Sn and In. *Journal of Physics F: Metal Physics*, 11(3):623–639.

[Fisher, 1962] Fisher, M. E. (1962). Relation between the specific heat and susceptibility of an antiferromagnet. *Philos. Mag.*, 7:1731.

[Fisher and Langer, 1968] Fisher, M. E. and Langer, J. S. (1968). Resistive anomalies at magnetic critical points. *Physical Review Letters*, 20:665.

[Fisk et al., 1991] Fisk, Z., Canfield, P. C., Beyermann, W. P., Thompson, J. D., Hundley, M. F., Ott, H. R., Felder, E., Maple, M. B., de la Torre, M. A. L., Visani, P., and Seaman, C. L. (1991). Massive electron state in ybbipt. *Physical Review Letters*, 67:3310.

[Fisk and Remeika, 1989] Fisk, Z. and Remeika, J. P. (1989). in *Handbook on the Physics and Chemistry of Rare Earths* vol. 12, edited by K.A. Gschneidner, Jr. and L. Eyring, page 53. Amsterdam: Elsevier.

[Fisk et al., 1988] Fisk, Z., Thompson, J. D., and Ott, H. R. (1988). Heavy-electrons: New materials. *Journal of Magnetism and Magnetic Materials*, 76-77:637–641.

[Fournier and Gratz, 1993] Fournier, J. M. and Gratz, E. (1993). in *Handbook on the Physics and Chemistry of Rare Earths* vol. 17, edited by K.A. Gschneidner, Jr., L. Eyring, G. H. Lander and G. R. Choppin, pages 409–537. North-Holland.

[Franse and Radwanski, 1993] Franse, J. J. M. and Radwanski, R. J. (1993). in *Handbook of Magnetic Materials* vol. 7 Edited by K.H.J. Buschow, pages 307–501. Amsterdam: Elsevier.

[Freeman, 1972] Freeman, A. J. (1972). in *Magnetic properties of rare earth metals* Edited by R. J. Elliott, page 245. London: Plenum Press.

[Freeman and Watson, 1962] Freeman, A. J. and Watson, R. E. (1962). Theoretical investigation of some magnetic and spectroscopic properties of rare-earth ions. *Phys. Rev.*, 127(6):2058–2075.

[Gerhardt et al., 1981] Gerhardt, W., Razavi, F., Schilling, J. S., Hüser, D., and Mydosh, J. A. (1981). Pressure dependence of the magnetic susceptibility of pure Pd to 3.7 GPa from 1.3 to 300 K. *Phys. Rev. B*, 24(11):6744–6746.

[Gerhardt et al., 1983] Gerhardt, W., Schilling, J. S., Olijnyk, H., and Smith, J. L. (1983). Temperature and field dependence of the magnetic susceptibility of $TiBe_2$ under high pressure. *Phys. Rev. B*, 28(10):5814–5821.

[Goto et al., 1989] Goto, T., Fukamichi, K., Sakakibara, T., and Komatsu, H. (1989). Itinerant electron metamagnetism in YCo_2. *Solid State Communications*, 72:945–947.

[Goto et al., 2001] Goto, T., Fukamichi, K., and Yamada, H. (2001). Itinerant electron metamagnetism and peculiar magnetic properties observed in $3d$ and $5f$ intermetallics. *Physica B: Condensed Matter*, 300:167–185.

[Goto et al., 1990] Goto, T., Sakakibara, T., Murata, K., Komatsu, H., and Fukamichi, K. (1990). Itinerant electron metamagnetism in YCo_2 and $LuCo_2$. *Journal of Magnetism and Magnetic Materials*, 90 & 91:700–702.

[Gratz et al., 1995] Gratz, E., Resel, R., Burkov, A. T., Bauer, E., Markosyan, A. S., and Galatanu, A. (1995). The transport properties of RCo_2 compounds. *Journal of Physics: Condensed Matter*, 7:6687–6706.

[Gschneidner and Pecharsky, 2006] Gschneidner, Jr., K. A. and Pecharsky, V. K. (2006). Binary rare earth laves phases: an overview. *Zeitschrift für Kristallographie*, 221(5-7):375–381.

[Hayden et al., 1986] Hayden, S. M., Lonzarich, G. G., and Skriver, H. L. (1986). Electronic structure of the strongly-exchange-enhanced paramagnet Ni_3Ga. *Phys. Rev. B*, 33:4977–4986.

[Hewson, 1993] Hewson, A. C. (1993). *The Kondo Problem to Heavy Fermions*. Cambridge University Press.

[Hossain et al., 2005] Hossain, Z., Geibel, C., Weickert, F., Radu, T., Tokiwa, Y., Jeevan, H., Gegenwart, P., and Steglich, F. (2005). Yb-based heavy-fermion metal situated close to a quantum critical point. *Physical Review B (Condensed Matter and Materials Physics)*, 72:094411–4.

[Huang and Han, 1988] Huang, K. and Han, R. Q. (1988). *Solid State Physics*. High Education press, Beijing.

[Hutchings, 1964] Hutchings, M. T. (1964). Point-charge calculations of energy levels of magnetic ions in crystalline electric fields. *Solid State Physics*, 16:252.

[I Turek and Blugel, 2003] I Turek, J Kudrnovsky, G. B. and Blugel, S. (2003). Ab initio theory of exchange interactions and the curie temperature of bulk Gd. *Journal of Physics: Condensed Matter*, 15(17):2771–2782.

[Ikeda et al., 1984] Ikeda, K., Gschneidner, K. A., Stierman, R. J., Tsang, T.-W. E., and McMasters, O. D. (1984). Quenching of spin fluctuations in the highly enhanced paramagnets RCo_2 ($R = Sc, Y$, or Lu). *Physical Review B*, 29:5039.

[Jamieson and Manchester, 1972] Jamieson, H. C. and Manchester, F. D. (1972). The magnetic susceptibility of Pd, PdH and PdD between 4 and 300 K. *J. Phys. F: Met. Phys.*, 2:323–336.

[Jeong et al., 2006] Jeong, T., Kyker, A., and Pickett, W. E. (2006). Fermi velocity spectrum and incipient magnetism in $TiBe_2$. *Physical Review B (Condensed Matter and Materials Physics)*, 73:115106–9.

[Kadowaki and Woods, 1986] Kadowaki, K. and Woods, S. B. (1986). Universal relationship of the resistivity and specific heat in heavy-fermion compounds. *Solid State Communications*, 58:507–509.

[Kasuya, 1956] Kasuya, T. (1956). A theory of metallic ferro- and antiferromagnetism on Zener's model. *Progress of Theoretical Physics*, 16:45.

[Kittel, 1996] Kittel, C. (1996). *Introduction to solid state physics*. Wiley New York.

[Knapp and Jones, 1972] Knapp, G. S. and Jones, R. W. (1972). Determination of the electron-phonon enhancement factor from specific-heat data. *Physical Review B*, 6:1761.

[Ko et al., 2008] Ko, H., Safa-Sefat, A., Jia, S., Bud'ko, S. L., Canfield, P. C., and Miller, G. J. (2008). unpublished.

[Kondo, 1964] Kondo, J. (1964). Resistance minimum in dilute magnetic alloys. *Progress of Theoretical Physics*, 32:37.

[Kontani, 2004] Kontani, H. (2004). Generalized kadowaki-woods relation in heavy fermion systems with orbital degeneracy. *Journal of the Physical Society of Japan*, 73:515.

[Kripyakevich and Zarechnyuk, 1968] Kripyakevich, P. I. and Zarechnyuk, O. S. (1968). RCr_2Al_{20} compounds in systems of rare earth metals and calcium, and their crystal structures. *Dopov. Akad. Nauk Ukr. RSR, Ser. A*, 30:364–367.

[Larkin and Mel'nikov, 1972] Larkin, A. I. and Mel'nikov, V. I. (1972). Magnetic impurities in an almost magnetic metal. *Soviet Physics JETP*, 34(3):656–661.

[Larson et al., 2004] Larson, P., Mazin, I. I., and Singh, D. J. (2004). Magnetism, critical fluctuations, and susceptibility renormalization in Pd. *Physical Review B (Condensed Matter and Materials Physics)*, 69(6):064429.

[Lea et al., 1962] Lea, K. R., Leask, M. J. M., and Wolf, W. P. (1962). the raising of angular momentum degeneracy of f-electron terms by cubic crystal fields. *J. Phys. Chem. Solids*, 23:1381–1405.

[Lemaire, 1966] Lemaire, R. (1966). Magnetic properties of the intermetallic compounds of cobalt with the rare earth metals and yttrium. *Cobalt*, 33:201–211.

[Maebashi et al., 2002] Maebashi, H., Miyake, K., and Varma, C. M. (2002). Singular effects of impurities near the ferromagnetic quantum-critical point. *Physical Review Letters*, 88(22):226403.

[Matsukura et al., 1998] Matsukura, F., Ohno, H., Shen, A., and Sugawara, Y. (1998). Transport properties and origin of ferromagnetism in (Ga, Mn)As. *Phys. Rev. B*, 57:R2037–R2040.

[Matthias et al., 1978] Matthias, B. T., Giorgi, A. L., Struebing, V. O., and Smith, J. L. (1978). Itinerant antiferromagnetism of $TiBe_2$. *Physics Letters A*, 69(3):221.

[Mattis, 1965] Mattis, D. C. (1965). *The Theory of magnetism: an introduction to the study of cooperative phenomena*. Harper and Row, New York.

[Miyake et al., 1989] Miyake, K., Matsuura, T., and Varma, C. M. (1989). Relation between resistivity and effective mass in heavy-fermion and A15 compounds. *Solid State Communications*, 71:1149–1153.

[Moriya, 1985] Moriya, T. (1985). *Spin fluctuations in itinerant electron magnetism*. Springer-Verlag, Berlin.

[Morosan, 2005] Morosan, E. (2005). *Field-induced magnetic phase transitions and correlated electronic states in the hexagonal* RAgGe *and* RPtIn *series*. PhD dissertation, Iowa State University.

[Morosan et al., 2005] Morosan, E., Bud'ko, S. L., and Canfield, P. C. (2005). Magnetic ordering and effects of crystal electric field anisotropy in the hexagonal compounds RPtIn(R = Y, Gd − Lu). *Physical Review B*, 72(1):014425–16.

[Morosan et al., 2006] Morosan, E., Bud'ko, S. L., Mozharivskyj, Y. A., and Canfield, P. C. (2006). Magnetic-field-induced quantum critical point in YbPtIn and $YbPt_{0.98}In$ single crystals. *Physical Review B (Condensed Matter and Materials Physics)*, 73:174432–17.

[Movshovich et al., 1994] Movshovich, R., Lacerda, A., Canfield, P. C., Thompson, J. D., and Fisk, Z. (1994). Low-temperature phase diagram of YbBiPt. In *The 6th joint magnetism and magnetic materials (MMM)-intermag conference*, volume 76, pages 6121–6123, Albuquerque, New Mexico (USA). AIP.

[Moze et al., 1998] Moze, O., Tung, L. D., Franse, J. J. M., and Buschow, K. H. J. (1998). Crystal structure and magnetic properties of CeV_2Al_{20} and $CeCr_2Al_{20}$. *Journal of Alloys and Compounds*, 268:39–41.

[Mulay and Boudreaux, 1976] Mulay, L. N. and Boudreaux, E. A. (1976). *Theory and applications of molecular diamagnetism.* Wiley.

[Mydosh, 1993] Mydosh, J. A. (1993). *Spin Glass: An Experimental Introduction.* Taylor and Francis, London.

[Mydosh et al., 1968] Mydosh, J. A., Budnick, J. I., Kawatra, M. P., and Skalski, S. (1968). Magnetic ordering in palladium-iron alloys. *Physical Review Letters*, 21(18):1346.

[Myers, 1999] Myers, K. D. (1999). *Anisotropic magnetization and transport properties of* $RAgSb_2$(R = Y, La − Nd, Sm, Gd − Tm). PhD dissertation, Iowa State University.

[Myers et al., 1999] Myers, K. D., Bud'ko, S. L., Fisher, I. R., Islam, Z., Kleinke, H., Lacerda, A. H., and Canfield, P. C. (1999). Systematic study of anisotropic transport and magnetic properties of $RAgSb_2$(R = Y, La − Nd, Sm, Gd − Tm). *Journal of Magnetism and Magnetic Materials*, 205:27–52.

[N Tsujii and Kosuge, 2003] N Tsujii, K. Y. and Kosuge, K. (2003). Deviation from the kadowaki-woods relation in Yb-based intermediate-valence systems. *Journal of Physics: Condensed Matter*, 15(12):1993–2003.

[Nasch et al., 1997] Nasch, T., Jeitschko, W., and Rodewald, U. C. (1997). Ternary rare earth transition metal zinc compounds RT_2Zn_{20} with $T = Fe, Ru, Co, Rh,$ andNi. *Zeitschrift fuer Naturforschung, B: Chemical Sciences*, 52:1023–1030.

[Neumann and Ziebeck, 1995] Neumann, K. U. and Ziebeck, K. R. A. (1995). Arrott plots for rare earth alloys with crystal field splitting. *Journal of Magnetism and Magnetic Materials*, 140-144:967–968.

[Nieuwenhuys, 1975] Nieuwenhuys, G. J. (1975). Magnetic behaviour of cobalt, iron and manganese dissolved in palladium. *Advances in Physics*, 24:515–591.

[Pamplin, 1980] Pamplin, B. R. (1980). *Crystal Growth*. Pergamon.

[Perlov et al., 2000] Perlov, A. Y., Halilov, S. V., and Eschrig, H. (2000). Rare-earth magnetism and adiabatic magnon spectra. *Phys. Rev. B*, 61(6):4070–4081.

[Pfleiderer et al., 2001] Pfleiderer, C., Uhlarz, M., Hayden, S. M., Vollmer, R., v. Lohneysen, H., Bernhoeft, N. R., and Lonzarich, G. G. (2001). Coexistence of superconductivity and ferromagnetism in the d-band metal $ZrZn_2$. *Nature*, 412:58–61.

[Pierre, 1982] Pierre, J. (1982). in *Magnetism of Metals and Alloys* Edited by M. Cyrot, pages 245–293. North-Holland.

[Rajan, 1983] Rajan, V. T. (1983). Magnetic susceptibility and specific heat of the coqblin-schrieffer model. *Phys. Rev. Lett.*, 51:308–311.

[Rasul and Hewson, 1984] Rasul, J. W. and Hewson, A. C. (1984). Bethe ansatz and $1/n$ expansion results for n-fold degenerate magnetic impurity models. *Journal of Physics C: Solid State Physics*, 17:2555–2573.

[Ruderman and Kittel, 1954] Ruderman, M. A. and Kittel, C. (1954). Indirect exchange coupling of nuclear magnetic moments by conduction electrons. *Phys. Rev.*, 96(1):99.

[Saiga et al., 2008] Saiga, Y., Matsubayashi, K., Fujiwara, T., Kosaka, M., Katano, S., Hedo, M., Matsumoto, T., and Uwatoko, Y. (2008). Pressure-induced magnetic transition in a single crystal of $YbCo_2Zn_{20}$. *Journal of the Physical Society of Japan*, 77:053710.

[Schubert, 1964] Schubert, K. (1964). *Kristallstrukturen zweikomponentiger Phasen*. Springer-Verlag, Berlin/Göttingen/Heidelberg.

[Seeger et al., 1995] Seeger, M., Kronmüller, H., and Blythe, H. J. (1995). The magnetic phase transition in $ZrZn_2$. *Journal of Magnetism and Magnetic Materials*, 139:312–322.

[Shannon, 1976] Shannon, R. D. (1976). Revised effective ionic radii and systematic studies of interatomic distances in halides and chalcogenides. *Acta crystallographica. Section A, Crystal physics, diffraction, theoretical and general crystallography*.

[Sheldrick and SHELXTL, 2000] Sheldrick, G. M. and SHELXTL, D. (2000). Windows/NT version 6.12, bruker analytical X-ray instruments. *Inc., Madison, WI, USA*.

[Shimizu, 1961] Shimizu, M. (1961). Effects of s-d exchange interaction and temperature-independent paramagnetism on susceptibilities of nickel, palladium and platinum. *Journal of the Physical Society of Japan*, 16:1114.

[Shimizu, 1981a] Shimizu, M. (1981a). Itinerant electron magnetism. *Reports on Progress in Physics*, 44(4):329–409.

[Shimizu, 1981b] Shimizu, M. (1981b). Itinerant electron metamagnetism. *Journal de Physique*, 43:155–163.

[Shimizu et al., 1963] Shimizu, M., Takahashi, T., and Katsuki, A. (1963). Magnetic susceptibility and electronic specific heat of transition metals and alloys II. Pd metal and $Pd-Ag$ and $Pd-Rh$ alloys. *Journal of the Physical Society of Japan*, 18:240–248.

[Stevens, 1952] Stevens, K. W. H. (1952). Matrix elements and operator equivalents connected with the magnetic properties of rare earth ions. *Proceedings of the Physical Society. Section A*, 65:209–215.

[Stewart, 1984a] Stewart, A. M. (1984a). Paramagnetic properties of the RCo_2 compounds (R=rare earth). *Journal of Physics C: Solid State Physics*, 17:1557–1574.

[Stewart, 1984b] Stewart, G. R. (1984b). Heavy-fermion systems. *Reviews of Modern Physics*, 56:755.

[Stewart, 2001] Stewart, G. R. (2001). Non-fermi-liquid behavior in d- and f-electron metals. *Reviews of Modern Physics*, 73:797.

[Stewart, 2006] Stewart, G. R. (2006). Addendum: Non-fermi-liquid behavior in d- and f-electron metals. *Reviews of Modern Physics*, 78:743–11.

[Stoe, 2002] Stoe, X. (2002). *AREA-Software Suite for the STOE IPDS II*. Stoe & Cie GmbH, Darmstadt, Germany.

[Szytula and Leciejewicz, 1994] Szytula, A. and Leciejewicz, J. (1994). *Handbook of Crystal Structures and Magnetic Properties of Rare Earth Intermetallics*. CRC Press.

[Takahashi and Shimizu, 1965] Takahashi, T. and Shimizu, M. (1965). Magnetic properties of Pd metal and $Pd-Rh$ and $Pd-Ag$ alloys containing Co and Fe atoms. *Journal of the Physical Society of Japan*, 20:26–35.

[Tanaka and Harima, 1998] Tanaka, S. and Harima, H. (1998). Mass enhancement factor and fermi surface in YCo_2. *Journal of the Physical Society of Japan*, 67:2594–2597.

[Thiede et al., 1998] Thiede, V. M. T., Jeitschko, W., Niemann, S., and Ebel, T. (1998). $EuTa_2Al_{20}$, $Ca_6W_4Al_{43}$ and other compounds with $CeCr_2Al_{20}$ and $Ho_6Mo_4Al_{43}$ type structures and some magnetic properties of these compounds. *Journal of Alloys and Compounds*, 267:23–31.

[Timm et al., 2005] Timm, C., Raikh, M. E., and von Oppen, F. (2005). Disorder-induced resistive anomaly near ferromagnetic phase transitions. *Physical Review Letters*, 94:036602.

[Tsujii et al., 2005] Tsujii, N., Kontani, H., and Yoshimura, K. (2005). Universality in heavy fermion systems with general degeneracy. *Physical Review Letters*, 94(5):057201.

[Villars and Calvert, 1996] Villars, P. and Calvert, L. D. (1996). *Pearson's handbook of crystallographic data for intermetallic phases*. ASM International Materials Park, OH.

[Wiegmann, 1980] Wiegmann, P. B. (1980). Exact solution of *sd* exchange model at $t = 0$. *Soviet Physics JETP Letter*, 31:392.

[Wilson, 1953] Wilson, A. H. (1953). *The theory of metals*. Cambridge University Press.

[Wilson, 1975] Wilson, K. G. (1975). The renormalization group: Critical phenomena and the kondo problem. *Reviews of Modern Physics*, 47:773.

[Wohlfarth and Rhodes, 1962] Wohlfarth, E. P. and Rhodes, P. (1962). Collective electron metamegnetism. *Philosophical Magazine*, 7:1817.

[Yamada, 1993] Yamada, H. (1993). Metamagnetic transition and susceptibility maximum in an itinerant-electron system. *Phys. Rev. B*, 47(17):11211–11219.

[Yamada and Terao, 1998] Yamada, H. and Terao, K. (1998). High-field magnetism of $TiBe_2$. *Physica B: Condensed Matter*, 246-247:502–504.

[Yelland et al., 2005] Yelland, E. A., Yates, S. J. C., Taylor, O., Griffiths, A., Hayden, S. M., and Carrington, A. (2005). Ferromagnetic properties of $ZrZn_2$. *Physical Review B (Condensed Matter and Materials Physics)*, 72:184436–9.

[Yeung et al., 1986] Yeung, I., Roshko, R. M., and Williams, G. (1986). Arrott-plot criterion for ferromagnetism in disordered systems. *Phys. Rev. B*, 34:3456–3457.

[Yosida, 1957] Yosida, K. (1957). Magnetic properties of $Cu-Mn$ alloys. *Phys. Rev.*, 106(5):893–898.

[Zener, 1951] Zener, C. (1951). Interaction between the d shells in the transition metals. *Physical Review*, 81:440.

[Ziman, 1979] Ziman, J. M. (1979). *Principles of the Theory of Solids*. Cambridge University Press.